



UNIVERSITA' DEGLI STUDI DI CATANIA

Ph.D. in Biotechnology
Curricula Molecular Biotechnology
(XXXV cycle)

Salvatore Antonio Maria Cubisino

**Channel-forming proteins: from
mitochondria to SARS-CoV-2.**

**Functional and structural characterization using
respirometric and molecular dynamics techniques**

Ph.D. thesis

Supervisor: Prof. Vito De Pinto

Coordinator: Prof. Vito De Pinto

Academic Years 2019-2022

*“Don’t you worry, child
See heaven’s got a plan for you”
(Swedish house mafia)*

Affiliations

1. Department of Biomedical and Biotechnological Sciences, University of Catania, Catania, Italy
2. Department of Physics, University of Cagliari, I-09042 Monserrato (Ca), Italy

Other research experiences

4 months in the laboratory of prof. Ulrich Kleinekathofer at the Jacobs University of Bremen, Germany

3 months in the laboratory of prof. Matteo Ceccarelli at the University of Cagliari , Italy

Keywords

High-Resolution Respirometry, mitochondria, VDAC1, α -synuclein, MPP+, Parkinson's disease, SH-SY5Y cells, HAP-1 cells, SARS-CoV-2, COVID-19, Envelope protein, Molecular Dynamics, Planar Lipid Bilayer

Abbreviation

OMM	Outer Mitochondrial Membrane
IMM	Inner Mitochondrial Membrane
MRC	Mitochondrial Chain Respiratory
HRR	High Resolution Respirometry
SUIT	Substrate-Uncoupler-Inhibitor Titration
FCR	Flux Control Ratio
POS	Polarographic Oxygen Sensor
VDAC	Voltage Dependent Anion-selective Channel
APAF-1	Apoptotic Protease Activating Factor 1
αSyn	α -synuclein
MPTP	1-methyl-4-phenyl-1,2,3,6-tetrahydropyridine
MPP+	1-methyl-4-phenylpyridinium
MAO	Monoamine Oxidase
ATP	Adenosine triphosphate
ADP	Adenosine diphosphate
NAD	Nicotinamide adenine dinucleotide
NADP	Nicotinamide adenine dinucleotide phosphate
ROS	Reactive Oxygen Species
SARS-CoV-2	Severe Acute Respiratory Syndrome coronavirus 2
MERS	Middle East Respiratory Syndrome
E2	Envelope protein from SARS-CoV-2
S	Spike protein
N	Nucleocapsid protein
M	Membrane protein
E	Envelope protein

PLB	Planar Lipid Bilayer
MD	Molecular Dynamics
DiPhPC	1,2-Diphytanoyl-3-phosphocholine
DOPS	1,2-Dioleoyl-sn-glycero-3-phospho-L-serine
DOPC	1,2-Dioleoyl-sn-glycero-3-phosphocoline
DOPE	1,2-Dioleoyl-sn-glycero-3-phosphoethanolamine
RMSD	Root Mean Square Deviation

SOMMARIO

Le proteine sono macromolecole formate anche da migliaia di unità di amminoacidi unite fra loro per mezzo di legami peptidici, in modo da formare catene variamente ripiegate la cui struttura tridimensionale è in stretta relazione con la funzione biologica svolta; in funzione della loro funzionalità le proteine possono essere distinte in diversi gruppi, tra i quali gli enzimi, le proteine di trasporto, le proteine strutturali, le proteine di difesa e le proteine regolatrici.

In funzione della loro selettività, le proteine di trasporto possono essere distinte in porine, canali ionici. A prescindere lo studio di tali proteine è di particolare interesse perché favoriscono il passaggio da un ambiente cellulare all'altro, regolando i vari processi cellulari. Tra le principali porine riconosciute, vi è VDAC (Voltage Dependent Anion Channel), che tra le sue funzioni ha il trasporto di numerose molecole, tra cui ioni e metaboliti vari, tra cui composti vari coinvolti nei processi neurodegenerativi, come gli aggregati di α -sinucleina, principali costituenti dei corpi di Lewy.

In questo lavoro di tesi, viene approfondito il ruolo che VDAC1 può avere nella regolazione delle funzioni di respirazione mitocondriale, attraverso specifiche tecniche di respirometria. In maniera analoga verrà analizzato anche il ruolo degli aggregati di α -sinucleina e della tossina MPP+, entrambe coinvolte nell'insorgenza del morbo di Parkinson. In tutti i lavori qui riportati sono stati valutati i vari stati di respirazione, in funzione di specifici stimoli applicati, in modo da valutare la risposta della catena respiratoria ma più in generale la variazione delle funzioni cellulari.

Nella seconda parte di questo lavoro di tesi, invece verrà caratterizzata un canale ionico sia dal punto di vista strutturale che da quello funzionale. Si tratta della envelope protein, una delle principali proteine strutturali derivanti dal virus SARS-CoV-2. Tale proteina, inizialmente tradotta in forma monomerica, tende ad oligomerizzare formando un pentamero, al cui centro della struttura è presente un poro che favorisce il trasporto di corrente ionica. Ai fini di comprendere l'esatta funzione di questo poro sono state eseguite delle simulazioni di dinamica molecolare, delle predizioni di docking e sono stati effettuati degli esperimenti di elettrofisiologia, attraverso l'applicazione della tecnica Planar Lipid Bilayer. I risultati ottenuti

hanno permesso di evidenziare una possibile distribuzione strutturale in grado di giustificare l'attività ionica del canale, ma soprattutto il meccanismo di regolazione di flusso ionico dovuto principalmente al legame di ioni calcio proprio lungo la struttura della stessa proteina E2.

ABSTRACT

Proteins are macromolecules consisting of up thousands of amino acids units linked by peptide bonds to form variously folded chains whose three-dimensional structure is closely related to the biological function they perform. Depending on their functionality, proteins can be classified into different groups, including enzymes, transport proteins, structural proteins, defence proteins and regulatory proteins.

Depending on their selectivity, transport proteins can be divided into porins and ion channels. However, the study of such proteins is of particular interest because they facilitate the passage from one cellular environment to another and regulate various cellular processes. Among the most important known porins is VDAC (Voltage Dependent Anion Channel), whose functions include the transport of many molecules, including ions and various metabolites and compounds involved in neurodegenerative processes, such as α -synuclein aggregates, the main constituents of Lewy bodies.

This thesis will investigate the role that VDAC1 may play in the regulation of mitochondrial respiratory functions using specific respirometry techniques. Similarly, the role of α -synuclein aggregates and the MPP⁺ toxin, both of which are implicated in the pathogenesis of Parkinson's disease, will also be analysed. In all the work reported here, the different respiratory states have been evaluated, as a function of specific stimuli applied, in order to assess the response of the respiratory chain but more generally the variation in cellular functions.

In the second part of this thesis, an ion channel will be characterised both structurally and functionally. This is the envelope protein, one of the major structural proteins of the SARS-CoV-2 virus. This protein, which is initially translated in monomeric form, tends to oligomerise to form a pentamer, with a pore at the centre of structure, which favours the transport of ionic currents. In order to understand the exact function of this pore, molecular dynamics simulations, docking predictions and electrophysiological experiments were carried out using the Planar Lipid Bilayer technique. The results obtained have made it possible to highlight a

possible structural distribution capable of justifying the ionic activity of the channel, but above all the mechanism of ionic flux regulation due mainly due to the binding of calcium ions along the structure of the E2 protein itself.

TABLE OF CONTENTS

1	Introduction	1
2	Respirometric studies about the VDAC1 and neurodegenerative molecules roles in respiration process.....	4
2.1	HRR methodology	5
2.2	Respirometric states	7
2.2.1	Routine-state	7
2.2.2	Oxphos-state	8
2.2.3	Leak-state	9
2.2.4	ET-state.....	10
2.2.5	Rox-state	11
2.3	Aim of the respirometric analysis	12
2.4	Macromolecules and chemicals involved in the experiments	13
2.4.1	Voltage dependent anion channel	13
2.4.2	α -synuclein	16
2.4.3	MPP+	18
2.5	Results and discussions of the respirometric analysis.....	19
2.5.1	VDAC1 knockout effects mitochondrial oxygen consumption triggering a rearrangement of ETC by impacting on complex I activity.....	19
2.5.2	α -Synuclein A53T promotes mitochondrial proton gradient dissipation and depletion of the organelle respiratory reserve in a neuroblastoma cell line	20
2.5.3	High-Resolution Respirometry reveals MPP+ mitochondrial toxicity mechanism in a cellular model of Parkinson's disease	21
3	Computational and electrophysiological studies on structure and functionalities of the envelope protein from SARS-CoV-2.....	23
3.1	What is a Virus?	23
3.2	The coronaviridae family	24
3.3	SARS-CoV- 2	26
3.4	Replication process of SARS-CoV-2	26
3.5	Envelope Protein	29
3.6	Aim of the characterization of the envelope protein	30
3.7	Brief introduction to techniques	31
3.7.1	Planar lipid Bilayer.....	31
3.7.2	Molecular Dynamics simulations	33
3.7.3	Binding-site prediction	38

3.8 Results and discussion of the characterization of the envelope protein.....	40
3.8.1 Material and Methods	40
3.8.2 Results.....	42
3.8.3 Conclusions	50
4. General Conclusions	52
Other Activities	54
References	55
Article 1 - VDAC1 knockout effects mitochondrial oxygen consumption triggering a rearrangement of ETC by impacting on complex I activity, published on IJMS, 2023 Feb 12; 24(4):3687.....	73
Article 2 - α -Synuclein A53T promotes mitochondrial proton gradient dissipation and depletion of the organelle respiratory reserve in a neuroblastoma cell line, published on Life (Basel). 2022 Jun 15; 12(6):894.....	95
Articles 3 - High-Resolution Respirometry reveals MPP+ mitochondrial toxicity mechanism in a cellular model of Parkinson's disease, published on IJMS. 2020 Oct 22; 21 (21):7809	106
Article 4 - Post-translational modification analysis of VDAC1 in ALS-SOD1 model cells reveals specific asparagine and glutamine deamidation, published on Antioxidants (Basel). 2020 Dec 2;9(12):1218.....	122
Article 5 - Specific Post-translational Modifications of VDAC3 in ALS-SOD1 Model Cells Identified by High-Resolution Mass Spectrometry, published on IJMS 2022 Dec 13; 23(24):15853	145

1. INTRODUCTION

One of the things that makes the world of science so fascinating is the possibility of discovering something new every day. This includes protein characterization, whose discoveries had a major impact on many scientific fields, including medicine and pharmacology. In fact, thanks to research into structural and functional properties of a given protein complex, it has been possible to develop new methods of detecting pathologies, new drugs and new theories, that can be used to improve several aspects of everyday life. In the biomedical field, nowadays, one of the most important research topics is the pathological aspect of neurodegeneration. Much remains to be indeed discovered about such kind of diseases as Parkinson's, Alzheimer's, amyotrophic lateral sclerosis, etc.

Recently, a notable paper showed that a simple interaction between a channel protein present in the outer mitochondrial membrane, VDAC1, the Voltage Dependent Anion-selective Channel isoform 1, and the mutated form of an enzyme controlling cell radical compounds, superoxide dismutase 1 (SOD1), may be crucial in the onset of ALS. Moreover, a putative agonist compound to counteract the effect of this interaction has been identified [35]. This work was the starting point for a series of studies aimed at assessing the impact that the involvement of specific proteins, in particular VDAC1, may have on the pathogenesis of various diseases, with a particular focus on neurodegeneration. VDAC1 is a key protein in the regulation of many cellular functions, as it facilitates the passage of many molecules from one environment to within the cell [45]. Given this definition and the fact that among the various metabolites that pass through this porin are ADP and ATP, the energetic exchange money produced by cellular respiration, we wanted to test the effects of deletion/inhibition of VDAC1 on this process. In addition, VDAC1 promotes the passage through the membrane of other molecules with fundamental functions in neurodegeneration. These include α -synuclein monomers. Aggregates of it form Lewy bodies [65], one of the main components leading to the onset of Parkinson's disease. In particular, mutations in the α -synuclein gene have been shown not only to increase the formation of these aggregates, but also to affect cellular respiratory functions by inhibiting some of the subunits that make up the complexes of the mitochondrial respiratory chain. In parallel with the research on the effects of α -synuclein, studies have also been carried out on a toxin, MPP⁺, which is also involved in the

pathology of Parkinson's disease, and in this case too, a possible variation in the properties of the complexes involved in cellular respiration has been taken into account.

In the case of VDAC1, as well as α -synuclein and MPP+, a respirometry-based study was carried out using a special technique, high-resolution respirometry, which makes it possible to assess in real time how oxygen consumption occurs at the cellular level by stimulating the mitochondrial respiratory chain in an appropriate way, using specific substrates. In this way, it is possible to see the effects of possible deletion/inhibition of VDAC1 or treatment of cells with molecules that lead to the onset of neurodegeneration, and to develop strategies to counteract these effects.

Unfortunately, research into neurodegeneration is not the only thing that has happened recently. Just in the last few years, everyone's life has been affected by the onset of a pandemic due to the rapid spread of the SARS-CoV-2 virus. Thousands of lives were lost to this virus, mainly due to a lack of preparedness in dealing with an "enemy" about which very little was known. The research world was therefore mobilised to find possible solutions, which could be drugs or vaccines, to counteract the pathological effects of such incumbent infection. SARS-CoV-2 is a single-stranded RNA virus that, once inside the cell, encodes a large number of proteins, including four structural proteins that tend to destabilize the functional balance in the cellular environment [104-107]. These proteins have been the subject of a great deal of research, precisely because their characterization has provided enough information to develop therapies that might even slow down the course of the infection. In reality, no definitive solution has yet been found to counteract the effects of this virus. For this reason, one of these structural proteins, the envelope protein, has been studied and characterised both structurally and functionally, with the aim of understanding whether it is possible to achieve an inhibitory effect on the virus by acting directly on this protein. A computational approach will be presented to provide more information on the three-dimensional arrangement of the envelope protein once it has reached the membrane, and an experimental approach will be presented to provide a better understanding of the effects due to the activity of this compound.

Although from an experimental point of view, the projects described here seem to be very far apart, in reality they are closer than ever. In fact, both the analysis of VDAC1 and that of the envelope protein and the molecules involved in neurodegeneration share a common goal: the structural and functional characterization of the protein. In addition, both proteins have

pore-forming features. Without the knowledge of the protein organization, a real starting point, which, as will be shown in the following chapters, can be achieved in several ways, it is not possible to get a possible final solution capable of counteracting the effects of any pathology. For this reason, this thesis will present different approaches with the sole aim of obtaining a complete characterization of proteins in order to fully understand which features can be exploited to develop scientific innovations, both from a biomedical and a biotechnological point of view.

2. RESPIROMETRIC STUDIES ABOUT THE VDAC1 AND NEURODEGENERATIVE MOLECULES ROLES IN RESPIRATION PROCESS

Mitochondria are one of the major organelles in eukaryotic cells. They are defined as the powerhouse of the cell because they produce ATP through oxidative phosphorylation. In particular, the outer mitochondrial membrane (OMM) contains protein channels, such as VDAC (Voltage Dependent Anion Channel), that allows the ATP/ADP exchange with the cytosol [1]. Conversely the inner mitochondrial membrane (IMM) contains all the protein complexes that constitute the mitochondrial respiratory chain (MRC), responsible for ATP production following the reaction of oxygen with the products of various metabolic pathways. In fact, the mechanism that allows oxygen to interact involves a series of redox reactions that take place in the different complexes of the MRC. Each electron donor (the initial electrons are derived coenzymes such as NADH and FADH₂) gives electrons to an acceptor with a higher redox potential, which in turn gives these electrons to another acceptor, until these electrons are passed on to oxygen, the final acceptor in the chain. The mitochondrial respiratory chain consists of four complexes plus ATP synthase:

- **Complex I or NADH dehydrogenase:** it receives two electrons from NADH, which are transferred to the coenzyme Q via a series of iron-sulphur complex. A total of four protons are transferred from complex I to the intermembrane space.
- **Complex II or Succinate dehydrogenase:** it receives two electrons from the FADH₂, which is linked to succinate oxidation in the Krebs cycle. Like complex I, electrons are transferred to coenzyme Q, but complex II doesn't act as a proton pump.
- **Complex III or cytochrome c oxidoreductase:** it accepts electrons from coenzyme Q and transfers them to cytochrome c. For each pair of electrons, four protons are transferred to the complex IV
- **Complex IV or cytochrome c oxidase:** it accepts electrons from cytochrome c, favoring oxygen reduction to water. This complex produces two protons from each pair of electrons.

The free energy (ΔG) provided by the electron flux is also related to the generation of a proton gradient across the mitochondrial membrane. Thus, part of this free energy is used to transport protons into the intermembrane space, while the other part is maintained as an electrochemical potential. The proton flux moves from the intermembrane space into the mitochondrial matrix, mediated by specific IMM channels, and generates the free energy for ATP synthesis within the ATP synthase. In this process the proton flux is related to the ADP phosphorylation.

One way of describing mitochondrial properties in relation to a specific cellular system is to analyze the oxidative phosphorylation process described above in as much detail as possible. To do this, a specific oxygraphic approach called High Resolution Respirometry (HRR) could be applied, using the Oroboros O2k technologies. The advantage of an oxygraphic experiment is that it can analyze small amounts of samples of different types, such as intact cells, isolated mitochondria, permeabilized cells and homogenate tissue [2,3,4,5]. In HRR, the protocols used are mainly aimed at evaluating changes in oxygen concentrations in relation to the activity of the protein complexes that constitute the mitochondrial respiratory chain. In order to obtain a wide range of information, each protocol provides for the addition of substrates that specifically modify the functionality of the complexes; the added substrates can be either stimulators or inhibitors of the respiratory chain. The series of protocols that could be performed during an HRR experiment is called SUIT (Substrate-Uncoupler-Inhibitor Titration).

2.1 HRR METHODOLOGY

The Oroboros O2k instrumentation gave us the ability to analyze two different samples simultaneously in two different respirometric chambers (Fig.1). Each of these has of total volume of 2cm^3 and can therefore hold 2mL of cell volume. A magnetic stirrer, is placed inside the chamber and maintained at a constant speed of 750rpm: this magnet has the function of keeping the solution agitated by uniformly promoting the distribution of oxygen in the chamber. The respirometric chamber is internally connected with the Polarographic Oxygen Sensor (POS), an electrode whose purpose is to quantify the amount of oxygen consumed by the mitochondria during the experiment. The POS is able to quantify oxygen thanks to the presence of an oxygen-permeable membrane that promotes a process of electrical polarization; therefore, this membrane is able to detect oxygen as a function of its chemical activity (since oxygen is naturally present in gaseous form, its chemical activity is expressed

as a function of pressure measurements). This detection leads to the formation of electrical dipoles between the cathode and anode of the electrode. The electric dipoles obtained allow the formation of an electric field whose intensity is directly proportional to the oxygen pressure contained in the respirometric chamber [6]. This electric field is detected by a special detector which allows it to be transferred to a display so that the data obtained can be visualized in a special software called DatLab, which allows the progress of the oxygen analysis to be followed in real time.

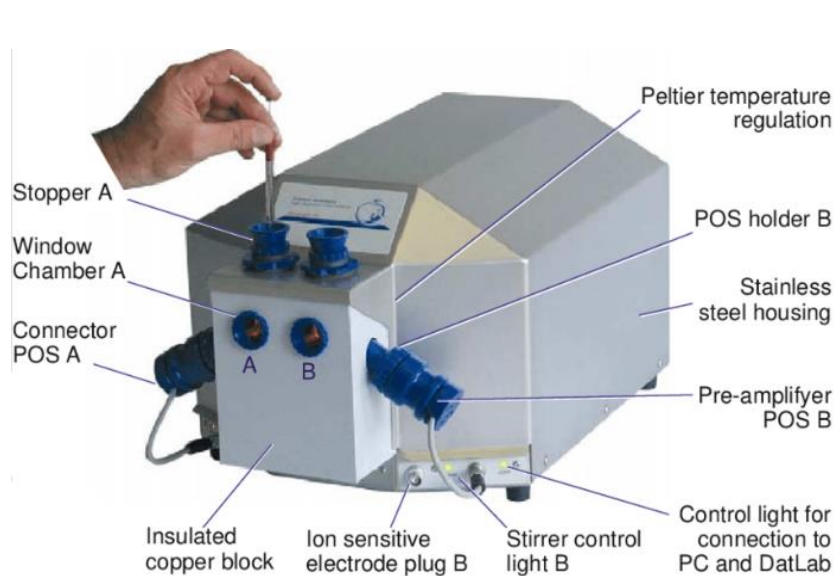


Fig.1 Schematic representation of a respirometer from Oroboros O2k technologies. The letters A and B indicate the respirometric chambers that can hold 2mL of volume

However, the main parameters monitored during the oxygraphy experiment are the oxygen concentration $[O_2]$ in the chamber and the derived oxygen flow J_{O_2} .

Oxygen concentration $[O_2]$ indicates the exact amount of oxygen present in the respirometric chamber as a function of time. To quantify this function, a time interval of one second is set. Therefore, all data displayed on the DatLab are related to the amount of oxygen detected for each second of the experiment. Conventionally, the oxygen concentration is represented by the blue line in the final graph obtained. Mathematically, the oxygen concentration is determined by the following law [7]

$$[O_2](t) = C_{\text{raw}}(t) + \tau \frac{dC_{\text{raw}}}{dt} \quad (1)$$

Where C_{raw} is an exponential function obtained by the quantification of oxygen activity, while τ is a temporal exponential constant derived from the electrode. Oxygen concentration is expressed in nmol/cm^3 or in μM .

The other parameter that is taken into account is the oxygen flow, J_{O_2} , which is the oxygen consumption that occurs during each step of the experiment. Similarly to concentration, oxygen flux is also a data point that is monitored as a function of time. Conventionally, oxygen flux is represented by a red line in the final graph obtained on DatLab. Mathematically, J_{O_2} is defined as the first derivative of the oxygen concentration [8]:

$$J_{O_2} = -\frac{d[O_2]}{dt} * 1000 - \{[O_2](t) * 0.025 - 1.5\} \quad (2)$$

The oxygen flux J_{O_2} is expressed in $\text{pmol}/(\text{s} * \text{cm}^3)$.

After careful analysis, these two parameters allow, to determine trends in mitochondrial function according to the oxygen consumed.

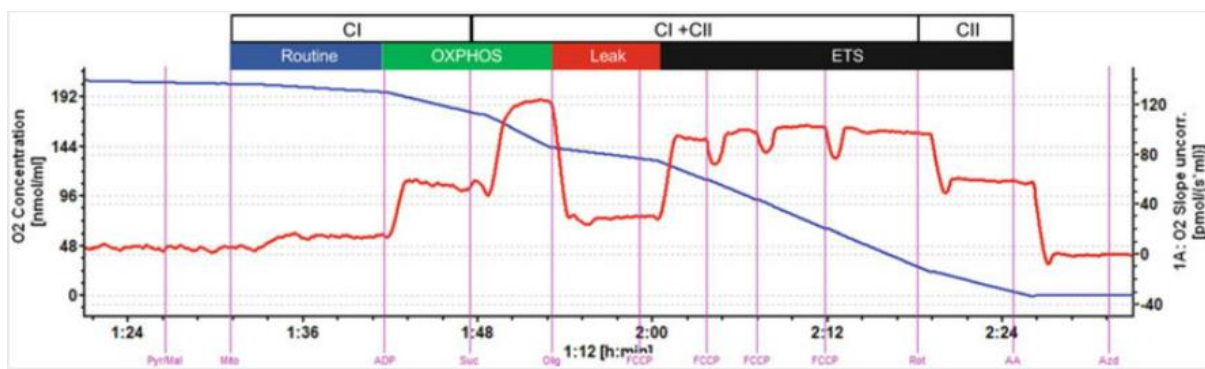


Fig.2 Reference respirometric curve shows in blue oxygen concentration variation, while in red oxygen flux is reported. Moreover, several respirometric states are reported (described with more detail in the next paragraph) [9]

2.2 RESPIROMETRIC STATES

Oxygen flow measurements are performed according to respiratory states and then by applying appropriate and specific SUI protocols. Regardless of the protocol used, the respiratory states that can be included in the analysis are ROUTINE, OXPHOS, LEAK, ET and ROX.

2.2.1 ROUTINE-state

The first respiratory state that is always observed, provided that we are working with intact cells and isolated mitochondria, is the ROUTINE (R) state. It is an intrinsic measure of

respiration that take place inside the cell. The ROUTINE value is obtained at the beginning of each respirometry experiment. Initially, there is an initial stabilization period of the samples, which is carried out in open chambers, promoting continuous oxygen exchange. Once the oxygen flow signal has stabilized, the respirometry chambers are closed, there is no oxygen exchange with the external environment and the O₂ consumption data of the sample under analysis is provided [10].

2.2.2 OXPHOS-state

The OXPHOS-state is the state in which the oxidative phosphorylation process is maximally stimulated, following the addition of specific stimulatory substrates, including:

- *Glutamate, malate* and *piruvate* that stimulate anaplerotic reactions of the tricarboxylic acid (TCA) cycle involving NAD⁺ co-enzyme and consequently stimulate the activity of complex I of the respiratory chain;
- *Succinate* that stimulates the activity of complex II of the respiratory chain
- *ADP* that activates the ATP production inside the ATP synthase

The oxygen flux value measured at this point, $J_{P \gg O_2}$, is derived from the combination of two individual flow factors: $J_{P \gg}$ and J_{O_2} . These two parameters depend on the amount of the charges that cross the inner mitochondrial membrane to stimulate the F_o subunit of ATP synthase and the charges that accumulate in the intermembrane space to form the proton gradient. From a mathematical point of view, the coupling that occurs in the course of the phosphorylation process and oxidation within the respiratory chain is more emphasized. The ratio indicating the progress of the coupling process is as follows:

$$\frac{P \gg}{O_2} = \frac{\left(\frac{H_{pos}^+}{O_2}\right)}{\left(\frac{H_{neg}^+}{P \gg}\right)} \quad (3)$$

Where with the ratio $\frac{H_{pos}^+}{O_2}$ indicates the stoichiometry related to the production of protons during the oxidation process, depending on the activity of complexes I, II and IV; while the ratio $\frac{H_{neg}^+}{P \gg}$ indicates the protons that have entered in the intermembrane space and have re-entered the mitochondrial matrix, promoting ATP synthesis [11].

In addition to evaluating the coupling process, the OXPHOS state can also be used to observe the contributions of each complex to the respiration process [12,13]. Initially, only substrates that tend to stimulate complex I activity can be added, increasing the level of NADH and thus measuring the non-phosphorylating activity of complex I. The condition just described is called *state-2*. Once the oxygen flux signal related to state 2 has stabilized, a saturating concentration of ADP is added to quantify the phosphorylation activity related only to the functioning of complex I (*state-3*). Then, succinate is added, so as to promote the stimulation of complex II in order to obtain the maximum OXPHOS value, as described in (3). To quantify the phosphorylating contribution of complex II, it is necessary to inhibit the activity of complex I by introducing rotenone, a molecule that acts directly on NADH dehydrogenase [14], by binding to the active site of the enzyme and no longer promoting its reduction process. The difference between the total OXPHOS and OXHPOS value obtained after the addition of rotenone is indicative of the degree of activity of complex II. With regard to the evaluation of complex III and complex IV, it is possible to inhibit the maximal value of OXPHOS respectively with antimycin A or sodium azide [15, 16].

2.2.3 LEAK-state

The leak-state is the state in which a dissipation of the proton gradient is observed, mainly due to inhibition of ATP synthase. The substrate added to achieve this state is oligomycin, which is recognized as the major inhibitor of the F_0 subunit of ATP synthase [17]. The inhibitory effect occurs precisely at the proton channel, which is critical for oxidative phosphorylation and as a direct effect there will be a significant reduction in the flow of electrons through the transport chain. Therefore, the protons produced by the activity of complex I, II and IV will begin to accumulate in the intermembrane space, increasing the proton concentration in the relative gradient and consequently the proton force. When a maximum value of protonic force for the electrochemical gradient is reached, inhibitory feedback is generated towards the respiratory chain complexes, leading to a decrease in oxygen consumption.

OXPHOS-related state-2, can therefore be considered a LEAK state, as it is the only state in which the phosphorylation process is not active. In this case, it is not necessary to add oligomycin as a substrate, but digitonin or saponin, reagents that promote cell permeabilization and consequent leakage of cell substrates (including ADP) [18]. When using

digitonin, it is important to use sufficient amounts to permeabilize only plasma membranes and not those associated with organelles. The amount of digitonin required for permeabilization varies depending on the cell line.

The difference between a LEAK state obtained by oligomycin addition and a LEAK state obtained by cell membrane permeabilization lies in the formation of the proton gradient: in state-2 there is partial gradient formation (no proton dissipation due to ATP synthase inhibition), whereas in the other LEAK state, the proton gradient is at its maximum value. Therefore, the expected result regarding oxygen consumption is to obtain a flux value $J_{O_2,L}$ higher than the flux $J_{O_2,0}$:

$$J_{O_2,L}(\text{LEAK state}) > J_{O_2,0} (\text{State 2})$$

2.2.4. ET-state

The electron transfer state (ET-state) is defined as the uncoupled state at a kinetically-saturating concentration of O_2 and occurs when an electron is transferred from one atom or molecule to another such chemical entity. In the specific case of respirometry, the transfer refers to protons that form the proton gradient in the intermembrane space. The chemical molecules involved in this process, are called protonophores, and they facilitate the movement of protons from the intermembrane space into the mitochondrial matrix. Once the transfer process has taken place, a dissipation phase of oxidative phosphorylation begins: in fact, the respiratory phase and thus the activity of the various complexes is again promoted. Normally, the ET-state is stimulated after the LEAK state has been observed, so no phosphorylation is observed as the ATP synthase is still inhibited by oligomycin. The transfer process is associated with the facilitated diffusion of protons, by means of the protonophores mentioned above. Molecules capable of performing this function include CCCP (Carbonyl cyanide m-chlorophenyl hydrazone) and FCCP (Carbonyl cyanide p-trifluoro-methoxyphenyl hydrazone) [19], molecules of acidic and hydrophobic nature that are able to bind the proton in the intermembrane space. As a result of proton binding, the protonophores acquire alkaline properties, that allow them to cross the inner mitochondrial membrane and reach the matrix space. During the evaluation of the ET-state, there is a $J_{P \gg} = 0$, while a maximum value is observed for the flux related to oxygen consumption, J_{O_2} . The total flux value measured in the ET-state (E) is always compared with the corresponding flux value of the OXPHOS-state(P):

- If $E > P$, the OXPHOS capacity is less than the ET capacity. Therefore, the phosphorylation system tends to limit respiratory function to the total energy requirements of the organism [20,21];
- If $E = P$, the phosphorylation capacity found in OXPHOS exceeds the ET capacity and therefore the OXPHOS capacity is not limited by the phosphorylation system in a particular electron transfer state. The ET-state varies between species and tissues and changes as a result of pathologies due to defects in the phosphorylation system. Furthermore this condition may be associated with putative mitochondrial damage [22];
- If $E < P$, the analysis system is damaged. This condition cannot be used to analyze the starting cell sample. In most cases, such artefacts can be caused either by an incorrect digitonin assay, during permeabilization, or by excessive oligomycin use during inhibition [23].

As the value of the ET-state represents the maximum value of respiration, it can be used to verify the actual operation of the respiratory chain. Flux Control Ratios (FCRs) are ratios of oxygen flux in different respiratory control states, normalized to the maximum flux in a common reference state. For the specific SUIT protocol adopted during the experiment it is possible to observe the trend of coupling process and substrate control independently. By comparing the FCRs of the different respiratory states analyzed, it is also possible to assess respiratory reserve, i.e. the total production of extra ATP that can be produced in the OXPHOS- or ROUTINE-state in the event of an energy demand [24].

2.2.5 ROX-state

ROX status is the final step in any respirometric analysis. In this case the residual oxygen is evaluated. This is the value of residual oxygen consumed when all the respiratory chain complexes have been inhibited. Since ROX indicates the amount of oxygen consumed in the cell, independent of the functions of the respiratory chain, this value is normally used analytically. In fact, it represents a baseline, to be subtracted from the individual flow values obtained for each respiratory state analyzed.

2.3 AIM OF THE RESPIROMETRIC ANALYSIS

The High-Resolution Respirometry methodologies described above have been used to evaluate the respirometric profile of different type of cells (among these neuroblastoma and HAP1), after treatment with exogenous molecules or gene deletion. All respirometric analyses were performed using the two-chamber system O2k-FluoRespirometer (Oroboros Instruments, Innsbruck, Austria).

The first work reported here focuses on the impact of VDAC1 gene knock out on cellular respiration. VDAC1 main function is to regulate the flux of several substrates that are directly involved in the activation of the complexes and the ATP synthase of the mitochondrial respiratory chain respiratory. However, not much is known about the involvement of VDAC1 in the regulation of the mitochondrial respiration. To this aim, the near-haploid human HAP1 cell line, knockout for VDAC1, was exploited.

The second work reported here focuses on studying the role of the mutant α -synuclein A53T in altering mitochondrial properties. Indeed, the A53T mutation seems to be correlated with mitochondrial dysfunction, particularly in the process that leads to mitochondrial DNA damage and to the opening of the permeability transition pore. Therefore, in this work, we have overexpressed α Syn A53T in the neuroblastoma cell line SH-SY5Y and analysed the respiratory profile to investigate the effect of this molecule could also interfere, on the mitochondrial respiratory complexes.

The third work reported here focuses on in-depth analysis of the effects that MPP⁺ has along the mitochondrial respiratory chain complexes, using neuroblastoma SH-SY5Y differentiated cell line. In fact, it is known that MPP⁺ damages dopaminergic neurons of the substantia nigra in the brain and it is involved in Parkinson's disease. It is also known that MPP⁺ reduces the activity of complex I, leading to neuronal death. To investigate this effect due to MPP⁺ toxicity, SH-SY5Y neuroblastoma cells were differentiated with retinoic acid and treated with a high concentration (1mM) of the toxin. The neuronal-cell like were then analyzed using the High-Resolution Respirometry technique.

2.4 MACROMOLECULES AND CHEMICALS INVOLVED IN THE EXPERIMENTS

The following paragraphs provide a brief introduction to the main characteristics of the molecules that have been analysed, using High-Resolution Respirometry.

2.4.1 Voltage Dependent Anion Channel

Mitochondrial porins, also known as voltage-dependent anion selective channels (VDACs), are pore-forming molecules of the outer mitochondrial membrane (OMM) involved in the regulation of metabolic flux between the cytosol and mitochondria [25]. This feature allows VDAC to regulate the flux of Krebs cycle intermediates (pyruvate, succinate, malate and glutamate), ATP/ADP, ions (Na^+ , K^+ , Cl^-), nucleotides and NAD^+/NADH , thus supporting all cellular bioenergetics [26,27].

Three isoforms belonging to the VDAC family have been identified: VDAC1, VDAC2 and VDAC3. These isoforms are characterized by similar molecular weight (28-32kDa) and by the 70% of sequence similarity [28]. However, the genes for each VDAC protein are located on three different chromosomes, as shown and reported in Fig.3



Fig.3 It is reported the gene structure for VDAC isoforms. All these gene show the same number of coding exons, with exception for VDAC2 that show one exon more that encode for a short N-terminal sequence of 11 amino acids [29]

Among the isoforms, the most abundant at the outer mitochondrial membrane is VDAC1, although it has been observed that the oldest is VDAC3 [29,30].

The three-dimensional structure of human VDAC1 has been determined simultaneously by different research groups, but using different methods: Ujwal et al. used the X-ray crystallography [31], while Bayrhuber et al. used NMR spectroscopy technique [32]. Both structural analyses show that the structure of VDAC1 consists of 19 β -strands, which together form a β -barrel structure. The first and the last of these β -strands are antiparallel. In addition to this barrel structure, a small α -helix belonging to the N-terminal region of the protein was

observed, which tends to be positioned in the middle of the barrel structure. It is precisely in this part of the N-terminus that there is a glycine-rich region, which makes this α -helix very flexible [33]. This property allows VDAC1 to interact, without any particular steric interference, with molecules such as hexokinases [34,35] and members of the Bcl-2 family, which are involved in the process of apoptosis [36,37]. It was also observed that VDAC1 can interact with itself, forming oligomeric structures, through specific binding sites expressed along its structure [38,39].



Fig.4 3D structure of hVDAC1 obtained by X-ray cristallography at 2.3Å of resolution. This structer is recorded at Protein Data Bank with PDB ID:2JK4

Structural evidence for VDAC2 has been reported experimentally by X-ray crystallography with 2.8Å resolution [40]. The information obtained are not related to the human protein, but to the zebrafish. The 3D structure of VDAC3 has not yet been determined.

VDAC role in apoptosis

Thanks to its interactions with proteins of the Bcl-2 family (in particular the pro-apoptotic factors Bax and Bak), VDAC1 is directly involved in the process of apoptosis. As a result of this interaction, molecules such as cytochrome c and Smac/Diablo can more easily cross the outer mitochondrial membrane and enter the cytoplasm [41]. The release of cytochrome c from the mitochondrion triggers a series of cascade reactions that ultimately lead to cell death: once cytochrome c reaches the cytoplasm, it binds to the *Apaf-1* (apoptotic protease activating factor 1) molecule, which promotes its oligomerization. Apaf-1 oligomers are then recruited and immediately activate pro-caspase 9, which in turn activates caspase 3. This molecule

initiates a process of degradation of cellular proteins, which, as mentioned, leads to a state of cell death [42].

Conversely, VDAC2 prevents Bak activation and inhibits the mitochondrial pathway that lead to apoptosis [43]. VDAC3 interacts with pro-apoptotic factors, generating a series of reactions similar to those reported for VDAC1 [44].

VDAC1 is mainly involved in cellular trafficking

The main function of VDAC is to promote the transport of a wide range of molecules, and for this reason it has been referred as the “sole channel”, capable of uniquely regulating the flow of ions, nucleotides and metabolites up to 5000Da [45]. By modulating its activity, VDAC1 appears to be directly involved in many metabolic processes. For example, VDAC1 is involved in the transport of fatty acid such as carnitine palmitoyltransferase (CPT1a) from the cytoplasm to the mitochondria. When this molecule arrives in the mitochondrion, it triggers a series of cascade reactions that will lead to the β -oxidation process within the mitochondrial matrix [46].

VDAC is also involved in the regulation of oxidative stress; reactive oxygen species (ROS), generated in the mitochondrion after cytochrome c reduction during respiration are released into the cytoplasm by VDAC1. This event leads to an increase in cellular cytotoxicity, which can, in turn, promote neuronal death. In this context, recent studies assess the ability of ROS to induce a series of post-translational modifications as described by Pittalà et al. [47].

The VDAC functions are outlined and summarized in fig.5

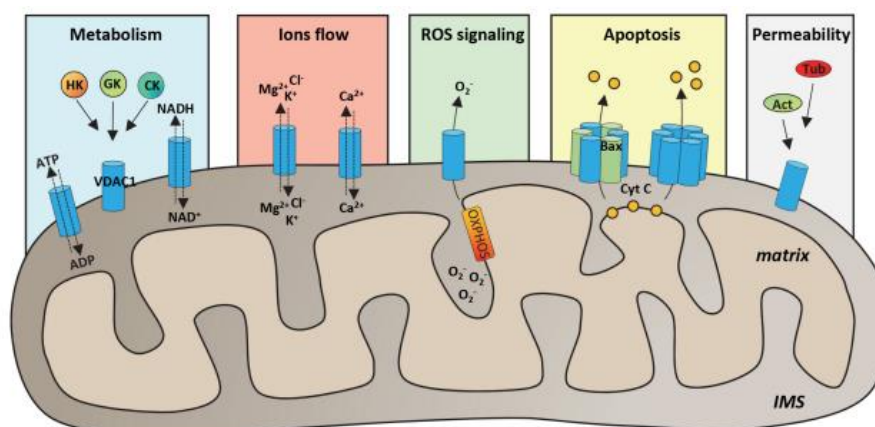


Fig.5 These graphic indicates the high number of process in which VDAC is involved. Among these the transportation of metabolits as ATP/ADP, NADH/NAD⁺ and ions flow with symport mechanism. Other functions are related to radical transportation to cytoplasm and interaction with pro-apoptotic molecule [36].

A lot of molecules that inhibit the functions of VDAC1 have been identified, as reported by Magri and Reina in [36]. Among these molecules there are VBIT-4 and VBIT-12, which act by entering the cell, interacting directly with VDAC1 and reducing its channel conductance activity [48,49]. Furthermore, the expression of VDAC1 can also be regulated by specific hypoxic conditions within the cell: indeed, it has been observed that the overexpression of HIF-1 α (Hypoxia-inducible factor 1-alpha) or NRF-1 (Nuclear Respiratory Factor 1) factors, which bind to the promoter region of the VDAC1 gene, can affect the expression of this protein [50].

Electrophysiological features

The exact mechanism by which VDAC promotes molecular transport is not yet been understood. What is known is that the transition between the open and the closed state of the channel is voltage dependent. This was demonstrated by testing the electrophysiological activity of this protein, using Planar Lipid Bilayer experiments. Different forms of VDAC from different organisms (human, mouse, yeast, etc...) have been studied [51,52]. VDAC1 maintain an open state for potentials of ± 20 mV, with an average conductance of 3,5-4 nS in a 1M KCl salt solution. Under this conductivity condition, VDAC1 shows anion selectivity [26]. Voltages higher than ± 25 mV close the channel that become permeable to small ions. In the close state, the conductance is half that of open state and the ion selectivity changes showing increased cation selectivity. Although the full gating mechanism has not yet been demonstrates, it is thought that flexibility due to the α -helix at the N-terminus may be involved to some extent.

2.4.2 α -synuclein

α -Synuclein (α Syn) is a small neuronal protein, mainly expressed in the presynaptic terminals of the brain, but also in the neuronal system of other tissues such as kidney, liver, lung, cerebrospinal fluid and red blood cells [53,54]. From a functional point of view, α -synuclein can be considered a multifunctional protein. Along its structure there many active sites that interacts with several molecules, therefore α Syn is involved in numerous cellular process. For example, α -Synuclein is involved in the interaction with and regulation of the enzymatic activity, of molecules such as phospholipase D or tyrosine hydroxylase [55,56]; other active sites may be involved in the regulation of the cellular cytoskeleton through interaction with tubulin [57]. Structurally, α Syn consists of 140 amino acid residues, of which the first 11

residues of the N-terminal domain form an amphipathic α -helix, similar to that found in the structure of apolipoproteins. In apolipoproteins, this sequence promotes the binding and transport of lipid molecules; therefore given the high degree of similarity between these two structures it was hypothesized and demonstrated, that α Syn may also be involved in lipid transport processes. Westphal & Chandra have observed that the synuclein molecule induces membrane curvature and transforms large vesicles into highly curved tubules and membrane vesicles [58], typical consequences of lipid binding and transport. It has also been observed that α Syn molecules share a high degree of structural homology with chaperone proteins for other intracellular proteins; again there are experimental evidences showing that α Syn may also function as a molecular chaperone [59,60,61].

In cells, α Syn is mainly localized in the cytoplasm, although further studies have shown how it can be localized within the mitochondria [62]. The overexpression and knock out loss of α -synuclein has shown that this molecule can regulate mitochondrial functions by interfering with substrates that promote the activity of complexes (particularly complex I) during mitochondrial respiration and consequently ATP synthesis [63,64].

However, α -synuclein is known to play a key role in neurodegenerative diseases, in particular Parkinson's disease: in fact α Syn molecules are involved in the formation of Lewy bodies, not in monomeric form, but in the form of toxic oligomers and amyloid fibrils [65]. The aggregation process occurs because of the strong affinity of cupric ions (Cu^{2+}) for active sites present in the N-terminal region of the α -synuclein monomers [66]. Also inherent to the mechanism of formation of such aggregates, it has been observed that C-terminal proteolytic cleavage, depending on residues 109-140, can increase the oligomerizing activity of the monomers [67]. In its aggregated form, α -synuclein enters the inner mitochondrial membrane using VDAC channels [68].

α -Synuclein is translated from the SNCA gene, and missense mutations, observed in this gene, can change the physiological conformation of SNCA gene to a pathological form. In particular, the following major mutations have been found: A30P, E46K, H50Q, G51D and A53T. A30P, E46K, H50Q and G51D modify the secondary structure of the protein, leading to an increase in the process of fibril aggregation and in the toxicity of the protein [69,70,71,72]. Conversely A53T mutation not only favors the process of fibril aggregation, but also seems to correlate with mitochondrial dysfunction: analysis on transgenic mice have shown that α -synuclein aggregates promote mitochondrial DNA with and the opening of the permeability transition

pore [73], thus activating the cell death process. Again, analyzing mouse samples, it was observed that the same events described previously are precursors of neurodegenerative pathologies [74]. In addition, it has been observed that the A53T mutation form may somehow affect the maximum levels of mitochondrial respiration [75].

2.4.3 MPP+

MPTP (1-methyl-4-phenyl-1,2,3,6-tetrahydropyridine) is an organic compound that, once released in the body, uses its lipophilic properties to cross the blood-brain barrier (BBB) and reach the brain. Pharmacologically, it is a secondary compound formed during the synthesis of meperidine, a synthetic opioid drug. MPTP is not toxic [76, 77].

Once released in the brain, MPTP is oxidized to MPP⁺ (1-methyl-4-phenylpyridinium) (Fig.6), a very toxic molecule that tends to accumulate mainly in the neuronal cells of the substantia nigra. The oxidation reaction is only catalyzed by monoamine oxidase B (MAO-B); despite high structural similarity other forms of monoamine oxidase do not catalyze this reaction [78]:

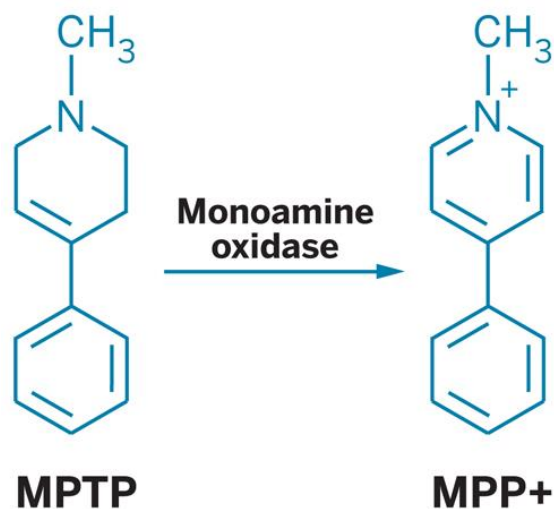


Fig.6 MPTP in presence of Monoamine oxidase B is oxidised to MPP⁺. Here are reported the chemical structure of MPTP and MPP⁺ molecules

Once MPP⁺ has been obtained, it begins to accumulate in the mitochondrion and reaches a concentration that leads to toxicity at the cellular level. The first effects of toxicity, are manifested by a reduction in the activity of complex I of the respiratory chain. In fact, there is a decrease in ATP production and an increase in the production of Reactive Oxygen Species (ROS) [79, 80]. Due to the lack of ATP, which is unable to counteract the radical effects within the cell, neuronal death occurs. In addition to causing neuronal death, other effects of MPP⁺

toxicity within brain neurons include reduction of catecholamine synthesis, reduction of dopamine levels and the inactivation of enzymes such as tyrosine hydroxylase.

Because of the effects shown at the cellular level due to its toxicity, MPP⁺ has been studied as a possible precursor to neurodegenerative diseases, resulting as a precursor of Parkinson's disease. A series of experiments to test the MPP⁺ effect on organisms were conducted. Experiments on monkeys showed, that after injection of a high concentration of MPTP, there is a drastic reduction in dopaminergic neurons in the substantia nigra and pars compacta areas (typical effect of Parkinson's disease) [81,82]. Moreover for other organisms, as for example rats, the different protein composition around the Blood-Brain-Barriers, lead the MPTP oxidation before that it can cross the membrane and enter inside the neuron. This was due to the presence of a high concentration of monoamine oxidase B and to the fact that MPP⁺ is not lipophilic like MPTP and is unable to cross this membrane and reach the neurons of the substantia nigra [83,84]. To counteract the effects of MPP⁺, attempts have been made to find specific inhibitors of MAO-B, including selegiline [85] and rasagiline [86] molecules, but with unsuccessful results.

2.5 RESULTS AND DISCUSSIONS OF THE RESPIROMETRIC ANALYSIS

This part of the PhD thesis includes three different papers, that are summarized in this paragraph. The three articles ("VDAC1 knockout affects mitochondrial oxygen consumption triggering a rearrangement of ETC by impacting on complex I activity", " α -Synuclein A53T promotes mitochondrial proton gradient dissipation and depletion of the organelle respiratory reserve in a neuroblastoma cell line", "High-Resolution Respirometry reveals MPP⁺ mitochondrial toxicity mechanism in a cellular model of Parkinson's disease") are annexed to the thesis.

2.5.1 VDAC1 knockout affects mitochondrial oxygen consumption triggering a rearrangement of ETC by impacting on complex I activity

This work investigates the possible role of VDAC1 in the regulation of mitochondrial respiratory chain functions. Near-haploid human HAP1 cells knockout for VDAC1 (Δ VDAC1) were used to perform respirometric experiments, while near-haploid human HAP1 parental cells were used as control. We chose the HAP1 cell line because it promotes genic knockouts;

HAP1 knockouts are created using the CRISPR-Cas9 system to introduce frameshift mutations into the coding sequence of genes of interest.

Respirometric analysis revealed a drastic drop in respiration rates in terms of oxygen flux for each respiratory states that was evaluated, in HAP1 Δ VDAC1 cells. These data were confirmed by results obtained in parental cells exposed to the VDAC1 inhibitor VBIT-12.

The Flux Control Ratios demonstrate that the contributions to respiration by the ROUTINE and OXPHOS states are significantly higher in HAP1 Δ VDAC1 cells. These results correlate with a significant reduction in the respiratory reserve and excess and imply that VDAC1 deficiency somehow increases the requirement of the cell energy to perform its function. Although a reduction was observed in the oxygen fluxes, FCRs analysis of state-3 showed that in HAP1 Δ VDAC1 cells there is a greater contribution to oxidation by complex I. The latter result is also supported by the determination of NAD⁺/NADH ratio in favour of the oxidized form, obtained after evaluation of cellular content of nicotinic coenzymes (NAD⁺, NADH, NADP⁺ and NADPH), by chromatographic separation.

These data support the idea of a organization of the mitochondrial chain, which is still active, despite the lack of a key protein such as VDAC1. Indeed, HAP1 Δ VDAC1 cells draw more on the respiratory reserve, mainly due to an increased activity of complex I. The decrease in the respiratory reserve may indicate a dysfunctional mitochondrial parameter, a pathological feature of the neurodegenerative process.

2.5.2 α -Synuclein A53T promotes mitochondrial proton gradient dissipation and depletion of the organelle respiratory reserve in a neuroblastoma cell line

α -Synuclein has already been directly implicated in neurodegenerative diseases, known as synucleinopathies. Among these diseases, one of the most studied is Parkinson's disease, in which α Syn forms toxic aggregates, in part due a missense mutation that occurs at alanine 53, which is converted to a threonine. This mutation also promotes mitochondrial dysfunction, although the mechanisms of action are still unclear. To further investigate this function, High Resolution Respirometry was performed by overexpressing α Syn A53T in the SH-SY5Y neuroblastoma cell-line. We chose the SH-SY5Y cell-line because of its neurodegenerative properties and for its previous use in Parkinson's disease research, as reported by Xicoy et al. [87]. Similarly , SH-SY5Y cells were transfected with α Syn WT and empty control vector, to

provide a reference parameter for analysis. The concentration of α Syn used to transfect the cells was only sufficient to induce changes in respiratory functions and therefore no cell death phenomena were observed. Respiriometric analysis indicated a decrease in maximal respiration, expressed in terms of oxygen flow, only with the mutant form of α Syn. This result was expected and is in line with what has been observed in previous work on primary neuronal and N2A cells [88,89]. Analysing the Flux Control Ratios, an increase in the respiration process in the OXPHOS state is observed in α Syn A53T. However, this variation, is not due to any change in the activity of NADH- or succinate-dehydrogenase. This change in the OXPHOS state is associated with the observed increase in the dissipation state (LEAK-state), which in this case corresponds to the state-2 of respiration. Since the total OXPHOS component is the sum of the oxidative contribution (state-2 or LEAK in this case) and the component related to the ATP production, the total of the coupling process will never be 100% of the total OXPHOS contribution. Therefore, an increase only in the LEAK-state alone can be interpreted as an increase in the dyscoupling process in the respiratory functions. This pathological condition can normally be induced by certain cellular stress conditions, such as the accumulation of misfolded protein, in this case represented by the possible aggregation of α Syn monomers. Since it is not possible to determine whether the response observed at the respiratory level is a cause or an effect of the overexpression of α Syn A53T, it can only be stated that this increase in the LEAK-state is a cellular response due to the presence of the mutant, and to counteract this molecule, the mitochondria require more energy production. Indeed, comparing the respiratory reserve values, it can be seen that the cells treated with the mutant form of α -synuclein required more energy production than the control samples.

2.5.3 High-Resolution Respirometry reveals MPP+ mitochondrial toxicity mechanism in a cellular model of Parkinson's disease

The MPP+ toxin accumulates in dopaminergic neurons and produces a toxic effect, including a reduction in the activity of complex I of the mitochondrial respiratory chain. To further investigate about this effect, SH-SY5Y neuroblastoma cells were differentiated with retinoic acid and subsequently treated with high concentrations of MPP+ toxin. To perform HRR, SH-SY5Y neuroblastoma differentiated cells but no treated with MPP+ as used as control.

Respirometric analysis showed that there was a drastic reduction in oxygen flow in each condition examined. These data could be correlated with the reduction in cell viability,

supporting the hypothesis that the toxic effect of MPP⁺ may lead to mitochondrial dysfunction, including a decrease in organelle mass [90].

Analyzing the FCRs, the first striking finding is related to an increase in the LEAK state in treated cells. This respiratory state correlates with the integrity of the inner mitochondrial membrane: since there is no ATP production in the LEAK state, the proton gradient tends to accumulate in the intermembrane space. Therefore, an increase in the LEAK state can be interpreted as an increase in the oxidation state along the respiratory chain, but this increase can only be related to a lower degree of dissipation of the proton gradient along the intermembrane space. As a result of these considerations, the increase in the LEAK state can be correlated with damage to the integrity of the IMM. The data obtained for the LEAK state provide further confirmation of what is already known, namely that the presence of MPP⁺ decreases ATP production but increases ROS production.

Also, from the FCRs analysis, it was observed that there was not much variation in the OXPHOS contribution from the maximum respiration value. This result might seem to contradict what is already known, namely that MPP⁺ toxicity reduces complex I activity. However, by performing a single analysis of the complexes, it was observed that complex II increases its activity to compensate for the reduction of complex I activity. In conclusion, it seems that after treatment with the toxin, the cellular metabolism readjusts itself so that it can continue to perform its functions.

3. COMPUTATIONAL AND ELECTROPHYSIOLOGICAL STUDIES ON STRUCTURE AND FUNCTIONALITIES OF THE ENVELOPE PROTEIN FROM SARS-CoV-2

3.1 WHAT IS A VIRUS?

A virus is a small infectious agent that can only multiply in living cells of animals, plants or bacteria. Typically, most viruses vary in diameter from 20 nanometres to a size range of 250-400nm, but in certain cases some viruses can be as large as 1 micron [91].

A virus particle is mainly constituted of short sequences of nucleic acid, which can be in the form of ribonucleic acid (RNA) or deoxyribonucleic acid (DNA). A major difference in the arrangement of genetic material between a cell and a virus is that in viruses the DNA can be either single-stranded or double-stranded. This genetic material is all contained within a structure called virion. Inside the virion, the DNA or RNA is surrounded by a protein call capsid: the union of capsid and nucleic acid forms the nucleocapsid. In some viruses, the nucleocapsid is in turn surrounded by a lipoprotein structure called envelope containing the viral protein (peplomers or spike) [92,93]. Based on the shape of the capsid protein, viruses can be divided into helical and icosahedral structure. In addition, a small number of viruses have a complex architecture, although the previously reported molecular characteristics remain unchanged (Fig.7) [92]

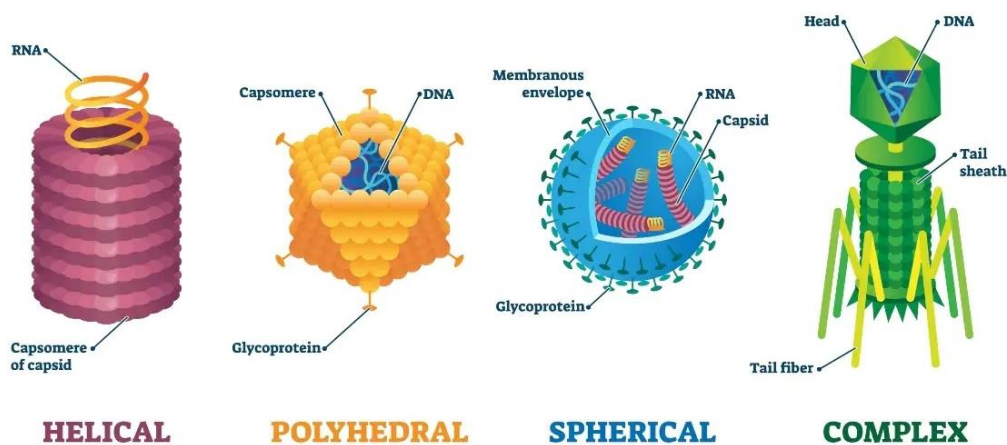


Fig.7 The different forms that can take are shown. It can be seen that in each of these forms the nucleotide sequence is always contained within the capsid, while the outer structure can vary depending on the glycoprotein composition of the envelope.

Without a host cell, viruses cannot carry out their life-sustaining functions or reproduce. They cannot synthesize proteins, because they lack ribosomes and must use the ribosomes of their host cells to translate viral messenger RNA into viral proteins. In addition, viruses do not produce or store energy in the form of ATP, but obtain their energy and all other metabolic functions from the host cell. They also use the host cell to synthesize amino acids, nucleotides and lipids. These are the reasons why viruses are so dangerous to living cells, and once inside the host, they start making new copies of themselves very quickly. After infection, the virus immediately enters in the cytoplasm of the host cell and sheds its viral coat into smaller cellular vesicles, releasing its genetic material into the cytoplasm for replication.

Based on how the genetic material is distributed within the virus and how the replication mechanism is activated after infection, viruses are divided into 7 different group according to the Baltimore Classification System [93]:

- Group I: double-stranded DNA viruses;
- Group II: single-stranded DNA viruses;
- Group III: double-stranded RNA viruses;
- Group IV: positive-sense single-stranded RNA viruses;
- Group V: negative-sense single-stranded RNA viruses;
- Group VI: RNA viruses that reverse transcribe
- Group VII: DNA viruses that reverse transcribe

There are also a number of ways in which viruses can be classified. These include the group to which they belong, the host species and the disease they cause [94].

3.2 THE CORONAVIRIDAE FAMILY

The members of the family *Coronaviridae*, a monophyletic group in the order Nidovirales, are enveloped, positive stranded RNA viruses with helical capsids of three classes of vertebrates: mammals (corona- and toroviruses), birds (coronaviruses) and fish (bafiniviruses). This family of viruses consists of two subfamilies: *coronavirinae* and *torovirinae*.

Coronaviruses belong to the *coronavirinae* subfamily and are divided into four genera: Alphacoronavirus, Betacoronavirus, Deltacoronavirus and Gammacoronavirus [95,96], as reported in Fig.8

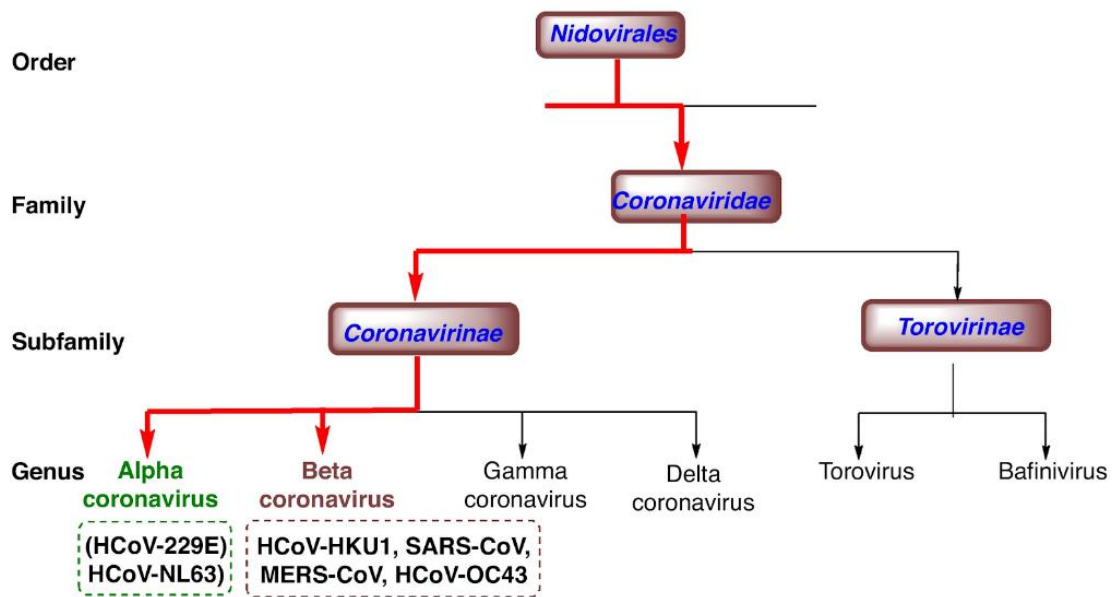


Fig.8 Taxonomy of the order nidovirales, to which the family containing SARS-CoV-2 belongs [97]

Alpha-coronaviruses is a type of coronavirus that is commonly found in bats and occasionally infects humans. The human pathogens for alpha-coronavirus are 229E and NL63. The morphological structure of the virus is similar to other coronaviruses, in fact there is has a crown-shaped appearance but the spike proteins on the outer surface of the virus are different in that they are not cleaved or split in any way. Beta-coronaviruses are a group of viruses that cause contagious human respiratory human disease including COVID-19, deriving from SARS-CoV-2. Similarly, to other coronavirus genera, beta-CoV possesses a protein called hemagglutinin esterase [98,99] and also has an nsp1 replicase polyprotein, which is not found in other types of coronavirus. Both of these proteins are directly involved in the process of virus replication. Gamma- and Delta-coronaviruses are commonly found in birds and they differ from the other genera by a unique reading frame in the genome and a unique transcriptional regulatory sequences (TRS), respectively.

Beyond SARS-CoV-2, other two beta-coronaviruses have a strong impact on human health: SARS-CoV and MERS-CoV. Severe Acute Respiratory Syndrome is a human disease associated with severe pneumonia, that occurred in 2002, while Middle East Respiratory Syndrome is a severe respiratory illness that was first identified in 2012. For both viruses, bats are thought to be the natural reservoir of the virus, but there is an intermediate host before human infection: palm civets in the case of SARS-CoV and dromedary camels in the case of MERS-CoV [100]. In both cases, high infection rates were recorded, but unlike later with SARS-CoV-2, these outbreaks were contained before they could spread globally.

3.3 SARS-CoV-2

The severe acute respiratory syndrome coronavirus 2 (SARS-CoV-2) pandemic is a potentially fatal respiratory disease that has created a global medical emergency with drastic economic and social consequences around the world. Discovered in Wuhan, China, in December 2019, SARS-CoV-2, is a single-stranded, positive-sense RNA virus that is not yet fully understood and continues to produce new variants and spread rapidly around the world.

Like other beta-coronaviruses, the SARS-CoV-2 genome consists of 14 open reading frames (ORFs) (Fig.9).

These include ORF1a and ORF1b, which occupy two-thirds of the total genome, and encode 16 non-structural proteins (nps) involved in the viral replication and transcription complex (RTC). These non-structural proteins can have multiple functions, including replicase, polymerase and RNA proofreading [101].

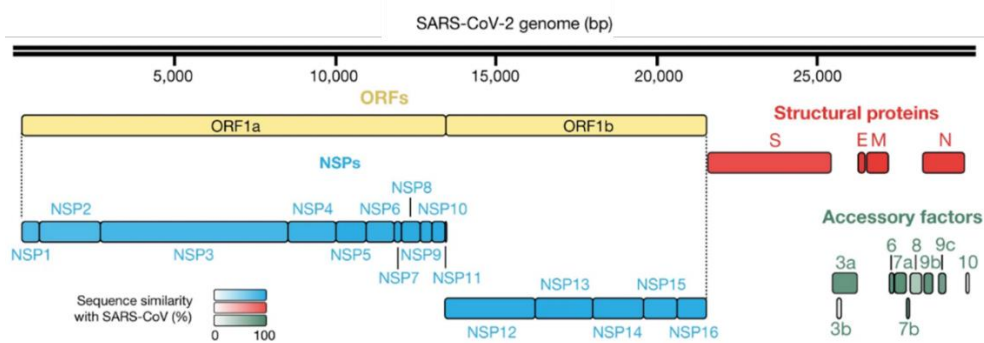


Fig.9 the entire genomic structure of SARS-CoV-2 is reported. It shows a full-length of ~ 29000 kb [102]

Other ORFs are ORF3a, ORF3b, ORF3c, ORF3d, ORF6, ORF7a, ORF7b, ORF8, ORF9b, ORF9c and ORF10, which encode accessory proteins that are essential for viral pathogenicity and mediate the virus-host response [103]. 4 ORFs encode for structural proteins called Spike (S), Membrane (M), Envelope (E) and Nucleocapsid (N), which are considered key targets for antiviral drug development and assemble with the positive-sensed single-stranded RNA genome to form SARS-CoV-2 virions.

The Spike protein has always been one of the main areas of research interest, as it is the protein that promotes interaction with the host cell receptor, which in the case of SARS-CoV-2 is angiotensin-converting enzyme 2 (ACE2). Spike is a glycoprotein with a homotrimeric structure favored by the conservation of a triptophan-rich region. It can be divided into two distinct functional subunits: S1 and S2. The S1 subunit contains the sequence for the receptor-

binding domain (RBD), which is direct responsible for the interaction with the ACE2 receptor; instead the S2 subunit contains repeated amino acid regions that mediate the fusion of the virus with the cellular membrane [104,105].

The membrane protein is the most abundant structural protein and is involved in virus assembly, membrane budding and in the first phase of the viral pathogenesis. From a structural point-of-view, recent cryo-EM analyses highlight that the M protein structure is composed of dimers or in certain case, oligomers [106].

The nucleocapsid protein is one of the most abundant proteins in the virus infected-cells [107]. The main function of N protein is to coat the viral genome to form an helicoidal nucleocapsid that remains protected within the viral envelope [108]. Other functions associated with N protein, once released into host cells, are to be involved in processes such as interferon inhibition, RNA interference and apoptosis [109,110]

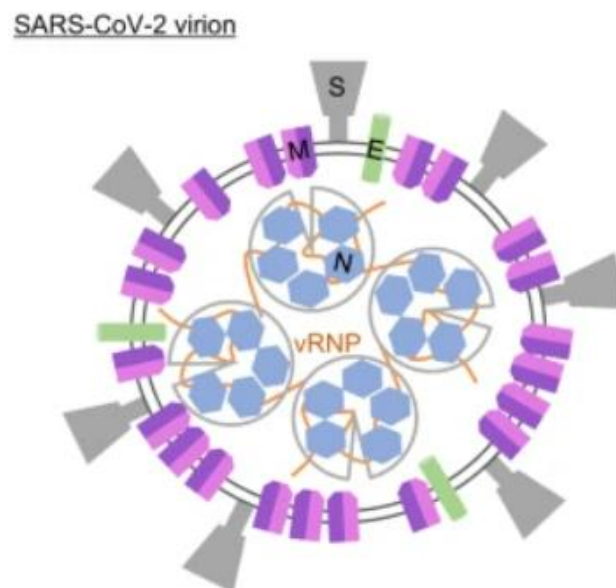


Fig.10 Arrangement of structural proteins along the virion envelope (Spike, Envelope and Membrane) and within the virus (Nucleocapsid) [106]

3.4 REPLICATION PROCESS OF SARS-CoV-2

Replication of SARS-CoV-2 begins when the S1 subunit of spike protein interacts with the ACE2 receptor [111,112], which is more localized in lung, heart and intestinal cells. Following this interaction, the serine protease TMPRSS2 cleaves both the receptor and the spike protein,

releasing the S2 subunit [113]. This domain forms the endosome, which favours the entry of the virion into the cell. Before the pH of the endosome becomes too high, the virion exits the endosome, releasing the genome. Translation of the first polyproteins, pp1a and pp1ab, takes place in the ribosome. The proteins produced include the RNA-dependent RNA-polymerase (nsp12), the RNA helicase (nsp13) and two proteases (nsp3 and nsp5), which initiate the viral RNA transcription process and subsequent virion replication [114,115,116]. The structural proteins S, E, M and N move to the ERGIC complex to fulfil their functions, while the new virions are assembled, after interactions of M proteins, and released from the cell by exocytosis.

The entire steps, that describe the replicative process of SARS-CoV-2 are illustrated in Fig.11

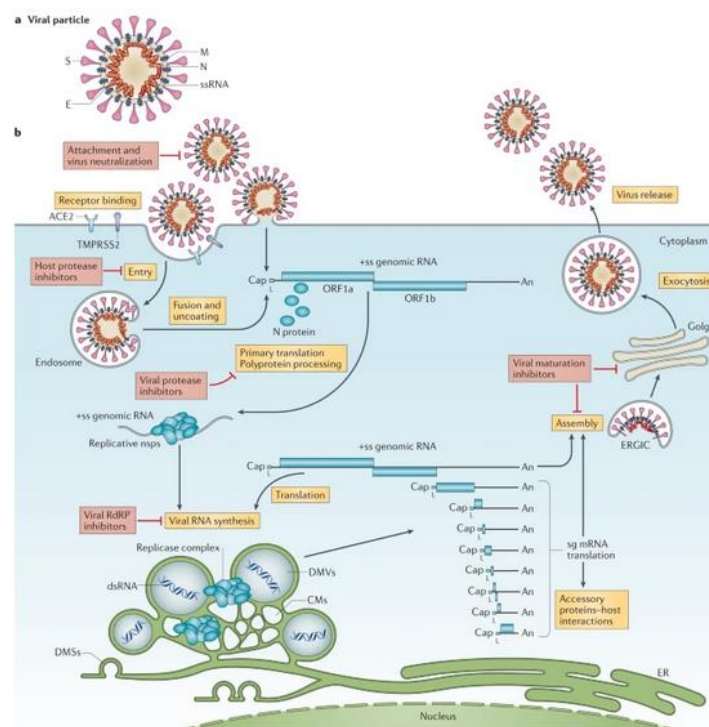


Fig.11 Graphical representation of the replication process of SARS-CoV-2. After interacting with the ACE2 receptore, the protease TMPRSS2 cleaves the spike, favouring the release of the S2 subunit. The formation of an endosome allows the virus to enter inside the host cell, and through the ribosome starts the process of translation. After translation structural proteins move to ERGIC complex and Golgi compartments and Finally structural proteins are released inside the host cell, while the newly assembled virus is released by exocytosis

3.5 ENVELOPE PROTEIN

Among the structural proteins reported so far, the envelope protein (E2) from SARS-CoV-2, is the target of this study. It is the smallest of the structural proteins and is highly conserved

among different viral subtypes, although its role in viral invasion, replication and release is not well understood. Together with the membrane protein M, E2 is required for the assembly of the viral envelope. Accordingly, the absence of E2 significantly reduces viral titres and cripples viral maturation [117,118]. Moreover, mutation of the protein E sequence induces apoptosis [119]. As previously described, the envelope protein is highly expressed during the coronavirus replication cycle but it is poorly incorporated into the virions, being mainly located in internal membranes, i.e in the ERGIC complex and Golgi compartments [120].

Structurally, E2 is an integral membrane protein of 75 amino acids (aa); primary and secondary structures show that the N-terminus (first seven amino acid residues) is formed by a short hydrophilic chain, followed by a large α -helix hydrophobic transmembrane domain (TMD) of 25aa and a long hydrophilic C-terminus [121]. Two α -helix motifs have been also identified in the C-terminal domain, although they are shorter than the one observed in TMD. The C-terminus has a cytosolic orientation and, thanks to this position, the envelope protein is able to interact with other viral and host proteins. In particular, the interaction between the envelope protein and the membrane protein was found to involve the C-terminal domains of both proteins [122]. Furthermore, at the beginning of the C-terminus, the triple cysteine motif (C40, C43 and C44) has been proposed to associate with the cysteine-rich C-terminal region of S protein, while the C-terminal DLLV sequence has been identified as a PDZ-binding motif that binds to the host cell polarity signaling protein PALS1 and enhances the destruction of epithelial integrity, thereby fueling the inflammatory process [121].

The envelope protein of SARS-CoV-2 shows a high degree of homology (represented by the 95% of amino acid sequence identity) with the envelope protein (E) of SARS-CoV. Therefore, what is known about the three-dimensional structure of the E2 protein comes from previous experiments on the earlier form of the virus. In 2018 a solid-state NMR structure revealed that the TMD of the E protein self-assembles into a homo-pentamer (Fig.12) [123] following previous experiments that demonstrated the multimeric assembly of E [124]. Regarding the 3D structure of E2, a further NMR analysis was performed only on the TMD domain [125], but the mechanism allowing the pentamer formation is still unclear. Furthermore, computational studies on monomeric E2 showed that the transmembrane α -helix is tilted in the membrane, while the C-terminal α -helices are free to move around it. This flexibility, resulting from the movement of the C-terminus, induces membrane curvature [126].

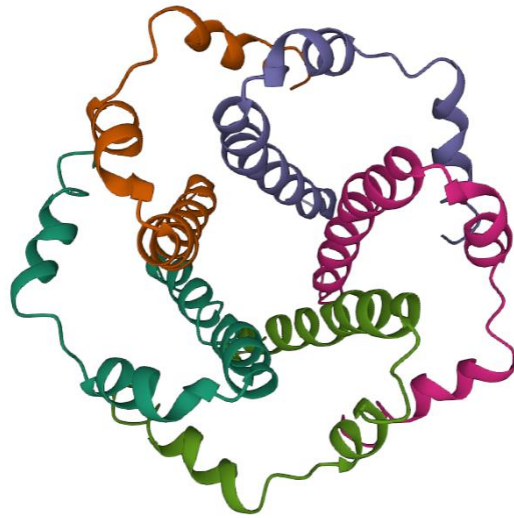


Fig.12 Three-dimensional structure obtained by NMR spectroscopy for SARS-CoV Envelope protein. Spectroscopy was used to identify one monomer, while the orientation of the others was predicted by docking. All data are deposited in the Protein Data Bank under PDB ID: 5X29

The self-assembly of TMD from the different monomers suggested the formation of a pore with putative ion channel activity. Planar Lipid Bilayer and patch-clamp recordings suggest, that this channel exhibits voltage-dependence with cation selectivity [119,127,128,129]. In addition, its intracellular expression increases Golgi intracellular pH and alters Ca^{2+} homeostasis [130], ultimately promoting the activation of a pro-inflammatory cascade with worsening of several respiratory symptoms.

3.6 AIM OF THE CHARACTERIZATION OF THE ENVELOPE PROTEIN

SARS-CoV-2 had a big impact on our daily lives during the first months of the 20's decade. As previously reported, SARS-CoV-2 consists mainly of four structural proteins: Spike (S), Envelope (E), Membrane (M) and Nucleocapsid (N). While the Spike, which is responsible for virus binding the virus to its surface receptor on target cells, has undoubtedly been the focus of much therapeutic and vaccine development effort, the Envelope protein is emerging as a worthy candidate as well. One of the keys of E from SARS-CoV-2 (E2) is the monomeric oligomerisation into a pentameric structure with putative ion channel activity. In order to make the E2 protein a concrete target from a pharmacological point of view, more detailed characterization of its functional properties is necessary. Therefore, in this first part of my PhD thesis, I will report on all the techniques that have been carried out to obtain more

information about the E2 functionality of E2, focusing on the properties of the ion channel. In particular, before performing Molecular Dynamics simulations, the entire 3D structure of E2 was reconstructed using specific Homology Modelling software. To carry out the MD simulations, I spent three months during my PhD period, in the laboratory of Prof. Matteo Ceccarelli at the University of Cagliari. Another computational approach to understand more about the ionic channel activity of E2 was carried out using metal-binding structure prediction docking analysis, to observe how calcium ions can bind to the E2 structure, to favour ion passage through the channel. Finally, the electrophysiological properties of E2 were determined after expression of the recombinant protein by performing Planar Lipid Bilayer experiments using as saline solution gradient concentration of CaCl_2 and KCl.

3.7 BRIEF INTRODUCTION TO TECHNIQUES

In this paragraph will be explained the theory behind all techniques used to achieve the PhD goals regarding the characterization of the Envelope protein from SARS-CoV-2 main functions:

3.7.1 PLANAR LIPID BILAYER

Ion channels are pore-forming membrane proteins that allow ions to pass through the channel pore. Their functions include establishing a resting membrane potential, shaping action potentials and other electrical signals [131]. Thus, the ion channel can be thought of as an electrical device that generates fast and long-range electrical signals along the cell-membrane [132]. To investigate the properties of ion channel, electrophysiological technique such as Planar Lipid Bilayer (PLB) could be used.

Planar Lipid Bilayer, also known as Black Lipid Membranes (BLM), measures channel gating at the single channel level, specifically on membrane vesicles, synthetic and recombinant ion channels. It can measure transmembrane currents of 1pA to 20nA [133].

Generally, the main common approaches used to perform a PLB analysis are:

- *voltage-clamp method*, in which the membrane voltage is held constant and the transmembrane current required to maintain this voltage is measured;
- *current-clamp method*, in which the transmembrane voltage resulting from ion channel activity is detected. In a current-clamp experiment, the current value is always constant.

The PLB assembly consists mainly of a Delrin cuvette with a small aperture of variable diameter from 50 μm to 250 μm . To the side of this opening are defined the *cis*- and *trans*-regions. These two compartments are filled with a salt solution, such as KCl, CaCl_2 or NaCl, and they are usually connected to the amplification head stage via KCl agar bridges and silver/silver chloride (Ag/AgCl) electrodes. A Lipid membrane is produced around this aperture, using the Langmuir-Blodgett (LB) method (also known as the painting method): a lipid solution is applied across the aperture separating the *cis* and the *trans* sides of the chamber. Lipid monolayers at the water-air interface are brought together when lifted above the aperture [134]. The resulting lipid bilayer is a capacitor capable of storing charge in the electric field.

Before adding the protein channel, it is necessary that the lipid membrane reaches a capacity of approximately 110-150 pF. Capacitance (C) is directly proportional to the surface area of the membrane, as shown by the equation:

$$C = \frac{\epsilon A}{d} \quad (4)$$

Where ϵ represent the dielectric constant, while the distance d represents the thickness of the bilayer. Current flow inside the chamber is given by the following equation:

$$I = C \frac{dV}{dt} \quad (5)$$

Where I is the capacitive current and dV/dt is the variation of voltage potential during time.

To assess the activity of the ion channel, the conductance (G) of ions at the single channel level is obtained after insertion of the protein within the lipid bilayer. The conductance is measured directly from the ratio between the value of the recorded current (I) and the voltage applied (V):

$$G = \frac{I}{V} \quad (6)$$

In addition, the reverse potential (V_{rev}) can be measured to characterize ion channel activity. The reverse potential for an ion channel is defined as the membrane voltage at which the net current through the channel is zero. The voltage gradient at which this equilibrium is reached

is the equilibrium potential for the ion and it can be calculated by Goldman-Hodgkin-Katz equation:

$$V_{rev} = \frac{RT}{F} \ln \left(\frac{\sum_i^n p_M^+ [M_i^+]_{out} + \sum_i^n p_A^- [A_i^-]_{out}}{\sum_i^n p_M^+ [M_i^+]_{in} + \sum_i^n p_A^- [A_i^-]_{out}} \right) \quad (7)$$

Where M represents the monovalent positive ionic species and A represents the monovalent negative species. From the GHK equation it can be seen that the contribution of any given ion is determined not only by its concentration gradient across the plasma membrane, but also by its relative membrane permeability (p), defined as the ability of an ion to cross the membrane in relation to the number of channels open inside the membrane. Also related to the reverse potential is the ion selectivity for the channel: a negative V_{rev} value indicates anion selectivity, whereas a positive V_{rev} indicates cation selectivity.

3.7.2 MOLECULAR DYNAMICS SIMULATIONS

Molecular dynamics (MD) is a computational technique used to simulate the motion of a molecular system. This technique requires an interaction potential from which interatomic forces can be calculated and equations of motion that govern the dynamics of the system can be established [135]. In general, MD simulations allow the study of the dynamics of the evolution of a physical and chemical system at the atomic and molecular levels.

The first MD simulations date back to the 1950s, when Alder and Wrainwright used MD to study simple fluids using rigid models that represented atoms as disks and hard sphered [136,137]. From this first simulation, the MD technique developed in parallel with both new discoveries in chemistry and physics, such as the use of Lennard-Jones potential to characterize atomic interactions in the liquid argon [138], and with the technological advances in the software used, such as the generation of supercomputers with high computing capacity. In fact, it is now possible to simulate hundreds of nanoseconds of a very flexible complex system in a few days, with high accuracy using dedicated supercomputers.

Molecular Dynamics can be seen as a dynamic extension of molecular mechanics. Molecules are characterized computationally as parameters that express their physical properties after evaluation of the laws describing classical physics. What is added in an MD simulations in the application of Newton' second law of dynamics. This law states that rate of change over time of the momentum of a body is equal in magnitude and direction to the force applied to it; the momentum of a body is equal to the product of its mass and its velocity. A force applied to a

body can change the magnitude of its momentum or its direction or both. The force applied to make this change is therefore directly proportional to the scalar product of mass and acceleration. This law can be expressed by the following equation:

$$\vec{F} = m * \vec{a} \quad (8)$$

considering a single point in the one-dimensional space with known spatial coordinates, the velocity at a given instant t is equal to:

$$v = \frac{dx}{dt} \quad (9)$$

While the acceleration with respect to the same point is defined as:

$$a = \frac{d^2x}{dt^2} \quad (10)$$

Moreover, molecular mechanics provides a potential V for each parameterized molecule, from which the force exerted by the molecule on a point in space can be derived as follows

$$F = \frac{dV}{dx} \quad (11)$$

Combining the (8), (9), (10) and (11), Newton' second law can be rewritten as:

$$\frac{dV}{dx} = m * \frac{d^2x}{dt^2} \quad (12)$$

By integrating this equation, it is possible to obtain trajectories that describe the variation in space, velocity and acceleration of the atoms that make up the proteic system. To correctly define a trajectory it is always necessary to know the initial conditions of the system. For proteins in particular, the preliminary spatial coordinates can be obtained from the Protein Data Bank (data previously obtained by experimental techniques such as X-ray cristallography, NMR spectroscopy, Cryo-EM, etc...), while the initial velocity distributions are obtained directly from the positions of each individual particle, using the Verlet or the Leap-Frog algorithms [139].

Force field

The potential energy reported in (12) could be described as a set of parameters which together take the name of a force field. In the context of molecular modelling, a force field is

a computational method used to estimate the forces between atoms within molecules (bonded terms) and also between molecules (unbonded terms):

$$E_{\text{total}} = E_{\text{bonded}} + E_{\text{non-bonded}} \quad (13)$$

Where each term is used depends in turn on other factors:

$$E_{\text{bonded}} = E_{\text{stretching}} + E_{\text{bending}} + E_{\text{torsional}} \quad (14)$$

$$E_{\text{non-bonded}} = E_{\text{electrostatic}} + E_{\text{van der Waals}} \quad (15)$$

The energetic term associated with the stretching motion depends on the distance separating the two interacting atoms in the final and initial system configurations (Δx). The harmonic oscillator is used as the reference system and can be represented by Hooke's law. The value of k indicates the elastic constant [N/m].

$$\vec{F}_{\text{st}} = -k * \vec{\Delta x} \quad (16)$$

The bending motion depends on the bending of a given group of atoms in space. Hooke's law can be mathematically adapted to this process by considering the angular coordinates ($\Delta\theta$), instead of the spatial coordinates

$$\vec{F}_{\text{ben}} = -k * \vec{\Delta\theta} \quad (17)$$

The torsional motion depends on the rotational motion that can characterize the protein system. The mathematical model used to describe these phenomena is as follows:

$$E_{\text{tor}} = \sum A [1 + \cos(n\tau - \Phi)] \quad (18)$$

Where A is a parameter that controls the amplitude of the rotation, n controls the periodicity and Φ regulates the phase shift along the axis of rotation.

Regarding the parameters that correlate the value of unbound energy, the main electrostatic component is obtained by solving the Coulomb equation (19), while the main repulsive terms is obtained as a measure of the Lennard-Jones potential (20).

$$E_{\text{elec}} = \sum_i \sum_j \frac{q_i q_j}{r_{ij}} \quad (19)$$

$$E_{\text{vdw}} = \sum_i \sum_j \left(\frac{-A_{ij}}{r_{ij}^6} + \frac{B_{ij}}{r_{ij}^{12}} \right) \quad (20)$$

Over the years, it has been possible to observe that MD simulations allow to evaluate interactions that take place even at long distances, but in this case these interactions are very weak and can interfere with the final result of the simulation: the application of a 14Å cut-off therefore allows to evaluation of the strongest interactions within the system.

The most commonly used force fields used in Molecular Dynamics are CHARMM and AMBER, which differ due to different interpretations of the various energetic terms (e.g CHARMM also considers bending motion also for the dihedral angle, whereas AMBER does not) and to different methods for deriving the atomic charge in the protein.

In reality, it should be noted that the equations (13), (14) and (15) may have additional specific terms depending on the property that needs to be evaluated. In fact, the force field file obtained, can be divided into two parts: the parametric one, which indicates the parameters that allow the force field value to be derived, and the topological one, which indicates the group to which the atoms involved in an interaction belong (in the case of a protein, these groups are the individual amino acids).

MD simulation step

There are several steps that need to be taken to derive an MD simulation. After selecting the appropriate force field (CHARMM is usually used to simulate biological compounds), the preliminary calculation of energies and forces is performed by solving equation (12). In this case, the potential energy V is obtained by applying the force field. This calculation is carried out using the finite difference method. In this method, in addition to evaluating the properties that describe the entire system at $t = 0$, it is possible to evaluate the evolution of space and velocity over a small-time range, called the time step (Δt). In this way, it is possible to monitor the evaluation of each property at any moment of the simulation.

Once the initial properties of the system have been calculated, *energy minimization* step is performed. In this step, a transition is performed from the initial configuration to a close configuration with the lowest energy. This step is fundamental because it removes structural forcing that could lead to too high energy and to the non-convergence of the integration algorithm. One of the criteria used to perform the energy minimization is based on the

calculation of the potential energy gradient and the relative comparison between the two conformations considered (steepest descent). After energy minimization, the *equilibration phase* begins, first at constant temperature and then at constant pressure. Normally, the reference values taken for the system correspond to a temperature of 300K and a pressure of 1 atm. In this case an NPT ensemble is considered. Alternatively, an NVT ensemble can be used where the value of the volume is held constant, instead of the pressure. In both the NPT and NVT ensembles, the number of particles (N) in the system doesn't change.

To keep the T value stable, the Berendsen thermostat [140] is the main algorithm used. This algorithm simulates the coupling of the system to a thermal bath outside the T_0 temperature. The magnitude of the interaction between this thermostated bath and the system is determined by an arbitrarily chosen time constant τ . The Berendsen thermostat is controlled by the following mathematical law:

$$\frac{dT}{dt} = \frac{T_0 - T(t)}{\tau} \quad (21)$$

Alternatively, the Nosè-Hoover thermostat can be used [141,142]. This algorithm uses the principles of the Berendsen thermostat, but with a correction in the lines of the algorithm relative to the kinetic energy calculation mechanism.

Instead, the pressure could be evaluated using the Parrinello-Rahman barostat [143] is used to evaluate the constant pressure value in the NPT canonical set.

After the equilibration phase, the *production step* is carried out. In this step, the MD simulation is carried out with the application of an external electric field (E) along the whole dimension of the z-axis (L_z). For this purpose, a specific transmembrane voltage (V) has been chosen and thus the value of the applied electric field is obtained by the following law:

$$\vec{E}_z = \frac{V}{L_z} \quad (22)$$

In this way, every charged particle feels about a force

$$\vec{F} = q * \vec{E} \quad (23)$$

Thus, by applying a constant potential along the z-axis, all system are distributed in such a way as to obtain detailed trajectory files, in which the behavior of the whole system is as realistic as possible.

Parallel tempering

As previously reported, the equilibration step is one of the most important, since it defines the simulation conditions of the biological system are defined. To improve this step, a new algorithm called parallel tempering (PT) has recently been added.

In parallel tempering several copies of a system, called replicas, are simulated simultaneously at a ladder of temperatures, that can vary from the one most relevant to the system to a temperature high enough to cross energetic barriers [144]. After a certain time, the replicas are swapped to another configuration at different temperatures, based on the stochastic Metropolis criterion [145]. Therefore, the classical equilibration in the NPT (or NVT) ensemble is followed by a long-PT simulation using a range of temperatures chosen according to the transition temperature for the complex system under analysis.

3.7.3 BINDING SITE PREDICTION

Because of the electrophysiological analysis and molecular dynamics simulations, it may be crucial to analyze the presence of possible active sites along the entire structure of the envelope protein.

Docking algorithms can be used to predict the presence of binding sites. Overall, molecular docking is a bioinformatics tool that can be used to study the interaction of two or more molecules. Specifically, the application of this algorithm allows to recognition of the correct poses of ligands in the binding pocket of a protein, in order to predict the affinity between the ligand and the same protein. These putative interactions can be evaluated using a specific score function based on the total energy of the system analyzed [146].

A ligand is the complementary partner molecule that binds to the receptor for an effective biomolecular response [147]. The nature of a ligand can be variable and can be a small drug molecule, a whole protein or a metal ion. Therefore, it is possible to classify docking in:

- Protein-small molecule docking;
- Protein-protein docking
- Metal Binding site prediction

Docking protocols can be described as a combination of two components: a search strategy and a scoring function [148]. The search strategy should generate an algorithm that allows to

obtain several configurations containing the experimentally determined binding mode. In particular, this algorithm will be directly linked to the rotamer libraries of each protein, thus providing the possibility of analyzing the interaction using a large number of conformations that can characterize the proteins under consideration. These conformations are randomly selected according to the different degrees of freedom of the translational and rotational motions that each amino acid can be involved in. Therefore, the main parameter taken into account for the generation of a different conformation will be the movement of the side chain.

The starting point for performing a docking analysis is to search a PDB file containing all the data relating to the 3D structure. In the case of missing residues, it is necessary to reconstruct the entire structure using specific Homology Modelling software. One of the most common methods to observe the docking process is the application of the Fast Fourier Transform (TFF) principle [149,150]. This algorithm can be described in several steps: first, a simplified energetic score function is applied, representing the steric fit and possibly hydrophobics/hydrophilics contacts. In the second step, a new score function is applied, but only to the 20000 conformations that obtained the best score in the first phase; this new evaluation criterion considers other energetic terms such as electrostatic interactions and possible solvation. The biological complexes characterized by the lowest score at the end of this second phase are classified as hits. The term hit is used to describe the best of all conformations. Finally, all hits are analyzed considering the variation of the energy function through the movement of the side chain. All hits (especially for protein-protein docking and when the ligand is represented by a small peptide) should be analyzed according to the contact areas (ODA function) to obtain the specific amino acids involved in the interaction with the ligand.

Another method for assessing the binding site in a protein is the Fragment Transformation [151,152], a method commonly used to evaluate the interaction of a protein with a metal template.

In this case, the protein structure is broken down into a series of fragments, called queries. All these queries are designed to interact with the metal ion and the variation in structure similarity is used as a score function to detect a possible binding site. For each query, the structural similarity is evaluated according to an alignment of $C\alpha$ in the conformation

Electrophysiological recordings

Electrophysiological experiments were performed using the Planar Lipid Bilayer (PLB) technique according to [153,154,155]. In brief, 1% DiPhPC (Avanti Polar Lipids, Alabaster, AL) in n-decane was used for painting bilayer membranes with an approximate 110-150 pF capacity on a 200 μm aperture of a Delrin cuvette (Warner Instruments). Single channel recordings were carried out in symmetrical 1M CaCl_2 , 10mM HEPES, pH 6 and at $\pm 100\text{mV}$ applied following addition of ~ 50 ng of the purified protein to the *cis* side of the chamber. Voltage-dependence and ion selectivity were investigated in 0.05M to 1M asymmetric CaCl_2 gradient using a 10mHz triangular voltage wave from -100 to +200 mV. Current traces were recorded using the BC-535 Bilayer Clamp amplifier (Warner instruments) and data were digitally filtered using a low-pass-filter at 300 Hz and a sampling frequency of 10 kHz with the Axon Digidata 1550 Acquisition System (Warner Instruments). Pore conductance (G) was calculated as the ratio of channel current (I) to applied voltage (V). At least three independent experiments were repeated for each condition.

Molecular Dynamics Simulations

For Molecular Dynamics simulations we prepared two different structural systems. The first one (Model_A) was obtained by homology modelling (using Modeller 10.1) employing the E protein PDB files as initial coordinates (PDB ID: 5X29) and adding the specific missing residues. The other structure (Model_B) was obtained after re-orientation of each monomeric domain. The CHARMM-GUI web server (available for free after registration at <https://www.charmm-gui.org>) was used to prepare both cell-like systems. First of all, the rebuilt protein was inserted in a lipid bilayer system consists of 75 DOPC (1,2-Dioleoyl-sn-glycero-3-phosphocoline), 25 DOPS (1,2-Dioleoyl-sn-glycero-3-phospho-L-serine) and 25 DOPE (1,2-Dioleoyl-sn-glycero-3-phosphoethanolamine) molecules, for both the upperleaflet and the lowerleaflet. Lipids form an xy-plane with initial size of 105Å x 105Å. The bilayer-protein complex was then immersed in an explicit water solution (TIP3 model) with several ionic concentrations: 150 mM KCl, 50 mM KCl + 50 mM CaCl_2 .

The related files for energy minimization, equilibration and production were directly provided by CHARMM-GUI, and the GROMACS version 2020.2 was used to run them using the CHARMM force field. Equilibration steps were performed for a total of 200ns using an NPT ensemble and, which RMSD (Root-Mean Square Deviation) was used to evaluate system

stability. Pressure and temperature were held constant at 1 atm and 310 K using the Berendsen coupling scheme during equilibration. Instead for the production run (1 μ s), the Parrinello-Rahman coupling scheme was employed. Moreover, electrostatic interactions were treated with the smooth particle-mesh Ewald technique. Finally, MD simulations were performed in the NPT ensemble (1 μ s), by the application of an external electric field (E) along the entire dimension of z-axis (L_z). To do this, a specific transmembrane voltage (V) has been chosen, knowing that $V = E * L_z$. In this way, each charged particle feels about a force $F = qE$. Thus, applying a constant potential along the z-axis, all system ions are distributed in a manner to obtain detailed trajectory files, in which the behavior of the total system is realistic as possible.

Ca²⁺ binding site predictions

To evaluate the presence of putative Ca²⁺ binding sites along the entire structure of E2, the software MIB2: Metal Ion-Binding site prediction and modelling server (available at <http://bioinfo.cmu.edu.tw/MIB2/>) was used. As no complete 3D structure of the envelope protein is available, this software allows the direct reconstruction of the tertiary structure from the primary sequence by homology modelling. All structures obtained are analysed without the use of constraints. Binding site evaluation is performed using the (PS)² method as described in [156].

3.8.2 RESULTS

Model_A: simulations and analysis

We simulated the proposed pentameric model starting from the NMR structure (Model_A) embedded in a bilayer and solvated in 50mM KCl and 50mM CaCl₂. The pentameric initial structure is represented in Fig.13 (top): the central pore is solvated and water is also present at the periphery near the amphiphilic helices. Our simulation results are in line with other very recent data [128]: after equilibration and release of constraints, the supposed pentameric structure, with the longest helices forming a bundle, collapses to a closed structure (Fig.13 bottom). The long helices form a tight central bundle and water is extruded. The same collapsed structure is obtained when we use either different composition of the membrane, or enhanced sampling methods for simulations, even when we prolong the equilibration with the help of constraints

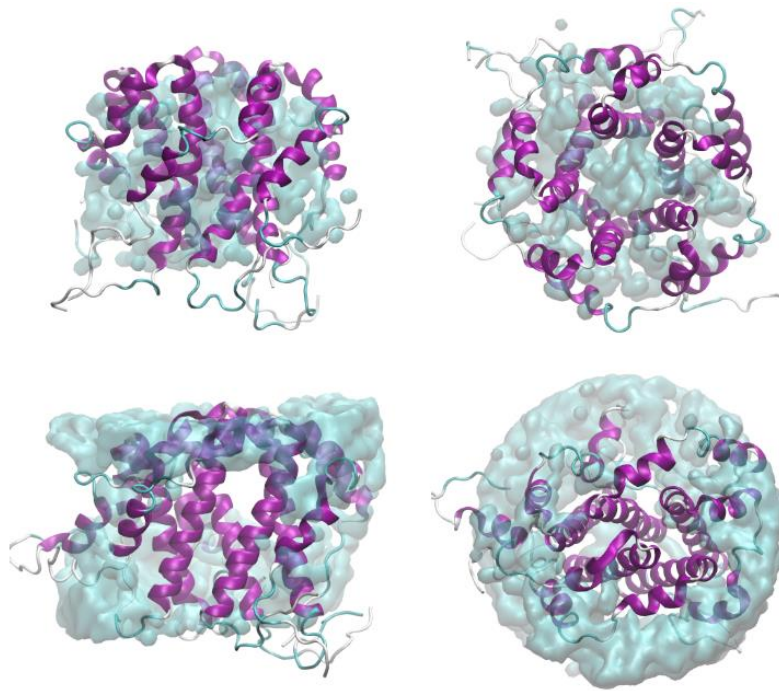


Fig.13 pentameric structure of Model_A before (top) and after (bottom) the release of constraints. Water molecules in contact with the protein are represented in cyan as surface. Left: side view; Right: top view

The analysis of the standard MD simulation trajectory reveals that after the initial rearrangement bringing to the collapse, the oligomer seems stable on the microsecond timescale. The RMSD (Fig.14A) calculated for each unit after the fitting on the entire pentamer shows that only one subunit (SU2) deviates from the entire oligomer, suggesting a potential arrangement as a tetramer. Despite the collapse of the central pore, water is present in the membrane around the short helices, toward the exterior of the central helix bundle, as shown in the last conformer of our trajectory (Fig.1-bottom). To better appreciate the lack of a water-pore, in Fig.14B, we superimposed the water density, calcium density and position of hydrophobic residue (we selected the c-alpha coordinates) on the XY plane. As we can see, the central region is occupied by hydrophobic residues and water is absent (Fig.14B). Interestingly, calcium ions prefer to stay where water is present and on the supposed luminal mouth with two prominent peaks. Neither potassium or chloride ions can occupy the central part.

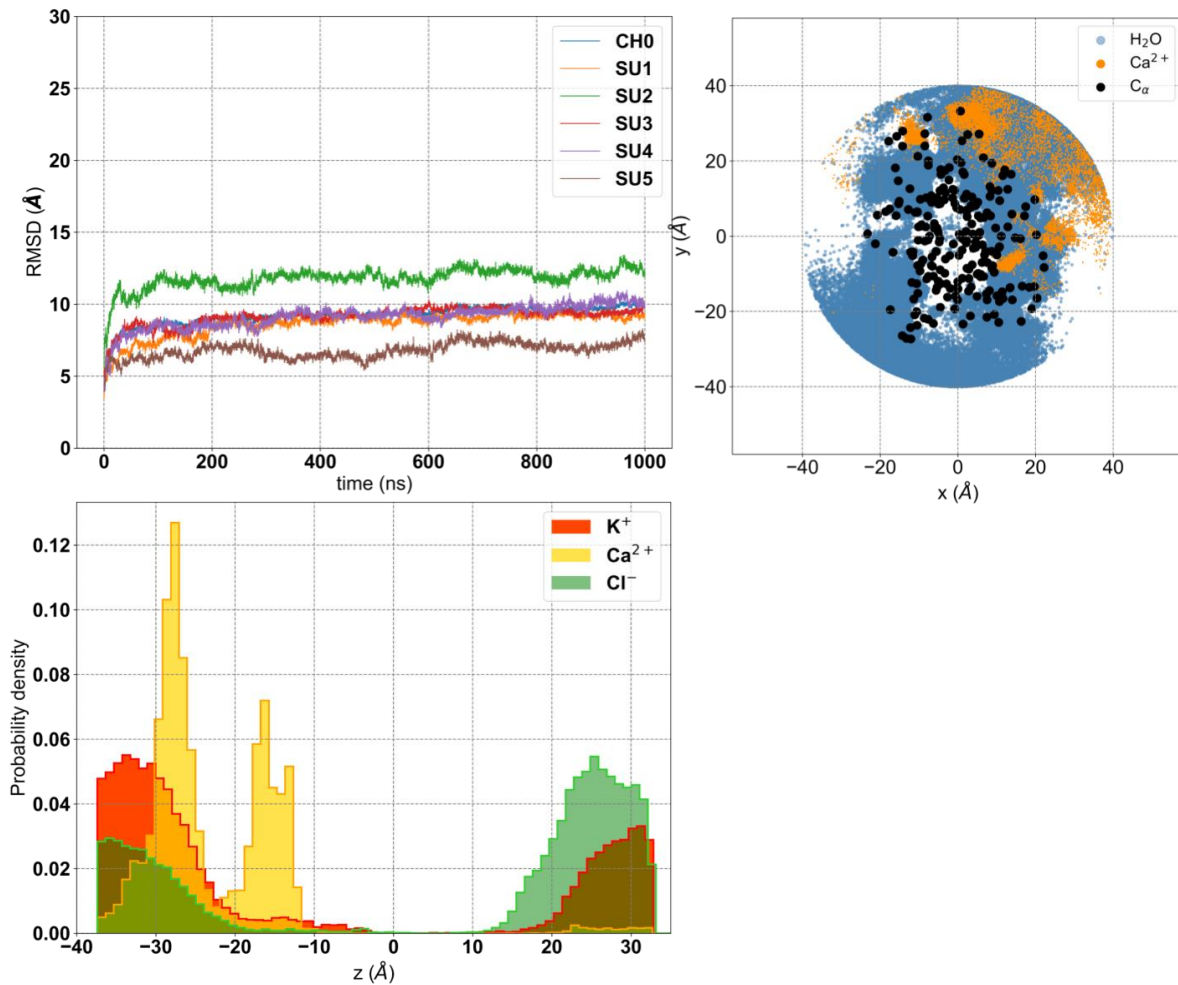


Fig.14 Analysis of 1 μ s production run trajectory of Model_A. A: RMSD deviation of each subunit (SU1-5) compared to the entire structure (CH0) along the 1 μ s trajectory. B: projection on the XY plane of coordinates extracted from the 1 μ s trajectory for water molecules, calcium ions and c-alpha of hydrophobic residues. C: density along Z axis of ions

To verify the possibility for ions to be transported laterally, we applied an external electric field of +100mV, again simulating the Model_A for 2 μ s. No movement of ions is visible, and even increasing the voltage to 400mV, we do not see any net movement of ions. In agreement with previous investigations, with this arrangement of the pentamer we do not have a net transport of ions on the microsecond time scale.

Model_B as a new arrangement

Our analysis of Model_A revealed the presence of water in the membrane with formation of lateral discontinuous water paths through the membrane, near the short amphipathic helices, though not sufficient to transport ions. We decided to test another arrangement of monomers, orienting them in the opposite direction, with the short amphipathic helices

toward the interior and the long hydrophobic helices toward the exterior, in direct contact with the membrane. This arrangement would favor the aggregation of the short amphipathic helices and perhaps the formation of a larger central hydrophilic pore. This arrangement has been suggested before the NMR structure appeared [121]. In figure 15 is reported a graphical comparison between the two models taken into consideration for this analysis:

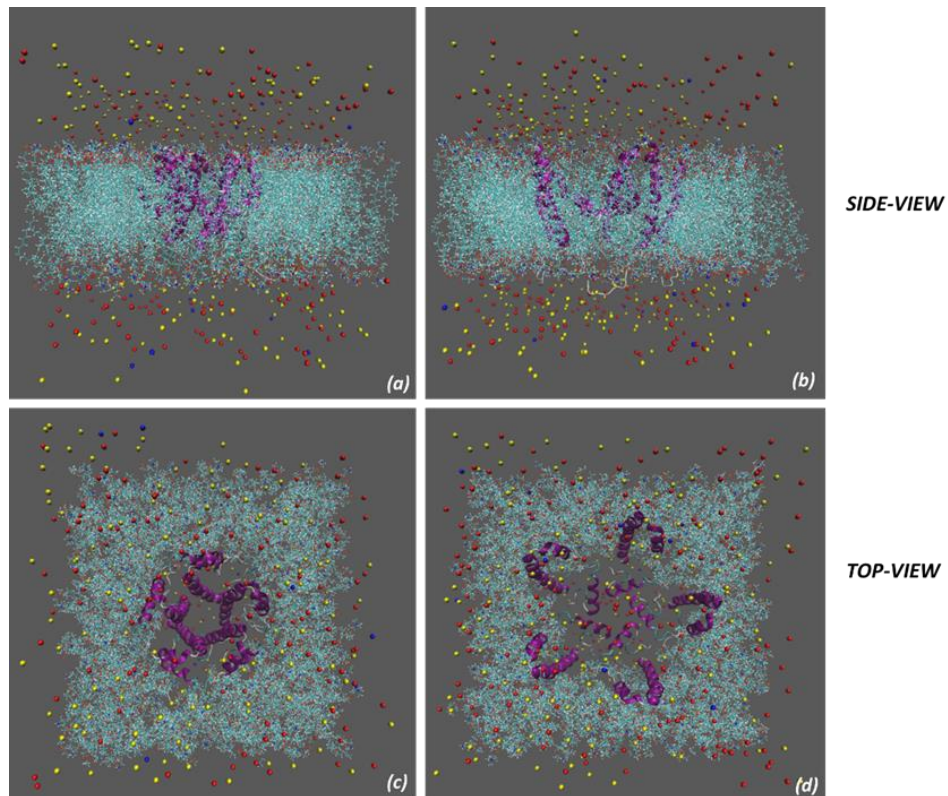


Fig. 15 Representation of E-2 protein in a cell-like system in a side-view and in a top view built with CHARMM-GUI. It is reported a comparison between the PDB representation model (a,c) and the new predicted structure of E-2 (b,d).

It is dictated by an expected arrangement of proteins in the membrane, with the hydrophobic helices toward the membrane and the amphipathic ones forming a central hydrophilic pore.

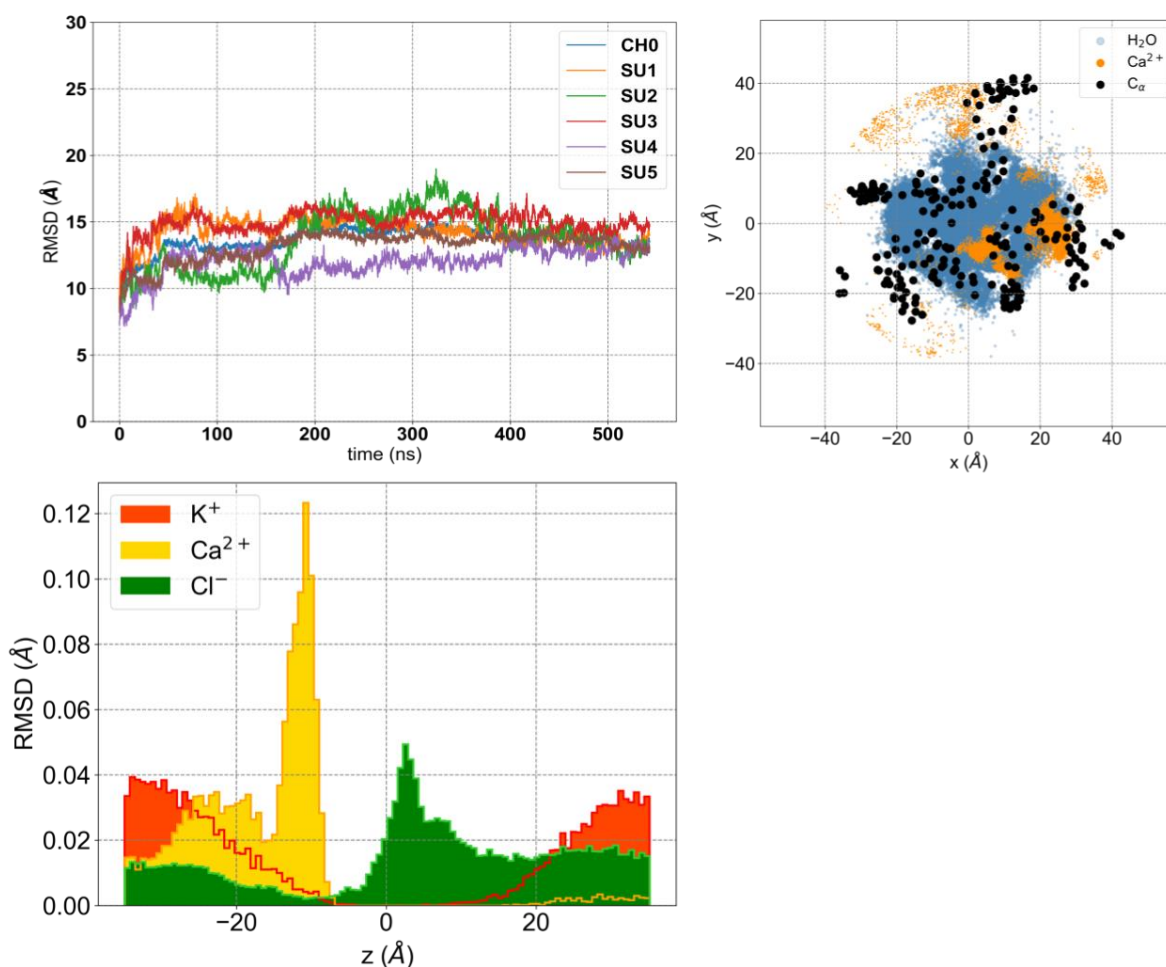


Fig.16 Analysis of 1 μ s production run trajectory of model_B. A: RMSD deviation of each subunit (SU1-5) compared to the entire structure (CH0) along the 1 μ s trajectory. B: projection on the XY plane of coordinates extracted from the 1 μ s trajectory for water molecules, calcium ions and c-alpha of hydrophobic residues. C: density along Z axis of ions

We performed the same equilibration and production run as for Model_A, followed by the same analysis presented in Fig.3 on the 1 μ s trajectory. The RMSD indicates that all five subunits are stable on the microsecond time scale (Fig.16A). Water molecules can now create a central pore free from hydrophobic residues, now placed externally (Fig.16B). Moreover, calcium ions stay more centrally than before, and we see a large density of chloride ions inside the membrane layer (Fig. 16C).

In silico electrophysiology

In both models, we tested the formation of a water pore able to conduct ions by applying an external electric field and calculating the transport of ions. We used a value of the external field compatible with experiments, ± 100 mV, applied on a trajectory of 1 microsecond started after equilibration. In this case we detected a low conductance on the first trajectory (1pS at

100mV means $0.6 \text{ q}/\mu\text{s}$). We also checked the stability of the oligomer upon application of the external field by calculating the RMSD as done above.

	Conductance (pS)			
	+100mV		-100mV	
	150mM KCl	50mM KCl + 50mM CaCl ₂	150mM KCl	50mM KCl + 50mM CaCl ₂
Model_A		26	//	//
Model_B	8	610	-2	310

Tab.1 Conductance revealed after $1\mu\text{s}$ of simulations for model_A and model_B with different ion concentrations. The potential applied to generate the electric field is $\pm 100\text{mV}$

Our results are summarized in Tab.1. We calculated the accumulation of charges as function of time, $Q(t)$. At 150mM KCl concentration and no calcium, we see that Model_B predicts a conductance of less than 10pS. This value does not represent a net movement because when we fit separately the accumulation of positive and negative ions we see that both move in the same direction, thus it has to be considered a zero net current. On the other hand, upon calcium addition, we see a large current, 610pS. Instead for Model_A, we have no net current detected during simulations, with only exception at +100mV in the presence of calcium: in this case the conductance value obtained is still significantly lower than that observed under the same condition in model_B.

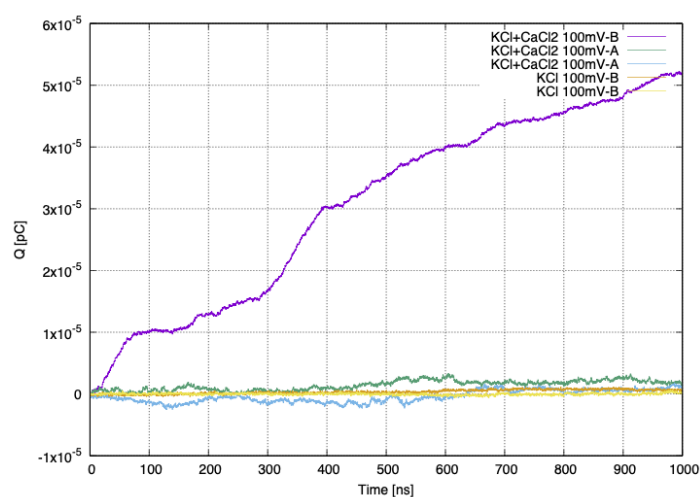


Fig. 17 Conductance measured after $1\mu\text{s}$ and reported as accumulation of charges in function of time. The slope of $Q(t)$ divided by the external potential represents the conductance. In purple is represented the conductance value measured for model_B at 50mM KCl + 50mM CaCl₂ with in a potential of +100mV, while other curve represents the model_A and model_B without calcium ions condition.

The model_B is the only arrangement of the protein E2 predicting the presence of water in the membrane forming a stable pore. This water-pore can transport ions and the presence of calcium acts as an amplifier of the ionic current. Interestingly, calcium accumulates on the lumen part, and our positive potential corresponds to having the same electric field between the lumen and the cytosol in cells. The dipole of long helices is aligned in the same direction as the electric field with positive voltage. From the analysis of the RMSD, we see that at positive voltage, the pentameric structure is stable, as we obtained on the trajectory without electric field. On the other hand, at negative voltage one of the units deviates by more than 5Å from the mean structure

PLB measurements demonstrates E2 inserts into artificial membrane as a multimer

Before evaluating membrane insertion, western blot analysis probing for recombinant E2 was carried out. As shown in Fig.18A, two protein bands were detected by anti-6XHisTag at approximately 25kDa and 17kDa, presumably corresponding to the oligomeric and monomeric states, respectively, as already reported in [123]. Bilayer electrophysiological recordings in symmetrical 1M CaCl₂ solution (pH 6.0) at ± 100mV applied revealed E2 inserts as channels of $\sim 2 \pm 0.4$ nS that quickly move to low-conducting or closed states of approximately 700-800 pS. No insertions were detectable at lower membrane potentials (± 50mV). The pore preference towards anions or cations (ion selectivity) was calculated under asymmetrical bi-ionic conditions. The fully open state of E2 reconstituted in a 1% DiPhPC membrane immersed in 1.0M (trans) to 0.05M (cis) asymmetric CaCl₂ gradient and evaluated in the range of 0 to ± 200mV, exhibited a reversal potential (Ψ_{rev}) of +56mV, indicative of cation selectivity. The corresponding ratio between Cl⁻ and Ca²⁺, P_{Cl}/P_{Ca} , was calculated according to the Goldman-Hodgkin-Katz equation (see eq. (7)).

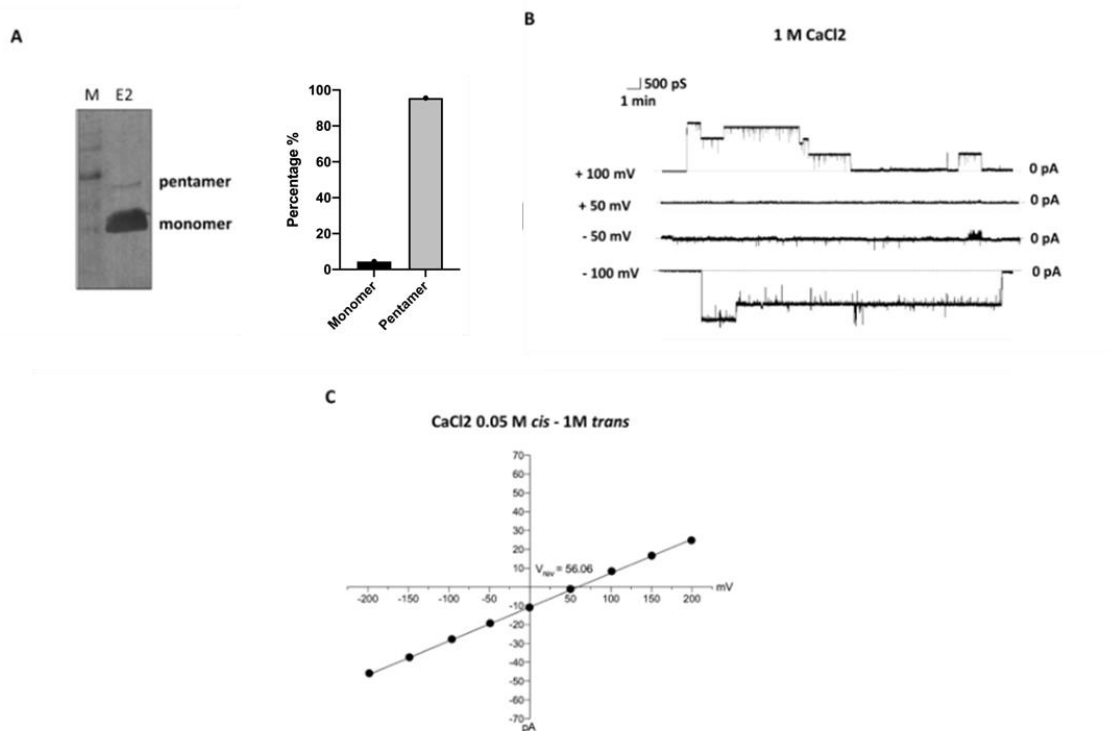


Fig.18 (A) Western blot analysis of SARS-CoV-2 protein E with anti-6xHis and quantification of monomeric and pentameric forms. **(B)** Representative current trace of E-2 recorded at ± 100 mV in 1M CaCl₂. **(C)** Ion selectivity measurements in 1M (trans) to 0.05M (cis) CaCl₂ solution upon application of a triangular voltage ramp of 0 \pm 200mV

Prediction of ion binding sites prediction reveals an inclination of C-terminal to interact with ion calcium

Based on the observations from both the electrophysiological data and the analysis of the trajectory files obtained from the MD simulations, it was possible to hypothesize how calcium could favour the process of permeation of the pore by both potassium and chloride ions, as well as by calcium ions themselves. To assess whether ion calcium binds to the protein in any way, a process was carried out to predict the active sites specific to this ion along the entire structure of E2. It was observed that there is a greater predisposition to bind calcium ions along the entire C-terminal sequence: specifically, the best scores were obtained for 45N-46I, 72D-69R, 72D-73L putative binding sites, as reported in Tab.2. Moreover, a single predicted binding site, was found at the beginning of the TMD.

	Binding residues	Score
1	45N, 46I	2.858
2	72D, 73L	2.084
3	42Y, 45N, 46I, 48N	1.561
4	69R, 72D	1.534
5	45N, 46I, 48N	1.406
6	15N, 16S	1.262
7	64N, 65L	1.255
8	72D, 73L, 75V	1.226

Tab.2 Predicted binding sites along the entire structure of E2

This analysis was carried out from the amino acid sequence of the envelope protein, as there is no entire tertiary structure contained in Protein Data Bank. The amino acidic sequence is a common element for both Model_A and Model_B. From the result obtained, it can be hypothesized that the orientation adopted by the C-terminus in the Model_B structure exposes more of the amino acid residues involved in the interaction with calcium ions. In addition, these interactions could change the size of the pore diameter, thus favoring ionic passage. Moreover, the result reported here is in line with what is already known about the interaction of the calcium ion with amino acids: in fact, Ca²⁺ interacts mainly with residues with carboxylated ends, such as aspartic and glutamic acid, but also with any negative charges that may be present in the side chains of asparagine, glutamine, serine, threonine and tyrosine [157,158,159]

3.8.3 CONCLUSIONS

The envelope protein of SARS-CoV-2 is one of the major structural proteins translated and released within the host cell organism. In this work, molecular dynamics simulation and electrophysiological experiments were performed to characterize this protein both structurally and functionally. The starting point for our analysis was the tertiary structure revealed for the SARS-CoV envelope protein, in which the protein monomers are arranged to form the pentameric structure previously hypothesized for E2.

MD simulations have shown how, in the reference structure (model_A), when an external electric field is applied, one of the monomeric subunits tends to move away, favoring the formation of a tetramer. Furthermore, analysis of the arrangement of the water molecules

shows how they dispose outside of the molecule, as opposed to the central area where the pore is formed: even charges such as calcium, potassium and chloride are arranged towards the outside of the molecule. Simulations of the passage of current through the pore have shown very little permeation of ions through the channel.

Therefore, on the basis of what was observed for model_A, a new structure was hypothesized in which the most hydrophilic domains, i.e. those related to the C-terminus, were positioned towards the centre of the structure to form a pore with hydrophilic properties. This property has been confirmed by repeating the same analytical procedure for model_A and observing how the water and ions tend to arrange themselves right at the centre of this structure. From a stability point of view, the pentameric structure also seems to be maintained over time. In silico electrophysiology analyses have shown that model_B has a greater ion transport activity than model_A, particularly in the presence of calcium ions.

This was also observed by carrying out electrophysiological experiments, with artificial membrane reconstruction in DPhPC. The presence of high calcium ion concentrations showed high conductance values and a tendency for the channel to have cation-selective properties. It was also observed that along the structure of the whole protein, and in particular along the C-terminal domain, there are several specific binding sites for the calcium ions. It is therefore possible to hypothesize that calcium binding to the protein triggers a mechanism that facilitates the passage of the ionic current through the channel, which also favors possible dyshomeostasis processes as reported by Nieto-Torres et al. [130]

In conclusion, the hypothesis of this new structural model makes it possible to be more aware of the means that may be necessary to implement further strategies to counteract the action of SARS-CoV-2 at the cellular level.

4. GENERAL CONCLUSION

In summary, the work presented here has highlighted several approaches that can be used to characterize a protein both structurally and functionally.

On the one hand, the respirometric approach was described, which makes it possible to assess in great detail the possible changes that can occur in a cellular organism when it is subjected to certain conditions. Such conditions may involve the overexpression of a protein using a suitable transfection technique (as in the case of the work reported on the overexpression of α -synuclein in SH-SY5Y neuroblastoma cells) or the deletion of a gene (as in the case of the work on the deletion of the VDAC1 channel protein). The aim was to observe the effect of these proteins on the regulation of cellular respiration. In the case of α Syn, its effect on the regulation of complex I activity was already known, but the mechanisms by which this activity was regulated had not yet been clarified. Indeed, in the case of VDAC1, a protein located in the outer mitochondrial membrane, the effects on the regulation of mitochondrial respiration are mainly assessed by the lack of transport of substrates involved in cellular metabolic pathways. In both cases, it was observed that the mitochondrion had reorganized the activity of the various complexes of the mitochondrial respiratory chain, which continued to produce ATP, in order to generate the necessary amount of energy to counteract the stimuli previously applied. In reality, the respirometric approach is also a good method for assessing the evolution of cellular respiration in certain pathological conditions. This is the case of the work presented on the MPP⁺ toxin involved in Parkinson's disease. A neurodegenerative condition was imposed by first differentiating SH-SY5Y neuroblastoma cells with retinoic acid and then treating them with the MPP⁺ toxin. In this work, the different states of respiration were evaluated with a view to possible treatments that could be carried out to promote a recovery, even if only partial, of cell functions [5].

The other methodological aspect presented in this thesis was the computational aspect in combination with electrophysiological techniques, in which the envelope protein obtained from SARS-CoV-2 was characterized. The computational part was carried out by using Molecular Dynamics simulations and active site predictions by using docking, while the electrophysiological part was carried out through the application of Planar Lipid Bilayer with the generation of an artificial 1% DPhPC membrane. The combination of these two aspects has made it possible to identify the possible key elements capable of regulating one the main

functions of the envelope protein, namely the formation of a pore capable of facilitating the passage of ion current. In reality, the work to characterize the envelope protein has a dual purpose: to understand the mechanism that regulate the functions of this protein and to understand how to counteract them. In this case, we have only focused on the first aspect, but this can be used as a starting point to devise specific strategies to counteract these elements and thus inhibit the functions of the envelope protein.

OTHER ACTIVITIES

During my PhD, I have joined to other activities in my research team. In particular, I carried out computational analyses to evaluate the conformational changes along the entire structure of the proteins VDAC1 (**Article 4**) and VDAC3 (**Article 5**), following the detection of post-translational modifications (PTMs) induced in both proteins by oxidative stress. Specifically, I evaluated how the proteins deviated from their original conformations after the induction of PTMs by calculating the RMSD parameter and making Ramachandran plots. Both works were carried out in collaboration with the research group of prof. Salvatore Foti and Prof. Rosaria Saletti at the University of Catania. All of these works are annexed to this thesis.

REFERENCES

- [1] Fang D, Maldonado EN. *VDAC Regulation: A Mitochondrial Target to Stop Cell Proliferation*. *Adv Cancer Res*. 2018;138:41-69. doi: 10.1016/bs.acr.2018.02.002
- [2] Pecinová A, Drahota Z, Nůsková H, Pecina P, Houštěk J. *Evaluation of basic mitochondrial functions using rat tissue homogenates*. *Mitochondrion*. 2011 Sep;11(5):722-8. doi: 10.1016/j.mito.2011.05.006
- [3] Cacabelos D, Ramírez-Núñez O, Granado-Serrano AB, Torres P, Ayala V, Moiseeva V, Povedano M, Ferrer I, Pamplona R, Portero-Otin M, Boada J. *Early and gender-specific differences in spinal cord mitochondrial function and oxidative stress markers in a mouse model of ALS*. *Acta Neuropathol Commun*. 2016 Jan 13;4:3. doi: 10.1186/s40478-015-0271-6
- [4] Magrì A, Risiglione P, Caccamo A, Formicola B, Tomasello MF, Arrigoni C, Zimbone S, Guarino F, Re F, Messina A. *Small Hexokinase 1 Peptide against Toxic SOD1 G93A Mitochondrial Accumulation in ALS Rescues the ATP-Related Respiration*. *Biomedicines*. 2021 Aug 3;9(8):948. doi: 10.3390/biomedicines9080948
- [5] Leggio L, L'Episcopo F, Magrì A, Ulloa-Navas MJ, Paternò G, Vivarelli S, Bastos CAP, Tirolo C, Testa N, Caniglia S, Risiglione P, Pappalardo F, Serra A, García-Tárraga P, Faria N, Powell JJ, Peruzzotti-Jametti L, Pluchino S, García-Verdugo JM, Messina A, Marchetti B, Iraci N. *Small Extracellular Vesicles Secreted by Nigrostriatal Astrocytes Rescue Cell Death and Preserve Mitochondrial Function in Parkinson's Disease*. *Adv Healthc Mater*. 2022 Oct;11(20):e2201203. doi: 10.1002/adhm.202201203
- [6] E.Gnaiger, *Polarographic Oxygen Sensors, the Oxygraph and High-Resolution Respirometry to assess mitochondrial function*, 2008, doi [10.1002/9780470372531.ch12](https://doi.org/10.1002/9780470372531.ch12)
- [7] Gnaiger E. *Bioenergetics at low oxygen: dependence of respiration and phosphorylation on oxygen and adenosine diphosphate supply*. *Respir Physiol*. 2001 Nov 15;128(3):277-97. doi: 10.1016/s0034-5687(01)00307-3
- [8] Steinlechner-Maran R, Eberl T, Kunc M, Margreiter R, Gnaiger E. *Oxygen dependence of respiration in coupled and uncoupled endothelial cells*. *Am J Physiol*. 1996 Dec;271(6 Pt 1):C2053-61. doi: 10.1152/ajpcell.1996.271.6.C2053
- [9] Long Q, Huang L, Huang K, Yang Q. *Assessing Mitochondrial Bioenergetics in Isolated Mitochondria from Mouse Heart Tissues Using Oroboros 2k-Oxygraph*. *Methods Mol Biol*. 2019;1966:237-246. doi: 10.1007/978-1-4939-9195-2_19.

- [10] Gnaiger E *Mitochondrial pathways and respiratory control. An introduction to OXPHOS analysis*. 5th ed. 2020 <https://doi.org/10.26124/bec:2020-0002>
- [11] E.Gnaiger et al., *Mitochondrial respiratory states and rates*, MitoFit Preprint Arch (2019) doi:10.26124/mitofit:190001.v5
- [12] Mohsin AA, Thompson J, Hu Y, Hollander J, Lesnefsky EJ, Chen Q. *Endoplasmic reticulum stress-induced complex I defect: Central role of calcium overload*. Arch Biochem Biophys. 2020 Apr 15;683:108299. doi: 10.1016/j.abb.2020.108299
- [13] Rudler DL, Hughes LA, Perks KL, Richman TR, Kuznetsova I, Ermer JA, Abudulai LN, Shearwood AJ, Viola HM, Hool LC, Siira SJ, Rackham O, Filipovska A. *Fidelity of translation initiation is required for coordinated respiratory complex assembly*. Sci Adv. 2019 Dec 20;5(12):eaay2118. doi: 10.1126/sciadv.aay2118
- [14] Hou WL, Yin J, Alimujiang M, Yu XY, Ai LG, Bao YQ, Liu F, Jia WP. *Inhibition of mitochondrial complex I improves glucose metabolism independently of AMPK activation*. J Cell Mol Med. 2018 Feb;22(2):1316-1328. doi: 10.1111/jcmm.13432
- [15] Ma X, Jin M, Cai Y, Xia H, Long K, Liu J, Yu Q, Yuan J. *Mitochondrial electron transport chain complex III is required for antimycin A to inhibit autophagy*. Chem Biol. 2011 Nov 23;18(11):1474-81. doi: 10.1016/j.chembiol.2011.08.009
- [16] Gandhirajan RK, Bodnar Y, Pasqual-Melo G, Bekeschus S. *Mitochondrial complex IV Inhibition and Exogenous Oxidants Potently Synergize in Melanoma Cell Death Induction*. Clinical Plasma Medicine 9,supplement 2018 19-20. doi: 10.1016/j.cpme.2017.12.031
- [17] Shchepina LA, Pletjushkina OY, Avetisyan AV, Bakeeva LE, Fetisova EK, Izyumov DS, Saprunova VB, Vyssokikh MY, Chernyak BV, Skulachev VP. *Oligomycin, inhibitor of the F₀ part of H⁺-ATP-synthase, suppresses the TNF-induced apoptosis*. Oncogene. 2002 Nov 21;21(53):8149-57. doi: 10.1038/sj.onc.1206053
- [18] Miyamoto K, Yamashita T, Tsukiyama T, Kitamura N, Minami N, Yamada M, Imai H. *Reversible membrane permeabilization of mammalian cells treated with digitonin and its use for inducing nuclear reprogramming by Xenopus egg extracts*. Cloning Stem Cells. 2008 Dec;10(4):535-42. doi: 10.1089/clo.2008.0020
- [19] Woronowicz K, Olubanjo OB, Sha D, Kay JM, Niederman RA. *Effects of the protonophore carbonyl-cyanide *m*-chlorophenylhydrazone on intracytoplasmic membrane assembly in Rhodobacter sphaeroides*. Biochim Biophys Acta. 2015 Oct;1847(10):1119-28. doi: 10.1016/j.bbabi.2015.06.002

- [20] Lemieux H, Semsroth S, Antretter H, Höfer D, Gnaiger E. *Mitochondrial respiratory control and early defects of oxidative phosphorylation in the failing human heart*. Int J Biochem Cell Biol. 2011 Dec;43(12):1729-38. doi: 10.1016/j.biocel.2011.08.008
- [21] Pesta D, Hoppel F, Macek C, Messner H, Faulhaber M, Kobel C, Parson W, Burtscher M, Schocke M, Gnaiger E. *Similar qualitative and quantitative changes of mitochondrial respiration following strength and endurance training in normoxia and hypoxia in sedentary humans*. Am J Physiol Regul Integr Comp Physiol. 2011 Oct;301(4):R1078-87. doi: 10.1152/ajpregu.00285.2011
- [22] Aragonés J, Schneider M, Van Geyte K, Fraisl P, Dresselaers T, Mazzone M, Dirx R, Zacchigna S, Lemieux H, Jeoung NH, Lambrechts D, Bishop T, Lafuste P, Diez-Juan A, Harten SK, Van Noten P, De Bock K, Willam C, Tjwa M, Grosfeld A, Navet R, Moons L, Vandendriessche T, Deroose C, Wijeyekoon B, Nuyts J, Jordan B, Silasi-Mansat R, Lupu F, Dewerchin M, Pugh C, Salmon P, Mortelmans L, Gallez B, Gorus F, Buyse J, Sluse F, Harris RA, Gnaiger E, Hespel P, Van Hecke P, Schuit F, Van Veldhoven P, Ratcliffe P, Baes M, Maxwell P, Carmeliet P. *Deficiency or inhibition of oxygen sensor Phd1 induces hypoxia tolerance by reprogramming basal metabolism*. Nat Genet. 2008 Feb;40(2):170-80. doi: 10.1038/ng.2007.62
- [23] Doerrier C, Garcia-Souza LF, Krumschnabel G, Wohlfarter Y, Mészáros AT, Gnaiger E. *High-Resolution Fluorescence Respirometry and OXPHOS Protocols for Human Cells, Permeabilized Fibers from Small Biopsies of Muscle, and Isolated Mitochondria*. Methods Mol Biol. 2018;1782:31-70. doi: 10.1007/978-1-4939-7831-1_3
- [24] Desler C, Hansen TL, Frederiksen JB, Marcker ML, Singh KK, Juel Rasmussen L. *Is There a Link between Mitochondrial Reserve Respiratory Capacity and Aging?* J Aging Res. 2012;2012:192503. doi: 10.1155/2012/192503
- [25] Di Rosa MC, Guarino F, Conti Nibali S, Magrì A, De Pinto V. *Voltage-Dependent Anion Selective Channel Isoforms in Yeast: Expression, Structure, and Functions*. Front Physiol. 2021 May 19;12:675708. doi: 10.3389/fphys.2021.675708
- [26] Benz R. *Permeation of hydrophilic solutes through mitochondrial outer membranes: review on mitochondrial porins*. Biochim Biophys Acta. 1994 Jun 29;1197(2):167-96. doi: 10.1016/0304-4157(94)90004-3
- [27] Rostovtseva T, Colombini M. *VDAC channels mediate and gate the flow of ATP: implications for the regulation of mitochondrial function*. Biophys J. 1997 May;72(5):1954-62. doi: 10.1016/S0006-3495(97)78841-6

- [28] Manzo G, Serra I, Magrí A, Casu M, De Pinto V, Ceccarelli M, Scorciapino MA. *Folded Structure and Membrane Affinity of the N-Terminal Domain of the Three Human Isoforms of the Mitochondrial Voltage-Dependent Anion-Selective Channel*. ACS Omega. 2018 Sep 30;3(9):11415-11425. doi: 10.1021/acsomega.8b01536
- [29] Messina A, Reina S, Guarino F, De Pinto V. *VDAC isoforms in mammals*. Biochim Biophys Acta. 2012 Jun;1818(6):1466-76. doi: 10.1016/j.bbame.2011.10.005
- [30] De Pinto V, Guarino F, Guarnera A, Messina A, Reina S, Tomasello FM, Palermo V, Mazzoni C. *Characterization of human VDAC isoforms: a peculiar function for VDAC3?* Biochim Biophys Acta. 2010 Jun-Jul;1797(6-7):1268-75. doi: 10.1016/j.bbabi.2010.01.031
- [31] Ujwal R, Cascio D, Colletier JP, Faham S, Zhang J, Toro L, Ping P, Abramson J. *The crystal structure of mouse VDAC1 at 2.3 Å resolution reveals mechanistic insights into metabolite gating*. Proc Natl Acad Sci U S A. 2008 Nov 18;105(46):17742-7. doi: 10.1073/pnas.0809634105
- [32] Bayrhuber M, Meins T, Habeck M, Becker S, Giller K, Villinger S, Vonrhein C, Griesinger C, Zweckstetter M, Zeth K. *Structure of the human voltage-dependent anion channel*. Proc Natl Acad Sci U S A. 2008 Oct 7;105(40):15370-5. doi: 10.1073/pnas.0808115105
- [33] Hiller S, Garces RG, Malia TJ, Orekhov VY, Colombini M, Wagner G. *Solution structure of the integral human membrane protein VDAC-1 in detergent micelles*. Science. 2008 Aug 29;321(5893):1206-10. doi: 10.1126/science.1161302
- [34] Shoshan-Barmatz V, Mizrahi D. *VDAC1: from structure to cancer therapy*. Front Oncol. 2012 Nov 29;2:164. doi: 10.3389/fonc.2012.00164.
- [35] Magrí A, Belfiore R, Reina S, Tomasello MF, Di Rosa MC, Guarino F, Leggio L, De Pinto V, Messina A. *Hexokinase I N-terminal based peptide prevents the VDAC1-SOD1 G93A interaction and re-establishes ALS cell viability*. Sci Rep. 2016 Oct 10;6:34802. doi: 10.1038/srep34802
- [36] Magrí A, Reina S, De Pinto V. *VDAC1 as Pharmacological Target in Cancer and Neurodegeneration: Focus on Its Role in Apoptosis*. Front Chem. 2018 Apr 6;6:108. doi: 10.3389/fchem.2018.00108
- [37] Arbel N, Shoshan-Barmatz V. *Voltage-dependent anion channel 1-based peptides interact with Bcl-2 to prevent antiapoptotic activity*. J Biol Chem. 2010 Feb 26;285(9):6053-62. doi: 10.1074/jbc.M109.082990

- [38] Keinan N, Tyomkin D, Shoshan-Barmatz V. *Oligomerization of the mitochondrial protein voltage-dependent anion channel is coupled to the induction of apoptosis*. Mol Cell Biol. 2010 Dec;30(24):5698-709. doi: 10.1128/MCB.00165-10
- [39] Geula S, Naveed H, Liang J, Shoshan-Barmatz V. *Structure-based analysis of VDAC1 protein: defining oligomer contact sites*. J Biol Chem. 2012 Jan 13;287(3):2179-90. doi: 10.1074/jbc.M111.268920
- [40] Schredelseker J, Paz A, López CJ, Altenbach C, Leung CS, Drexler MK, Chen JN, Hubbell WL, Abramson J. *High resolution structure and double electron-electron resonance of the zebrafish voltage-dependent anion channel 2 reveal an oligomeric population*. J Biol Chem. 2014 May 2;289(18):12566-77. doi: 10.1074/jbc.M113.497438
- [41] Madesh M, Hajnóczky G. *VDAC-dependent permeabilization of the outer mitochondrial membrane by superoxide induces rapid and massive cytochrome c release*. J Cell Biol. 2001 Dec 10;155(6):1003-15. doi: 10.1083/jcb.200105057
- [42] Tsujimoto Y. *Bcl-2 family of proteins: life-or-death switch in mitochondria*. Biosci Rep. 2002 Feb;22(1):47-58. doi: 10.1023/a:1016061006256
- [43] Cheng EH, Sheiko TV, Fisher JK, Craigen WJ, Korsmeyer SJ. *VDAC2 inhibits BAK activation and mitochondrial apoptosis*. Science. 2003 Jul 25;301(5632):513-7. doi: 10.1126/science.1083995
- [44] Reina S, Guarino F, Magrì A, De Pinto V. *VDAC3 As a Potential Marker of Mitochondrial Status Is Involved in Cancer and Pathology*. Front Oncol. 2016 Dec 23;6:264. doi: 10.3389/fonc.2016.00264
- [45] Shoshan-Barmatz V, Shteinfer-Kuzmine A, Verma A. *VDAC1 at the Intersection of Cell Metabolism, Apoptosis, and Diseases*. Biomolecules. 2020 Oct 26;10(11):1485. doi: 10.3390/biom10111485
- [46] Lee K, Kerner J, Hoppel CL. *Mitochondrial carnitine palmitoyltransferase 1a (CPT1a) is part of an outer membrane fatty acid transfer complex*. J Biol Chem. 2011 Jul 22;286(29):25655-62. doi: 10.1074/jbc.M111.228692
- [47] Pittalà MGG, Reina S, Cubisino SAM, Cucina A, Formicola B, Cunsolo V, Foti S, Saletti R, Messina A. *Post-Translational Modification Analysis of VDAC1 in ALS-SOD1 Model Cells Reveals Specific Asparagine and Glutamine Deamidation*. Antioxidants (Basel). 2020 Dec 2;9(12):1218. doi: 10.3390/antiox9121218

- [48] Ben-Hail D, Begas-Shvartz R, Shalev M, Shteinfer-Kuzmine A, Gruzman A, Reina S, De Pinto V, Shoshan-Barmatz V. *Novel Compounds Targeting the Mitochondrial Protein VDAC1 Inhibit Apoptosis and Protect against Mitochondrial Dysfunction*. J Biol Chem. 2016 Nov 25;291(48):24986-25003. doi: 10.1074/jbc.M116.744284
- [49] Verma A, Pittala S, Alhozeel B, Shteinfer-Kuzmine A, Ohana E, Gupta R, Chung JH, Shoshan-Barmatz V. *The role of the mitochondrial protein VDAC1 in inflammatory bowel disease: a potential therapeutic target*. Mol Ther. 2022 Feb 2;30(2):726-744. doi: 10.1016/j.ymthe.2021.06.024
- [50] Guarino F, Zinghirino F, Mela L, Pappalardo XG, Ichas F, De Pinto V, Messina A. *NRF-1 and HIF-1 α contribute to modulation of human VDAC1 gene promoter during starvation and hypoxia in HeLa cells*. Biochim Biophys Acta Bioenerg. 2020 Dec 1;1861(12):148289. doi: 10.1016/j.bbabi.2020.148289
- [51] Magrì A, Karachitos A, Di Rosa MC, Reina S, Conti Nibali S, Messina A, Kmita H, De Pinto V. *Recombinant yeast VDAC2: a comparison of electrophysiological features with the native form*. FEBS Open Bio. 2019 Jul;9(7):1184-1193. doi: 10.1002/2211-5463.12574
- [52] Colombini M. *Measurement of VDAC permeability in intact mitochondria and in reconstituted systems*. Methods Cell Biol. 2007;80:241-60. doi: 10.1016/S0091-679X(06)80012-9
- [53] Jakes R, Spillantini MG, Goedert M. *Identification of two distinct synucleins from human brain*. FEBS Lett. 1994 May 23;345(1):27-32. doi: 10.1016/0014-5793(94)00395-5
- [54] Nakai M, Fujita M, Waragai M, Sugama S, Wei J, Akatsu H, Ohtaka-Maruyama C, Okado H, Hashimoto M. *Expression of alpha-synuclein, a presynaptic protein implicated in Parkinson's disease, in erythropoietic lineage*. Biochem Biophys Res Commun. 2007 Jun 22;358(1):104-10. doi: 10.1016/j.bbrc.2007.04.108
- [55] Gorbatyuk OS, Li S, Nguyen FN, Manfredsson FP, Kondrikova G, Sullivan LF, Meyers C, Chen W, Mandel RJ, Muzyczka N. *α -Synuclein expression in rat substantia nigra suppresses phospholipase D2 toxicity and nigral neurodegeneration*. Mol Ther. 2010 Oct;18(10):1758-68. doi: 10.1038/mt.2010.137
- [56] Baptista MJ, O'Farrell C, Daya S, Ahmad R, Miller DW, Hardy J, Farrer MJ, Cookson MR. *Co-ordinate transcriptional regulation of dopamine synthesis genes by alpha-synuclein in human neuroblastoma cell lines*. J Neurochem. 2003 May;85(4):957-68. doi: 10.1046/j.1471-4159.2003.01742.x

- [57] Lee HJ, Khoshaghideh F, Lee S, Lee SJ. *Impairment of microtubule-dependent trafficking by overexpression of alpha-synuclein*. Eur J Neurosci. 2006 Dec;24(11):3153-62. doi: 10.1111/j.1460-9568.2006.05210.x
- [58] Westphal CH, Chandra SS. *Monomeric synucleins generate membrane curvature*. J Biol Chem. 2013 Jan 18;288(3):1829-40. doi: 10.1074/jbc.M112.418871
- [59] Ostrerova N, Petrucelli L, Farrer M, Mehta N, Choi P, Hardy J, Wolozin B. *alpha-Synuclein shares physical and functional homology with 14-3-3 proteins*. J Neurosci. 1999 Jul 15;19(14):5782-91. doi: 10.1523/JNEUROSCI.19-14-05782.1999
- [60] Ahn M, Kim S, Kang M, Ryu Y, Kim TD. *Chaperone-like activities of alpha-synuclein: alpha-synuclein assists enzyme activities of esterases*. Biochem Biophys Res Commun. 2006 Aug 11;346(4):1142-9. doi: 10.1016/j.bbrc.2006.05.213
- [61] Burré J, Sharma M, Tsetsenis T, Buchman V, Etherton MR, Südhof TC. *Alpha-synuclein promotes SNARE-complex assembly in vivo and in vitro*. Science. 2010 Sep 24;329(5999):1663-7. doi: 10.1126/science.1195227
- [62] Bernal-Conde LD, Ramos-Acevedo R, Reyes-Hernández MA, Balbuena-Olvera AJ, Morales-Moreno ID, Argüero-Sánchez R, Schüle B, Guerra-Crespo M. *Alpha-Synuclein Physiology and Pathology: A Perspective on Cellular Structures and Organelles*. Front Neurosci. 2020 Jan 23;13:1399. doi: 10.3389/fnins.2019.01399
- [63] Ludtmann MHR, Angelova PR, Horrocks MH, Choi ML, Rodrigues M, Baev AY, Berezhnov AV, Yao Z, Little D, Banushi B, Al-Menhali AS, Ranasinghe RT, Whiten DR, Yapom R, Dolt KS, Devine MJ, Gissen P, Kunath T, Jaganjac M, Pavlov EV, Klenerman D, Abramov AY, Gandhi S. *alpha-synuclein oligomers interact with ATP synthase and open the permeability transition pore in Parkinson's disease*. Nat Commun. 2018 Jun 12;9(1):2293. doi: 10.1038/s41467-018-04422-2
- [64] Di Maio R, Barrett PJ, Hoffman EK, Barrett CW, Zharikov A, Borah A, Hu X, McCoy J, Chu CT, Burton EA, Hastings TG, Greenamyre JT. *alpha-Synuclein binds to TOM20 and inhibits mitochondrial protein import in Parkinson's disease*. Sci Transl Med. 2016 Jun 8;8(342):342ra78. doi: 10.1126/scitranslmed.aaf3634
- [65] de Oliveira GAP, Silva JL. *Alpha-synuclein stepwise aggregation reveals features of an early onset mutation in Parkinson's disease*. Commun Biol. 2019 Oct 11;2:374. doi: 10.1038/s42003-019-0598-9

- [66] rinivasan E, Chandrasekhar G, Chandrasekar P, Anbarasu K, Vickram AS, Karunakaran R, Rajasekaran R, Srikumar PS. *Alpha-Synuclein Aggregation in Parkinson's Disease*. Front Med (Lausanne). 2021 Oct 18;8:736978. doi: 10.3389/fmed.2021.736978
- [67] Binolfi A, Rodriguez EE, Valensin D, D'Amelio N, Ippoliti E, Obal G, Duran R, Magistrato A, Pritsch O, Zweckstetter M, Valensin G, Carloni P, Quintanar L, Griesinger C, Fernández CO. *Bioinorganic chemistry of Parkinson's disease: structural determinants for the copper-mediated amyloid formation of alpha-synuclein*. Inorg Chem. 2010 Nov 15;49(22):10668-79. doi: 10.1021/ic1016752
- [68] Rostovtseva TK, Gurnev PA, Protchenko O, Hoogerheide DP, Yap TL, Philpott CC, Lee JC, Bezrukov SM. *α -Synuclein Shows High Affinity Interaction with Voltage-dependent Anion Channel, Suggesting Mechanisms of Mitochondrial Regulation and Toxicity in Parkinson Disease*. J Biol Chem. 2015 Jul 24;290(30):18467-77. doi: 10.1074/jbc.M115.641746
- [69] Krüger R, Kuhn W, Müller T, Voitalla D, Graeber M, Kösel S, Przuntek H, Epplen JT, Schöls L, Riess O. *Ala30Pro mutation in the gene encoding alpha-synuclein in Parkinson's disease*. Nat Genet. 1998 Feb;18(2):106-8. doi: 10.1038/ng0298-106
- [70] Boyer DR, Li B, Sun C, Fan W, Zhou K, Hughes MP, Sawaya MR, Jiang L, Eisenberg DS. *The α -synuclein hereditary mutation E46K unlocks a more stable, pathogenic fibril structure*. Proc Natl Acad Sci U S A. 2020 Feb 18;117(7):3592-3602. doi: 10.1073/pnas.1917914117
- [71] Khalaf O, Fauvet B, Oueslati A, Dikiy I, Mahul-Mellier AL, Ruggeri FS, Mbefo MK, Vercruyse F, Dietler G, Lee SJ, Eliezer D, Lashuel HA. *The H50Q mutation enhances α -synuclein aggregation, secretion, and toxicity*. J Biol Chem. 2014 Aug 8;289(32):21856-76. doi: 10.1074/jbc.M114.553297
- [72] Lesage S, Anheim M, Letournel F, Bousset L, Honoré A, Rozas N, Pieri L, Madiona K, Dürr A, Melki R, Verny C, Brice A; French Parkinson's Disease Genetics Study Group. *G51D α -synuclein mutation causes a novel parkinsonian-pyramidal syndrome*. Ann Neurol. 2013 Apr;73(4):459-71. doi: 10.1002/ana.23894
- [73] Chen M, Liu J, Lu Y, Duan C, Lu L, Gao G, Chan P, Yu S, Yang H. *Age-dependent alpha-synuclein accumulation is correlated with elevation of mitochondrial TRPC3 in the brains of monkeys and mice*. J Neural Transm (Vienna). 2017 Apr;124(4):441-453. doi: 10.1007/s00702-016-1654-y

- [74] Chen L, Xie Z, Turkson S, Zhuang X. *A53T human α -synuclein overexpression in transgenic mice induces pervasive mitochondria macroautophagy defects preceding dopamine neuron degeneration.* J Neurosci. 2015 Jan 21;35(3):890-905. doi: 10.1523/JNEUROSCI.0089-14.2015
- [75] Li L, Nadanaciva S, Berger Z, Shen W, Paumier K, Schwartz J, Mou K, Loos P, Milici AJ, Dunlop J, Hirst WD. *Human A53T α -synuclein causes reversible deficits in mitochondrial function and dynamics in primary mouse cortical neurons.* PLoS One. 2013 Dec 31;8(12):e85815. doi: 10.1371/journal.pone.0085815
- [76] Langston JW. *The MPTP Story.* J Parkinsons Dis. 2017;7(s1):S11-S19. doi: 10.3233/JPD-179006
- [77] Kopin IJ. *MPTP: an industrial chemical and contaminant of illicit narcotics stimulates a new era in research on Parkinson's disease.* Environ Health Perspect. 1987 Nov;75:45-51. doi: 10.1289/ehp.877545
- [78] Di Monte DA, Wu EY, Irwin I, Delaney LE, Langston JW. *Biotransformation of 1-methyl-4-phenyl-1,2,3,6-tetrahydropyridine in primary cultures of mouse astrocytes.* J Pharmacol Exp Ther. 1991 Aug;258(2):594-600. PMID: 1907660
- [79] Ramsay RR, Salach JI, Singer TP. *Uptake of the neurotoxin 1-methyl-4-phenylpyridine (MPP+) by mitochondria and its relation to the inhibition of the mitochondrial oxidation of NAD+-linked substrates by MPP+.* Biochem Biophys Res Commun. 1986 Jan 29;134(2):743-8. doi: 10.1016/s0006-291x(86)80483-1
- [80] Ramsay RR, Kowal AT, Johnson MK, Salach JI, Singer TP. *The inhibition site of MPP+, the neurotoxic bioactivation product of 1-methyl-4-phenyl-1,2,3,6-tetrahydropyridine is near the Q-binding site of NADH dehydrogenase.* Arch Biochem Biophys. 1987 Dec;259(2):645-9. doi: 10.1016/0003-9861(87)90531-5
- [81] Burns RS, Markey SP, Phillips JM, Chiueh CC. *The neurotoxicity of 1-methyl-4-phenyl-1,2,3,6-tetrahydropyridine in the monkey and man.* Can J Neurol Sci. 1984 Feb;11(1 Suppl):166-8. doi: 10.1017/s0317167100046345
- [82] Langston JW, Langston EB, Irwin I. *MPTP-induced parkinsonism in human and non-human primates--clinical and experimental aspects.* Acta Neurol Scand Suppl. 1984;100:49-54.
- [83] Riachi NJ, Harik SI, Kalaria RN, Sayre LM. *On the mechanisms underlying 1-methyl-4-phenyl-1,2,3,6-tetrahydropyridine neurotoxicity. II. Susceptibility among mammalian species correlates with the toxin's metabolic patterns in brain microvessels and liver.* J Pharmacol Exp Ther. 1988 Feb;244(2):443-8.

- [84] Riachi NJ, LaManna JC, Harik SI. *Entry of 1-methyl-4-phenyl-1,2,3,6-tetrahydropyridine into the rat brain*. J Pharmacol Exp Ther. 1989 Jun;249(3):744-8
- [85] Tetrad JW, Langston JW. *The effect of deprenyl (selegiline) on the natural history of Parkinson's disease*. Science. 1989 Aug 4;245(4917):519-22. doi: 10.1126/science.250284
- [86] Olanow CW, Rascol O, Hauser R, Feigin PD, Jankovic J, Lang A, Langston W, Melamed E, Poewe W, Stocchi F, Tolosa E; ADAGIO Study Investigators. *A double-blind, delayed-start trial of rasagiline in Parkinson's disease*. N Engl J Med. 2009 Sep 24;361(13):1268-78. doi: 10.1056/NEJMoa080933
- [87] Xicoy H, Wieringa B, Martens GJ. *The SH-SY5Y cell line in Parkinson's disease research: a systematic review*. Mol Neurodegener. 2017 Jan 24;12(1):10. doi: 10.1186/s13024-017-0149-0
- [88] Li L, Nadanaciva S, Berger Z, Shen W, Paumier K, Schwartz J, Mou K, Loos P, Milici AJ, Dunlop J, Hirst WD. *Human A53T α -synuclein causes reversible deficits in mitochondrial function and dynamics in primary mouse cortical neurons*. PLoS One. 2013 Dec 31;8(12):e85815. doi: 10.1371/journal.pone.0085815
- [89] Fu MH, Wu CW, Lee YC, Hung CY, Chen IC, Wu KLH. *Nrf2 activation attenuates the early suppression of mitochondrial respiration due to the α -synuclein overexpression*. Biomed J. 2018 Jun;41(3):169-183. doi: 10.1016/j.bj.2018.02.005
- [90] Bose A, Beal MF. *Mitochondrial dysfunction in Parkinson's disease*. J Neurochem. 2016 Oct;139 Suppl 1:216-231. doi: 10.1111/jnc.13731
- [91] Taylor MW. *What Is a Virus?* Viruses and Man: A History of Interactions. 2014 Jul 22:23–40. doi: 10.1007/978-3-319-07758-1_2
- [92] Burrell CJ, Howard CR, Murphy FA. *Virion Structure and Composition*. Fenner and White's Medical Virology. 2017:27–37. doi: 10.1016/B978-0-12-375156-0.00003-5
- [93] Koonin EV, Krupovic M, Agol VI. *The Baltimore Classification of Viruses 50 Years Later: How Does It Stand in the Light of Virus Evolution?* Microbiol Mol Biol Rev. 2021 Aug 18;85(3):e0005321. doi: 10.1128/MMBR.00053-21
- [94] Louten J. *Virus Structure and Classification*. Essential Human Virology. 2016:19–29. doi: 10.1016/B978-0-12-800947-5.00002-8
- [95] https://ictv.global/report_9th/RNApos/Nidovirales

- [96] Leao JC, Gusmao TPL, Zarzar AM, Leao Filho JC, Barkokebas Santos de Faria A, Morais Silva IH, Gueiros LAM, Robinson NA, Porter S, Carvalho AAT. *Coronaviridae-Old friends, new enemy!* Oral Dis. 2022 Apr;28 Suppl 1(Suppl 1):858-866. doi: 10.1111/odi.13447
- [97] Pillaiyar T, Meenakshisundaram S, Manickam M. *Recent discovery and development of inhibitors targeting coronaviruses.* Drug Discov Today. 2020 Apr;25(4):668-688. doi: 10.1016/j.drudis.2020.01.015
- [98] Zeng Q, Langereis MA, van Vliet AL, Huizinga EG, de Groot RJ. *Structure of coronavirus hemagglutinin-esterase offers insight into corona and influenza virus evolution.* Proc Natl Acad Sci U S A. 2008 Jul 1;105(26):9065-9. doi: 10.1073/pnas.0800502105
- [99] Rabaan AA, Al-Ahmed SH, Haque S, Sah R, Tiwari R, Malik YS, Dhama K, Yatoo MI, Bonilla-Aldana DK, Rodriguez-Morales AJ. *SARS-CoV-2, SARS-CoV, and MERS-COV: A comparative overview.* Infez Med. 2020 Ahead Of Print Jun 1;28(2):174-184. PMID: 32275259
- [100] Song Z, Xu Y, Bao L, Zhang L, Yu P, Qu Y, Zhu H, Zhao W, Han Y, Qin C. *From SARS to MERS, Thrusting Coronaviruses into the Spotlight.* Viruses. 2019 Jan 14;11(1):59. doi: 10.3390/v11010059.
- [101] Perlman S, Netland J. *Coronaviruses post-SARS: update on replication and pathogenesis.* Nat Rev Microbiol. 2009 Jun;7(6):439-50. doi: 10.1038/nrmicro2147
- [102] Gordon DE et al *A SARS-CoV-2 protein interaction map reveals targets for drug repurposing.* Nature. 2020 Jul;583(7816):459-468. doi: 10.1038/s41586-020-2286-9
- [103] V'kovski P, Kratzel A, Steiner S, Stalder H, Thiel V. *Coronavirus biology and replication: implications for SARS-CoV-2.* Nat Rev Microbiol. 2021 Mar;19(3):155-170. doi: 10.1038/s41579-020-00468-6
- [104] Li F. *Structure, Function, and Evolution of Coronavirus Spike Proteins.* Annu Rev Virol. 2016 Sep 29;3(1):237-261. doi: 10.1146/annurev-virology-110615-042301
- [105] Tortorici MA, Veesler D. *Structural insights into coronavirus entry.* Adv Virus Res. 2019;105:93-116. doi: 10.1016/bs.aivir.2019.08.002
- [106] Zhang Z, Nomura N, Muramoto Y, Ekimoto T, Uemura T, Liu K, Yui M, Kono N, Aoki J, Ikeguchi M, Noda T, Iwata S, Ohto U, Shimizu T. *Structure of SARS-CoV-2 membrane protein essential for virus assembly.* Nat Commun. 2022 Aug 5;13(1):4399. doi: 10.1038/s41467-022-32019-3

- [107] Bai Z, Cao Y, Liu W, Li J. *The SARS-CoV-2 Nucleocapsid Protein and Its Role in Viral Structure, Biological Functions, and a Potential Target for Drug or Vaccine Mitigation*. *Viruses*. 2021 Jun 10;13(6):1115. doi: 10.3390/v13061115
- [108] Masters PS. *The molecular biology of coronaviruses*. *Adv Virus Res*. 2006;66:193-292. doi: 10.1016/S0065-3527(06)66005-3
- [109] Kopecky-Bromberg SA, Martínez-Sobrido L, Frieman M, Baric RA, Palese P. *Severe acute respiratory syndrome coronavirus open reading frame (ORF) 3b, ORF 6, and nucleocapsid proteins function as interferon antagonists*. *J Virol*. 2007 Jan;81(2):548-57. doi: 10.1128/JVI.01782-06
- [110] Surjit M, Liu B, Chow VT, Lal SK. *The nucleocapsid protein of severe acute respiratory syndrome-coronavirus inhibits the activity of cyclin-cyclin-dependent kinase complex and blocks S phase progression in mammalian cells*. *J Biol Chem*. 2006 Apr 21;281(16):10669-81. doi: 10.1074/jbc.M509233200
- [111] Chan KK, Dorosky D, Sharma P, Abbasi SA, Dye JM, Kranz DM, Herbert AS, Procko E. *Engineering human ACE2 to optimize binding to the spike protein of SARS coronavirus 2*. *Science*. 2020 Sep 4;369(6508):1261-1265. doi: 10.1126/science.abc0870
- [112] Yang J, Petitjean SJL, Koehler M, Zhang Q, Dumitru AC, Chen W, Derclaye S, Vincent SP, Soumillon P, Alsteens D. *Molecular interaction and inhibition of SARS-CoV-2 binding to the ACE2 receptor*. *Nat Commun*. 2020 Sep 11;11(1):4541. doi: 10.1038/s41467-020-18319-6
- [113] Huggins DJ. *Structural analysis of experimental drugs binding to the SARS-CoV-2 target TMPRSS2*. *J Mol Graph Model*. 2020 Nov;100:107710. doi: 10.1016/j.jmgm.2020.107710
- [114] Hillen HS, Kocic G, Farnung L, Dienemann C, Tegunov D, Cramer P. *Structure of replicating SARS-CoV-2 polymerase*. *Nature*. 2020 Aug;584(7819):154-156. doi: 10.1038/s41586-020-2368-8
- [115] Mirza MU, Froeyen M. *Structural elucidation of SARS-CoV-2 vital proteins: Computational methods reveal potential drug candidates against main protease, Nsp12 polymerase and Nsp13 helicase*. *J Pharm Anal*. 2020 Aug;10(4):320-328. doi: 10.1016/j.jpha.2020.04.008
- [116] Armstrong LA, Lange SM, Dee Cesare V, Matthews SP, Nirujogi RS, Cole I, Hope A, Cunningham F, Toth R, Mukherjee R, Bojkova D, Gruber F, Gray D, Wyatt PG, Cinatl J, Dikic I, Davies P, Kulathu Y. *Biochemical characterization of protease activity of Nsp3 from SARS-CoV-*

2 and its inhibition by nanobodies. PLoS One. 2021 Jul 16;16(7):e0253364. doi: 10.1371/journal.pone.0253364

[117] DeDiego ML, Alvarez E, Almazán F, Rejas MT, Lamirande E, Roberts A, Shieh WJ, Zaki SR, Subbarao K, Enjuanes L. *A severe acute respiratory syndrome coronavirus that lacks the E gene is attenuated in vitro and in vivo.* J Virol. 2007 Feb;81(4):1701-13. doi: 10.1128/JVI.01467-06

[118] Kuo L, Masters PS. *The small envelope protein E is not essential for murine coronavirus replication.* J Virol. 2003 Apr;77(8):4597-608. doi: 10.1128/jvi.77.8.4597-4608.2003

[119] Xia B, Shen X, He Y, Pan X, Liu FL, Wang Y, Yang F, Fang S, Wu Y, Duan Z, Zuo X, Xie Z, Jiang X, Xu L, Chi H, Li S, Meng Q, Zhou H, Zhou Y, Cheng X, Xin X, Jin L, Zhang HL, Yu DD, Li MH, Feng XL, Chen J, Jiang H, Xiao G, Zheng YT, Zhang LK, Shen J, Li J, Gao Z. *SARS-CoV-2 envelope protein causes acute respiratory distress syndrome (ARDS)-like pathological damages and constitutes an antiviral target.* Cell Res. 2021 Aug;31(8):847-860. doi: 10.1038/s41422-021-00519-4

[120] McClenaghan C, Hanson A, Lee SJ, Nichols CG. *Coronavirus Proteins as Ion Channels: Current and Potential Research.* Front Immunol. 2020 Oct 9;11:573339. doi: 10.3389/fimmu.2020.573339

[121] Schoeman D, Fielding BC. *Coronavirus envelope protein: current knowledge.* Virol J. 2019 May 27;16(1):69. doi: 10.1186/s12985-019-1182-0

[122] Kumar P, Kumar A, Garg N, Giri R. *An insight into SARS-CoV-2 membrane protein interaction with spike, envelope, and nucleocapsid proteins.* J Biomol Struct Dyn. 2023 Feb;41(3):1062-1071. doi: 10.1080/07391102.2021.2016490

[123] Surya W, Li Y, Torres J. *Structural model of the SARS coronavirus E channel in LMPG micelles.* Biochim Biophys Acta Biomembr. 2018 Jun;1860(6):1309-1317. doi: 10.1016/j.bbamem.2018.02.017

[124] Liao Y, Lescar J, Tam JP, Liu DX. *Expression of SARS-coronavirus envelope protein in Escherichia coli cells alters membrane permeability.* Biochem Biophys Res Commun. 2004 Dec 3;325(1):374-80. doi: 10.1016/j.bbrc.2004.10.050

[125] Mandala VS, McKay MJ, Shcherbakov AA, Dregni AJ, Kolocouris A, Hong M. *Structure and drug binding of the SARS-CoV-2 envelope protein transmembrane domain in lipid bilayers.* Nat Struct Mol Biol. 2020 Dec;27(12):1202-1208. doi: 10.1038/s41594-020-00536-8

- [126] Kuzmin A, Orekhov P, Astashkin R, Gordeliy V, Gushchin I. *Structure and dynamics of the SARS-CoV-2 envelope protein monomer*. Proteins. 2022 May;90(5):1102-1114. doi: 10.1002/prot.26317
- [127] Verdiá-Báguena C, Aguilera VM, Queralt-Martín M, Alcaraz A. *Transport mechanisms of SARS-CoV-E viroporin in calcium solutions: Lipid-dependent Anomalous Mole Fraction Effect and regulation of pore conductance*. Biochim Biophys Acta Biomembr. 2021 Jun 1;1863(6):183590. doi: 10.1016/j.bbamem.2021.183590
- [128] Mehregan A, Pérez-Conesa S, Zhuang Y, Elbahnsi A, Pasini D, Lindahl E, Howard RJ, Ulens C, Delemotte L. *Probing effects of the SARS-CoV-2 E protein on membrane curvature and intracellular calcium*. Biochim Biophys Acta Biomembr. 2022 Oct 1;1864(10):183994. doi: 10.1016/j.bbamem.2022.183994
- [129] Cabrera-Garcia D, Bekdash R, Abbott GW, Yazawa M, Harrison NL. *The envelope protein of SARS-CoV-2 increases intra-Golgi pH and forms a cation channel that is regulated by pH*. J Physiol. 2021 Jun;599(11):2851-2868. doi: 10.1113/JP281037
- [130] Nieto-Torres JL, Verdiá-Báguena C, Jimenez-Guardeño JM, Regla-Nava JA, Castaño-Rodríguez C, Fernandez-Delgado R, Torres J, Aguilera VM, Enjuanes L. *Severe acute respiratory syndrome coronavirus E protein transports calcium ions and activates the NLRP3 inflammasome*. Virology. 2015 Nov;485:330-9. doi: 10.1016/j.virol.2015.08.010
- [131] Abdul Kadir L, Stacey M, Barrett-Jolley R. *Emerging Roles of the Membrane Potential: Action Beyond the Action Potential*. Front Physiol. 2018 Nov 21;9:1661. doi: 10.3389/fphys.2018.01661
- [132] Oiki S, Iwamoto M. *Lipid Bilayers Manipulated through Monolayer Technologies for Studies of Channel-Membrane Interplay*. Biol Pharm Bull. 2018;41(3):303-311. doi: 10.1248/bpb.b17-00708
- [133] Maher J, Allen M. *Planar lipid bilayers in recombinant ion channel research*. Methods. 2018 Sep 1;147:206-212. doi: 10.1016/j.ymeth.2018.03.003
- [134] Takeuchi S. *Formation of Planar Lipid Bilayer Membranes and Vesicles using microfluidic technology*. Advances in Planar Lipid Bilayer Membranes and liposomes, 2010 11;87-100. doi: 10.1016/S1554-4516(10)11004-7
- [135] Sottriffer, CA. *Molecular Dynamics Simulations in Drug Design*. In: Encyclopedic Reference of Genomics and Proteomics in Molecular Medicine 2006. doi: 10.1007/3-540-29623-9_0820

- [136] Alder BJ and Wainwright TE, *Studies in Molecular Dynamics.I.General Method*. J.Chem.Phys 1959 31, 459
- [137] Alder BJ and Wainwright TE, *Studies in Molecular Dynamics.II.Behavior of a small number of elastic spheres*. J.Chem.Phys 1960 33, 1439
- [138] Rahman A. *Correlations in the motion of atoms in liquid argon*, Phys.Rev, 1964 136, A405
- [139] Skeel, R.D. *Variable step size destabilizes the Störmer/leapfrog/verlet method*. BIT 1993 33, 172–175 doi:10.1007/BF01990352
- [140] Berendsen HJC, Postma JPM, van Gunsteren WF, DiNola A, Haak JR, *Molecular dynamics with coupling to an external bath*, J.Chem.Phys 1984, 81, 3684 doi: 10.1063/1.448118
- [141] Nosè S. A unified formulation of the constant temperature molecular dynamics methods, J.Chem.Phys 1984, 81, 511 doi: 10.1063/1.447334
- [142] Hoover WG. *Canonical dynamics: Equilibrium phase-space distributions*. Phys Rev A Gen Phys. 1985 Mar;31(3):1695-1697. doi: 10.1103/physreva.31.1695
- [143] Parrinello, M. and Rahman, A. *Polymorphic Transitions in Single Crystals: A New Molecular Dynamics Method*. Journal of Applied Physics, 1981, 52, 7182-7190 doi: 10.1063/1.328693
- [144] Sindhikara DJ, Emerson DJ, Roitberg AE. *Exchange Often and Properly in Replica Exchange Molecular Dynamics*. J Chem Theory Comput. 2010 Sep 14;6(9):2804-8. doi: 10.1021/ct100281c
- [145] Liao Q. *Enhanced sampling and free energy calculations for protein simulations*. Prog Mol Biol Transl Sci. 2020;170:177-213. doi: 10.1016/bs.pmbts.2020.01.006
- [146] Dar AM, Mir S, *Molecular Docking: Approaches, Types, Applications and Basic Challenges*. J Anal Bioanal Tech 2017 8: 356. doi: 10.4172/2155-9872.1000356
- [147] Roy K, Kar S and Das RN, *Understanding the basics of QSAR for applications in pharmaceutical sciences and risk assessment* 2015 doi: 10.1016/C2014-0-00286-9
- [148] Taylor RD, Jewsbury PJ, Essex JW. *A review of protein-small molecule docking methods*. J Comput Aided Mol Des. 2002 Mar;16(3):151-66. doi: 10.1023/a:1020155510718
- [149] Nguyen TH, Zhou HX, Minh DDL. *Using the fast fourier transform in binding free energy calculations*. J Comput Chem. 2018 Apr 30;39(11):621-636. doi: 10.1002/jcc.25139
- [150] Padhorny D, Kazennov A, Zerbe BS, Porter KA, Xia B, Mottarella SE, Kholodov Y, Ritchie DW, Vajda S, Kozakov D. *Protein-protein docking by fast generalized Fourier transforms on 5D*

rotational manifolds. Proc Natl Acad Sci U S A. 2016 Jul 26;113(30):E4286-93. doi: 10.1073/pnas.1603929113

[151] Lu CH, Lin YS, Chen YC, Yu CS, Chang SY, Hwang JK. *The fragment transformation method to detect the protein structural motifs*. Proteins. 2006 May 15;63(3):636-43. doi: 10.1002/prot.20904

[152] Lin YF, Cheng CW, Shih CS, Hwang JK, Yu CS, Lu CH. *MIB: Metal Ion-Binding Site Prediction and Docking Server*. J Chem Inf Model. 2016 Dec 27;56(12):2287-2291. doi: 10.1021/acs.jcim.6b00407

[153] Checchetto V, Reina S, Magrì A, Szabo I, De Pinto V. *Recombinant human voltage dependent anion selective channel isoform 3 (hVDAC3) forms pores with a very small conductance*. Cell Physiol Biochem. 2014;34(3):842-53. doi: 10.1159/000363047

[154] Reina S, Checchetto V, Saletti R, Gupta A, Chaturvedi D, Guardiani C, Guarino F, Scorciapino MA, Magrì A, Foti S, Ceccarelli M, Messina AA, Mahalakshmi R, Szabo I, De Pinto V. *VDAC3 as a sensor of oxidative state of the intermembrane space of mitochondria: the putative role of cysteine residue modifications*. Oncotarget. 2016 Jan 19;7(3):2249-68. doi: 10.18632/oncotarget.6850

[155] Conti Nibali S, Di Rosa MC, Rauh O, Thiel G, Reina S, De Pinto V. *Cell-free electrophysiology of human VDACS incorporated into nanodiscs: An improved method*. Biophys Rep (N Y). 2021 Sep 8;1(1):None. doi: 10.1016/j.bpr.2021.100002

[156] Lu CH, Chen CC, Yu CS, Liu YY, Liu JJ, Wei ST, Lin YF. *MIB2: metal ion-binding site prediction and modeling server*. Bioinformatics. 2022 Sep 15;38(18):4428-4429. doi: 10.1093/bioinformatics/btac534

[157] Kretsinger RH, Uversky VN, Permyakov EA, *Encyclopedia of metalloproteins*

[158] Pidcock E, Moore GR. *Structural characteristics of protein binding sites for calcium and lanthanide ions*. J Biol Inorg Chem. 2001 Jun;6(5-6):479-89. doi: 10.1007/s007750100214

[159] Bennick A, McLaughlin AC, Grey AA, Madapallimattam G. *The location and nature of calcium-binding sites in salivary acidic proline-rich phosphoproteins*. J Biol Chem. 1981 May 25;256(10):4741-6

ACKNOWLEDGEMENTS

Alla fine di questo percorso di dottorato non posso fare altro che notare il cambiamento avvenuto in me nel rapportarmi verso questa disciplina. Non è più solamente una questione di imparare un concetto da applicare nella risoluzione di un problema, ma si tratta di indagare quanto più a fondo possibile in modo da poter scoprire sempre qualcosa di nuovo, che a volte possa avere un impatto fondamentale nelle nostre vite quotidiane. Tutto questo non sarebbe stato possibile da realizzarlo da solo e per questo motivo voglio ringraziare tutti coloro che fanno parte del laboratorio gestito dal professore De Pinto e dalla professoressa Messina. Il professore Vito De Pinto, mio tutor durante questo periodo, è sempre stato molto disponibile nell'ascoltarmi e nel favorire un confronto nella comprensione di quanto veniva ottenuto nei molteplici esperimenti. A lui sarò sempre grato per avermi dato la possibilità di poter iniziare questo percorso e per aver sempre creduto nelle mie capacità, anche quando ero io il primo a dubitarne. In particolar modo, però voglio ringraziare la dott.ssa Simona Reina, che in questi anni mi ha guidato nell'entrare all'interno di questo mondo, quanto appreso dalle sue abilità di logica e di ragionamento, rappresentano per me il modello a cui ispirarmi nel prossimo futuro, sempre possibilmente nel mondo della ricerca. Inoltre non solo mi ha aiutato ad andare avanti nei miei progetti di lavoro, ma è stata in grado di riprendermi quando preso dallo sconforto non riuscivo ad andare più avanti. Ho imparato molto seguendo anche il dott. Andrea Magrì, molti concetti che oggi riesco ad applicare con semplicità, li ho appresi grazie ai molteplici confronti avuti con lui. Anche la prof.ssa Angela Messina e la prof.ssa Francesca Guarino hanno sempre creduto nelle mie abilità e lo hanno sempre mostrato coinvolgendomi in varie attività di laboratorio, nonostante io fossi più che convinto di non poter riuscire ad esaudire le loro richieste.

Non dimentico ovviamente il contributo che i miei colleghi di laboratorio mi hanno dato. Loro mi hanno supportato e principalmente sopportato in questi anni. Mi hanno dato quella parola di conforto nei momenti più difficili o al limite mi hanno fatto fare una risata in modo da distrarmi completamente dai miei pensieri. Per questo quanto fatto da Cristiana, Giuseppe, Iolanda, Xena, Daniela, Stefano, Maria Carmela, Pierpaolo e Federica è stato fondamentale e voglio cogliere quest'occasione per dirgli grazie di tutto.

Tutto ciò ha avuto un grande impatto in me in questi anni e per questo non smetterò mai di ringraziare tutti voi per quello che avete fatto per me.

Infine un sentito ringraziamento va nei confronti del prof. Matteo Ceccarelli e del dott. Stefan Milenkovic che mi hanno ospitato nel loro gruppo di ricerca per tre mesi, permettendomi di poter apprendere molto del mondo della biologia computazionale e di poter arricchire il mio bagaglio culturale.

Article 1.

International Journal of Molecular Sciences

VDAC1 knockout affects mitochondrial oxygen consumption triggering a rearrangement of ETC by impacting on complex I activity

Andrea Magri^{1,2,*}, Salvatore Antonio Maria Cubisino^{3†}, Giuseppe Battiato³, Cristiana Lucia Rita Lipari³, Stefano Conti Nibali³, Miriam Wissam Saab⁴, Alessandra Pittalà⁴, Angela Maria Amorini⁴, Vito De Pinto^{2,3}, Angela Messina^{1,2}

¹ Department of Biological, Geological and Environmental Sciences, University of Catania, Via S.Sofia 64, 95125 Catania, Italy

² we.MitoBiotech S.R.L, C.so Italia 174, 95125, Catania, Italy

³ Department of Biomedical and Biotechnological Sciences, University of Catania, Via S. Sofia 64, 95125, Catania, Italy

⁴ Department of Biomedical and Biotechnological Sciences, Division of Medical Biochemistry, University of Catania, Via S.Sofia 97, 95123, Catania, Italy

† These authors have equally contributed



Article

VDAC1 Knockout Affects Mitochondrial Oxygen Consumption Triggering a Rearrangement of ETC by Impacting on Complex I Activity

Andrea Magri^{1,2,*}, Salvatore Antonio Maria Cubisino^{3,†}, Giuseppe Battiato³, Cristiana Lucia Rita Lipari³, Stefano Conti Nibali³, Miriam Wissam Saab⁴, Alessandra Pittalà⁴, Angela Maria Amorini⁴, Vito De Pinto^{2,3} and Angela Messina^{1,2}

¹ Department of Biological, Geological and Environmental Sciences, University of Catania, Via S. Sofia 64, 95125 Catania, Italy

² we.MitoBiotech S.R.L., C.so Italia 174, 95125 Catania, Italy

³ Department of Biomedical and Biotechnological Sciences, University of Catania, Via S. Sofia 64, 95125 Catania, Italy

⁴ Department of Biomedical and Biotechnological Sciences, Division of Medical Biochemistry, University of Catania, Via S. Sofia 97, 95123 Catania, Italy

* Correspondence: andrea.magri@unict.it

† These authors contributed equally to this work.

Abstract: Voltage-Dependent Anion-selective Channel isoform 1 (VDAC1) is the most abundant isoform of the outer mitochondrial membrane (OMM) porins and the principal gate for ions and metabolites to and from the organelle. VDAC1 is also involved in a number of additional functions, such as the regulation of apoptosis. Although the protein is not directly involved in mitochondrial respiration, its deletion in yeast triggers a complete rewiring of the whole cell metabolism, with the inactivation of the main mitochondrial functions. In this work, we analyzed in detail the impact of VDAC1 knockout on mitochondrial respiration in the near-haploid human cell line HAP1. Results indicate that, despite the presence of other VDAC isoforms in the cell, the inactivation of VDAC1 correlates with a dramatic impairment in oxygen consumption and a re-organization of the relative contributions of the electron transport chain (ETC) enzymes. Precisely, in VDAC1 knockout HAP1 cells, the complex I-linked respiration (N-pathway) is increased by drawing resources from respiratory reserves. Overall, the data reported here strengthen the key role of VDAC1 as a general regulator of mitochondrial metabolism.

Keywords: mitochondria; VDAC1 knockout; HAP1 cells; complex I; respiratory reserve(s)



Citation: Magri, A.; Cubisino, S.A.M.; Battiato, G.; Lipari, C.L.R.; Conti Nibali, S.; Saab, M.W.; Pittalà, A.; Amorini, A.M.; De Pinto, V.; Messina, A. VDAC1 Knockout Affects Mitochondrial Oxygen Consumption Triggering a Rearrangement of ETC by Impacting on Complex I Activity. *Int. J. Mol. Sci.* **2023**, *24*, 3687. <https://doi.org/10.3390/ijms24043687>

Academic Editors: Dmitry B. Zorov and Francesco Pallotti

Received: 6 November 2022

Revised: 4 February 2023

Accepted: 10 February 2023

Published: 12 February 2023



Copyright: © 2023 by the authors. Licensee MDPI, Basel, Switzerland. This article is an open access article distributed under the terms and conditions of the Creative Commons Attribution (CC BY) license (<https://creativecommons.org/licenses/by/4.0/>).

1. Introduction

The Voltage-Dependent Anion-selective Channel (VDAC) is the most abundant and ubiquitously expressed family of pore-forming proteins of the outer mitochondrial membrane (OMM). Allowing for the passive diffusion of small, hydrophilic molecules up to 5000 Daltons, the VDAC proteins guarantee the permeability of the OMM by regulating the metabolic cross-talk between the mitochondria and the rest of the cell [1,2]. VDAC owes its name to its peculiar electrophysiological properties, established in artificial membrane reconstitution experiments more than three decades ago: the channel conductance changes according to the voltage applied, switching from high-conducting and anion-selective state to low-conducting and cation-selective states [3–5].

Three genes encode three highly conserved isoforms in mammals. They are named VDAC1, VDAC2, and VDAC3 in agreement with the order of their discovery [6]. The tridimensional structures of mouse or human VDAC1 [7–9] and zebrafish VDAC2 [10] are available, and share a common β -barrel transmembrane pore, made of 19 antiparallel β -strands, and an N-terminal domain organized as α -helix, confirmed also by in vitro

experiments [11]. Among the isoforms, VDAC1 is the most abundant, overcoming VDAC2 and VDAC3 by one or two orders of magnitude, respectively [12].

Being at the interface between cytosol and mitochondria, VDAC1 mainly regulates the flux of Krebs' cycle intermediates (pyruvate, succinate, malate, and glutamate), ADP/ATP, ions (Na^+ , K^+ , Cl^-), nucleotides, and NAD^+/NADH , thus supporting the whole cellular bioenergetics [13–16]. Furthermore, VDAC1 acts as an anchor for many cytosolic proteins, including Hexokinases and specific members of the Bcl-2 family, participating in the regulation of mitochondrial-mediated apoptosis [17–20]. In light of these considerations, VDAC1 has rapidly become a pharmacological target in cancer and neurodegeneration [21–24]. Similar to isoform 1, VDAC2 is a key modulator of cell death and survival, exerting both pro- and anti-apoptotic functions by interacting with Bak and Bax [25–27]. The role of VDAC3 appears to be more intricate: it has specific electrophysiological features and post-translational modifications that significantly change with the redox environment [28–30]. Only recently, however, has our group definitely demonstrated that VDAC3 is a redox-sensing protein, protecting mitochondria from oxidative stress [31].

Much information about VDAC functions derives from gene inactivation studies. In the yeast *S. cerevisiae*, endowed with a single functional mitochondrial porin [32], inactivation of VDAC1 dramatically affects mitochondrial DNA maintenance and expression and organelle functioning, leading to a complete rewiring of the whole cell metabolism [33]. In mammals, knockout experiments are made more complicated to interpret due to the presence of the other isoforms, which can partially complement the lack of VDAC1. Interestingly, in mouse embryonic fibroblast VDAC1 deletion promotes a partial rearrangement of gene expression that triggers metabolic impairments and the accumulation of reactive oxygen species (ROS) [34], overlapping in part the changes already seen in yeast. Additionally, VDAC1 knockout makes H9c2 cells more susceptible to ROS-induced apoptosis [35], while in chronic myelogenous leukemia-derived cells it correlates with a slight reduction in mitochondrial mass and the hyperpolarization of the mitochondrial membranes [31]. Nevertheless, despite the important role played by VDAC1 for mitochondrial metabolism, its possible involvement in the regulation of mitochondrial respiration has not been adequately investigated yet.

Aimed at studying the above-mentioned mechanism, the near-haploid human HAP1 cells knockout for VDAC1 were used to conduct high-resolution respiration (HRR) experiments. Results clearly indicated that the lack of VDAC1 or its partial inhibition correlates with a reduction of oxygen consumption in the main respiratory states. At the same time, VDAC1 knockout cells undergo a re-arrangement of the respiration by increasing the relative efficiency of complex I-linked respiration, dissipating part of respiratory reserves. Overall, these findings remark on the pivotal role of VDAC1 as a key regulator of mitochondrial functionality.

2. Results

2.1. Characterization of HAP1 Δ VDAC1 Cells

HAP1 cells are endowed with a single copy of each chromosome and represent a powerful model for knockout studies [36]. As schematized in Figure 1A, the inactivation of VDAC1 expression was achieved by a deletion of 2 bp in exon VI of the corresponding gene. In the resulting cell line (namely Δ VDAC1), no protein band was detected by anti-VDAC1 antibody in Western blot experiments (Figure 1B). In contrast, cells of the parental line, expressing the wild type VDAC1 protein (here used as reference control), showed an easily detectable band at the expected molecular weight of ~32 kDa (Figure 1B). In addition, the expression level of the VDAC2 and VDAC3 isoforms was also tested. In this regard, no significant differences were detected between Δ VDAC1 and the parental cells, as confirmed by quantification (Figure 1B). Thus, unlike in other cell lines [12], the non-expression of VDAC1 in HAP1 cells does not affect the expression of the other VDAC isoforms. Similarly to what was previously observed [31], VDAC1 knockout did not alter cell proliferation or viability: as shown in Figure 1C, the growth curve of the Δ VDAC1 HAP1

cells is almost overlapped to the parental one; furthermore, no significant differences were observed upon MTT assay (Figure 1D). Contrariwise, a slight but significant reduction in the mitochondrial mass was confirmed in knockout cells of -10.5% , in comparison to parental HAP1 ($p = 0.0012$, $n = 3$), as revealed by the quantification of MitoTracker fluorescence signal by flow cytometry (Figure 1E).

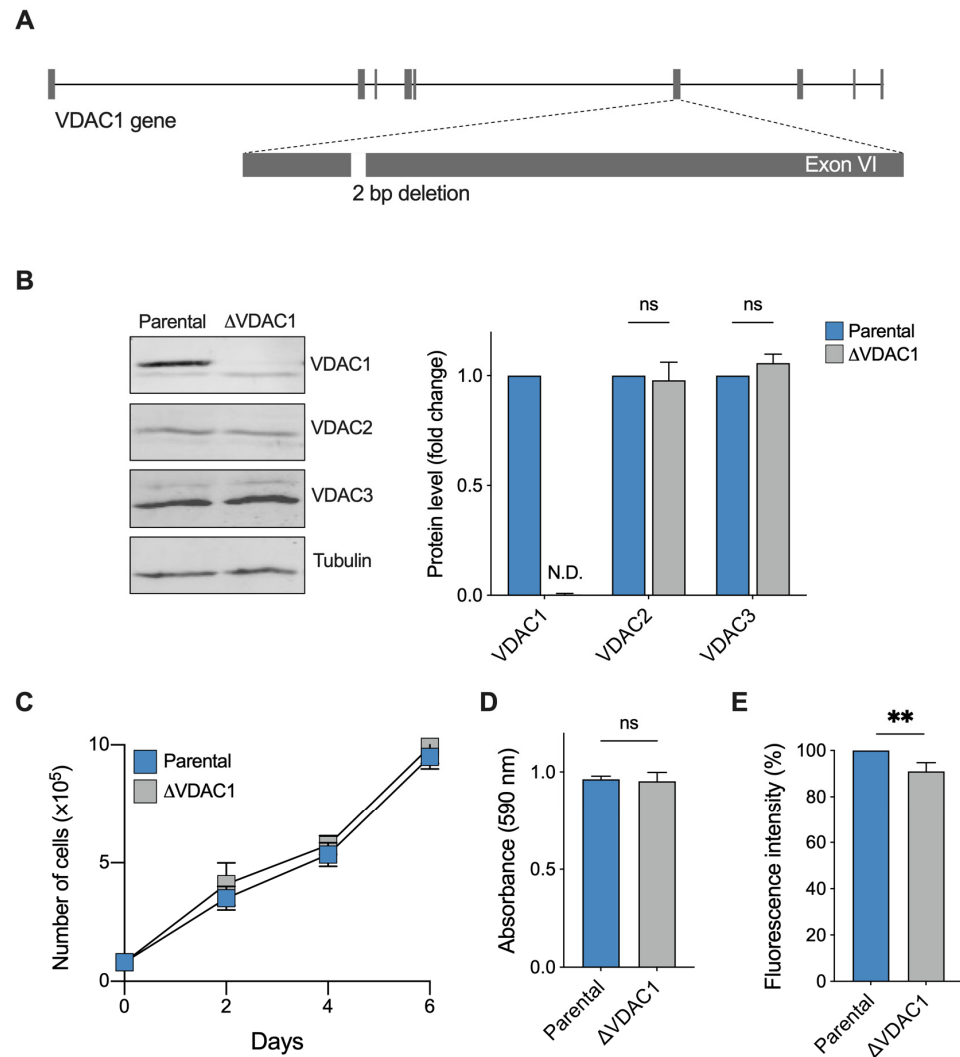


Figure 1. Phenotypical characterization of HAP1 cells used in this work. (A) Schematization of VDAC1 knock-out: a 2 bp deletion in the exon VI of VDAC1 gene was performed. (B) Representative Western blotting (left) and the relative protein level quantification (right) of total lysates from parental and Δ VDAC1 cells, showing the expression of the three VDAC isoforms. As expected, no VDAC1 protein band was detected in knock-out cells. N.D.—not detectable. (C) Proliferation assay showing no significant difference between samples. Data are shown as mean \pm SD of $n = 3$ independent counts and statistically analyzed by two-way ANOVA; ns—not significant. (D) Cell viability analysis by MTT assay showing no significant difference between samples. (E) Quantification of the MitoTracker signal in parental and Δ VDAC1 cells by flow cytometry. A slight but significant difference of approximately 10% was observed. Data in (D,E) are expressed as mean \pm SEM of $n = 3$ independent counts and statistically analyzed by unpaired t -test, with ** $p < 0.01$; ns—not significant.

2.2. Deletion of VDAC1 Gene or Inhibition of Its Protein Affects Oxygen Consumption of HAP1 Cells

The overall oxygen consumption of HAP1 cells was investigated by HRR. This technique allows for the measurement of oxygen flow relative to different respiratory states, as well as the contribution of each state or specific electron transport chain (ETC) complexes

to the achievement of the maximal respiratory capacity [37]. For this purpose, a Substrate-Uncoupler-Inhibitor-Titration (SUIT) protocol was used as schematized in Figure 2A in addition to a representative curve of HAP1 parental cells. Particularly, the curve shows variations in the oxygen consumption upon the addition of specific molecules. Briefly, respiration in the presence of endogenous substrates (ROUTINE state) was measured in intact cells; then, through a mild permeabilization of plasma membranes and stimulation with specific substrates and ADP, the oxidative phosphorylation-linked respiration (OXPHOS state) was assessed; finally, the maximal electron input to electron transport (ET) chain was determined by titration with an uncoupler.

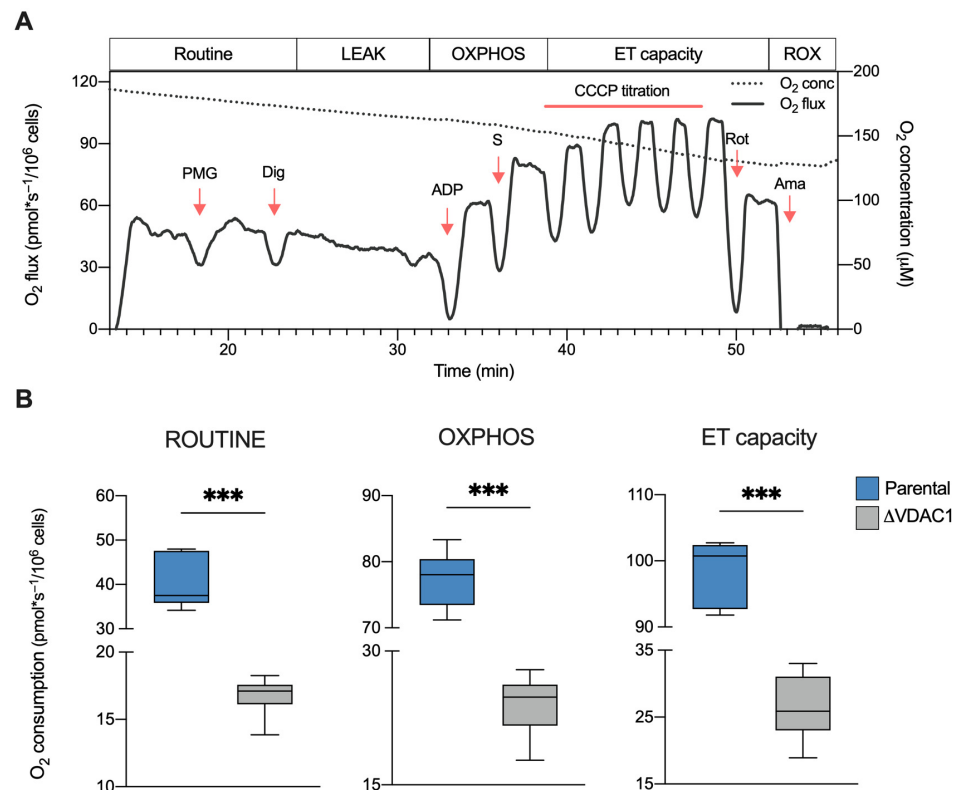


Figure 2. Oxygen consumption in HAP1 cells. (A) Representative curve of mitochondrial respiratory profile of parental HAP1 cells along with the SUIT protocol used for both intact and permeabilized cells. P—pyruvate; M—malate; G—glutamate; Dig—digitonin; S—succinate; Rot—rotenone; Ama—antimycin. (B) Quantitative analysis of the oxygen consumption rate of ROUTINE, OXPPOS, and maximal ET capacity in HAP1 cells, expressed as pmol/second per million cells. A significant reduction of oxygen consumption was observed in each state for Δ VDAC1 cells in comparison to parental. Data are shown as median \pm SEM of $n = 6$ independent experiments and statistically analyzed by unpaired t -test, with *** $p < 0.001$.

The same protocol was then applied to Δ VDAC1 cells, and the oxygen consumption in the main respiratory states was calculated and compared with the control (see Supplementary Figure S1 for a representative curve of Δ VDAC1 cells). As displayed in Figure 2B, the knockout of VDAC1 dramatically affects the oxygen flows in all the analyzed states. Precisely, Δ VDAC1 cells displayed about 58% of flux reduction in intact cells (ROUTINE) and of about 68% after cell permeabilization and the stimulation of the OXPPOS activity ($p < 0.001$ vs. parental HAP1, $n = 6$). Additionally, the oxygen consumption linked to the maximal capacity was reduced by approximately 76% ($p < 0.001$ vs. parental HAP1, $n = 6$).

On the basis of these results, we queried whether these reductions were directly due to the VDAC1 inactivation or to VDAC1-independent changes occurring in our knockout model. To this aim, parental HAP1 cells were exposed to a sublethal dose of VBIT-12, a specific

VDAC1 inhibitor. VBIT are a group of small, cell-penetrating molecules able to interact with VDAC1 that are known for their ability to reduce the channel conductance [38,39]. In this specific case, an HRR analysis was limited to intact cells by measuring the ROUTINE state and maximal ET capacity (Figure 3A). Notably, these parameters were evaluated after a rapid treatment with VBIT-12 to avoid any eventual side effects due to the prolonged exposure to the molecule. As reported in Figure 3B, a significant reduction of the respiration was observed in VBIT-12 treated cells, consisting of -22% for the ET capacity ($p = 0.01$ vs. DMSO treated cells, $n = 6$). Although not significant, a similar decreasing trend was observed also for ROUTINE state ($p = 0.07$, $n = 6$). On the contrary, no significant effect of VBIT-12 was noticed in the Δ VDAC1 cells exposed to the molecule (Supplementary Figure S2), suggesting that VBIT-12 exerts its inhibitory action on VDAC1 specifically.

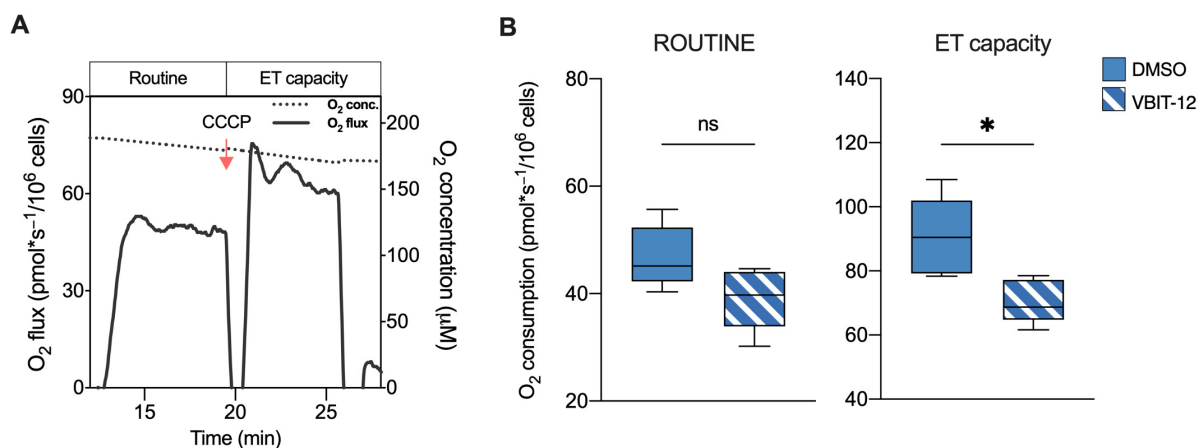


Figure 3. Oxygen consumption in HAP1 cells upon exposure to VBIT-12. **(A)** A representative curve of mitochondrial respiratory profile of parental HAP1 intact cells along with the SUIT protocol here used. Uncoupler CCCP was added for the achievement of maximal respiratory capacity. **(B)** Quantitative analysis of the oxygen consumption rate of ROUTINE and maximal ET capacity in HAP1 parental cells previously treated with VBIT-12 or DMSO (control). A significant reduction of ET capacity was observed in treated cells. Data are expressed as pmol/second per million cells and shown as median \pm SEM of $n = 6$ independent experiments. Data were statistically analyzed by unpaired t -test, with $* p < 0.05$; ns—not significant.

Taken together, these results clearly support a pivotal role of VDAC1 in the regulation of mitochondrial respiration.

2.3. VDAC1 Knockout Changes the Contribution of Respiratory States or Complexes to ET Capacity

Next, the relative contribution of each respiratory state or ETC complex to the achievement of the maximal capacity was investigated in an independent manner from mitochondrial mass or other external factors by analyzing the flux control ratios (FCRs) [37,40]. In Figure 4A, the relative contributions of ROUTINE and OXPHOS to the maximal respiration are shown. Surprisingly, the ROUTINE contribution was higher in Δ VDAC1 cells ($+37\%$, $p = 0.0053$ vs. parental HAP1, $n = 6$). In a similar manner, the relative contribution of OXPHOS was increased upon VDAC1 knockout of about 15% ($p = 0.004$ vs. parental HAP1, $n = 6$). Notably, the approach of ROUTINE and OXPHOS to the maximal respiration correlates with a significant reduction of the respiratory reserve (E-Reserve) and excess (E-Excess), respectively (Figure 4A, dashed histograms), that consist of bioenergetic supplies to which mitochondria can draw in the presence of further stimuli to produce extra ATP [41].

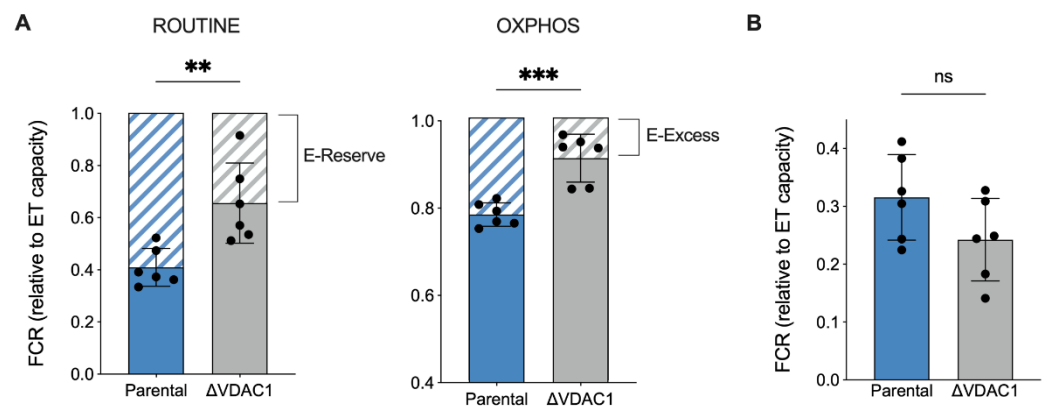


Figure 4. Analysis of flux control ratios (FCRs) in HAP1 cells. (A) The specific contribution of ROUTINE and OXPHOS states to ET capacity was calculated and demonstrated as FCRs, along with the respiratory reserves (dashed histograms), E-Reserve, and E-Excess. A significant increase in both FCR values was observed for Δ VDAC1 cells, which correspond to a proportional decrement of the reserves. (B) FCRs calculated for LEAK state. No significant differences were detected between parental and Δ VDAC1 cells. Data in (A,B) are shown as mean \pm SEM of $n = 6$ independent experiments and statistically analyzed by unpaired t -test, with ** $p < 0.01$ and *** $p < 0.001$; ns— not significant.

Based on previous results, we queried whether increases in the ROUTINE and OXPHOS contributions were due to a proportional raise in the non-phosphorylating component, the so-called LEAK state, here measured after permeabilization of the plasma membranes, i.e., allowing ADP to leave the cells. As reported in Figure 4B, however, the LEAK contribution was unvaried among the samples.

Next, we analyzed the respiration linked to the NADH-substrates (N-pathway) or succinate (S-pathway), namely the respiration coupled to complex I or II, respectively. Precisely, the N-pathway was achieved in the presence of saturating concentrations of pyruvate, malate, glutamate, and ADP, but not succinate. As schematized in Figure 5A, in this configuration electrons flow exclusively from complex I to complex III through the Q-junction. Alternatively, electrons may flow from complex II to the Q-junction in the presence of a saturating concentration of succinate and rotenone, a specific inhibitor of complex I (Figure 5B).

In term of oxygen consumption, the both N- and S-pathways followed a reduction in line with the typical respiratory profile of Δ VDAC1 cells (-65% and -82% respectively, $p < 0.001$ vs. parental HAP1, $n = 6$, Figure 5C). In addition, interesting differences emerged from a FCR analysis. Particularly, as displayed in Figure 5D, a significant increase in the relative contribution of the N-pathway was observed in the Δ VDAC1 cells ($+24\%$, $p = 0.0026$ vs. parental HAP1, $n = 6$), counterbalanced by a reduction in the relative contribution of the S-pathway (-34% , $p < 0.001$ vs. parental HAP1, $n = 6$).

Overall, the FCR analysis suggests that the increase in contribution of the ROUTINE and OXPHOS respiration previously observed in Δ VDAC1 cells is strictly dependent from complex I activity.

2.4. Mitochondrial Oxidation of NADH Is Increased in VDAC1 Knockout Cells

The cellular content of nicotinic coenzymes, in the form of phosphorylated and non-phosphorylated nicotinamide dinucleotides, renders a clear picture of both the redox status and the mitochondrial functionality. In this view, we analyzed the total concentration of the four different forms (NAD⁺, NADH, NADP⁺, and NADPH; see Table S1 for raw data) in extracts from parental and Δ VDAC1 HAP1 cells. As reported in Figure 6A, a dramatic decrease in the total nicotinic coenzyme pool was observed in the Δ VDAC1 sample (-40% , $p = 0.007$ vs. parental HAP1, $n = 4$).

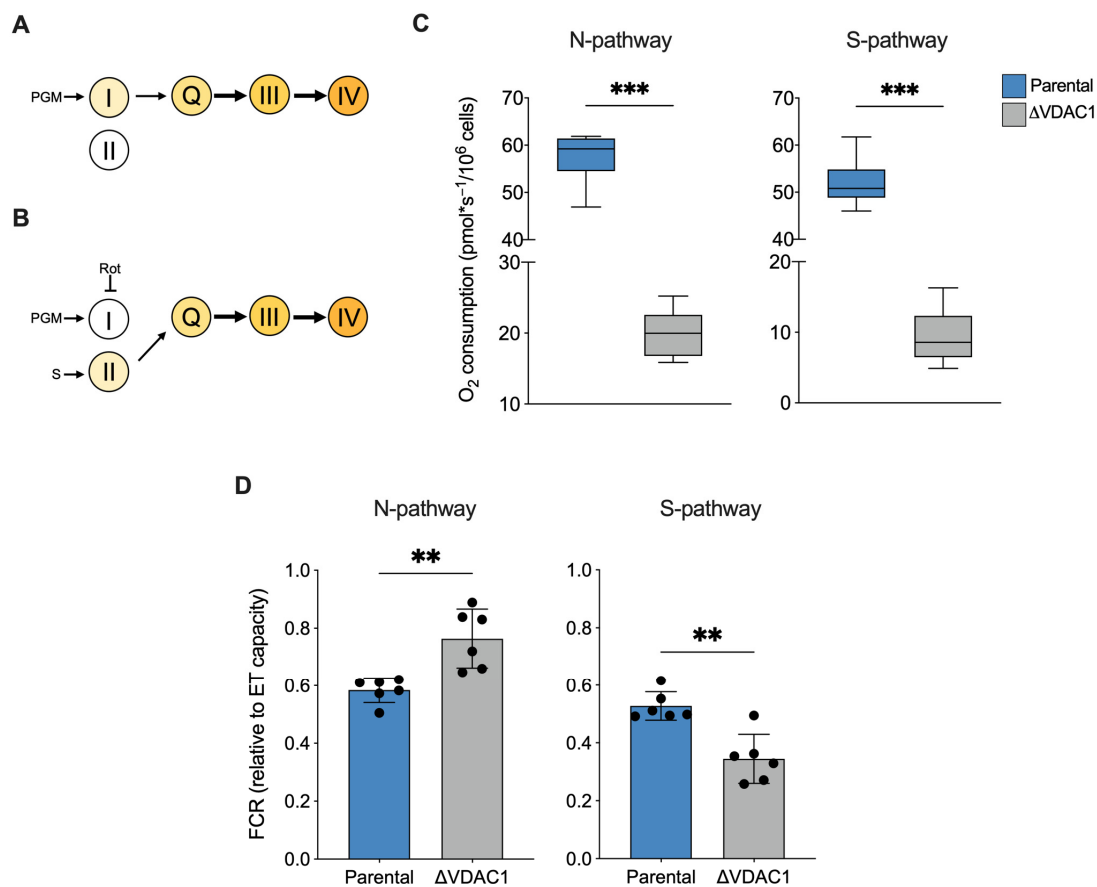


Figure 5. Analysis of N- and S-pathways in HAP1 cells. **(A,B)** Schematization of ET chain activity in our experimental HRR setup. Activation of complex III via Q-junction can occur exclusively by complex I or II, precisely by stimulating complex I with NADH-linked substrates and in the absence of succinate (N-pathway, **A**) or by stimulating complex II with succinate upon inhibition of complex I with rotenone (S-pathway, **B**). P—pyruvate; M—malate; G—glutamate; S—succinate; Rot—rotenone. **(C)** Quantitative analysis of the oxygen consumption rate of N- and S-pathway expressed as pmol/second per million cells. A significant reduction of oxygen consumption was observed in each state for Δ VDAC1 cells in comparison to parental. **(D)** FCRs calculated for N- and S-pathways revealed an increase of N- over the S-pathway in Δ VDAC1 cells. Data are shown as median (**C**) or means (**D**) \pm SEM of $n = 6$ independent experiments and statistically analyzed by unpaired t -test, ** $p < 0.01$ and *** $p < 0.001$.

Notably, this finding is in line with previous respirometric results, in which a modulation of mitochondrial efficiency was observed and, in particular, a new condition of limited oxygen utilization. Interestingly, the NAD^+/NADH increased by 20% ($p = 0.007$ vs. parental HAP1, $n = 4$, Figure 6B), possibly suggesting a higher rate of NADH oxidation at the level of complex I, ensuring a proper function of either OXPHOS or ET capacity and, preliminarily of the TCA cycle. According to these data, we noticed no significant differences between our samples in lactate concentration (Figure 6C), suggesting that the increased oxidation of NADH in Δ VDAC1 cells is prevalently mitochondrial rather than cytosolic via lactate dehydrogenase [42].

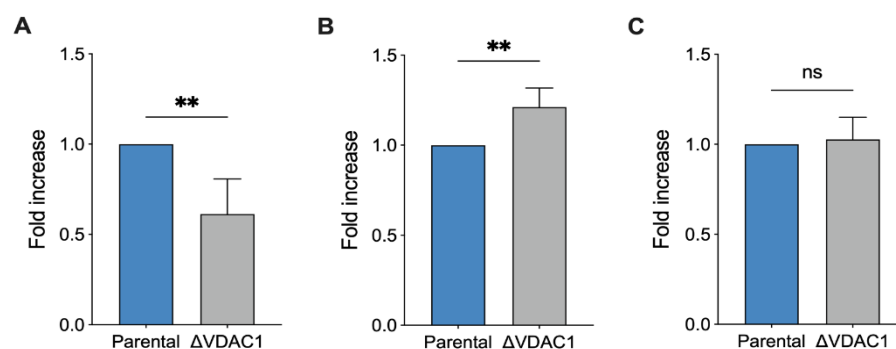


Figure 6. Analysis of NADH reduction in HAP1 cells. Quantitative analysis of total level of nicotinamide cofactors NAD⁺, NADH, NADP⁺, and NADPH (A), the ratio NAD⁺/NADH (B) and the overall level of lactate (C). The lower level of nicotinamide cofactors in ΔVDAC1 cells is counterbalanced by high ratio of NAD⁺/NADH value. Data are expressed as fold increase using parental HAP1 as control. Data are shown as median ± SEM of $n = 4$ independent experiments and statistically analyzed by unpaired t -test, with ** $p < 0.01$; ns—not significant.

2.5. VDAC1 Knockout Makes Cells More Sensitive to Rotenone but Not to Malonic Acid

In light of the previous observations, we finally assayed the effect of specific ETC complex inhibitors. For this purpose, a SUIIT protocol developed for intact cells was used. Briefly, the maximal ET capacity of each sample was reached by CCCP; then, variations in the respiration were monitored by titration with inhibitors.

Rotenone is a lipophilic, cell-permeable molecule, commonly used as a specific inhibitor of complex I and as toxin for mimicking molecular features of Parkinson's disease [43]. Figure 7A shows a representative curve of HAP1 parental cells along with the SUIIT protocol applied here. As reported, titration with non-saturating doses of rotenone in the nanomolar order induced a progressive reduction of the ET capacity in a dose–response manner, as expected. Particularly, at higher concentrations used here (16 nM), the ET capacity was reduced by approximately 50% in comparison to the untreated control (Figure 7B). A similar dose–response effect was observed with the ΔVDAC1 cells. However, in this specific case, the titration effect was more pronounced: not only was 2 nM of rotenone sufficient to halve ET capacity ($p = 0.0046$ vs. parental HAP1, $n = 3$) but, at higher concentrations, the toxin reduced the ET capacity by up to 80% of its original value ($p < 0.001$ vs. parental HAP1, $n = 3$, Figure 7B).

We repeated the experiment using malonic acid, which specifically inhibits complex II. As reported in Figure 7C,D, titration with malonic acid was better tolerated by HAP1 cells, both parental and VDAC1 knockout. In fact, at the highest concentration used here, the maximal inhibition achieved was about 30% in both samples. Regardless, no significant differences were observed between the parental and knockout cells (Figure 7D).

Once again, these results indicate the importance of complex I contribution to respiration for ΔVDAC1 cells bioenergetic.

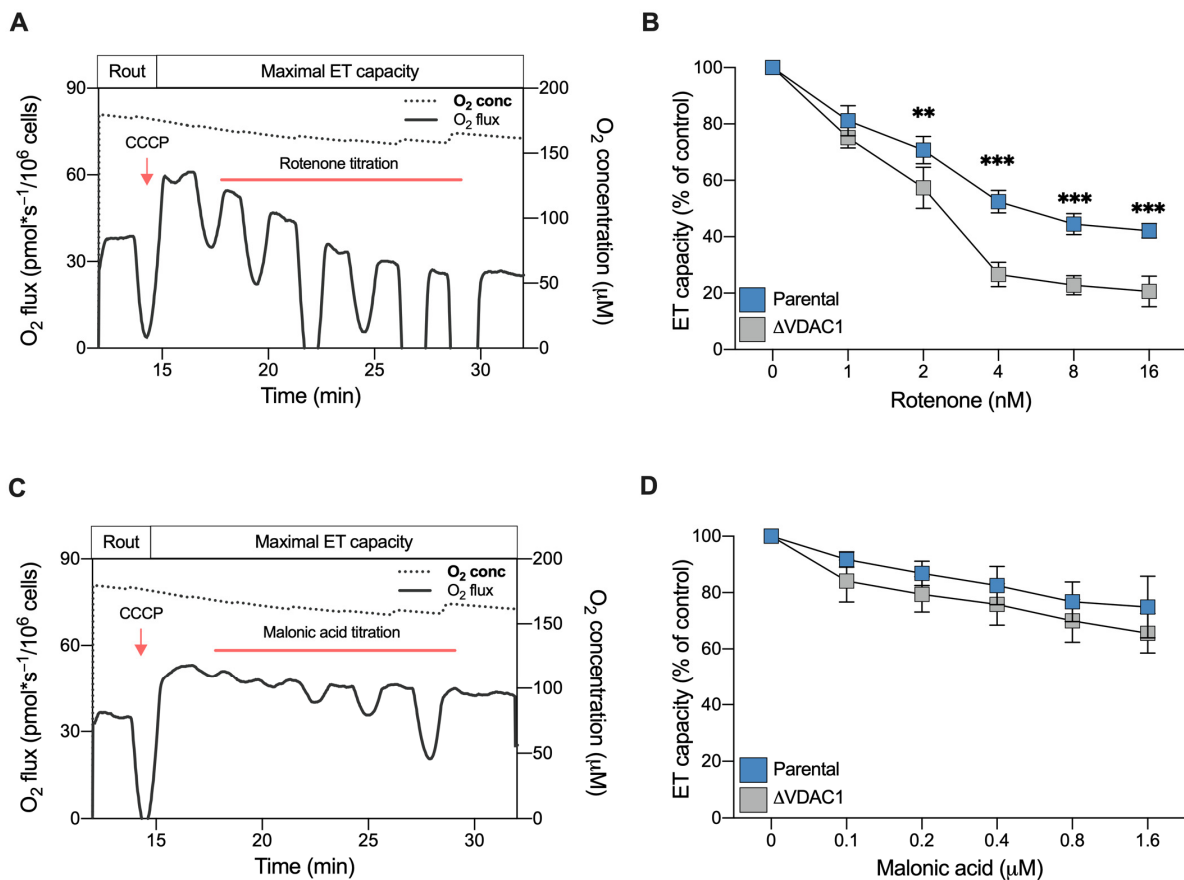


Figure 7. Sensitivity of HAP1 cells to complex I and II inhibitors assayed by HRR. (A) A representative curve of mitochondrial respiratory profile of parental HAP1 intact cells, in addition to the SUIT protocol used here. After achieving the of ET capacity with CCCP, respiration was monitored upon rotenone titration (1–16 nM). (B) Quantitative analysis of ET capacity upon rotenone titration showing a reduction for both parental and Δ VDAC1 cells. However, an increased sensitivity to rotenone was observed for Δ VDAC1 cells in comparison to the parental cells. (C) A representative curve of the mitochondrial respiratory profile of parental HAP1 intact cells, in addition to the SUIT protocol used here for malonic acid titration (0.1–1.6 μ M). (D) Quantitative analysis showing reduction of ET capacity upon titration with malonic acid. No significant difference in the respirometric profile was observed for parental and Δ VDAC1 cells. Data in (B,D) are shown as means \pm SEM of $n = 3$ independent experiments and statistically analyzed by a two-way ANOVA, with ** $p < 0.01$ and *** $p < 0.01$.

3. Discussion

Mitochondrial VDACs allow for the passive diffusion of the majority of substrates, feeding the Krebs's cycle and the respiratory enzymes of the ETC [1,17]. Moreover, they represent the most abundant proteins in the OMM, conferring its typical, sieve-like aspect, as revealed by atomic force microscopy experiments [44,45]. In the yeast *S. cerevisiae*, where the complete mitochondrial proteome was characterized, up to 19,000 copies of VDAC1 per single mitochondrion were estimated, an amount that exceeds by approximately ten times the copy number of the second most abundant protein, Tom40 [46]. For these reasons, VDACs are widely considered key players in the maintenance of the metabolic exchanges across the OMM.

Interested in characterizing the precise role of the main isoform, VDAC1, in respiration, a specific function of the mitochondrion, we used a VDAC1 knockout HAP1 cell line. The haploid line, HAP1, is a particularly advantageous model as gene knockout guarantees the total absence of the corresponding gene product. Specifically, the HAP1 Δ VDAC1 cell line we used is particularly suitable for our purposes because inactivation of the single copy of the VDAC1 gene does not lead to compensatory responses and subsequent changes

in the expression levels of the other VDAC isoforms. In addition, this cellular model can be easily used in HRR experiments in both intact or permeabilized protocols, as recently demonstrated by our group and an independent group [31,47].

Many interesting outcomes emerged from the detailed HRR analysis performed here. Firstly, despite the presence of other two isoforms, VDAC1 appears to be the preferential route for metabolites to move in and out of the mitochondria. In fact, VDAC1 inactivation dramatically affects the oxygen consumption of HAP1 cells in all three main respiratory states. This result cannot be explained only by the slight reduction in the mitochondrial mass observed here and elsewhere [31], and is confirmed by results achieved in experiments with VBIT-12.

Secondly, the relative contributions of ROUTINE and OXPHOS respiration to the maximal capacity are significantly higher in Δ VDAC1 than in parental cells. Surprisingly, this occurs without a proportional increase in the non-phosphorylating component of respiration. Even under physiological conditions, the mitochondrial coupling efficiency is always below 100% due to the proton gradient fraction, which is generated by the ETC and dissipates during a process known as proton leak [48]. An increase in the LEAK state is a common consequence of mitochondrial malfunctioning, as observed in the case of inner mitochondrial membrane damages or the overexpression of Uncoupling proteins, the latter being used by the cell as a protective strategy in the event of ROS accumulation or other stress stimuli [49,50]. Not coincidentally, many pathological conditions correlate with an increased LEAK respiration, which is widely recognized as a hallmark of mitochondrial dysfunction [40,51–54]. However, this was not the case for the Δ VDAC1 cells, as the specific contribution of the LEAK state in both HAP1 lines was comparable.

Thirdly, in Δ VDAC1 cells, the N-pathway is reduced in a similar manner to the S-pathway or total OXPHOS in terms of absolute values. Contrariwise, its increased FCR value, and specifically the sustained ratio of NAD^+/NADH in favor of the oxidized form, indicate a major contribution of complex I over complex II in activating the ETC in our setup. These data suggest that VDAC1 deficiency prompts the cells toward a re-arrangement of the mitochondrial metabolism which involves complex I. It is, indeed, no coincidence that Δ VDAC1 cells are more sensitive to rotenone but not to malonic acid, as demonstrated by our titration experiments.

Overall, this appears to be a strategy put in place by VDAC1 knockout cells to keep mitochondria still active, even when a pivotal protein such as VDAC1 is missing. Regardless, the process comes with a price: the knockout cells draw resources from the respiratory reserves that the mitochondria can rely on for the production of extra ATP during high-energy demands or in the presence of additional stress stimuli [41,55]. Similar to the increase in LEAK respiration, the limitation of respiratory reserves is emerging as a dysfunctional parameter and a common feature of many pathological conditions, precisely the neurodegenerative processes [51,56].

Comparable results were previously attained in the Δ POR1 yeast cells, which are devoid of endogenous VDAC1. Two genes in the yeast encode two porin isoforms, both showing the typical VDAC pores features in artificial membranes [57,58]. However, only VDAC1 is constitutively expressed. In fact, the expression of isoform 2 is negligible and occurs mainly in the presence of external stimuli [46,59]. In this context, the entire metabolism is rewired: the expression of mitochondrial genes is completely inhibited as a consequence of the dramatic reduction of mitochondrial DNA copies, and the cell is forced to switch toward a lipid-based metabolism [33]. Of course, in HAP1 cells, the consequences of VDAC1 inactivation are less severe due to the presence of the other isoforms: if, in Δ POR1, no alternatives to VDAC1 exist, higher eukaryotes VDAC2 and VDAC3 are concomitantly and constitutively expressed. They are finely regulated [60–62] and can partially compensate for the absence of VDAC1, as demonstrated by complementation assays [28,63]. This allows for not only metabolic exchanges, even limited, but also mitochondrial DNA maintenance and expression thanks to the import of nucleotides [31].

Interestingly, our results strengthen previous data regarding the existence of a functional link between VDAC proteins and specific enzymes located in the inner mitochondrial membrane (IMM), precisely, the adenine nucleotide carrier and the dicarboxylate carrier [64]. These observations emerged from the analysis of respiratory State 3 in isolated rat liver mitochondria and mitoplasts, i.e., mitochondria devoid of OMM, and thus of all VDAC isoforms. In mitoplasts, indeed, the oxygen consumption achieved in the presence of succinate was significantly lower than in the whole mitochondria, as was the sensitivity to specific inhibitors targeted to these IMM enzymes. Conversely, the addition of a VDAC-enriched OMM preparation to mitoplasts increased respiration and partially restored sensitivity to inhibitors [64]. Although our experimental conditions were different, in the presence of succinate and rotenone (S-pathway), we noticed a similar reduction of oxygen consumption. This suggests that complex II might also be affected by the lack of mitochondrial porin.

In conclusion, our work definitely indicates the key role of VDAC1 in respiration and remarks, once again, on the pivotal role of the main porin isoform in preserving the proper functioning of mitochondria.

4. Materials and Methods

4.1. Cell Lines Maintenance, Proliferation and Treatment

HAP1 are near-haploid human cells of leukemic origin. The HAP1 parental and knock-out VDAC1 cell lines were purchased from Horizon Discovery (Waterbeach, UK). Cells were maintained in Iscove's modified Dulbecco's media (IMDM, GIBCO, Waltham, MA, USA), supplemented with 10% of fetal bovine serum (GIBCO) and penicillin/streptomycin antibiotic (GIBCO) in a controlled environment (37 °C and 5% CO₂). The proliferation of the HAP1 parental and knockout cells was monitored over time (6 days, each 24 h) by microscopy using a Burker's chamber. At day 0, 80.000 cells per genotype were seeded in 12-well plates. Three independent cell-counting assays were conducted.

For the inhibition of VDAC1 activity, HAP1 parental or VDAC1 knock-out cells were exposed to 20 µM of VBIT-12 previously dissolved in DMSO, or to DMSO as a control, for 30 min in a controlled environment (37 °C and 5% CO₂) prior to HRR experiments.

4.2. Western Blotting Analysis

The total lysates from the parental and VDAC1 knock-out HAP1 cells were obtained from 10⁶ cells in a lysis buffer (50 mM Tris-HCl pH 7.4, 150 mM NaCl, EDTA 1 mM, 1% TRITON X-100, protease inhibitors cocktail). Protein samples were separated using SDS-PAGE electrophoresis and transferred to a PDVF membrane (GE Healthcare, Chicago, IL, USA). The membranes were blocked in 5% BSA in PBS with 0.1% Tween-20 at room temperature for 1h and incubated overnight at 4 °C with the following primary antibodies: VDAC1 (1:1000, Abcam, Cambridge, UK), VDAC2 (1:200, Abcam), VDAC3 (1:100, Abcam), and β-Tubulin (1:2000, Cell Signaling, Danvers, MA, USA). After washing, membranes were incubated with IRDye-conjugated secondary antibodies (1:25,000, Li-Cor Biosciences, Lincoln, NE, USA). Signals were detected by the Odyssey CLx Imaging System (Li-Cor Biosciences) and analyzed using Image Studio Lite software (Li-Cor Biosciences). The same software was used for quantification.

4.3. Cell Viability Assay

The viability of the parental and VDAC1 knock-out HAP1 cells was investigated using a 3-(4,5-dimethylthiazolyl-2)-2,5-diphenyltetrazoliumbromide (MTT) assay. Cells were plated in 96-well plates (10.000 cell/well), and MTT was added after 24 h to achieve a final concentration of 5 mg/mL. After incubation (37 °C, 3 h) and medium removal, the formazan crystals produced were dissolved in 100 µL of dimethyl sulfoxide. Absorbance at 590 nm was then determined using the Varioskan microplate reader (Thermo Fisher, Waltham, MA, USA). Three independent experiments were performed in triplicate.

4.4. Analysis of Mitochondrial Mass

The mitochondrial mass of the HAP1 lines was estimated by flow cytometry using a fluorescent probe whose accumulation into mitochondria is independent of the mitochondrial membrane potential. Adherent cells were incubated for 30 min at 37 °C with Krebs Ringer Buffered Saline (130 mM NaCl, 3.6 mM KCl, 10 mM HEPES, 2 mM NaHCO₃, 0.5 mM NaH₂PO₄, 0.5 mM MgCl₂, 1.5 mM CaCl₂, 4.5 g/L glucose, pH 7.42) and supplemented with 300 nM of Mito tracker Green (Thermo Fisher). Cells were then collected and analyzed at 490/516 nm using the CyFlow ML flow cytometer (Partec) system [31,53]. Data were acquired and gated using the FCS Express 4 software (DeNovo). Three sets of independent experiments, each performed in triplicate, were performed by analyzing approximately 20,000 cells for each condition.

4.5. High-Resolution Respirometry (HRR)

The characterization of mitochondrial respiration in the HAP1 lines was performed by HRR in the two-chamber system O2k-FluoRespirometer (Oroboros Instruments, Innsbruck, Austria). Specific SUIIT protocols, aimed at analyzing the principal respiratory states and/or the contribution of ET complexes to the maximal respiratory capacity, were adapted from [51,53,65].

The complete respiratory profile was attained as follows. The ROUTINE state was measured in intact cells in the presence of endogenous substrates. Then, cells were subjected to a mild permeabilization of the plasma membranes with 3 µM digitonin. The dissipative respiration, the LEAK state, was determined in the presence of 5 mM pyruvate, 2 mM malate, and 10 mM glutamate, but not adenylates [41,66]. The OXPHOS respiration was activated by the addition of saturating ADP concentration (2.5 mM), followed by supplementation with 10 mM succinate. The maximal ET capacity was observed by uncoupler titration using 0.5 µM of CCCP. The residual oxygen consumption, the ROX state, was finally achieved by inhibiting the ET chain with 2 µM rotenone and 2.5 µM antimycin.

Alternatively, HRR was used in intact cells to monitor changes in the ET capacity [67]. Briefly, after the stabilization of ROUTINE respiration, the maximal ET capacity was achieved by the addition of 1 µM of CCCP. Different concentrations of rotenone (1 to 16 nM) or malonic acid (0.1 to 1.6 µM) were directly added in the cuvette.

All experiments were performed in a Mir05 respiration buffer (Oroboros Instruments) at 37 °C under constant stirring. All chemicals were purchased from Sigma Aldrich (St. Louis, MO, USA).

4.6. Analysis of Respirometric States

Instrumental and chemical background fluxes were calibrated as a function of the oxygen concentration using DatLab software (v7.4.0.1, Oroboros Instruments). The rate of oxygen consumption corresponding to the ROUTINE, OXPHOS, and maximal ET capacity was corrected for the ROX and expressed as pmol/s per million cells. Flux control ratios (FCRs) relative to the maximal ET capacity, the reserve capacities, and the contribution of the N- and S-pathways to the respiratory profile were calculated as in [51,68].

4.7. Chromatographic Analysis of Energetic Metabolites

Analysis of coenzymes was driven on deproteinized samples following a method set up in our laboratories [69]. This protocol is eligible to protect labile compounds from oxidation or hydrolysis. Briefly, 1 mL of a precipitating solution (CH₃CN + KH₂PO₄ 10 mM pH 7.4; 3:1 *v:v*) was added to 3 × 10⁶ pelleted cells, vigorously mixed, and centrifuged at a high speed (20,890 × *g* for 10 min at 4 °C). The supernatant was supplemented with two volumes of chloroform to discharge acetonitrile and all hydrophobic contamination and centrifuged again under the conditions described above. Finally, an aqueous sample suitable for chromatographic separation was recovered. A P4000 pump (Thermo Electron, Waltham, MA, USA), drove HAP1 parental and ΔVDAC1 cellular extracts into a Hypersil column (250 × 4.6 mm, 5 µm particle size) according to a well-established binary gradi-

ent. Analyte identification and quantification were conducted using a highly sensitive UV6000LP diode array detector (Thermo Electron) equipped with a 5-cm light path flow cell and set up with a wavelength between 200 and 300 nm. A standard mixture run was used as reference control.

4.8. Determination of Intracellular Lactate

The intracellular lactate was tested by colorimetric assay as in [70]. Briefly, 50 μ L of cellular extracts were mixed with a lactate oxidase/peroxidase-based reagent in Tris buffer and 4-aminoantipyrine to create a colored adduct. The absorbance variation, directly proportional to lactate concentration, followed in an automatic microplate photometer Elx800 Box 998 (BioTek Instruments, Winooski, VT, USA) set up at 545 nm wavelength. This variation was compared to a standard curve.

4.9. Statistical Analysis

All data are expressed as means or a median with standard deviation. A minimum of three independent experiments were performed for each assay. Data were statistically analyzed by *t*-test or two-way ANOVA using Prism software (GraphPad, San Diego, CA, USA). The following values * $p < 0.05$, ** $p < 0.01$, *** $p < 0.001$ were taken as significant.

Supplementary Materials: The following supporting information can be downloaded at: <https://www.mdpi.com/article/10.3390/ijms24043687/s1>.

Author Contributions: Conceptualization, A.M. (Andrea Magri), V.D.P. and A.M. (Angela Messina); methodology, A.M. (Andrea Magri) and A.M.A.; validation, A.M. (Andrea Magri), A.M.A. and A.M. (Angela Messina); formal analysis, A.M. (Andrea Magri) and A.M.A.; investigation, A.M. (Andrea Magri), S.A.M.C., G.B., C.L.R.L., S.C.N., M.W.S. and A.P., data curation, A.M. (Andrea Magri) and A.M.A.; writing—original draft preparation, A.M. (Andrea Magri); writing—review and editing, A.M.A., V.D.P. and A.M. (Angela Messina); visualization, A.M. (Andrea Magri), S.A.M.C., G.B.; supervision, A.M. (Andrea Magri), A.M.A. and A.M. (Angela Messina); project administration, A.M. (Andrea Magri) and A.M. (Angela Messina); funding acquisition, V.D.P. and A.M. (Angela Messina). All authors have read and agreed to the published version of the manuscript.

Funding: This research was funded by PIACERI (grant no. ARVEST) and Proof of Concept (grant no. PEPSLA POC 01_00054), awarded to A. Messina, and PIACERI (grant no. VDAC) and CHANCE, awarded to V.D.P.

Institutional Review Board Statement: Not applicable.

Informed Consent Statement: Not applicable.

Data Availability Statement: Not applicable.

Acknowledgments: The authors acknowledge Varda Shoshan-Barmatz (Ben Gurion University of the Negev, Beer Sheva, Israel) for the kind gift of a VBIT-12 inhibitor, Marianna F. Tomasello (CNR, Catania) for the support in flow cytometry experiments, Giuseppe Lazzarino (University of Catania, Italy) for the useful discussion of the data and the financial support of AIM Linea 1—salute (AIM1833071) to A. Magri.

Conflicts of Interest: The authors declare no conflict of interest.

References

1. Shoshan-Barmatz, V.; De Pinto, V.; Zweckstetter, M.; Raviv, Z.; Keinan, N.; Arbel, N. VDAC, a Multi-Functional Mitochondrial Protein Regulating Cell Life and Death. *Mol. Asp. Med.* **2010**, *31*, 227–285. [[CrossRef](#)] [[PubMed](#)]
2. De Pinto, V. Renaissance of VDAC: New Insights on a Protein Family at the Interface between Mitochondria and Cytosol. *Biomolecules* **2021**, *11*, 107. [[CrossRef](#)] [[PubMed](#)]
3. Forte, M.; Adelsberger-Mangan, D.; Colombini, M. Purification and Characterization of the Voltage-Dependent Anion Channel from the Outer Mitochondrial Membrane of Yeast. *J. Membr. Biol.* **1987**, *99*, 65–72. [[CrossRef](#)] [[PubMed](#)]
4. Benz, R.; Wojtczak, L.; Bosch, W.; Brdiczka, D. Inhibition of Adenine Nucleotide Transport through the Mitochondrial Porin by a Synthetic Polyaniion. *FEBS Lett.* **1988**, *231*, 75–80. [[CrossRef](#)] [[PubMed](#)]

5. Nibali, S.C.; Di Rosa, M.C.; Rauh, O.; Thiel, G.; Reina, S.; De Pinto, V. Cell-Free Electrophysiology of Human VDACs Incorporated into Nanodiscs: An Improved Method. *Biophys. Rep.* **2021**, *1*, 100002. [[CrossRef](#)]
6. Messina, A.; Reina, S.; Guarino, F.; De Pinto, V. VDAC Isoforms in Mammals. *Biochim. Biophys. Acta Biomembr.* **2012**, *1818*, 1466–1476. [[CrossRef](#)]
7. Ujwal, R.; Cascio, D.; Colletier, J.P.; Faham, S.; Zhang, J.; Toro, L.; Ping, P.; Abramson, J. The Crystal Structure of Mouse VDAC1 at 2.3 Å Resolution Reveals Mechanistic Insights into Metabolite Gating. *Proc. Natl. Acad. Sci. USA* **2008**, *105*, 17742–17747. [[CrossRef](#)] [[PubMed](#)]
8. Hiller, S.; Garces, R.G.; Malia, T.J.; Orekhov, V.Y.; Colombini, M.; Wagner, G. Solution Structure of the Integral Human Membrane Protein VDAC-1 in Detergent Micelles. *Science* **2008**, *321*, 1206–1210. [[CrossRef](#)]
9. Bayrhuber, M.; Meins, T.; Habeck, M.; Becker, S.; Giller, K.; Villinger, S.; Vonrhein, C.; Griesinger, C.; Zweckstetter, M.; Zeth, K. Structure of the Human Voltage-Dependent Anion Channel. *Proc. Natl. Acad. Sci. USA* **2008**, *105*, 15370–15375. [[CrossRef](#)]
10. Schredelseker, J.; Paz, A.; López, C.J.; Altenbach, C.; Leung, C.S.; Drexler, M.K.; Chen, J.N.; Hubbell, W.L.; Abramson, J. High Resolution Structure and Double Electron-Electron Resonance of the Zebrafish Voltage-Dependent Anion Channel 2 Reveal an Oligomeric Population. *J. Biol. Chem.* **2014**, *289*, 12566–12577. [[CrossRef](#)]
11. Manzo, G.; Serra, I.; Magri, A.; Casu, M.; De Pinto, V.; Ceccarelli, M.; Scorciapino, M.A. Folded Structure and Membrane Affinity of the N-Terminal Domain of the Three Human Isoforms of the Mitochondrial Voltage-Dependent Anion-Selective Channel. *ACS Omega* **2018**, *3*, 11415–11425. [[CrossRef](#)]
12. De Pinto, V.; Guarino, F.; Guarnera, A.; Messina, A.; Reina, S.; Tomasello, F.M.; Palermo, V.; Mazzoni, C. Characterization of Human VDAC Isoforms: A Peculiar Function for VDAC3? *Biochim. Biophys. Acta Bioenerg.* **2010**, *1797*, 1268–1275. [[CrossRef](#)]
13. Benz, R. Permeation of Hydrophilic Solutes through Mitochondrial Outer Membranes: Review on Mitochondrial Porins. *BBA—Rev. Biomembr.* **1994**, *1197*, 167–196. [[CrossRef](#)] [[PubMed](#)]
14. Rostovtseva, T.; Colombini, M. VDAC Channels Mediate and Gate the Flow of ATP: Implications for the Regulation of Mitochondrial Function. *Biophys. J.* **1997**, *72*, 1954–1962. [[CrossRef](#)] [[PubMed](#)]
15. Gincel, D.; Shoshan-Barmatz, V. Glutamate Interacts with VDAC and Modulates Opening of the Mitochondrial Permeability Transition Pore. *J. Bioenerg. Biomembr.* **2004**, *36*, 179–186. [[CrossRef](#)]
16. Camara, A.K.S.; Zhou, Y.F.; Wen, P.C.; Tajkhorshid, E.; Kwok, W.M. Mitochondrial VDAC1: A Key Gatekeeper as Potential Therapeutic Target. *Front. Physiol.* **2017**, *8*, 460. [[CrossRef](#)] [[PubMed](#)]
17. Magri, A.; Reina, S.; De Pinto, V. VDAC1 as Pharmacological Target in Cancer and Neurodegeneration: Focus on Its Role in Apoptosis. *Front. Chem.* **2018**, *6*, 108. [[CrossRef](#)] [[PubMed](#)]
18. Nakashima, R.A. Hexokinase-Binding Properties of the Mitochondrial VDAC Protein: Inhibition by DCCD and Location of Putative DCCD-Binding Sites. *J. Bioenerg. Biomembr.* **1989**, *21*, 461–470. [[CrossRef](#)] [[PubMed](#)]
19. Schindler, A.; Foley, E. Hexokinase 1 Blocks Apoptotic Signals at the Mitochondria. *Cell. Signal.* **2013**, *25*, 2685–2692. [[CrossRef](#)]
20. Magri, A.; Belfiore, R.; Reina, S.; Tomasello, M.F.; Di Rosa, M.C.; Guarino, F.; Leggio, L.; De Pinto, V.; Messina, A. Hexokinase i N-Terminal Based Peptide Prevents the VDAC1-SOD1 G93A Interaction and Re-Establishes ALS Cell Viability. *Sci. Rep.* **2016**, *6*, 34802. [[CrossRef](#)]
21. Shteinfefer-Kuzmine, A.; Argueti, S.; Gupta, R.; Shvil, N.; Abu-Hamad, S.; Gropper, Y.; Hoeber, J.; Magri, A.; Messina, A.; Kozlova, E.N.; et al. A VDAC1-Derived N-Terminal Peptide Inhibits Mutant SOD1-VDAC1 Interactions and Toxicity in the SOD1 Model of ALS. *Front. Cell. Neurosci.* **2019**, *13*, 346. [[CrossRef](#)]
22. Magri, A.; Messina, A. Interactions of VDAC with Proteins Involved in Neurodegenerative Aggregation: An Opportunity for Advancement on Therapeutic Molecules. *Curr. Med. Chem.* **2017**, *24*, 4470–4487. [[CrossRef](#)]
23. Reina, S.; De Pinto, V. Anti-Cancer Compounds Targeted to VDAC: Potential and Perspectives. *Curr. Med. Chem.* **2017**, *24*, 4447–4469. [[CrossRef](#)] [[PubMed](#)]
24. Risiglione, P.; Zinghirino, F.; Di Rosa, M.C.; Magri, A.; Messina, A. Alpha-Synuclein and Mitochondrial Dysfunction in Parkinson's Disease: The Emerging Role of VDAC. *Biomolecules* **2021**, *11*, 718. [[CrossRef](#)] [[PubMed](#)]
25. Cheng, E.H.Y.; Sheiko, T.V.; Fisher, J.K.; Craigen, W.J.; Korsmeyer, S.J. VDAC2 Inhibits BAK Activation and Mitochondrial Apoptosis. *Science* **2003**, *301*, 513–517. [[CrossRef](#)] [[PubMed](#)]
26. Ma, S.B.; Nguyen, T.N.; Tan, I.; Ninnis, R.; Iyer, S.; Stroud, D.A.; Menard, M.; Kluck, R.M.; Ryan, M.T.; Dewson, G. Bax Targets Mitochondria by Distinct Mechanisms before or during Apoptotic Cell Death: A Requirement for VDAC2 or Bak for Efficient Bax Apoptotic Function. *Cell Death Differ.* **2014**, *21*, 1925–1935. [[CrossRef](#)]
27. Chin, H.S.; Li, M.X.; Tan, I.K.L.; Ninnis, R.L.; Reljic, B.; Scicluna, K.; Dagley, L.F.; Sandow, J.J.; Kelly, G.L.; Samson, A.L.; et al. VDAC2 Enables BAX to Mediate Apoptosis and Limit Tumor Development. *Nat. Commun.* **2018**, *9*, 4976. [[CrossRef](#)]
28. Reina, S.; Checchetto, V.; Saletti, R.; Gupta, A.; Chaturvedi, D.; Guardiani, C.; Guarino, F.; Scorciapino, M.A.; Magri, A.; Foti, S.; et al. VDAC3 as a Sensor of Oxidative State of the Intermembrane Space of Mitochondria: The Putative Role of Cysteine Residue Modifications. *Oncotarget* **2016**, *7*, 2249–2268. [[CrossRef](#)]
29. Queralt-Martín, M.; Bergdoll, L.; Teijido, O.; Munshi, N.; Jacobs, D.; Kuszak, A.J.; Protchenko, O.; Reina, S.; Magri, A.; De Pinto, V.; et al. A Lower Affinity to Cytosolic Proteins Reveals VDAC3 Isoform-Specific Role in Mitochondrial Biology. *J. Gen. Physiol.* **2020**, *152*, e201912501. [[CrossRef](#)]

30. Saletti, R.; Reina, S.; Pittalà, M.G.G.; Belfiore, R.; Cunsolo, V.; Messina, A.; De Pinto, V.; Foti, S. High Resolution Mass Spectrometry Characterization of the Oxidation Pattern of Methionine and Cysteine Residues in Rat Liver Mitochondria Voltage-Dependent Anion Selective Channel 3 (VDAC3). *Biochim. Biophys. Acta Biomembr.* **2017**, *1859*, 301–311. [[CrossRef](#)]
31. Reina, S.; Conti Nibali, S.; Tomasello, M.F.; Magrì, A.; Messina, A.; De Pinto, V. Voltage Dependent Anion Channel 3 (VDAC3) Protects Mitochondria from Oxidative Stress. *Redox Biol.* **2022**, *51*, 102264. [[CrossRef](#)]
32. Di Rosa, M.C.; Guarino, F.; Nibali, S.C.; Magrì, A.; De Pinto, V. Voltage-Dependent Anion Selective Channel Isoforms in Yeast: Expression, Structure, and Functions. *Front. Physiol.* **2021**, *12*, 675708. [[CrossRef](#)] [[PubMed](#)]
33. Magrì, A.; Di Rosa, M.C.; Orlandi, I.; Guarino, F.; Reina, S.; Guarnaccia, M.; Morello, G.; Spampinato, A.; Cavallaro, S.; Messina, A.; et al. Deletion of Voltage-Dependent Anion Channel 1 Knocks Mitochondria down Triggering Metabolic Rewiring in Yeast. *Cell. Mol. Life Sci.* **2020**, *77*, 3195–3213. [[CrossRef](#)] [[PubMed](#)]
34. Brahimi-Horn, M.C.; Giuliano, S.; Saland, E.; Lacas-Gervais, S.; Sheiko, T.; Pelletier, J.; Bourget, I.; Bost, F.; Féral, C.; Boulter, E.; et al. Knockout of Vdac1 Activates Hypoxia-Inducible Factor through Reactive Oxygen Species Generation and Induces Tumor Growth by Promoting Metabolic Reprogramming and Inflammation. *Cancer Metab.* **2015**, *3*, 8. [[CrossRef](#)] [[PubMed](#)]
35. Yang, M.; Sun, J.; Stowe, D.F.; Tajkhorshid, E.; Kwok, W.M.; Camara, A.K.S. Knockout of VDAC1 in H9c2 Cells Promotes Oxidative Stress-Induced Cell Apoptosis through Decreased Mitochondrial Hexokinase II Binding and Enhanced Glycolytic Stress. *Cell. Physiol. Biochem.* **2020**, *54*, 853–874. [[CrossRef](#)] [[PubMed](#)]
36. Essletzbichler, P.; Konopka, T.; Santoro, F.; Chen, D.; Gapp, B.V.; Kralovics, R.; Brummelkamp, T.R.; Nijman, S.M.B.; Bürckstümmer, T. Megabase-Scale Deletion Using CRISPR/Cas9 to Generate a Fully Haploid Human Cell Line. *Genome Res.* **2014**, *24*, 2059–2065. [[CrossRef](#)]
37. Pesta, D.; Gnaiger, E. High-Resolution Respirometry: OXPHOS Protocols for Human Cells and Permeabilized Fibers from Small Biopsies of Human Muscle. *Methods Mol. Biol.* **2012**, *810*, 25–58. [[CrossRef](#)]
38. Ben-Hail, D.; Begas-Shvartz, R.; Shalev, M.; Shteinfein-Kuzmine, A.; Gruzman, A.; Reina, S.; De Pinto, V.; Shoshan-Barmatz, V. Novel Compounds Targeting the Mitochondrial Protein VDAC1 Inhibit Apoptosis and Protect against Mitochondrial Dysfunction. *J. Biol. Chem.* **2016**, *291*, 24986–25003. [[CrossRef](#)]
39. Verma, A.; Pittala, S.; Alhozeel, B.; Shteinfein-Kuzmine, A.; Ohana, E.; Gupta, R.; Chung, J.H.; Shoshan-Barmatz, V. The Role of the Mitochondrial Protein VDAC1 in Inflammatory Bowel Disease: A Potential Therapeutic Target. *Mol. Ther.* **2022**, *30*, 726–744. [[CrossRef](#)] [[PubMed](#)]
40. Evinova, A.; Cizmarova, B.; Hatokova, Z.; Racay, P. High-Resolution Respirometry in Assessment of Mitochondrial Function in Neuroblastoma SH-SY5Y Intact Cells. *J. Memb. Biol.* **2020**, *253*, 129–136. [[CrossRef](#)]
41. Gnaiger, E. Capacity of Oxidative Phosphorylation in Human Skeletal Muscle. New Perspectives of Mitochondrial Physiology. *Int. J. Biochem. Cell Biol.* **2009**, *41*, 1837–1845. [[CrossRef](#)]
42. Yang, Y.; Sauve, A.A. NAD⁺ Metabolism: Bioenergetics, Signaling and Manipulation for Therapy. *Biochim. Biophys. Acta Proteins Proteom.* **2016**, *1864*, 1787–1800. [[CrossRef](#)]
43. Sherer, T.B.; Betarbet, R.; Testa, C.M.; Seo, B.B.; Richardson, J.R.; Kim, J.H.; Miller, G.W.; Yagi, T.; Matsuno-Yagi, A.; Greenamyre, J.T. Mechanism of Toxicity in Rotenone Models of Parkinson's Disease. *J. Neurosci.* **2003**, *23*, 10756–10764. [[CrossRef](#)] [[PubMed](#)]
44. Gonçalves, R.P.; Buzhynskyy, N.; Prima, V.; Sturgis, J.N.; Scheuring, S. Supramolecular Assembly of VDAC in Native Mitochondrial Outer Membranes. *J. Mol. Biol.* **2007**, *369*, 413–418. [[CrossRef](#)]
45. Gonçalves, R.P.; Buzhynskyy, N.; Scheuring, S. Mini Review on the Structure and Supramolecular Assembly of VDAC. *J. Bioenerg. Biomembr.* **2008**, *40*, 133–138. [[CrossRef](#)]
46. Morgenstern, M.; Stiller, S.B.; Lübbert, P.; Peikert, C.D.; Dannenmaier, S.; Drepper, F.; Weill, U.; Höß, P.; Feuerstein, R.; Gebert, M.; et al. Definition of a High-Confidence Mitochondrial Proteome at Quantitative Scale. *Cell Rep.* **2017**, *19*, 2836–2852. [[CrossRef](#)] [[PubMed](#)]
47. Seitaj, B.; Maull, F.; Zhang, L.; Wüllner, V.; Wolf, C.; Schippers, P.; la Rovere, R.; Distler, U.; Tenzer, S.; Parys, J.B.; et al. Transmembrane BAX Inhibitor-1 Motif Containing Protein 5 (TMBIM5) Sustains Mitochondrial Structure, Shape, and Function by Impacting the Mitochondrial Protein Synthesis Machinery. *Cells* **2020**, *9*, 2147. [[CrossRef](#)]
48. Jastroch, M.; Divakaruni, A.S.; Mookerjee, S.; Treberg, J.R.; Brand, M.D. Mitochondrial Proton and Electron Leaks. *Essays Biochem.* **2010**, *47*, 53–67. [[CrossRef](#)]
49. Porter, R.K. Mitochondrial Proton Leak: A Role for Uncoupling Proteins 2 and 3? *Biochim. Biophys. Acta Bioenerg.* **2001**, *1504*, 120–127. [[CrossRef](#)] [[PubMed](#)]
50. Cannon, B.; Shabalina, I.G.; Kramarova, T.V.; Petrovic, N.; Nedergaard, J. Uncoupling Proteins: A Role in Protection against Reactive Oxygen Species-or Not? *Biochim. Biophys. Acta Bioenerg.* **2006**, *1757*, 449–458. [[CrossRef](#)] [[PubMed](#)]
51. Risiglione, P.; Leggio, L.; Cubisino, S.A.M.; Reina, S.; Paternò, G.; Marchetti, B.; Magrì, A.; Iraci, N.; Messina, A. High-Resolution Respirometry Reveals Mpp⁺ Mitochondrial Toxicity Mechanism in a Cellular Model of Parkinson's Disease. *Int. J. Mol. Sci.* **2020**, *21*, 7809. [[CrossRef](#)] [[PubMed](#)]
52. Calabria, E.; Scambi, I.; Bonafede, R.; Schiaffino, L.; Peroni, D.; Potrich, V.; Capelli, C.; Schena, F.; Mariotti, R. Ascs-Exosomes Recover Coupling Efficiency and Mitochondrial Membrane Potential in an in Vitro Model of Als. *Front. Neurosci.* **2019**, *13*, 1070. [[CrossRef](#)]

53. Magrì, A.; Risiglione, P.; Caccamo, A.; Formicola, B.; Tomasello, M.F.; Arrigoni, C.; Zimbone, S.; Guarino, F.; Re, F.; Messina, A. Small Hexokinase 1 Peptide against Toxic SOD1 G93A Mitochondrial Accumulation in ALS Rescues the ATP-Related Respiration. *Biomedicines* **2021**, *9*, 948. [[CrossRef](#)] [[PubMed](#)]
54. Cheng, J.; Nanayakkara, G.; Shao, Y.; Cueto, R.; Wang, L.; Yang, W.Y.; Tian, Y.; Wang, H.; Yang, X. Mitochondrial Proton Leak Plays a Critical Role in Pathogenesis of Cardiovascular Diseases. *Adv. Exp. Med. Biol.* **2017**, *982*, 359–370. [[CrossRef](#)]
55. Lemieux, H.; Semsroth, S.; Antretter, H.; Höfer, D.; Gnaiger, E. Mitochondrial Respiratory Control and Early Defects of Oxidative Phosphorylation in the Failing Human Heart. *Int. J. Biochem. Cell Biol.* **2011**, *43*, 1729–1738. [[CrossRef](#)]
56. Risiglione, P.; Cubisino, S.A.M.; Lipari, C.L.R.; De Pinto, V.; Messina, A.; Magrì, A. α -Synuclein A53T Promotes Mitochondrial Proton Gradient Dissipation and Depletion of the Organelle Respiratory Reserve in a Neuroblastoma Cell Line. *Life* **2022**, *12*, 894. [[CrossRef](#)]
57. Guardiani, C.; Magrì, A.; Karachitos, A.; di Rosa, M.C.; Reina, S.; Bodrenko, I.; Messina, A.; Kmita, H.; Ceccarelli, M.; de Pinto, V. YVDAC2, the Second Mitochondrial Porin Isoform of *Saccharomyces Cerevisiae*. *Biochim. Biophys. Acta Bioenerg.* **2018**, *1859*, 270–279. [[CrossRef](#)]
58. Magrì, A.; Karachitos, A.; Di Rosa, M.C.; Reina, S.; Conti Nibali, S.; Messina, A.; Kmita, H.; De Pinto, V. Recombinant Yeast VDAC2: A Comparison of Electrophysiological Features with the Native Form. *FEBS Open Bio* **2019**, *9*, 1184–1193. [[CrossRef](#)] [[PubMed](#)]
59. Magrì, A.; Di Rosa, M.C.; Tomasello, M.F.; Guarino, F.; Reina, S.; Messina, A.; De Pinto, V. Overexpression of Human SOD1 in VDAC1-Less Yeast Restores Mitochondrial Functionality Modulating Beta-Barrel Outer Membrane Protein Genes. *Biochim. Biophys. Acta Bioenerg.* **2016**, *1857*, 789–798. [[CrossRef](#)]
60. Zinghirino, F.; Pappalardo, X.G.; Messina, A.; Nicosia, G.; De Pinto, V.; Guarino, F. VDAC Genes Expression and Regulation in Mammals. *Front. Physiol.* **2021**, *12*, 708695. [[CrossRef](#)] [[PubMed](#)]
61. Cesar, M.D.C.; Wilson, J.E. All Three Isoforms of the Voltage-Dependent Anion Channel (VDAC1, VDAC2, and VDAC3) Are Present in Mitochondria from Bovine, Rabbit, and Rat Brain. *Arch. Biochem. Biophys.* **2004**, *422*, 191–196. [[CrossRef](#)] [[PubMed](#)]
62. Leggio, L.; Guarino, F.; Magrì, A.; Accardi-Gheit, R.; Reina, S.; Specchia, V.; Damiano, F.; Tomasello, M.F.; Tommasino, M.; Messina, A. Mechanism of Translation Control of the Alternative *Drosophila Melanogaster* Voltage Dependent Anion-Selective Channel 1 MRNAs. *Sci. Rep.* **2018**, *8*, 5347. [[CrossRef](#)] [[PubMed](#)]
63. Reina, S.; Palermo, V.; Guarnera, A.; Guarino, F.; Messina, A.; Mazzoni, C.; De Pinto, V. Swapping of the N-Terminus of VDAC1 with VDAC3 Restores Full Activity of the Channel and Confers Anti-Aging Features to the Cell. *FEBS Lett.* **2010**, *584*, 2837–2844. [[CrossRef](#)]
64. Pronevich, L.A.; Mirzabekov, T.A.; Rozhdestvenskaya, Z.E. Mitochondrial porin regulates the sensitivity of anion carriers to inhibitors. *FEBS Lett.* **1989**, *247*, 330–332. [[CrossRef](#)] [[PubMed](#)]
65. Leggio, L.; L'episcopo, F.; Magrì, A.; Ulloa-Navas, J.; Paternò, G.; Vivarelli, S.; Bastos, C.A.P.; Tirolo, C.; Testa, N.; Caniglia, S.; et al. Small Extracellular Vesicles Secreted by Nigrostriatal Astrocytes Rescue Cell Death and Preserve Mitochondrial Function in Parkinson's Disease. *Adv. Healthc. Mater.* **2022**, *11*, e2201203. [[CrossRef](#)]
66. Chance, B.; Williams, G.R. Respiratory Enzymes in Oxidative Phosphorylation. III. The Steady State. *J. Biol. Chem.* **1955**, *217*, 409–427. [[CrossRef](#)]
67. Bețiu, A.M.; Chamkha, I.; Gustafsson, E.; Meijer, E.; Avram, V.F.; Frostner, E.Å.; Ehinger, J.K.; Petrescu, L.; Muntean, D.M.; Elmér, E. Cell-permeable Succinate Rescues Mitochondrial Respiration in Cellular Models of Amiodarone Toxicity. *Int. J. Mol. Sci.* **2021**, *22*, 11786. [[CrossRef](#)]
68. Gnaiger, E. Mitochondrial pathways and respiratory control. An introduction to OXPHOS analysis. *Bioenerg. Commun.* **2020**, *2*, 112. [[CrossRef](#)]
69. Lazzarino, G.; Amorini, A.M.; Fazzina, G.; Vagnozzi, R.; Signoretti, S.; Donzelli, S.; di Stasio, E.; Giardina, B.; Tavazzi, B. Single-Sample Preparation for Simultaneous Cellular Redox and Energy State Determination. *Anal. Biochem.* **2003**, *322*, 51–59. [[CrossRef](#)] [[PubMed](#)]
70. Artiss, J.D.; Karcher, R.E.; Cavanagh, K.T.; Collins, S.L.; Peterson, V.J.; Varma, S.; Zak, B. A Liquid-Stable Reagent for Lactic Acid Levels: Application to the Hitachi 911 and Beckman CX7. *Am. J. Clin. Pathol.* **2000**, *114*, 139–143. [[CrossRef](#)] [[PubMed](#)]

Disclaimer/Publisher's Note: The statements, opinions and data contained in all publications are solely those of the individual author(s) and contributor(s) and not of MDPI and/or the editor(s). MDPI and/or the editor(s) disclaim responsibility for any injury to people or property resulting from any ideas, methods, instructions or products referred to in the content.

Supplementary Data:

VDAC1 knockout affects mitochondrial oxygen consumption triggering a rearrangement of ETC by impacting on complex I activity



Supplementary Materials to:

VDAC1 knockout affects mitochondrial oxygen consumption triggering a rearrangement of ETC by impacting on complex I activity

Andrea Magri^{1,2†*}, Salvatore Antonio Maria Cubisino^{3†}, Giuseppe Battiato³, Cristiana Lucia Rita Lipari³, Stefano Conti Nibali³, Miriam Wissam Saab⁴, Alessandra Pittalà⁴, Angela Maria Amorini⁴, Vito De Pinto^{2,3}, Angela Messina^{1,2}

¹ Department of Biological, Geological and Environmental Sciences, University of Catania, Via S. Sofia 64, 95125 Catania, Italy; andrea.magri@unict.it (A. Magri); mess@unict.it (A. Messina).

² we.MitoBiotech S.R.L., C.so Italia 174, 95125 Catania, Italy.

³ Department of Biomedical and Biotechnological Sciences, University of Catania, Via S. Sofia 64, 95125 Catania, Italy; salvatore.cubisino@phd.unict.it (S.A.M.C.); giuseppe.battiato@phd.unict.it (G.B.); cristiana.lipari@phd.unict.it (C.L.R.L.); stefano.continibali@unict.it (S.C.N.); vdpbiofa@unict.it (V.D.P.).

⁴ Department of Biomedical and Biotechnological Sciences, Division of Medical Biochemistry, University of Catania, Via S.Sofia 97, 95123 Catania, Italy; miriam.saab@gmail.com (M.W.S.); alessandrapittala@gmail.com (A.P.); amorini@unict.it (A.M.A.).

* Correspondence: andrea.magri@unict.it.

† These authors have equally contributed

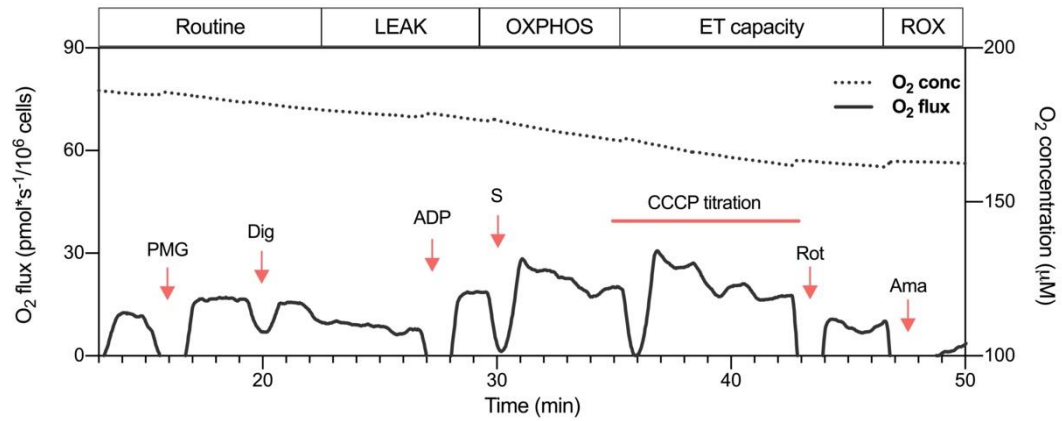


Figure S1. Oxygen consumption in HAP1 VDAC1 knock-out cells. A representative curve of mitochondrial respiratory profile of HAP1 Δ VDAC1 cells along with the SUIT protocol used in this work. P, pyruvate; M, malate; G, glutamate; Dig, digitonin; S, succinate; Rot, rotenone; Ama, antimycin.

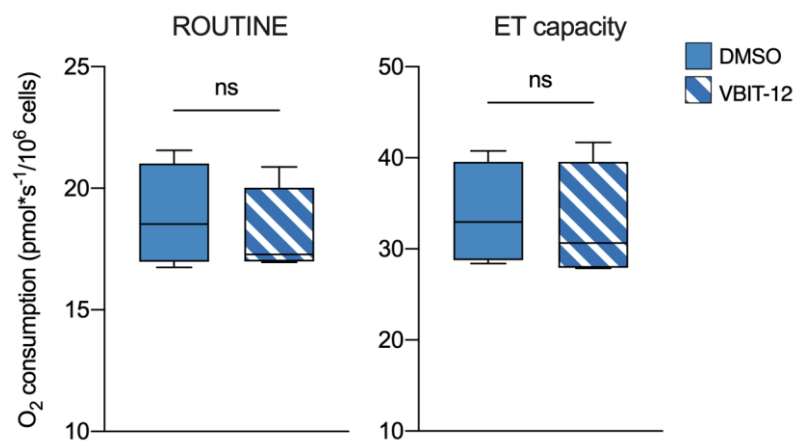


Figure S2. Analysis of VBIT-12 effect on respiration of Δ VDAC1 cells. Quantitative analysis of the oxygen consumption rates of ROUTINE and maximal ET capacity in HAP1 Δ VDAC1 cells previously treated with VBIT-12 or DMSO (control). No significant variation has been observed for both ROUTINE or ET capacity. Data are expressed as pmol/second per million cells and shown as median \pm SEM of n=6 independent experiments.

	NAD⁺	NADH	NADP⁺	NADPH
Parental	1.48 ± 0.64	0.18 ± 0.04	0.42 ± 0.19	0.11 ± 0.04
ΔVDAC1	0.87 ± 0.44	0.09 ± 0.41	0.22 ± 0.06	0.14 ± 0.04

Table S1. Raw data of the nicotinamide dinucleotides expressed as nmol/million cells. Data are relative to the quantification of each nicotinamide dinucleotide in HAP1 parental and VDAC1 knockout cells. Data are expressed as means ± SD of n=4 independent measurements.

Article 2.

Life

α -Synuclein A53T Promotes Mitochondrial Proton Gradient Dissipation and Depletion of the Organelle Respiratory Reserve in a Neuroblastoma Cell Line

Pierpaolo Risiglione¹, Salvatore Antonio Maria Cubisino¹, Cristiana Lucia Rita Lipari¹, Vito De Pinto^{1,2}, Angela Messina^{2,3} and Andrea Magri^{2,3}

¹ Department of Biomedical and Biotechnological Sciences, University of Catania, Via S. Sofia 64, 95125, Catania, Italy

² we.MitoBiotech S.R.L, C.so Italia 174, 95125, Catania, Italy

³ Department of Biological, Geological and Environmental Sciences, University of Catania, Via S.Sofia64, 95125 Catania, Italy

Article

α -Synuclein A53T Promotes Mitochondrial Proton Gradient Dissipation and Depletion of the Organelle Respiratory Reserve in a Neuroblastoma Cell Line

Pierpaolo Risiglione¹, Salvatore Antonio Maria Cubisino¹, Cristiana Lucia Rita Lipari^{1,2} , Vito De Pinto^{1,2} , Angela Messina^{2,3,*}  and Andrea Magri^{2,3,*} 

- ¹ Department of Biomedical and Biotechnological Sciences, University of Catania, Via S. Sofia 64, 95125 Catania, Italy; pierpaolo.risiglione@phd.unict.it (P.R.); salvatore.cubisino@phd.unict.it (S.A.M.C.); cristiana.lipari@phd.unict.it (C.L.R.L.); vdpbiofa@unict.it (V.D.P.)
- ² we.MitoBiotech S.R.L., Corso Italia 172, 95125 Catania, Italy
- ³ Department of Biological, Geological and Environmental Sciences, University of Catania, Via S. Sofia 64, 95125 Catania, Italy
- * Correspondence: mess@unict.it (A.M.); andrea.magri@unict.it (A.M.)

Abstract: α -synuclein (α Syn) is a small neuronal protein whose accumulation correlates with Parkinson's disease. α Syn A53T mutant impairs mitochondrial functions by affecting substrate import within the organelle, activity of complex I and the maximal respiratory capacity. However, the precise mechanism initiating the bioenergetic dysfunction is not clearly understood yet. By overexpressing α Syn A53T in SH-SY5Y cells, we investigated the specific changes in the mitochondrial respiratory profile using High-Resolution Respirometry. We found that α Syn A53T increases dissipative fluxes across the intermembrane mitochondrial space: this does not compromise the oxygen flows devoted to ATP production while it reduces the bioenergetic excess capacity of mitochondria, providing a possible explanation of the increased cell susceptibility observed in the presence of further stress stimuli.

Keywords: α Syn; mitochondrial dysfunction; Parkinson's disease; high-resolution respirometry



Citation: Risiglione, P.; Cubisino, S.A.M.; Lipari, C.L.R.; De Pinto, V.; Messina, A.; Magri, A. α -Synuclein A53T Promotes Mitochondrial Proton Gradient Dissipation and Depletion of the Organelle Respiratory Reserve in a Neuroblastoma Cell Line. *Life* **2022**, *12*, 894. <https://doi.org/10.3390/life12060894>

Received: 20 May 2022

Accepted: 14 June 2022

Published: 15 June 2022

Publisher's Note: MDPI stays neutral with regard to jurisdictional claims in published maps and institutional affiliations.



Copyright: © 2022 by the authors. Licensee MDPI, Basel, Switzerland. This article is an open access article distributed under the terms and conditions of the Creative Commons Attribution (CC BY) license (<https://creativecommons.org/licenses/by/4.0/>).

1. Introduction

α -synuclein (α Syn) is a small neuronal protein mainly expressed in the brain whose physiological function remains largely unknown. α Syn localizes principally at the synapsis, where it is believed to take part in the release of the neurotransmitter vesicles [1,2]. Despite the lack of an organized structure in solution, evidence suggests that α Syn exists in a dynamic equilibrium between a cytosolic unstructured and an N-terminal α -helix structured form, the last adopted when it binds the membranes [3,4]. A predominantly β -sheet conformation is adopted during α Syn aggregation processes into toxic oligomers and amyloid fibrils [5]. Fibrils are the main component of the Lewy bodies, intraneuronal inclusions typical of a group of neurodegenerative disorders collectively known as synucleinopathies and including Parkinson's disease (PD), dementia with Lewy bodies and multiple system atrophy [6].

Although it is mainly cytosolic, α Syn was detected in several subcellular compartments, such as mitochondria [7]. It has been proposed that α Syn crosses the outer mitochondrial membrane (OMM) by using VDAC pores [8,9]. Within the intermembrane space (IMS), α Syn seems to participate in the modulation of the mitochondrial bioenergetic functions [10]. In mice, the genetic knock-out of the α Syn gene, SNCA, significantly reduces the coupling between the electron transport through the respiratory complexes and the ATP production [11]. However, pathological forms have a harmful impact on mitochondrial functioning. For instance, α Syn aggregates affect ATP synthesis, complex I activity [12,13], and compromise the import of protein and substrates within the organelle [14,15].

The transition from a physiological conformation to pathological forms is often associated to missense mutations in SNCA gene. For instance, the substitution of alanine 53 in threonine (A53T) associates to the early onset of familial PD [16]. This mutation increases the rate of α Syn fibrils formation, leaving unvaried the ability of the protein to bind phospholipid membranes [17,18]. As widely reported in the literature, the expression of α Syn A53T correlates with mitochondrial dysfunction. In transgenic mice, A53T mutant accumulation induces mitochondrial DNA damage and the opening of the permeability transition pore [19]. In the same murine model, extensive mitophagy events precede dopamine depletion and neurodegeneration [20]. Furthermore, in primary cortical neurons, A53T promotes a decrease of the maximal respiratory capacity of mitochondria [21]. However, the precise mechanism by which the α Syn mutant initiates the impairment of mitochondrial bioenergetics remains largely unknown.

With this aim, in this work α Syn A53T was overexpressed in the neuroblastoma SH-SY5Y cell line and the respiratory profile was analyzed. Our findings indicate that overexpression of α Syn A53T, but not of the corresponding wild-type protein, affects the maximal respiratory capacity and promotes an increase of the dissipative-related respiration. This latter does not correlate with a decrease in flows related to mitochondrial ATP production upon stimulation of the oxidative phosphorylation system activity. Importantly, the combination of these events results in a drastic reduction of the energy excess capacity, a respiratory reserve on which mitochondria may draw in presence of stress conditions.

Overall, our results may help to understand the general impact of α Syn A53T on mitochondrial function and how this mutant may contribute to increase cell vulnerability to additional stress stimuli, such as oxidative stress, typical of PD and other synucleinopathies.

2. Materials and Methods

2.1. Cloning and Mutagenesis

The sequence encoding wild-type (WT) human α Syn was amplified by PCR from a stock plasmid and cloned in the modified pCMS-mtDsRED vector (Clontech, Mountain View, CA, USA) [22] in frame with the HA-tag at the C-terminal domain. Cloning was performed by PCR using available protocol [23]. The introduction of A53T mutation was achieved by site-directed mutagenesis on pCMS construct carrying α Syn WT by the QuickChange Site-Directed Mutagenesis kit (Stratagene, La Jolla, CA, USA) according to the manufacturer's instructions. All primers used in amplification, cloning and mutagenesis are listed in Table S1. All sequences were verified by sequencing.

2.2. Cell Line Maintenance, Transfection and Viability

The human neuroblastoma SH-SY5Y cell line was maintained in DMEM medium supplemented with 10% fetal bovine serum, 2 mM L-glutamine and 1% penicillin/streptomycin (Sigma-Aldrich, St. Louis, MO, USA) and kept in a controlled environment (37 °C and 5% CO₂). Cells were transfected with constructs carrying α Syn sequences or empty vector using K2 Transfection System (Biontex, Munich, Germany) according to manufacturers' instructions. All experiments were performed after 48 h from transfection.

Viability of transfected SH-SY5Y cells was determined by MTT assay [24]. Cells were seeded in 96-well plate and the colorimetric reaction was analyzed using the microplate reader Varioskan (Thermo Fisher Scientific, Waltham, MA, USA). For each condition tested, three independent experiments in triplicate were performed.

2.3. Western Blot

Whole lysates from transfected SH-SY5Y were separated on NuPAGE Bis-Tris polyacrylamide gels (Thermo Fisher Scientific, Waltham, MA, USA) and transferred to PVDF membranes (GE Healthcare, Chicago, IL, USA). After blocking, membranes were incubated with the following primary antibodies: anti α Syn (Abcam, Cambridge, UK, cat. no. ab80627, 1:1000), anti VDAC1 (Abcam, Cambridge, UK cat. no. ab14734, 1:1000), anti SDHA (Cell Signaling, Danvers, MA, USA, cat. no. 11998, 1:1000) and anti β -actin (Cell Signaling,

Danvers, MA, USA, cat. no. 4970, 1:2000). Afterwards, membranes were incubated with IRDye conjugated secondary antibodies (LI-COR Biosciences, Lincoln, NE, USA, 1:25,000). Signals were detected using Odyssey Imaging System (LI-COR Biosciences, Lincoln, NE, USA). Three independent experiments were performed.

2.4. High-Resolution Respirometry (HRR)

Mitochondrial respiration capacity of SH-SY5Y cells was analyzed in intact and permeabilized cells using the two-chamber system O2k-FluoRespirometer (Oroboros Instruments, Innsbruck, Austria) by HRR. All experiments were performed at 37 °C in respirometric buffer Mir05 (Oroboros Instruments, Innsbruck, Austria), under constant stirring.

The oxygen consumption in the different respiratory states was determined using a specific substrate-uncoupler-inhibitors titration (SUIT) protocol as in [25]. Respiration in intact cells, the ROUTINE state, was first measured. Plasma membranes were permeabilized with the addition of 4 µM digitonin and the LEAK state was measured in the presence of previously added pyruvate (5 mM) and malate (2 mM) but in absence of adenylates. OXPHOS state was achieved by the addition of glutamate and succinate (10 mM) in the presence of saturating concentrations of ADP (2.5 mM). The uncoupled maximal capacity of the electron transport (ET) system was attained by titration with carbonyl cyanide 3-chlorophenylhydrazone (CCCP, 0.5 µM). Afterwards, rotenone (2 µM) was added, allowing the measurement of the complex II activity in the ETS state. The residual oxygen consumption (ROX) was achieved by the addition of antimycin (2.5 µM respectively). All chemicals were purchased from Sigma-Aldrich (St. Louis, MO, USA). Six independent experiments were performed for each condition.

2.5. Analysis of Respirometric States

Instrumental and chemical background fluxes were calibrated as a function of oxygen concentration using DatLab software (version 7.4, Oroboros Instruments, Innsbruck, Austria). The rate of oxygen consumption in the respiratory states ROUTINE, LEAK, OXPHOS and ET capacity was corrected for the ROX and expressed as pmol/sec per million cells or as Flux Control Ratios (FCRs) relative to the ET capacity [26]. Oxygen flows relative to net respiration, coupling respiration and excess capacity were calculated as described [25].

2.6. Statistical Analysis

Data are expressed as a mean or median ± SD and statistically analyzed by one-way ANOVA following by Tukey's test using Prism software (version 9, GraphPad Inc., San Diego, CA, USA). Cells transfected with the empty vector were used as control. The values of * $p < 0.05$ and ** $p < 0.01$ were taken as significant.

3. Results

3.1. Characterization of SH-SY5Y Overexpressing αSyn A53T

In order to investigate the effect of αSyn A53T for mitochondrial respiration, the neuroblastoma cells SH-SY5Y were transiently transfected with a plasmid carrying αSyn A53T or WT encoding sequence, or the empty vector as control (hereafter simply named pCMS). The efficiency of cell transfection was verified after 48 h by Western blot, whereas the overall effect on cell viability was evaluated by MTT assay. As shown in Figure 1A, the transfection efficiently allowed the detection of an intense band at the expected molecular weight, consisting of the exogenous αSyn HA-tagged protein, in addition to the endogenous one. However, in accordance with the previous observation [27], the overexpression of αSyn A53T or WT achieved by transient transfection did not cause a significant loss of cell viability in our cellular model (Figure 1B).

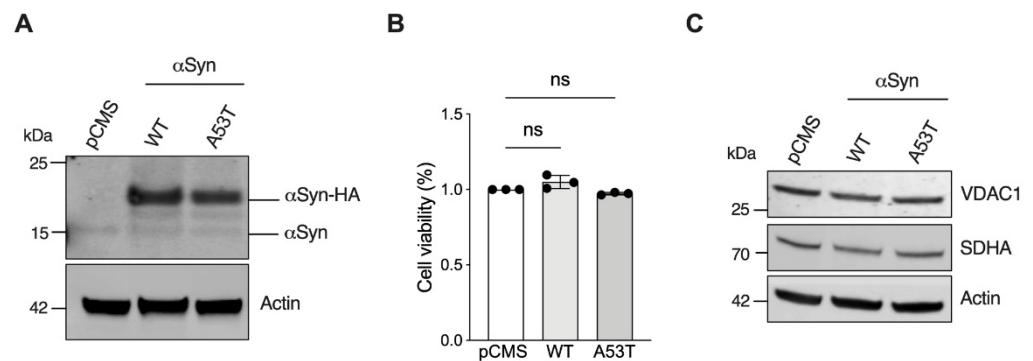


Figure 1. Analysis of α Syn WT and A53T expression in SH-SY5Y cells. **(A)** Representative Western blot of lysates obtained from SH-SY5Y previously transfected with the empty vector (pCMS) or constructs carrying α Syn WT or A53T. Exogenous α Syn expression is shown. Actin was used as loading control. **(B)** MTT assay of transfected SH-SY5Y. Data are expressed as a mean \pm SD of $n = 3$ independent experiments and analyzed by one-way ANOVA; ns, not significant. **(C)** Representative Western blot of same lysates as in A showing the levels of mitochondrial markers VDAC1 and SDHA. Actin was used as loading control.

By assaying the levels of specific mitochondrial markers upon transfection, we next estimated the mitochondrial mass. As displayed in Figure 1C, significant variations among the samples were observed neither for VDAC1 nor for SDHA, proteins located in the OMM and in the inner mitochondrial membrane (IMM), respectively.

3.2. α Syn A53T Reduces the Maximal Respiratory Capacity of SH-SY5Y Cells

The respiratory profile of transfected SH-SY5Y was then analyzed in detail. For this purpose, HRR and a specific SUIIT protocol were used, aimed at investigating the oxygen consumption in the main respiratory states. Figure 2A displays a representative respirometric curve of cells transfected with the empty vector showing changes in the oxygen flux following the addition of substrates, inhibitors or uncouplers. According to the protocol, oxygen consumption was measured before plasma membrane permeabilization, i.e., in the presence of endogenous substrates (ROUTINE state), or immediately after, in the presence of saturating ADP concentration and externally added substrates able to stimulate the oxidative phosphorylation (OXPHOS state). The subsequent titration with the uncoupler CCCP, up to the complete dissipation of the proton gradient, allowed us to analyze the maximal capacity of the electron transport system (ET capacity).

The same protocol was applied to SH-SY5Y cells expressing α Syn WT and A53T mutant and the oxygen flows correspondent to each previously described state were measured (see Table S2 for raw data). As reported in Figure 2B, no significant difference was noticed among our samples in ROUTINE or OXPHOS state. Conversely, the overexpression of α Syn A53T, but not of WT, correlated with a significant reduction of the oxygen flow corresponding to the maximal capacity (-15% vs. pCMS, $p = 0.04$), in agreement with previous observations [21,28]. Cell viability and mitochondrial mass being unvaried (see Figure 1), this result suggests that what we observed is directly related to the overexpression of α Syn A53T.

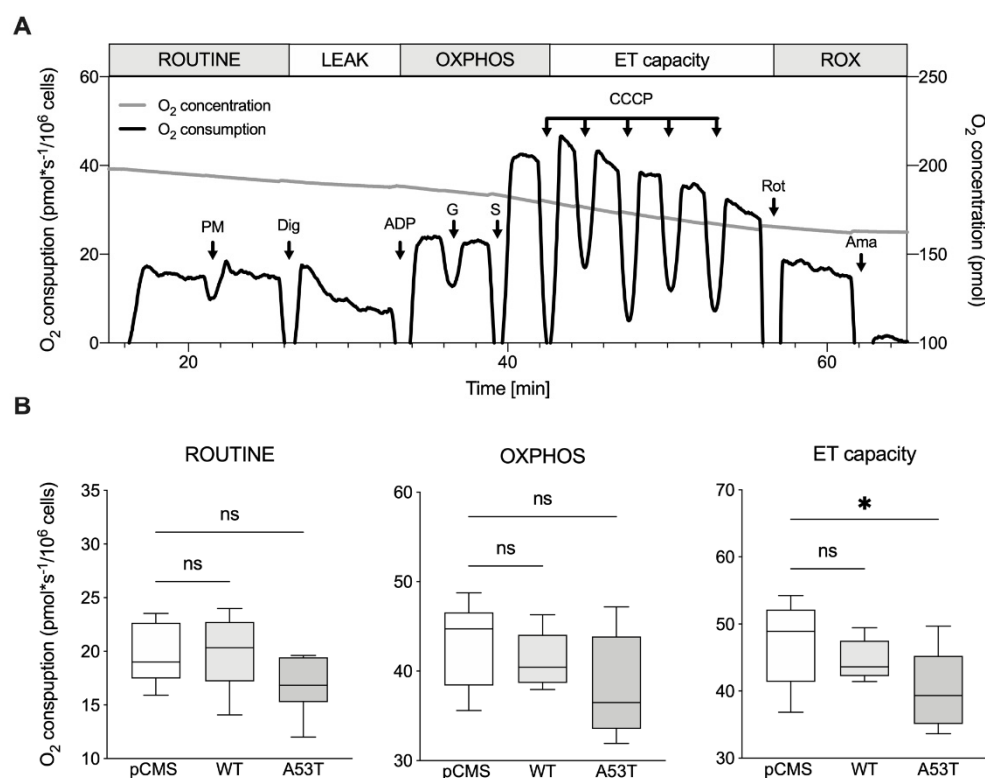


Figure 2. Respiratory profile of transfected SH-SY5Y cells. (A) Representative respirometric curve of SH-SY5Y transfected with the empty pCMS showing the oxygen consumption as a function of the time. The SUIIT protocol applied and the corresponding respiratory states achieved are also reported. Arrows indicate the addition of substrates: PM, pyruvate and malate; Dig, digitonin; G, glutamate; S, succinate; CCCP, carbonyl cyanide 3-chlorophenylhydrazone; Rot, rotenone; Ama, antimycin. (B) Quantitative analysis of the oxygen fluxes obtained for transfected SH-SY5Y in the main respiratory states ROUTINE, OXPPOS and maximal ET capacity. Data are expressed as a median \pm SD of $n = 6$ independent experiments and analyzed by one-way ANOVA with * $p < 0.05$; ns, not significant.

3.3. α Syn A53T Increases Oxidative Phosphorylation Related Flux but Not the ATP-Related One

In order to analyze the contribution of each respiratory state or complex to the maximal ET capacity, we analyzed the Flux Control Ratios (FCRs) [25,26]. As reported in Figure 3A, the oxygen rate measured in ROUTINE conditions was comparable among samples. Conversely, after cell permeabilization and upon external stimulation with specific substrates, an unexpected increase of the OXPPOS respiration rate was exclusively observed with α Syn A53T overexpression (+7% vs. pCMS, $p = 0.015$). Being the synthesis of ATP the goal of oxidative phosphorylation, we measured the net OXPPOS respiration, i.e. the oxygen consumption exclusively devoted to ADP phosphorylation. As reported in Figure 3B, no significant differences were observed among samples, suggesting that the previous increase observed in the total OXPPOS respiration does not correspond to a similar increase of ATP-related flow.

Activation of the ET system depends on the activation of complex I, complex II or both. The SUIIT protocol described in Figure 2A allowed us to investigate the specific contribution of each complex to the total OXPPOS flux. In particular, the complex I activity was measured before the addition of succinate (a specific activator of complex II), in the presence of pyruvate, malate and glutamate. Complex II activity was instead attained after the addition of succinate and the inhibition of complex I with rotenone. As indicated by the quantitative analysis in Figure 3C, neither the activity of complex I nor that of complex II varied in any condition tested, suggesting that the increased OXPPOS respiration observed in the presence of the α Syn mutant is independent from the functioning of both complexes.

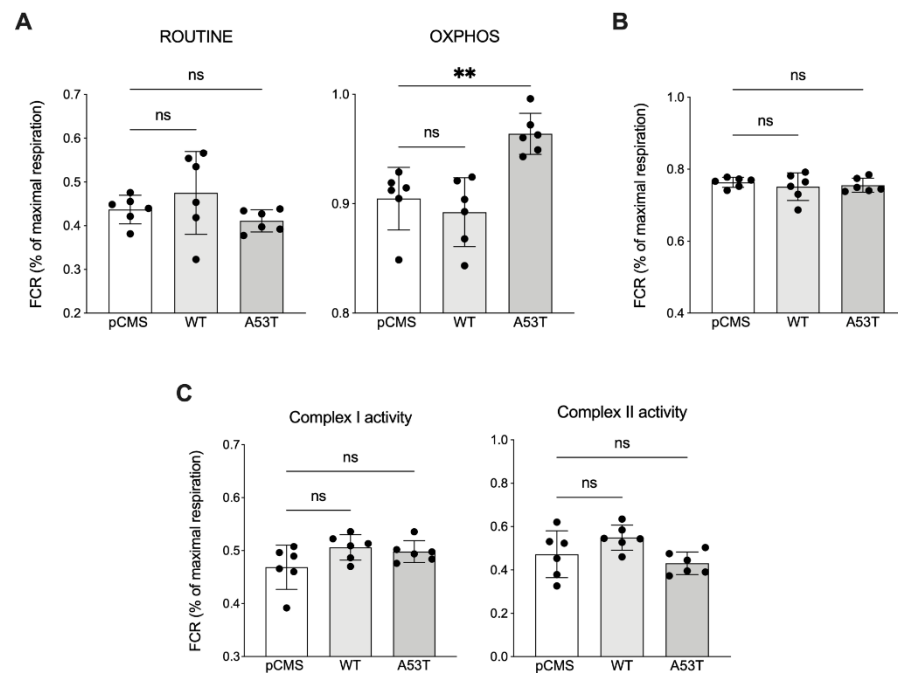


Figure 3. Analysis of the OXPHOS respiration in transfected SH-SY5Y cells. (A) Quantification of the specific contribution of ROUTINE and OXPHOS to the maximal ET capacity assayed in transfected SH-SY5Y cells. (B) Analysis of the net OXPHOS respiration in transfected cells, corresponding to the ADP phosphorylation flux. (C) Quantitative analysis of the specific contribution of complex I and complex II to the maximal ET capacity of transfected SH-SY5Y. Data are expressed as FCRs and as a mean \pm SD of $n = 6$ independent experiments. Data were analyzed by one-way ANOVA with $** p < 0.01$; ns, not significant.

3.4. α Syn A53T Increases LEAK Respiration and Diminishes the Excess Capacity of Mitochondria

The coupling between ET activity and ATP production does not match 100% since some protons can partially return to the matrix across the IMM independently from the ATP synthase [29]. The proton leak roughly accounts for 95% of respiration measured in our cells immediately after the mild permeabilization of plasma membranes, the so-called LEAK respiration. According to Figure 2A, in this state, the oxygen consumption is pushed by the activity of the respiratory chain in presence of pyruvate and malate, and simultaneous absence of adenylates [30]. Based on previous results, we queried whether the increased OXPHOS respiration linked to α Syn A53T was due to variation in the dissipative respiratory component. As reported in Figure 4A, a significant increase of LEAK respiration was detected in the presence of the α Syn mutant (+32% vs. pCMS, $p = 0.017$) but not with the WT. Not coincidentally, the percentage of oxygen consumption coupled to phosphorylating events, the ET coupling efficiency, decreased from 84% in control cells to 78% in α Syn A53T expressing cells ($p = 0.015$, Figure 4B). In contrast, cells expressing α Syn WT showed a coupling efficiency of about 86%, thus almost indistinguishable from that of the control.

Finally, we questioned how much the increase in the dissipative portion of the OXPHOS capacity affected the excess capacity of mitochondria, consisting of the respiratory reserve calculated as the difference between the oxygen consumption in OXPHOS and ET capacity. As reported in Figure 4C, in our experimental conditions, the excess capacity measured in the presence α Syn of A53T mutant was more than halved in comparison to cells expressing α Syn WT or the control (−55% vs. pCMS, $p = 0.01$). Overall, our results indicate that α Syn A53T leads to an increase of dissipative events across the IMM, which, in turn, are responsible for the drastic reduction of mitochondrial respiratory reserve.

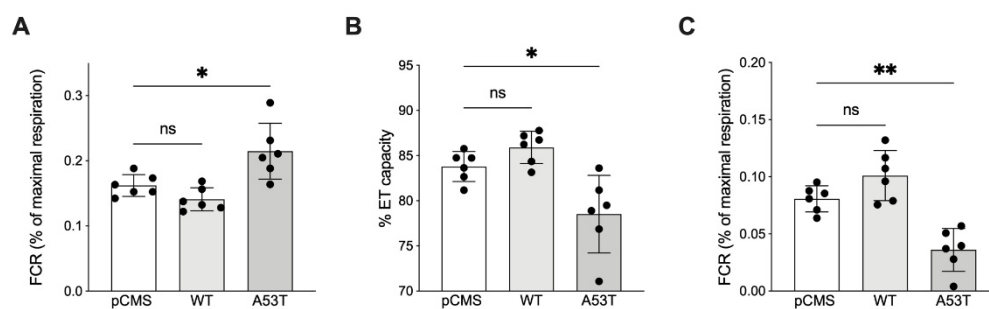


Figure 4. Analysis of the LEAK, coupling efficiency and excess capacity in transfected SH-SY5Y cells. (A) Analysis of the specific contribution of LEAK to the maximal ET capacity of transfected SH-SY5Y cells. (B) Analysis of the ET coupling efficiency, expressed as a percentage of the total ET capacity. (C) Quantitative analysis of the excess capacity of transfected SH-SY5Y. Data are expressed as FCRs or as a percentage of OXPHOS and as a mean \pm SD of $n = 6$ independent experiments. Data were analyzed by one-way ANOVA with * $p < 0.05$ and ** $p < 0.01$; ns, not significant.

4. Discussion

The impairment of mitochondrial bioenergetics is widely considered a key event for neurodegeneration. It depends on many factors, including the accumulation of misfolded proteins on the organelle surface, the increased oxidative stress, lipid peroxidation and calcium dysregulation [31,32]. Among misfolded proteins, α Syn is responsible for a broad set of neurodegenerative diseases namely synucleinopathies. The literature indicates that overexpression of the PD-related α Syn A53T drives mitochondrial dysfunction processes [19–21], albeit the precise basic mechanism is mostly unknown.

With this concern, we applied HRR to analyze any specific changes in the mitochondrial respiratory profile of neuroblastoma cells overexpressing α Syn mutant. In our conditions, transient transfection was not sufficient for inducing cell death, as already demonstrated by different groups in SH-SY5Y cells or in other models [27,28], nor mitochondrial mass reduction, as evinced from our experiments. At the same time, the presence of A53T correlated with a reduction of the oxygen consumption relative to the maximal ET capacity, overlapping with literature results attained in cortical primary neurons and N2A cells both expressing α Syn A53T [21,28]. Therefore, transient transfection allowed us to achieve high expression of exogenous α Syn proteins without affecting cell viability or mitochondrial mass, leading us to assume that changes in mitochondrial respiration were exclusively due to a direct effect of α Syn overexpression.

By applying a SUIT protocol specifically developed for the analysis of the whole respiratory profile of SH-SY5Y [25], we found that while α Syn WT never changed the respiratory parameters, A53T overexpression correlated with a significant and unexpected increase of the OXPHOS respiration, not in terms of absolute values but rather as contributing to the maximal respiration. This result, however, was not linked to increments in the activity of complex I or II, but associated with a proportional increase of the dissipative LEAK component. The phosphorylation of ADP to ATP is strictly coupled to the electron transfer from NADH or FADH₂ to oxygen through the respiratory complexes, a mechanism which allows the formation of the proton gradient. However, these two processes are not entirely coupled, due to the return of some protons to the matrix independently from ATP synthase [29]. In fact, OXPHOS capacity (P) is always partitioned into the dissipative LEAK component (L) and ADP-stimulated P-L net OXPHOS capacity, even in physiological conditions. This means that the coupling efficiency is not 100% and part of the proton gradient is dissipated by proton leak processes [29].

In general, proton leak depends on the integrity of the IMM and its lipid composition, abundance of ANT and carriers, and activity of uncoupling proteins (UCP) [33]. Under pathological conditions, the proportion of proton leak can increase defining a dyscoupled respiration state. It is thus important to note the difference between the physiological and regulated uncoupling and the pathological dyscoupling, the latter strictly related to

mitochondrial dysfunction. Many stress conditions, such as the accumulation of misfolded proteins, increase the partial dissipation of the proton gradient. For example, it has been recently demonstrated that aggregation of SOD1 mutants on the cytosolic surface of mitochondria, as occurred in an amyotrophic lateral sclerosis (ALS) model, increases LEAK respiration [34], while the displacement of SOD1 from the organelle reduces the LEAK flux up to physiological levels [35]. Notably, in the same ALS model, the increment of LEAK affects also the ATP-related flux [35]. In the presence of α Syn A53T we observed a similar increase of the LEAK respiration together with a proportional rise of the OXPHOS one. This allows the cell to counteract the dissipation of the proton gradient and maintain unaltered the ATP-related oxygen flow, as demonstrated by our experiments, thus meeting the energetic needs of the cells.

It should be considered that cells may use the LEAK respiration as a protective stress response: a mild dyscoupling of the proton gradient, indeed, could attenuate ROS production without impacting on energy production but contributing to prevent the oxidation of proteins and lipids [36]. Our experiments do not clarify whether the increase in the LEAK respiration is a cause or an effect of the presence of α Syn A53T. However, since no variation exists in the flux devoted to the ATP production between A53T and WT or empty vector, we can speculate that the observed increase in LEAK respiration may be a cell response put in place in order to counteract the presence of the mutant protein. To achieve this result, mitochondria draw resources from their excess capacity. Excess capacity is a respiratory reserve on which the mitochondria rely on in case of sudden high energy demands or when stress conditions occur [26]. The magnitude of this reserve can be reduced by an increase in LEAK respiration which, in turn, pushes the OXPHOS capacity toward the limit of the maximal respiration [37]. A contribution to the lessening of the mitochondrial excess capacity is also due to the decrease of maximal respiration itself [37]. These changes in mitochondrial respiration due to the A53T mutant may underlie the cellular susceptibility to additional stress stimuli such as aging and exposure to environmental toxins, as occurred in the case of MPP⁺ exposure [38].

In conclusion, with this work we outlined for the first time the importance of excess capacity for the proper maintenance of mitochondrial function.

Supplementary Materials: The following supporting information can be downloaded at: <https://www.mdpi.com/article/10.3390/life12060894/s1>, Table S1: List of primers used in this work for PCR cloning and mutagenesis; Table S2: Raw data of oxygen consumption of transformed cells in different respiratory states.

Author Contributions: Conceptualization, A.M. (Angela Messina) and A.M. (Andrea Magri); methodology, P.R. and A.M. (Andrea Magri); validation, P.R. and A.M. (Andrea Magri); formal analysis, V.D.P., A.M. (Angela Messina) and A.M. (Andrea Magri); investigation, P.R., S.A.M.C., C.L.R.L.; resources, V.D.P. and A.M. (Angela Messina); data curation, P.R., S.A.M.C. and A.M. (Andrea Magri); writing—original draft preparation, P.R. and A.M. (Andrea Magri); writing—review and editing, V.D.P. and A.M. (Angela Messina); visualization, A.M. (Andrea Magri); supervision, A.M. (Angela Messina) and A.M. (Andrea Magri); project administration, A.M. (Angela Messina) and A.M. (Andrea Magri); funding acquisition, V.D.P. and A.M. (Angela Messina). All authors have read and agreed to the published version of the manuscript.

Funding: This research was funded by PIACERI (grant no. ARVEST) and Proof of Concept (grant no. PEPSLA POC 01_00054) to A. Messina, PIACERI (grant no. VDAC) and CHANCHE to V.D.P.

Institutional Review Board Statement: Not applicable.

Informed Consent Statement: Not applicable.

Data Availability Statement: Not applicable.

Acknowledgments: The authors acknowledge the financial support of AIM Linea 1—Salute (AIM1833071) to A. Magri, and Fondi di Ateneo 2020–2022, Università di Catania, linea Open Access.

Conflicts of Interest: The authors declare no conflict of interest.

References

1. Bendor, J.T.; Logan, T.P.; Edwards, R.H. The Function of α -Synuclein. *Neuron* **2013**, *79*, 1044–1066. [[CrossRef](#)] [[PubMed](#)]
2. Sulzer, D.; Edwards, R.H. The physiological role of alpha-synuclein and its relationship to Parkinson's Disease. *J. Neurochem.* **2019**, *150*, 475–486. [[CrossRef](#)] [[PubMed](#)]
3. Burré, J.; Vivona, S.; Diao, J.; Sharma, M.; Brunker, A.T.; Südhof, T.C. Properties of native brain α -synuclein. *Nature* **2013**, *498*, E4–E6. [[CrossRef](#)] [[PubMed](#)]
4. Bartels, T.; Choi, J.G.; Selkoe, D.J. α -Synuclein occurs physiologically as a helically folded tetramer that resists aggregation. *Nature* **2011**, *477*, 107–110. [[CrossRef](#)] [[PubMed](#)]
5. Serpell, L.C.; Berriman, J.; Jakes, R.; Goedert, M.; Crowther, R.A. Fiber diffraction of synthetic α -synuclein filaments shows amyloid-like cross- β conformation. *Proc. Natl. Acad. Sci. USA* **2000**, *97*, 4897–4902. [[CrossRef](#)] [[PubMed](#)]
6. Spillantini, M.G.; Schmidt, M.L.; Lee, V.M.Y.; Trojanowski, J.Q.; Jakes, R.; Goedert, M. α -Synuclein in Lewy Bodies. *Nature* **1997**, *388*, 839–840. [[CrossRef](#)]
7. Bernal-Conde, L.D.; Ramos-Acevedo, R.; Reyes-Hernández, M.A.; Balbuena-Olvera, A.J.; Morales-Moreno, I.D.; Argüero-Sánchez, R.; Schuele, B.; Guerra-Crespo, M. Alpha-Synuclein Physiology and Pathology: A Perspective on Cellular Structures and Organelles. *Front. Neurosci.* **2019**, *13*, 1399. [[CrossRef](#)]
8. Rostovtseva, T.K.; Gurnev, P.A.; Protchenko, O.; Hoogerheide, D.P.; Yap, T.L.; Philpott, C.C.; Lee, J.C.; Bezrukov, S.M. α -Synuclein Shows High Affinity Interaction with Voltage-dependent Anion Channel, Suggesting Mechanisms of Mitochondrial Regulation and Toxicity in Parkinson Disease. *J. Biol. Chem.* **2015**, *290*, 18467–18477. [[CrossRef](#)]
9. Queralt-Martín, M.; Bergdoll, L.; Tejjido, O.; Munshi, N.; Jacobs, D.; Kuszak, A.J.; Protchenko, O.; Reina, S.; Magri, A.; De Pinto, V.; et al. A lower affinity to cytosolic proteins reveals VDAC3 isoform-specific role in mitochondrial biology. *J. Gen. Physiol.* **2020**, *152*, e201912501. [[CrossRef](#)]
10. Ellis, C.E.; Murphy, E.J.; Mitchell, D.C.; Golovko, M.Y.; Scaglia, F.; Barceló-Coblijn, G.C.; Nussbaum, R.L. Mitochondrial Lipid Abnormality and Electron Transport Chain Impairment in Mice Lacking α -Synuclein. *Mol. Cell. Biol.* **2005**, *25*, 10190–10201. [[CrossRef](#)]
11. Ludtmann, M.H.R.; Angelova, P.R.; Ninkina, N.N.; Gandhi, S.; Buchman, V.L.; Abramov, A.Y. Monomeric Alpha-Synuclein Exerts a Physiological Role on Brain ATP Synthase. *J. Neurosci.* **2016**, *36*, 10510–10521. [[CrossRef](#)] [[PubMed](#)]
12. Martínez, J.H.; Fuentes, F.; Vanasco, V.; Alvarez, S.; Alaimo, A.; Cassina, A.; Leskow, F.C.; Velazquez, F. Alpha-synuclein mitochondrial interaction leads to irreversible translocation and complex I impairment. *Arch. Biochem. Biophys.* **2018**, *651*, 1–12. [[CrossRef](#)] [[PubMed](#)]
13. Ludtmann, M.H.R.; Angelova, P.R.; Horrocks, M.H.; Choi, M.L.; Rodrigues, M.; Baev, A.Y.; Berezhnov, A.V.; Yao, Z.; Little, D.; Banushi, B.; et al. α -synuclein oligomers interact with ATP synthase and open the permeability transition pore in Parkinson's disease. *Nat. Commun.* **2018**, *9*, 2293. [[CrossRef](#)] [[PubMed](#)]
14. Di Maio, R.; Barrett, P.J.; Hoffman, E.K.; Barrett, C.W.; Zharikov, A.; Borah, A.; Hu, X.; McCoy, J.; Chu, C.T.; Burton, E.A.; et al. α -Synuclein binds to TOM20 and inhibits mitochondrial protein import in Parkinson's disease. *Sci. Transl. Med.* **2016**, *8*, 342ra78. [[CrossRef](#)]
15. Risiglione, P.; Zinghirino, F.; Di Rosa, M.C.; Magri, A.; Messina, A. Alpha-Synuclein and Mitochondrial Dysfunction in Parkinson's Disease: The Emerging Role of VDAC. *Biomolecules* **2021**, *11*, 718. [[CrossRef](#)]
16. Polymeropoulos, M.H.; Lavedan, C.; Leroy, E.; Ide, S.E.; Dehejia, A.; Dutra, A.; Pike, B.; Root, H.; Rubenstein, J.; Boyer, R.; et al. Mutation in the α -Synuclein Gene Identified in Families with Parkinson's Disease. *Science* **1997**, *276*, 2045–2047. [[CrossRef](#)]
17. Conway, K.A.; Harper, J.D.; Lansbury, P.T. Accelerated In Vitro Fibril Formation by a Mutant α -synuclein Linked to Early-Onset Parkinson Disease. *Nat. Med.* **1998**, *4*, 1318–1320. [[CrossRef](#)]
18. Flagmeier, P.; Meisl, G.; Vendruscolo, M.; Knowles, T.P.J.; Dobson, C.M.; Buell, A.K.; Galvagnion, C. Mutations associated with familial Parkinson's disease alter the initiation and amplification steps of α -synuclein aggregation. *Proc. Natl. Acad. Sci. USA* **2016**, *113*, 10328–10333. [[CrossRef](#)]
19. Martin, L.J.; Pan, Y.; Price, A.C.; Sterling, W.; Copeland, N.G.; Jenkins, N.A.; Price, D.L.; Lee, M.K. Parkinson's Disease -Synuclein Transgenic Mice Develop Neuronal Mitochondrial Degeneration and Cell Death. *J. Neurosci.* **2006**, *26*, 41–50. [[CrossRef](#)]
20. Chen, L.; Xie, Z.; Turkson, S.; Zhuang, X. A53T Human -Synuclein Overexpression in Transgenic Mice Induces Pervasive Mitochondria Macroautophagy Defects Preceding Dopamine Neuron Degeneration. *J. Neurosci.* **2015**, *35*, 890–905. [[CrossRef](#)]
21. Li, L.; Nadanaciva, S.; Berger, Z.; Shen, W.; Paumier, K.; Schwartz, J.; Mou, K.; Loos, P.; Milici, A.J.; Dunlop, J.; et al. Human A53T α -Synuclein Causes Reversible Deficits in Mitochondrial Function and Dynamics in Primary Mouse Cortical Neurons. *PLoS ONE* **2013**, *8*, e85815. [[CrossRef](#)] [[PubMed](#)]
22. Tomasello, M.F.; Guarino, F.; Reina, S.; Messina, A.; De Pinto, V. The Voltage-Dependent Anion Selective Channel 1 (VDAC1) Topography in the Mitochondrial Outer Membrane as Detected in Intact Cell. *PLoS ONE* **2013**, *8*, e81522. [[CrossRef](#)] [[PubMed](#)]
23. Bryksin, A.V.; Matsumura, I. Overlap extension PCR cloning: A simple and reliable way to create recombinant plasmids. *BioTechniques* **2010**, *48*, 463–465. [[CrossRef](#)] [[PubMed](#)]
24. Mosmann, T. Rapid colorimetric assay for cellular growth and survival: Application to proliferation and cytotoxicity assays. *J. Immunol. Methods* **1983**, *65*, 55–63. [[CrossRef](#)]

25. Risiglione, P.; Leggio, L.; Cubisino, S.A.M.; Reina, S.; Paternò, G.; Marchetti, B.; Magrì, A.; Iraci, N.; Messina, A. High-Resolution Respirometry Reveals MPP⁺ Mitochondrial Toxicity Mechanism in a Cellular Model of Parkinson's Disease. *Int. J. Mol. Sci.* **2020**, *21*, 7809. [[CrossRef](#)]
26. Gnaiger, E. Capacity of oxidative phosphorylation in human skeletal muscle: New perspectives of mitochondrial physiology. *Int. J. Biochem. Cell Biol.* **2009**, *41*, 1837–1845. [[CrossRef](#)]
27. Yiğit, E.N.; Sönmez, E.; Söğüt, M.S.; Çakır, T.; Kurnaz, I.A. Validation of an In-Vitro Parkinson's Disease Model for the Study of Neuroprotection. *Proc. West Mark. Ed. Assoc. Conf.* **2018**, *2*, 1559. [[CrossRef](#)]
28. Fu, M.-H.; Wu, C.-W.; Lee, Y.-C.; Hung, C.-Y.; Chen, I.-C.; Wu, K.L.H. Nrf2 activation attenuates the early suppression of mitochondrial respiration due to the α -synuclein overexpression. *Biomed. J.* **2018**, *41*, 169–183. [[CrossRef](#)]
29. Jastroch, M.; Divakaruni, A.S.; Mookerjee, S.; Treberg, J.R.; Brand, M.D. Mitochondrial proton and electron leaks. *Essays Biochem.* **2010**, *47*, 53–67. [[CrossRef](#)]
30. Chance, B.; Williams, G.R. Respiratory Enzymes in Oxidative Phosphorylation. III. The Steady State. *J. Biol. Chem.* **1955**, *217*, 409–427. [[CrossRef](#)]
31. Kumar, V.; Sami, N.; Kashav, T.; Islam, A.; Ahmad, F.; Hassan, M.I. Protein aggregation and neurodegenerative diseases: From theory to therapy. *Eur. J. Med. Chem.* **2016**, *124*, 1105–1120. [[CrossRef](#)] [[PubMed](#)]
32. Magrì, A.; Messina, A. Interactions of VDAC with Proteins Involved in Neurodegenerative Aggregation: An Opportunity for Advancement on Therapeutic Molecules. *Curr. Med. Chem.* **2017**, *24*, 4470–4487. [[CrossRef](#)]
33. Cadenas, S. Mitochondrial uncoupling, ROS generation and cardioprotection. *Biochim. Biophys. Acta Bioenerg.* **2018**, *1859*, 940–950. [[CrossRef](#)] [[PubMed](#)]
34. Calabria, E.; Scambi, I.; Bonafede, R.; Schiaffino, L.; Peroni, D.; Potrich, V.; Capelli, C.; Schena, F.; Mariotti, R. ASCs-Exosomes Recover Coupling Efficiency and Mitochondrial Membrane Potential in an in vitro Model of ALS. *Front. Neurosci.* **2019**, *13*, 1070. [[CrossRef](#)] [[PubMed](#)]
35. Magrì, A.; Risiglione, P.; Caccamo, A.; Formicola, B.; Tomasello, M.F.; Arrigoni, C.; Zimbone, S.; Guarino, F.; Re, F.; Messina, A. Small Hexokinase 1 Peptide against Toxic SOD1 G93A Mitochondrial Accumulation in ALS Rescues the ATP-Related Respiration. *Biomedicines* **2021**, *9*, 948. [[CrossRef](#)]
36. Brand, M.D. Uncoupling to survive? The role of mitochondrial inefficiency in ageing. *Proc. Exp. Gerontol.* **2000**, *35*, 811–820. [[CrossRef](#)]
37. Lemieux, H.; Semsroth, S.; Antretter, H.; Höfer, D.; Gnaiger, E. Mitochondrial respiratory control and early defects of oxidative phosphorylation in the failing human heart. *Int. J. Biochem. Cell Biol.* **2011**, *43*, 1729–1738. [[CrossRef](#)]
38. Kanda, S.; Bishop, J.F.; Eglitis, M.A.; Yang, Y.; Mouradian, M.M. Enhanced vulnerability to oxidative stress by α -synuclein mutations and C-terminal truncation. *Neuroscience* **2000**, *97*, 279–284. [[CrossRef](#)]

Article 3.

International Journal of Molecular Sciences

High-Resolution Respirometry Reveals MPP+ Mitochondrial Toxicity Mechanism in a Cellular Model of Parkinson's Disease

Pierpaolo Risiglione¹, Loredana Leggio², [Salvatore Antonio Maria Cubisino](#)¹, Simona Reina^{3,4}, Greta Paternò², Bianca Marchetti^{2,5}, Andrea Magri^{3,4}, Nunzio Iraci² and Angela Messina^{3,4}

¹ Department of Biomedical and Biotechnological Sciences, University of Catania, Via S. Sofia 64, 95125, Catania, Italy

² Department of Biomedical and Biotechnological Sciences, University of Catania, Torre Biologica, Via S. Sofia 97, 95125, Catania, Italy

³ Department of Biological, Geological and Environmental Sciences, University of Catania, V.le Andrea Doria 6, 95125 Catania, Italy




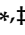
⁴ we.MitoBiotech S.R.L, C.so Italia 174, 95125, Catania, Italy

⁵ Neuropharmacology Section, OASI Research Institute-IRCCS, 94018 Troina (EN), Italy



Article

High-Resolution Respirometry Reveals MPP⁺ Mitochondrial Toxicity Mechanism in a Cellular Model of Parkinson's Disease

Pierpaolo Risiglione ^{1,†}, Loredana Leggio ^{2,†}, Salvatore A. M. Cubisino ¹, Simona Reina ^{3,4}, Greta Paternò ², Bianca Marchetti ^{2,5} , Andrea Magri ^{3,4,*} , Nunzio Iraci ^{2,‡} 
and Angela Messina ^{3,4,*} 

¹ Department of Biomedical and Biotechnological Sciences, University of Catania, V.le Andrea Doria 6, 95125 Catania, Italy; pierpaolo.risiglione@phd.unict.it (P.R.); salvatore.cubisino@phd.unict.it (S.A.M.C.)

² Department of Biomedical and Biotechnological Sciences, University of Catania, Torre Biologica, Via Santa Sofia 97, 95125 Catania, Italy; loredanaleggio@unict.it (L.L.); greta.paterno.gp@gmail.com (G.P.); biancamarchetti@libero.it (B.M.); nunzio.iraci@unict.it (N.I.)

³ Department of Biological, Geological and Environmental Sciences, University of Catania, V.le Andrea Doria 6, 95125 Catania, Italy; simona.reina@unict.it

⁴ we.MitoBiotech S.R.L., C.so Italia 172, 95125 Catania, Italy

⁵ Neuropharmacology Section, OASI Research Institute-IRCCS, 94018 Troina (EN), Italy

* Correspondence: andrea.magri@unict.it (A.M.); mess@unict.it (A.M.)

† These authors contributed equally to this work.

‡ These authors share the last authorship.

Received: 20 September 2020; Accepted: 20 October 2020; Published: 22 October 2020



Abstract: MPP⁺ is the active metabolite of MPTP, a molecule structurally similar to the herbicide Paraquat, known to injure the dopaminergic neurons of the nigrostriatal system in Parkinson's disease models. Within the cells, MPP⁺ accumulates in mitochondria where it inhibits complex I of the electron transport chain, resulting in ATP depletion and neuronal impairment/death. So far, MPP⁺ is recognized as a valuable tool to mimic dopaminergic degeneration in various cell lines. However, despite a large number of studies, a detailed characterization of mitochondrial respiration in neuronal cells upon MPP⁺ treatment is still missing. By using high-resolution respirometry, we deeply investigated oxygen consumption related to each respiratory state in differentiated neuroblastoma cells exposed to the neurotoxin. Our results indicated the presence of extended mitochondrial damage at the inner membrane level, supported by increased LEAK respiration, and a drastic drop in oxygen flow devoted to ADP phosphorylation in respirometry measurements. Furthermore, prior to complex I inhibition, an enhancement of complex II activity was observed, suggesting the occurrence of some compensatory effect. Overall our findings provide a mechanistic insight on the mitochondrial toxicity mediated by MPP⁺, relevant for the standardization of studies that employ this neurotoxin as a disease model.

Keywords: MPP⁺; mitochondria; Parkinson's disease; high-resolution respirometry; SH-SY5Y cells

1. Introduction

Parkinson's disease (PD) is a progressive age-related neurodegenerative disorder (ND) whose symptoms include motor system faults, such as resting tremors, rigidity and bradykinesia, and cognitive dysfunctions. These symptoms are the result of dopaminergic (DAergic) neurons loss within the *substantia nigra pars compacta* in the ventral midbrain and their terminal in the striatum, which lead consequently to striatal dopamine (DA) depletion [1]. The appearance of big spherical intraneuronal

inclusions in the brainstem and cortex, called Lewy bodies (LBs) that contain protein aggregates in which α -synuclein (α -syn) is the main structural component, is one of the most common histopathological PD features [2]. Neuroinflammation is another important hallmark of the disease. In this context, the glial compartment—astrocytes and microglia—are pivotal in PD onset and progression. Notably, depending on the signals released in the microenvironment, glia may have a dual role, either beneficial or detrimental for DAergic neurons and neural stem cells exposed to harmful stimuli [3].

As for the other NDs, the cause(s) of PD are ill-defined and currently, there is no cure to stop or reverse PD progression [4]. The transplantation of relevant cell types represents a promising therapeutic strategy. On the other hand, new cell-free approaches, such as those based on extracellular vesicles, are emerging as innovative nanotherapeutics [5,6]. In this context, the definition at the molecular level of toxicity mechanisms in PD is crucial to support the development of potential therapeutic avenues.

To date, about 90 genes were linked to familial PD onset [7]. Despite this, the etiology of the vast majority (up to 90%) of so-called “idiopathic” cases is multifactorial, recognized to arise from a combination of polygenic inheritance and environmental exposures [8,9]. Notably, a wide panel of environmental factors including neurotoxicants, commonly used as herbicides or pesticides, have long been recognized as critical risk factors for PD [10].

MPTP (1-methyl-4-phenyl-1,2,3,6-tetrahydropyridine) is a molecule structurally similar to the herbicide Paraquat and was the first neurotoxicant shown to induce in humans a profound parkinsonian syndrome [11,12]. MPTP injures, in a selective manner, the dopaminergic neurons in the nigrostriatal system, and when tested in various animal species, including non-human primates, it showed the ability to recapitulate most PD-like symptoms [13,14]: i.e., the long exposure to low MPTP doses promotes the increase of oxidative stress, α -syn fibrillization, and loss of mitochondrial functionality [15–17]. Since MPTP is a highly lipophilic compound, it rapidly crosses the blood–brain barrier and after systemic exposure, the toxin levels are already detectable in the brain within minutes. By itself, MPTP is not a toxic substance, however, once in the brain, it is metabolized to 1-methyl-4-phenyl-2,3-dihydropyridinium (MPDP) by the enzyme monoamine oxidase B (MAO-B) in non-dopaminergic cells (i.e., the astrocytes) [18]. Next, MPDP is oxidized to the active 1-methyl-4-phenylpyridinium (MPP^+) which is then released into the extracellular space, where it is taken up by the dopamine transporter (DAT) and is concentrated within the dopaminergic neurons, causing the specific loss of nigrostriatal neurons [19–21].

Within the cells, MPP^+ exerts its toxicity gathering in mitochondria, where it blocks the activity of NADH-ubiquinone oxidoreductase (complex I) of the mitochondrial electron transport system (ETS), leading to ATP depletion and reactive oxygen species (ROS) production [22–24]. Moreover, the prolonged exposure to the toxin causes a drastic inhibition of mtDNA-encoded respiratory subunits synthesis [25]. Despite these events having long been thought to be strictly related to DAergic neuronal loss in PD, another report suggests that neuronal death induced by MPP^+ is independent from complex I inhibition [26].

Neuroblastoma SH-SY5Y cells exposed to MPP^+ are one of the most used in vitro models in PD research. These cells, deriving from the SK-N-SH line, show a moderate activity of tyrosine hydroxylase (TH) and dopamine- β -hydroxylase, conferring to the line a catecholaminergic phenotype [27,28]. SH-SY5Y cells may be differentiated in order to induce a “more-neuronal” phenotype: the addition of retinoic acid (RA) to the cell culture medium, in a concentration ranging from 5 to 20 μ M, represents the best approach [29]. The differentiation time may vary from 1 to 21 days during which cells switch toward a neuronal and DAergic phenotype [29]. All these variations found in protocols for SH-SY5Y culture and differentiation possibly contribute to the different functional outcomes [30]: for instance, in specific circumstances, differentiation treatment increases susceptibility to neurotoxins exposure [31], while in others no change or even a decrease was observed [32].

The large use of this in vitro model, however, was not accompanied in the years by a detailed characterization of the mitochondrial respiration. By delivering MPP^+ to differentiated SH-SY5Y cells, in this work, we performed an in-depth analysis of oxygen flows corresponding to each respiratory

state using high-resolution respirometry (HRR). Beyond an expected slight decrease in complex I activity, an accentuated raise of the dissipative component of respiration was observed, indicating the presence of extended damage in the inner mitochondrial membrane (IMM). Moreover, we uncovered a previously unknown compensatory effect of succinate dehydrogenase (complex II) as a response to the partial block of complex I activity exerted by toxin treatment. Overall, our findings depict a more intricate mechanism of MPP⁺ mitochondrial toxicity.

2. Results

2.1. MPP⁺ Toxicity Assessment in Differentiated SH-SY5Y Cells

Neuroblastoma SH-SY5Y cells were differentiated with RA and serum reduction for nine days prior to MPP⁺ treatment, using the protocol schematized in Figure 1A. The differentiation induced morphological changes as highlighted in the brightfield and immunofluorescence images. In comparison with undifferentiated cells, RA-differentiated SH-SY5Y displayed thin and branching neurites usually resulting in a network formation (Figure 1B,C) [33]. Moreover, immunofluorescence analysis on RA-treated cells showed a decreased expression of the non-differentiated cell marker nestin (Figure 1D,F for quantification) and a higher expression of TH (Figure 1E,G for quantification), which plays a central role in DA synthesis [31]. In order to evaluate MPP⁺ mitochondrial toxicity on a DAergic model, RA-differentiated SH-SY5Y cells were exposed to increasing toxin concentration and cell viability was determined after 24 h, performing a dose–response curve. As shown in Figure 1H, cell viability varied from 89% to 64% ranging from 1 to 3 mM of MPP⁺. Based on this result, we selected the lowest MPP⁺ dose for further experiments assuming that, in this condition, any mitochondrial impairment is not ascribed to a consistent cell death but rather to the direct organelle damage caused by the neurotoxin.

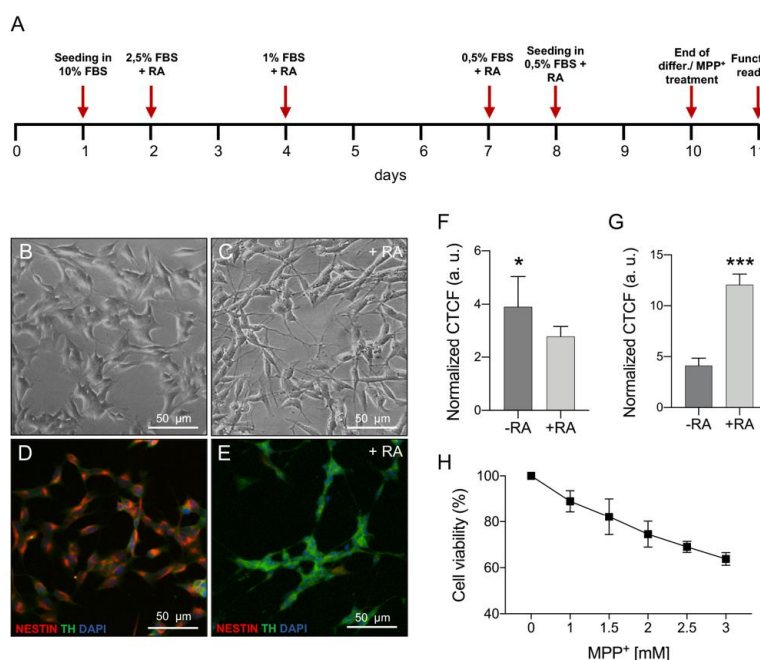


Figure 1. Phenotypic characterization of undifferentiated vs. differentiated SH-SY5Y cells and MPP⁺ dose–response curve. (A) Timeline of the differentiation protocol. (B,C) Brightfield images showing morphological differences between undifferentiated cells on day zero (B) and differentiated cells at day nine (C); RA, retinoic acid. (D,E) Immunofluorescence images showing the different expression of nestin (red) and TH (green) in undifferentiated (D) and differentiated (E) cells. (F,G) Relative quantification of nestin (F) and TH (G) in undifferentiated and differentiated cells. (H) Dose–response curve for selected MPP⁺ concentrations on differentiated SH-SY5Y cells. * $p < 0.05$ and *** $p < 0.001$.

2.2. MPP⁺ Drastically Reduces Oxygen Consumption Associated with the Main Respiratory States

The oxygen consumption profile of RA-differentiated SH-SY5Y cells was analyzed by HRR using a specific substrate-uncoupler-inhibitor titration (SUIT) protocol. This protocol allows the investigation of the main respiratory states exploiting both endogenous and externally added substrates, that reached mitochondria after cell permeabilization [34]. In Figure 2A, a representative trace of oxygen consumption of untreated cells (control) illustrates the SUIT protocol. Briefly, the physiological oxygen consumption, corresponding to ROUTINE state, was measured in intact cells. Then, endogenous substrates (including ADP) were forced to leave the cells by permeabilization of the plasma membrane. Therefore, the remaining oxygen consumption was related to the non-phosphorylating or LEAK state. The OXPHOS state, indicating the oxygen flow sustained by the mitochondrial respiratory chain, was achieved in the presence of pyruvate, malate, glutamate, succinate, and ADP, the last in saturating concentration. Next, the maximal respiratory ETS capacity was obtained at the optimal uncoupler concentration. Finally, the specific inhibition of complex I and III with rotenone and antimycin respectively, allowed for the determination of the residual respiration or ROX [34,35].

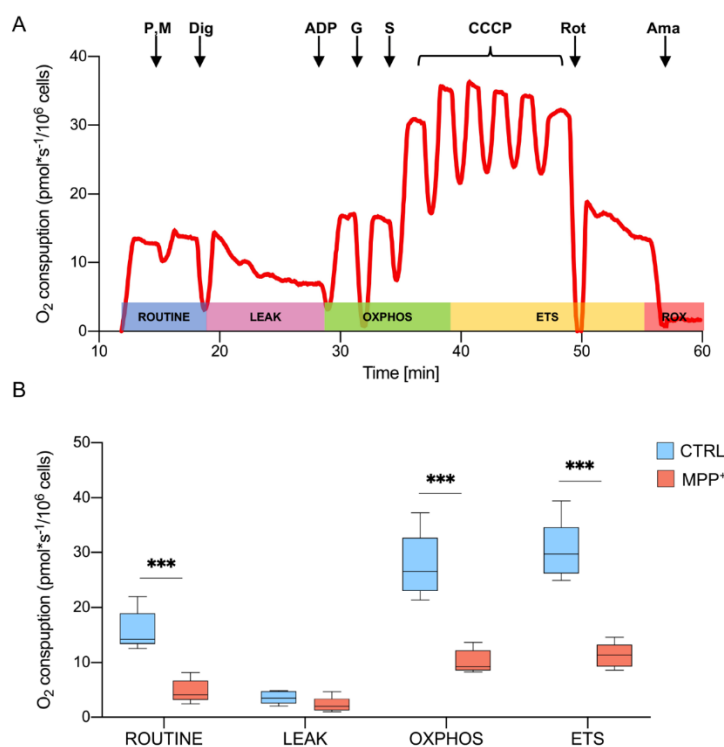


Figure 2. Oxygen consumption in differentiated SH-SY5Y cells. (A) The representative curve of mitochondrial respiratory function of untreated RA-differentiated SH-SY5Y cells assayed in MiR05 respiration medium at 37 °C. The respiratory states ROUTINE, LEAK, OXPHOS, ETS, and ROX were analyzed after the addition of specific substrates and inhibitors. P, pyruvate; M, malate; Dig, digitonin; G, glutamate; S, succinate; Rot, rotenone; Ama, antimycin. (B) Quantitative analysis of the oxygen consumption rate expressed as pmol/second per million cells of control and MPP⁺ treated cells calculated for ROUTINE, LEAK, OXPHOS, ETS. Data are shown as mean with standard deviation, with *** $p < 0.001$.

Oxygen consumption, corresponding to each respiratory state in cells treated with 1 mM MPP⁺ for 24 h, was monitored and compared to the control. The obtained values were corrected for the ROX and are reported in Figure 2B (see Supplementary Materials Table S1 for raw data). As shown, a dramatic reduction of oxygen flow was detected in ROUTINE (−70%, $p = 0.0004$, $n = 5$), OXPHOS (−70%, $p = 0.0003$, $n = 5$) and ETS (−62.7%, $p < 0.0001$, $n = 5$). Prior to a very moderate cell death,

as previously observed in the same condition, these results indicate that MPP⁺ severely affects the respiratory capacity of mitochondria.

2.3. MPP⁺ Increases the Dissipative Ratio of Oxygen Flux

The oxygen consumption depends on a sum of different factors, including obviously ETS activity but also mitochondrial mass and biogenesis, all features subjected to change upon MPP⁺ exposure. For instance, MPP⁺ increases autophagy and mitochondria degradation in SH-SY5Y cells [36,37], affects organelle morphology, mass and protein expression in RA-differentiated SH-SY5Y [25], and the mitochondrial dynamic in vivo [38].

Flux control ratios (FCRs), instead, express respiratory states independently of mitochondrial content since they are obtained by normalizing each flux for the maximum flux [34,35,39]. In Figure 3A (see also Supplementary Materials Table S2), ROUTINE, LEAK, and OXPHOS respiration are indicated as the ratio of maximal ETS capacity. As shown in the left panel, MPP⁺ treatment affected specifically the LEAK state: a significant increase (+63%) was observed in treated cells (0.19 ± 0.05 in control vs. 0.31 ± 0.09 in treated cells, $p = 0.046$, $n = 5$), while no significant differences were detected for ROUTINE and OXPHOS respiration between the samples. Since the LEAK state represents the amount of dissipative flux, this result suggests the presence of some injury at the IMM level which impinges on the proton gradient maintenance and, in turn, on ATP production [40]. As reported in the right panel, the phosphorylation-related flux is severely affected in ROUTINE (−71.9%, $p = 0.0009$, $n = 4$) and in a less dramatic manner in OXPHOS (−18.3%, $p = 0.0039$, $n = 4$). Accordingly, the respiratory reserve (RR), consisting of the extra ATP produced by oxidative phosphorylation in case of an increased energy demand [41,42] was found more than halved in MPP⁺ treated cells (Figure 3B, −55%, $p = 0.0002$, $n = 4$) (see also Supplementary Materials Table S3).

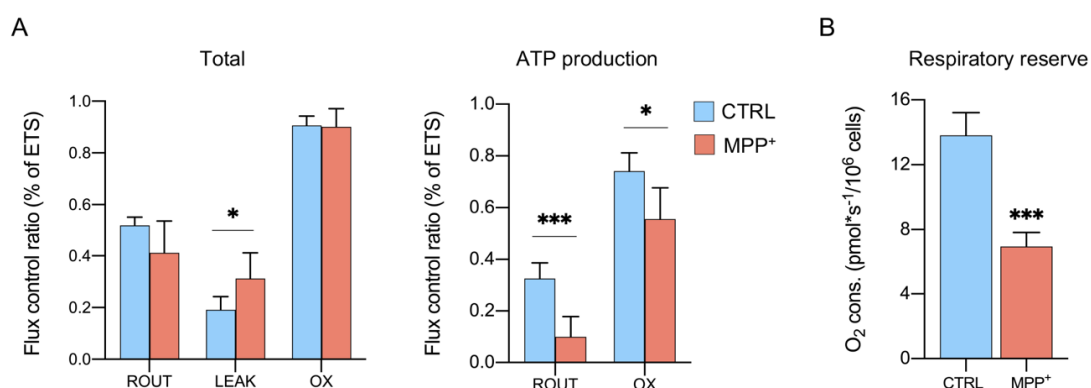


Figure 3. MPP⁺ effect on mitochondrial respiration. (A) Oxygen consumption measured in different respiratory states in the presence or not of MPP⁺, expressed as the total or ATP-related flux. Data are displayed as the flux control ratio (FCR) of the maximal ETS capacity. (B) Oxygen flux related to the respiratory reserve of cells in the presence or not of MPP⁺. All data are shown as means with standard deviation; * $p < 0.05$ and *** $p < 0.001$.

Taken together, these results suggest that neurotoxin affects IMM integrity decreasing substantially the phosphorylation processes.

2.4. MPP⁺ Reduces Coupling Efficiency in Each Respiratory State

Coupling efficiency represents another important parameter to evaluate MPP⁺ effect on mitochondrial respiration. It indicates the ratio of oxygen flux coupled to ADP phosphorylation in a specific respiratory state [35].

Figure 4A shows the coupling degree of the ROUTINE state. In control cells, about 63% of oxygen consumption is coupled with the phosphorylation process, while only 28% of the flux is coupled in

MPP⁺ treated cells (−62.9%, $p = 0.0026$, $n = 4$). Similarly, the coupling efficiency of OXPHOS and ETS was significantly decreased upon neurotoxin exposure, even if in a less dramatic manner. In particular, phosphorylation-related oxygen flux decreased from 78% (control cells) to 65% (MPP⁺ treated) in OXPHOS (−16.7%, $p = 0.0488$, $n = 4$) and from 80% to 68% in ETS (−15%, $p = 0.0426$, $n = 5$) as reported in Figure 4B,C.

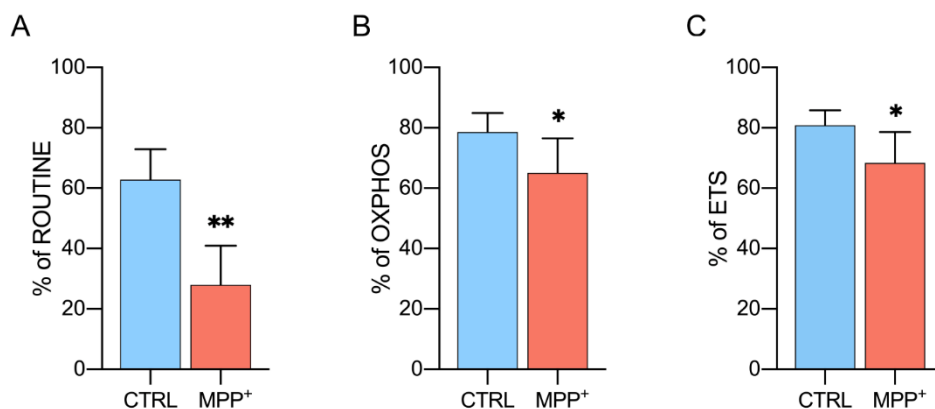


Figure 4. Coupling efficiency of different respiratory states. Rate of oxygen flux during ROUTINE (A), OXPHOS (B), and ETS (C) coupled with the ADP phosphorylation. Data are shown as the percentage of the reference state and expressed as means with standard deviation; * $p < 0.05$ and ** $p < 0.01$.

Overall, the observed reduction of coupling degree in all respiratory states confirms the strong impact of MPP⁺ on the phosphorylating flows previously described.

2.5. Activity of Complex II Is Increased Upon Complex I Inhibition

Since NADH-ubiquinone oxidoreductase is a specific target of MPP⁺ [22], HRR was used to evaluate the contribution of this specific complex to the OXPHOS respiration. This was achieved in the presence of pyruvate, malate, glutamate, and ADP but not of succinate, which conversely stimulates complex II. Figure 5A shows both the oxygen consumption level and the corresponding FCRs. As occurred for the other respiratory states, the oxygen level of OXPHOS sustained by complex I was found substantially lowered after MPP⁺ addition (−63.1%, $p = 0.0002$, $n = 5$). Similarly, a moderate decline of FCR was observed (−18%, $p = 0.0003$, $n = 4$). Accordingly, the degree of ATP-coupled respiration sustained exclusively by complex I was found significantly reduced (Figure 5B), varying from 69% of the control to 53% of MPP⁺ treated cells (−23%, $p = 0.043$, $n = 4$).

After total OXPHOS stimulation and ETS measurement, complex I was inhibited by using rotenone. With ETS calculated in the presence of all substrates (including succinate), the measurement was related to the specific contribution of complex II to ETS. Despite a general reduction of oxygen flux in the presence of MPP⁺ (−38.3%, $p = 0.0156$, $n = 5$, Table S1), Figure 5C indicates a significant increase (+81%) in the FCR compared to control ($p = 0.0084$, $n = 4$, Table S2) suggesting the existence of some compensatory mechanism(s) put in place by succinate dehydrogenase as a response to complex I inhibition.

To further investigate this aspect and clarify whether a direct link between complex II and the toxin exists, the activity of succinate dehydrogenase was specifically assayed with a distinct HRR protocol aimed to evaluate the electron flow into the Q-junction occurring independently from complex I. It is indeed known that, when complex I is stimulated (as occurred in the protocol in Figure 2A), oxaloacetate rapidly accumulates within mitochondria, acting as a potent inhibitor of complex II, already at low doses [39,43].

Figure 6A shows a representative oxygen consumption curve of untreated differentiated SH-SY5Y cells, along with the protocol used for complex II stimulation. Briefly, cells were permeabilized in the

presence of pyruvate and malate but complex I was immediately inhibited by rotenone, thus avoiding oxaloacetate accumulation. Next, the addition of ADP did not induce any response, as demonstrated by the oxygen flow curve kept around zero (Figure 6A). Then, complex II was activated by succinate. As a counter-proof, the addition of the succinate dehydrogenase inhibitor malonic acid brought the oxygen curve back to zero. The complex II-linked oxygen flows were analyzed for control and MPP⁺ treated cells, normalizing values for the convergent complex I + complex II electron supply flows [35,39]. The results are displayed in Figure 6B as substrate control factor (SCF). As reported, no significant difference in complex II activity was observed between samples (0.49 ± 0.03 in control vs. 0.52 ± 0.01 in treated cells, $p = 0.442$, $n = 3$). These data indicate that the enhancement of succinate dehydrogenase activity, previously observed in MPP⁺ treated cells (Figure 5C) likely depends on the inhibition of complex I activity, rather than from the toxin itself.

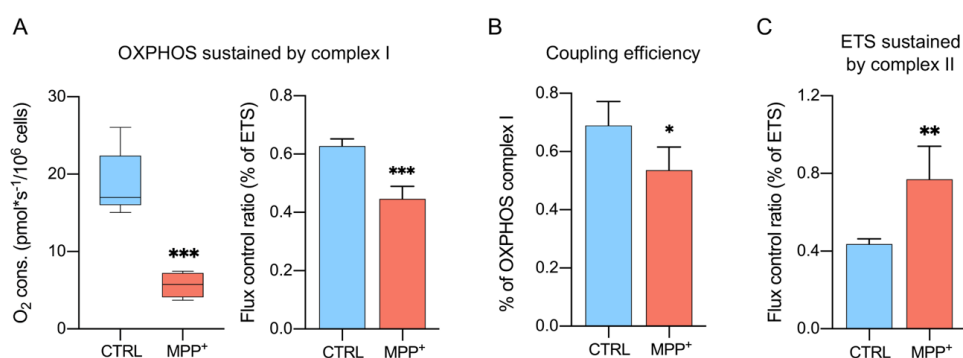


Figure 5. Specific contribution of complex I and complex II to different respiratory states. (A) Quantitative analysis of the oxygen consumption rate and the relative FCR of OXPHOS state sustained by complex I. Data were obtained by measuring OXPHOS respiration in the absence of succinate. (B) Rate of oxygen flux OXPHOS respiration sustained by complex I coupled with the ADP phosphorylation. (C) Quantitative analysis of the oxygen consumption rate and the relative FCR of ETS sustained by complex II. Data were obtained by measuring ETS after inhibition of complex I activity with rotenone. Data are shown as percentage of the reference state and expressed as means with standard deviation; * $p < 0.05$, ** $p < 0.01$, and *** $p < 0.001$.

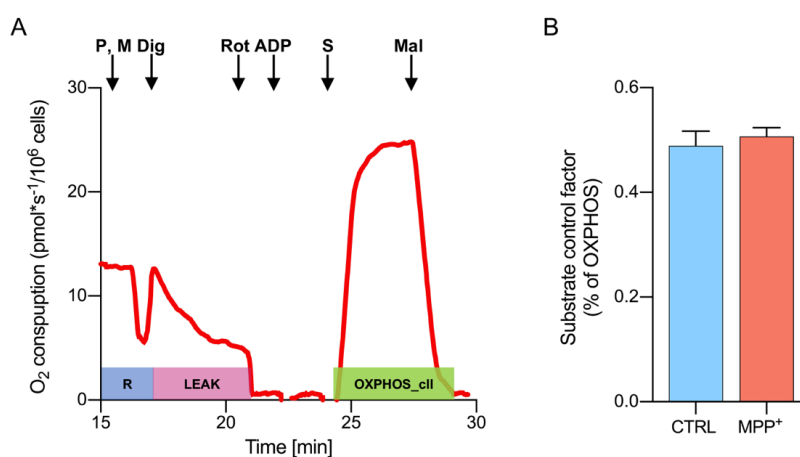


Figure 6. Activity of complex II assayed by HRR. (A) Representative curve of mitochondrial respiratory function of untreated RA-differentiated SH-SY5Y cells assayed in MiR05 respiration medium at 37 °C. The respiratory states ROUTINE, LEAK, and OXPHOS driven by complex II were obtained after the addition of specific substrates and inhibitors. P, pyruvate; M, malate; Dig, digitonin; Rot, rotenone; S, succinate; Mal, malonic acid. (B) Quantitative analysis of the oxygen consumption rate of control or MPP⁺ treated cells of OXPHOS sustained by complex II. Data are expressed as the percentage of the total OXPHOS and shown as SCRs (mean with standard deviation).

3. Discussion

Mitochondrial dysfunction is an important hallmark of PD, together with protein aggregation and oxidative stress. These features, however, are common to all NDs and are strictly interconnected. Protein aggregates interact with the cytosolic surface of mitochondria and impair metabolic exchanges with the organelle. A β oligomers in Alzheimer's disease [44,45], SOD1 mutants in Amyotrophic Lateral Sclerosis (ALS) [46–48], and α -syn in PD [49], all associate with the Voltage-Dependent Anion Channels (VDAC) isoform 1, reducing dramatically the mitochondria synthesized ATP availability [50]. VDACS are the most abundant mitochondrial porin, evolutionarily conserved from yeast to humans, playing a fundamental role for organelle physiology [51–53]. It has been recently demonstrated that a reduction of VDAC1 function affects mtDNA synthesis and, in turn, the expression of mitochondrial genes encoding for essential subunits of ETS enzymes [54]. Also, in PD models, VDAC1 favors α -syn translocation within mitochondria [55] where it is believed responsible for the impairment of complex I and IV activity [56,57]. Therefore, ETS damage represents a key event in mitochondrial dysfunction onset in PD.

Although, in a different way, the lipophilic cation MPP⁺ accumulates in mitochondria and inhibits the electron flow from complex I to coenzyme Q, contributing to ATP depletion and ROS increase [17,24,58]. For this reason, MPP⁺ is widely used for the induction of a PD-like phenotype in different in vitro models, such as the RA-differentiated SH-SY5Y cell line used herein, as a valid alternative to neuronal cells treatment with α -syn oligomers and fibrils, or to genetic models. Thus, it is crucial to understand the precise changes in mitochondrial respiration upon the MPP⁺ treatment. To this end, here we applied HRR technology highly sensitive and capable to deeply analyze oxygen consumption levels associated with each respiratory state and to ETS complexes.

We found that the treatment with 1 mM MPP⁺ on RA-differentiated cells resulted in a slight decrease of cell viability (~10%) in front of a drop of oxygen consumption associated with the main respiratory states, up to 70%. These data indicate that MPP⁺ exerts a specific mitochondrial toxicity, possibly depending on a reduction of both mitochondrial functionality and organelle mass [22,33,34]. Focusing on the specific differences within mitochondria, we performed a rigorous analysis of FCRs from which at least two intriguing results came out.

First, a significant increase of the dissipative flux, the LEAK state, was observed in cells upon MPP⁺ exposure. The LEAK state depends mainly on the IMM integrity and on proton and electron leaking. In the case of IMM injury, protons by-pass ATP synthases, promoting a decrease in ATP production, and electrons escape the ETS pathway, as they are addressed to other substrates, increasing thus ROS formation [59]. The rise in LEAK respiration indicates the presence of extensive IMM damage in MPP⁺ treated cells and this explains data in the literature about ATP depletion and oxidative stress induction [37,60]. Accordingly, oxygen flows devoted to ATP synthesis (the so-called net respiration) were found significantly decreased, drastically in ROUTINE and in a moderate manner during OXPHOS. This result was strengthened by a similar reduction in the coupling degree measured in all respiratory states.

Second, in the presence of MPP⁺ the contribution of complex I to the OXPHOS respiration was remarkably reduced, as expected. At the same time, a significant increase in complex II activity during ETS was detected, indicating a compensatory mechanism put in place by complex II as a response to the partial inhibition of NADH-ubiquinone oxidoreductase and/or to the toxin. However, the same effect was not as strong as when the complex II activity was tested in association with the complete inhibition of complex I. Nonetheless, this result is not so surprising. It is known that a reduction of complex I activity, as found in MPP⁺ treated cells, negatively impacts on malate dehydrogenase (MDH) activity, as a result of NAD⁺ to NADH redox shift, affecting in turn oxaloacetate synthesis [39]. Since oxaloacetate is a potent inhibitor/modulator of succinate dehydrogenase, especially in nervous tissues [43], it is reasonable to speculate that complex II is less subjected to oxaloacetate inhibition in MPP⁺ treated cells, due to the low activity of complex I. Notably, the main difference in the SUIT protocols applied here consists in the use of saturating rotenone concentration at different stages. Accordingly, in Figure 2A,

rotenone was added after complex I stimulation, allowing oxaloacetate to accumulate, whereas in Figure 6A complex I was directly inhibited, in order to avoid any eventual increase of oxaloacetate concentration. Therefore, the higher activity of complex II observed in the Parkinson's-like phenotype, i.e., where complex I is only partially inhibited by MPP⁺ (as in Figure 5C) and not completely with the saturating rotenone concentration (as technically required for Figure 6 experiments), likely represents a response to complex I inhibition, rather than a direct effect of the neurotoxin. Other studies showed results in agreement with those found here. For example, Calabria and colleagues have found a compensatory effect ascribed to complex II, as well as an increase in LEAK respiration in NSC-34 cells expressing the SOD1 G93A mutant, a model of ALS [61]. Notably, this was explained as a response to the decreased activity of complex I, exerted by the SOD1 mutant [61]. Taken together, these findings depict the existence of a common rescue mechanism put in place by complex II in response to different stimuli (toxins, protein aggregates) affecting complex I activity. Furthermore, these effects can be only partially ascribed to the direct complex I impairment promoted by MPP⁺. In fact, it is known that cells use LEAK respiration as a protective strategy under certain circumstances. IMM contains a group of transporters called uncoupling proteins (UCPs), whose function is to partially dissipate the mitochondrial membrane potential in the form of heat [62,63]. The inhibition of complex I increases oxygen radical formation that is counteracted by the dissipation of a part of hyperpolarized IMM potential, a process known as “mild uncoupling”, with the final aim to neutralize the ROS effect [64]. Not coincidentally, a time- and dose-dependent induction of UCP2, 4, and 5 expression in neuronal cells was observed after exposure to MPP⁺ [65]. Notably, UCP4 overexpression exerts a neuroprotective effect on SH-SY5Y upon MPP⁺ treatment and stimulates complex II activity by its direct interaction, thus promoting an ATP level increase [66–68]. A cartoon depicting our proposed model is displayed in Figure 7.

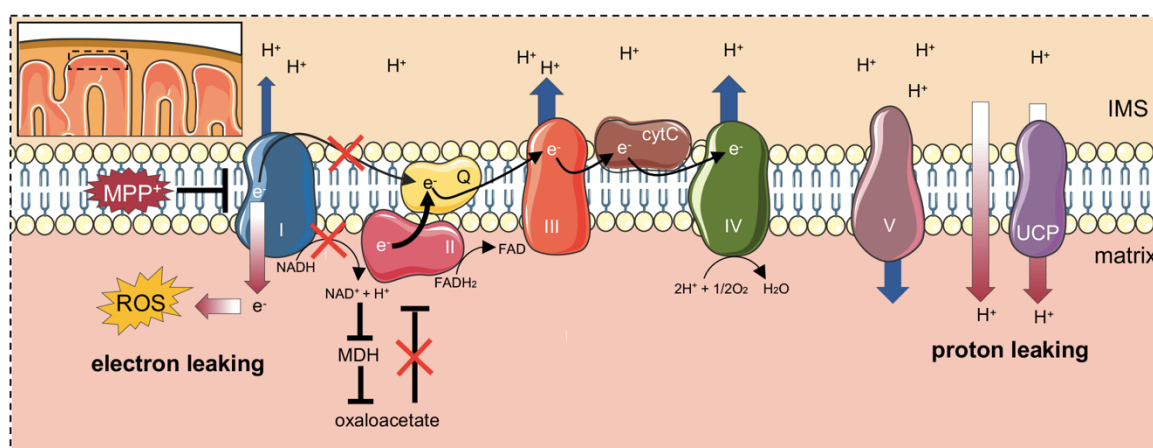


Figure 7. Proposed mechanism of MPP⁺ toxicity at the IMM level. MPP⁺ promotes the impairment of complex I activity. Electrons are then addressed towards other substrates, increasing ROS production (electron leaking). The reduced activity of complex I affects MDH activity as well as the accumulation of the Krebs cycle intermediates and complex II inhibitor oxaloacetate. In this perspective, the activity of complex II raises since it is less subjected to oxaloacetate inhibition. MPP⁺ also induces UCPs gene expression. The increased activity of UCP proteins dissipates partially the proton gradients (proton leaking), a mechanism called “mild uncoupling” and aimed to counteract ROS damage. Original figure (created with <https://smart.servier.com> tools).

In any case, although moderate, the MPP⁺ dose regimen here applied in SH-SY5Y cells was higher compared to those generally used in the highly vulnerable primary dopaminergic neurons, that are severely injured upon exposure to ≤ 50 μ M MPP⁺ or to the false neurotransmitter 6-hydroxydopamine [69]. Therefore, further studies are needed to disclose the herein described

mitochondrial effects of MPP⁺ on primary mesencephalic neuronal cultures, that will be relevant for dopaminergic neuron physiopathology.

In conclusion, by using high-resolution respirometry tools we have identified and explained the bioenergetics fault and recovery found in MPP⁺ treated cells, where mitochondria complex I was inhibited. By a precise analysis, we demonstrated the relevance of complex II in this recovery mechanism. These results are relevant to understand the mitochondria dysfunction in PD, and possibly in other NDs.

4. Materials and Methods

4.1. Cell Culture and Differentiation

The neuroblastoma cell line SH-SY5Y was purchased from ICLC (Interlab Cell Line Collection, accession number ICLC HTL95013; obtained from depositor European Collection of Authenticated Cell Cultures (ECACC)) and maintained in MEM/F12 medium supplemented with 10% fetal bovine serum, 2 mM L-glutamine and 1% penicillin/streptomycin. For cell differentiation, the protocol was adapted from [31,70]. Briefly, MEM/F12 was replaced with DMEM/F12 and 10 μ M all-trans RA (Sigma Aldrich, St. Louis, MO, USA) was added. The medium was changed every three days, lowering the serum amount to reach the final concentration of 0.5% by the seventh day. Cells were seeded at a density of 3×10^5 cells/cm² in 6, 24, or 96 well plates.

4.2. Immunofluorescence

Cells seeded on poly-L-lysine coated glass coverslips (Sigma Aldrich) were fixed after treatment with 4% paraformaldehyde and stained with primary mouse anti-nestin antibody (sc-23927, Santa Cruz, 1:50) and with rabbit anti-TH (Tyrosine hydroxylase) antibody (AB152, Sigma-Aldrich, 1:250). Nuclei were stained with DAPI (Merck, Kenilworth, NJ, USA). Donkey anti-mouse Alexa Fluor 546 or donkey anti-rabbit Alexa Fluor 488 secondary antibodies were used (Thermo Fisher, Waltham, MA, USA). Fluorescence intensity was quantified using ImageJ software. Values are indicated as normalized corrected total cell fluorescence (CTCF) expressed as arbitrary units (A.U.).

4.3. MPP⁺ Treatment and Cell Viability

Treatment with MPP⁺ (Sigma Aldrich) was performed on day 10 of the differentiation protocol. Cells seeded in 96-well black microplates were treated for 24 h with the reported final concentrations of neurotoxin. The dose–response curve was performed using the following doses: 1, 1.5, 2, 2.5, and 3 mM. Cell viability was determined using the Celltiter-Blue Cell Viability Assay (Promega, Madison, WI, USA) according to the manufacturers' recommendations. Fluorescence intensity was measured using the microplate reader Varioskan (Thermo Scientific, Waltham, MA, USA).

4.4. High-Resolution Respirometry (HRR) Analysis

Mitochondrial respiration capacity of RA-differentiated SH-SY5Y was analyzed by HRR using the two-chamber system O2k-FluoRespirometer (Oroboros Instruments, Innsbruck, Austria). Cells were harvested, counted, and resuspended in the mitochondrial respiration buffer Mir05 (Oroboros Instrument). All the experiments were performed at 37 °C under constant stirring of 750 rpm. Oxygen consumption in the various respiratory states was determined using a SUIT modified protocol [31] and the contribution of specific mitochondrial complexes to respiratory capacity was investigated.

ROUTINE respiration was measured in intact cells. Permeabilization of the plasma membrane was achieved by using the mild detergent digitonin (Sigma Aldrich) at the final concentration of 4.07 μ M. This concentration was previously determined in order to allow the access of substrates across the plasma membranes but without compromising mitochondrial membranes integrity. LEAK was measured after plasma membrane permeabilization and in the presence of previously added pyruvate and malate. A total of 5 mM pyruvate (P), 2 mM malate (M), and 10 mM glutamate (G) (Sigma Aldrich) were added

in order to activate complex I. OXPHOS capacity was recorded at saturating concentrations of 2.5 mM ADP (Sigma Aldrich) after the addition of 10 mM succinate (S) (Sigma Aldrich). The simultaneous presence of all substrates in the cuvette allowed the determination of the total OXPHOS activity. The uncoupled maximal ETS capacity was determined by titration with the uncoupler carbonyl cyanide 3-chlorophenylhydrazone, CCCP (Sigma Aldrich, 0.5 μ M) up to the complete dissipation of the proton gradient. The residual oxygen consumption (ROX) respiration was achieved by addition of rotenone and antimycin (Sigma Aldrich, 2 and 2.5 μ M respectively).

4.5. Complex II Activity Analysis

Independent activity of complex II (succinate dehydrogenase) was measured by HRR with a specific protocol modified from [39]. Permeabilized cells were treated with 2 μ M rotenone in the presence of pyruvate and malate (5 and 2 mM respectively) [39]. Activity of complex II (OXPHOS sustained by complex II) was achieved by stimulation with 10 mM succinate in the presence of saturating ADP concentrations (2.5 mM). As counter-proof, the complex II inhibitor malonic acid (Sigma Aldrich, 5 mM) was added at the end of the experiment. In parallel, a control experiment performed without rotenone was carried out to achieve the total OXPHOS respiration. This state was used as a reference for normalization.

4.6. Data Analysis

Instrumental and chemical background fluxes were opportunely calibrated as a function of oxygen concentration using DatLab software (Oroboros Instruments). Rate of oxygen consumption in the respiratory states ROUTINE, LEAK, OXPHOS, maximal ETS capacity was corrected for the ROX. The oxygen respiratory flux was expressed as pmol/s per million cells or as FCRs calculated for each state relative to the maximal uncoupled ETS capacity (used in this work as the reference state) [34,35]. Oxygen flux coupled to ATP synthesis was determined by correcting each state for the LEAK respiration and expressed as FCRs [34,35]. Coupling efficiencies were calculated by correcting each state for LEAK respiration and expressing it as a ratio of the total capacity in that specific state, as indicated [34,35]. The activity of complex II was calculated as SCFs normalizing the oxygen flux linked to complex II for the convergent flux of complex I + complex II, both measured during OXPHOS stimulation [39].

4.7. Statistical Analysis

All data are expressed as means with standard deviation. At least three independent experiments were performed. Data were statistically analyzed by t-test using GraphPad Prism software. The following values * $p < 0.05$, ** $p < 0.01$, *** $p < 0.001$ were taken as significant.

Supplementary Materials: Supplementary materials can be found at <http://www.mdpi.com/1422-0067/21/21/7809/s1>. Table S1. Oxygen flux calculated for each respiratory state corrected for the ROX respiration in untreated (CTRL) and MPP+ treated cells; Table S2. FCR calculated for each respiratory state as ETS percentage in untreated (CTRL) and MPP+ treated cells; Table S3. FCR calculated for net and coupling respiration and E-R capacity factor.

Author Contributions: Conceptualization, A.M. (Andrea Magri), N.I., and A.M. (Angela Messina); methodology, A.M. (Andrea Magri), N.I., and A.M. (Angela Messina); analysis, P.R. and A.M. (Andrea Magri); investigation, P.R., L.L., S.A.M.C., G.P., and A.M. (Andrea Magri); resources, A.M. (Andrea Magri), N.I., and A.M. (Angela Messina); data curation, P.R., L.L., S.R., and A.M. (Andrea Magri); writing—original draft preparation, A.M. (Andrea Magri); writing—review and editing, S.R., B.M., A.M. (Angela Messina), and N.I.; supervision, N.I. and A.M. (Angela Messina); project administration, A.M. (Andrea Magri), N.I., and A.M. (Angela Messina); funding acquisition, A.M. (Andrea Magri), N.I., and A.M. (Angela Messina). All authors have read and agreed to the published version of the manuscript.

Funding: This research was funded by AIM Linea 1 Salute (AIM1833071) to A. Magri, Brains2South (Fondazione con il Sud—Bando Capitale Umano ad Alta Qualificazione 2015, grant no. 2015-PDR-0219) to N.I., PIACERI (grant no. ARVEST) and Proof of Concept (grant no. PEPSLA POC 01_00054) to A. Mess.

Acknowledgments: The authors acknowledge Fondi di Ateneo 2020–2022, Università di Catania, linea Open Access. The authors acknowledge Vito De Pinto (University of Catania) for the useful discussion.

Conflicts of Interest: The authors declare no conflict of interest.

Abbreviations

PD	Parkinson's disease
ND	Neurodegenerative disease
DA	Dopamine
LBs	Lewy's bodies
MPTP	1-methyl-4-phenyl-1,2,3,6-tetrahydropyridine
MPP ⁺	1-methyl-4-phenylpyridinium ion
ETS	Electron transport system
HRR	High-resolution respirometry
RA	Retinoic acid
TH	Tyrosine hydroxylase
SUIT	Substrate-uncoupler-inhibitor titration
FCR	Flux control ratio
SCF	Substrate control factor
IMM	Inner mitochondrial membrane
OMM	Outer mitochondrial membrane

References

1. Kalia, L.V.; Lang, A.E. Parkinson's disease. *Lancet* **2015**, *386*, 896–912. [[CrossRef](#)]
2. Kim, W.S.; Kagedal, K.; Halliday, G.M. Alpha-synuclein biology in Lewy body diseases. *Alzheimer's Res. Ther.* **2014**, *6*, 73. [[CrossRef](#)] [[PubMed](#)]
3. Marchetti, B.; Leggio, L.; L'Episcopo, F.; Vivarelli, S.; Tirolo, C.; Paternò, G.; Giachino, C.; Caniglia, S.; Serapide, M.F.; Iraci, N. Glia-Derived Extracellular Vesicles in Parkinson's Disease. *J. Clin. Med.* **2020**, *9*, 1941. [[CrossRef](#)]
4. Hirsch, E.C.; Jenner, P.; Przedborski, S. Pathogenesis of Parkinson's disease. *Mov. Disord.* **2013**, *28*, 24–30. [[CrossRef](#)] [[PubMed](#)]
5. Leggio, L.; Paternò, G.; Vivarelli, S.; Episcopo, F.L.; Tirolo, C.; Raciti, G.; Pappalardo, F.; Giachino, C.; Caniglia, S.; Serapide, M.F.; et al. Extracellular Vesicles as Nanotherapeutics for Parkinson's Disease. *Biomolecules* **2020**, *10*, E1327. [[CrossRef](#)]
6. Leggio, L.; Arrabito, G.; Ferrara, V.; Vivarelli, S.; Paternò, G.; Marchetti, B.; Pignataro, B.; Iraci, N. Mastering the Tools: Natural versus Artificial Vesicles in Nanomedicine. *Adv. Healthc. Mater.* **2020**, e2000731. [[CrossRef](#)] [[PubMed](#)]
7. Bandres-Ciga, S.; Diez-Fairen, M.; Kim, J.J.; Singleton, A.B. Genetics of Parkinson's disease: An introspection of its journey towards precision medicine. *Neurobiol. Dis.* **2020**, *137*, 104782. [[CrossRef](#)]
8. Marchetti, B. Nrf2/Wnt resilience orchestrates rejuvenation of glia-neuron dialogue in Parkinson's disease. *Redox Biol.* **2020**, *36*, 101664. [[CrossRef](#)]
9. Toffoli, M.; Vieira, S.R.L.; Schapira, A.H.V. Genetic causes of PD: A pathway to disease modification. *Neuropharmacology* **2020**, *170*, 108022. [[CrossRef](#)]
10. Marchetti, B. Wnt/ β -catenin signaling pathway governs a full program for dopaminergic neuron survival, neurorescue and regeneration in the MPTP mouse model of Parkinson's disease. *Int. J. Mol. Sci.* **2018**, *19*, 3743. [[CrossRef](#)]
11. William Langston, J.; Ballard, P.; Tetrud, J.W.; Irwin, I. Chronic parkinsonism in humans due to a product of meperidine-analog synthesis. *Science* **1983**, *219*, 979–998. [[CrossRef](#)] [[PubMed](#)]
12. Langston, J.W.; Forno, L.S.; Tetrud, J.; Reeves, A.G.; Kaplan, J.A.; Karluk, D. Evidence of active nerve cell degeneration in the substantia nigra of humans years after 1-methyl-4-phenyl-1,2,3,6-tetrahydropyridine exposure. *Ann. Neurol.* **1999**, *46*, 598–605. [[CrossRef](#)]
13. Jackson-Lewis, V.; Przedborski, S. Protocol for the MPTP mouse model of Parkinson's disease. *Nat. Protoc.* **2007**, *2*, 141–151. [[CrossRef](#)]
14. Langston, J.W. The MPTP story. *J. Parkinsons. Dis.* **2017**, *7*, S11–S19. [[CrossRef](#)] [[PubMed](#)]
15. Baltazar, M.T.; Dinis-Oliveira, R.J.; de Lourdes Bastos, M.; Tsatsakis, A.M.; Duarte, J.A.; Carvalho, F. Pesticides exposure as etiological factors of Parkinson's disease and other neurodegenerative diseases-A mechanistic approach. *Toxicol. Lett.* **2014**, *230*, 85–103. [[CrossRef](#)] [[PubMed](#)]

16. Vaccari, C.; El Dib, R.; de Camargo, J.L.V. Paraquat and Parkinson's disease: A systematic review protocol according to the OHAT approach for hazard identification. *Syst. Rev.* **2017**, *6*, 98. [[CrossRef](#)] [[PubMed](#)]
17. Maiti, P.; Manna, J.; Dunbar, G.L.; Maiti, P.; Dunbar, G.L. Current understanding of the molecular mechanisms in Parkinson's disease: Targets for potential treatments. *Transl. Neurodegener.* **2017**, *6*, 28. [[CrossRef](#)]
18. Di Monte, D.A.; Wu, E.Y.; Irwin, I.; Delanney, L.E.; Langston, J.W. Biotransformation of 1-methyl-4-phenyl-1,2,3,6-tetrahydropyridine in primary cultures of mouse astrocytes. *J. Pharmacol. Exp. Ther.* **1991**, *258*, 594–600.
19. Heikkila, R.E.; Hess, A.; Duvoisin, R.C. Dopaminergic neurotoxicity of 1-methyl-4-phenyl-1,2,5,6-tetrahydropyridine in mice. *Science* **1984**, *224*, 1451–1453. [[CrossRef](#)]
20. Javitch, J.A.; D'Amato, R.J.; Strittmatter, S.M.; Snyder, S.H. Parkinsonism-inducing neurotoxin, N-methyl-4-phenyl-1,2,3,6-tetrahydropyridine: Uptake of the metabolite N-methyl-4-phenylpyridine by dopamine neurons explains selective toxicity. *Proc. Natl. Acad. Sci. USA* **1985**, *82*, 2173–2177. [[CrossRef](#)]
21. Watanabe, Y.; Himeda, T.; Araki, T. Mechanisms of MPTP toxicity and their implications for therapy of Parkinson's disease. *Med. Sci. Monit.* **2005**, *11*, RA17–RA23. [[PubMed](#)]
22. Nicklas, W.J.; Vyas, I.; Heikkila, R.E. Inhibition of NADH-linked oxidation in brain mitochondria by 1-methyl-4-phenyl-pyridine, a metabolite of the neurotoxin, 1-methyl-4-phenyl-1,2,5,6-tetrahydropyridine. *Life Sci.* **1985**, *36*, 2503–2508. [[CrossRef](#)]
23. Bose, A.; Beal, M.F. Mitochondrial dysfunction in Parkinson's disease. *J. Neurochem.* **2016**, *139*, 216–231. [[CrossRef](#)]
24. Mapa, M.S.T.; Le, V.Q.; Wimalasena, K. Characteristics of the mitochondrial and cellular uptake of MPP+, as probed by the fluorescent mimic, 4'I-MPP+. *PLoS ONE* **2018**, *13*, e0197946. [[CrossRef](#)] [[PubMed](#)]
25. Zhu, J.H.; Gusdon, A.M.; Cimen, H.; Van Houten, B.; Koc, E.; Chu, C.T. Impaired mitochondrial biogenesis contributes to depletion of functional mitochondria in chronic MPP+ toxicity: Dual roles for ERK1/2. *Cell Death Dis.* **2012**, *3*, e312. [[CrossRef](#)]
26. Choi, W.S.; Kruse, S.E.; Palmiter, R.D.; Xia, Z. Mitochondrial complex I inhibition is not required for dopaminergic neuron death induced by rotenone, MPP+, or paraquat. *Proc. Natl. Acad. Sci. USA* **2008**, *105*, 15136–15141. [[CrossRef](#)]
27. Biedler, J.L.; Schachner, M. Multiple Neurotransmitter Synthesis by Human Neuroblastoma Cell Lines and Clones. *Cancer Res.* **1978**, *38*, 3751–3757.
28. Ross, R.A.; Biedler, J.L. Presence and Regulation of Tyrosinase Activity in Human Neuroblastoma Cell Variants in Vitro. *Cancer Res.* **1985**, *45*, 1628–1632.
29. Pählman, S.; Ruusala, A.I.; Abrahamsson, L.; Mattsson, M.E.K.; Esscher, T. Retinoic acid-induced differentiation of cultured human neuroblastoma cells: A comparison with phorbol ester-induced differentiation. *Cell. Differ.* **1984**, *14*, 135–144. [[CrossRef](#)]
30. Xicoy, H.; Wieringa, B.; Martens, G.J.M. The SH-SY5Y cell line in Parkinson's disease research: A systematic review. *Mol. Neurodegener.* **2017**, *12*, 10. [[CrossRef](#)]
31. Lopes, F.M.; Schröder, R.; Júnior, M.L.C. da F.; Zanutto-Filho, A.; Müller, C.B.; Pires, A.S.; Meurer, R.T.; Colpo, G.D.; Gelain, D.P.; Kapczinski, F.; et al. Comparison between proliferative and neuron-like SH-SY5Y cells as an in vitro model for Parkinson disease studies. *Brain Res.* **2010**, *1337*, 85–94. [[CrossRef](#)]
32. Cheung, Y.T.; Lau, W.K.W.; Yu, M.S.; Lai, C.S.W.; Yeung, S.C.; So, K.F.; Chang, R.C.C. Effects of all-trans-retinoic acid on human SH-SY5Y neuroblastoma as in vitro model in neurotoxicity research. *Neurotoxicology* **2009**, *30*, 127–135. [[CrossRef](#)]
33. Teppola, H.; Sarkanen, J.R.; Jalonen, T.O.; Linne, M.L. Morphological Differentiation Towards Neuronal Phenotype of SH-SY5Y Neuroblastoma Cells by Estradiol, Retinoic Acid and Cholesterol. *Neurochem. Res.* **2016**, *41*, 731–747. [[CrossRef](#)]
34. Pesta, D.; Gnaiger, E. High-resolution respirometry: OXPHOS protocols for human cells and permeabilized fibers from small biopsies of human muscle. *Methods Mol. Biol.* **2012**, *810*, 25–58.
35. Gnaiger, E.; MitoEAGLE Task Group. Mitochondrial physiology. *Bioenerg. Commun.* **2020**, *1*. [[CrossRef](#)]
36. Zhu, J.H.; Horbinski, C.; Guo, F.; Watkins, S.; Uchiyama, Y.; Chu, C.T. Regulation of autophagy by extracellular signal-regulated protein kinases during 1-methyl-4-phenylpyridinium-induced cell death. *Am. J. Pathol.* **2007**, *170*, 75–86. [[CrossRef](#)]
37. Zilocchi, M.; Finzi, G.; Lualdi, M.; Sessa, F.; Fasano, M.; Alberio, T. Mitochondrial alterations in Parkinson's disease human samples and cellular models. *Neurochem. Int.* **2018**, *118*, 61–72. [[CrossRef](#)]

38. Dukes, A.A.; Bai, Q.; Van Laar, V.S.; Zhou, Y.; Ilin, V.; David, C.N.; Agim, Z.S.; Bonkowsky, J.L.; Cannon, J.R.; Watkins, S.C.; et al. Live imaging of mitochondrial dynamics in CNS dopaminergic neurons in vivo demonstrates early reversal of mitochondrial transport following MPP+ exposure. *Neurobiol. Dis.* **2016**, *95*, 238–249. [[CrossRef](#)] [[PubMed](#)]
39. Gnaiger, E. Capacity of oxidative phosphorylation in human skeletal muscle. New perspectives of mitochondrial physiology. *Int. J. Biochem. Cell Biol.* **2009**, *41*, 1837–1845. [[CrossRef](#)] [[PubMed](#)]
40. Djafarzadeh, S.; Jakob, S.M. High-resolution respirometry to assess mitochondrial function in permeabilized and intact cells. *J. Vis. Exp.* **2017**, *120*, 54985. [[CrossRef](#)]
41. Pflieger, J.; He, M.; Abdellatif, M. Mitochondrial complex II is a source of the reserve respiratory capacity that is regulated by metabolic sensors and promotes cell survival. *Cell Death Dis.* **2015**, *6*, e1835. [[CrossRef](#)] [[PubMed](#)]
42. Evinova, A.; Cizmarova, B.; Hatokova, Z.; Racay, P. High-Resolution Respirometry in Assessment of Mitochondrial Function in Neuroblastoma SH-SY5Y Intact Cells. *J. Membr. Biol.* **2020**, *253*, 12–136.
43. Stepanova, A.; Shurubor, Y.; Valsecchi, F.; Manfredi, G.; Galkin, A. Differential susceptibility of mitochondrial complex II to inhibition by oxaloacetate in brain and heart. *Biochim. Biophys. Acta Bioenerg.* **2016**, *1857*, 1561–1568. [[CrossRef](#)] [[PubMed](#)]
44. Manczak, M.; Reddy, P.H. Abnormal interaction of VDAC1 with amyloid beta and phosphorylated tau causes mitochondrial dysfunction in Alzheimer's disease. *Hum. Mol. Genet.* **2012**, *21*, 5131–5146. [[CrossRef](#)]
45. Smilansky, A.; Dangoor, L.; Nakdimon, I.; Ben-Hail, D.; Mizrahi, D.; Shoshan-Barmatz, V. The voltage-dependent anion channel 1 mediates amyloid β toxicity and represents a potential target for Alzheimer disease therapy. *J. Biol. Chem.* **2015**, *290*, 30670–30683. [[CrossRef](#)]
46. Israelson, A.; Arbel, N.; Da Cruz, S.; Ilieva, H.; Yamanaka, K.; Shoshan-Barmatz, V.; Cleveland, D.W. Misfolded mutant SOD1 directly inhibits VDAC1 conductance in a mouse model of inherited ALS. *Neuron* **2010**, *67*, 575–587. [[CrossRef](#)] [[PubMed](#)]
47. Magri, A.; Belfiore, R.; Reina, S.; Tomasello, M.F.; Di Rosa, M.C.; Guarino, F.; Leggio, L.; De Pinto, V.; Messina, A. Hexokinase i N-terminal based peptide prevents the VDAC1-SOD1 G93A interaction and re-establishes ALS cell viability. *Sci. Rep.* **2016**, *6*, 34802. [[CrossRef](#)]
48. Shteinfein-Kuzmine, A.; Argueti, S.; Gupta, R.; Shvil, N.; Abu-Hamad, S.; Gropper, Y.; Hoeber, J.; Magri, A.; Messina, A.; Kozlova, E.N.; et al. A VDAC1-Derived N-Terminal Peptide Inhibits Mutant SOD1-VDAC1 Interactions and Toxicity in the SOD1 Model of ALS. *Front. Cell. Neurosci.* **2019**, *13*, 346. [[CrossRef](#)] [[PubMed](#)]
49. Rostovtseva, T.K.; Gurnev, P.A.; Protchenko, O.; Hoogerheide, D.P.; Yap, T.L.; Philpott, C.C.; Lee, J.C.; Bezrukov, S.M. α -synuclein shows high affinity interaction with voltage-dependent anion channel, suggesting mechanisms of mitochondrial regulation and toxicity in Parkinson disease. *J. Biol. Chem.* **2015**, *290*, 18467–18477. [[CrossRef](#)]
50. Magri, A.; Messina, A. Interactions of VDAC with proteins involved in neurodegenerative aggregation: An opportunity for advancement on therapeutic molecules. *Curr. Med. Chem.* **2017**, *24*, 4470–4487. [[CrossRef](#)]
51. Leggio, L.; Guarino, F.; Magri, A.; Accardi-Gheit, R.; Reina, S.; Specchia, V.; Damiano, F.; Tomasello, M.F.; Tommasino, M.; Messina, A. Mechanism of translation control of the alternative *Drosophila melanogaster* Voltage Dependent Anion-selective Channel 1 mRNAs. *Sci. Rep.* **2018**, *8*, 5347. [[CrossRef](#)] [[PubMed](#)]
52. Magri, A.; Di Rosa, M.C.; Tomasello, M.F.; Guarino, F.; Reina, S.; Messina, A.; De Pinto, V. Overexpression of human SOD1 in VDAC1-less yeast restores mitochondrial functionality modulating beta-barrel outer membrane protein genes. *Biochim. Biophys. Acta Bioenerg.* **2016**, *1857*, 789–798. [[CrossRef](#)] [[PubMed](#)]
53. Messina, A.; Reina, S.; Guarino, F.; De Pinto, V. VDAC isoforms in mammals. *Biochim. Biophys. Acta Biomembr.* **2012**, *1818*, 1466–1476. [[CrossRef](#)] [[PubMed](#)]
54. Magri, A.; Di Rosa, M.C.; Orlandi, I.; Guarino, F.; Reina, S.; Guarnaccia, M.; Morello, G.; Spampinato, A.; Cavallaro, S.; Messina, A.; et al. Deletion of Voltage-Dependent Anion Channel 1 knocks mitochondria down triggering metabolic rewiring in yeast. *Cell. Mol. Life Sci.* **2020**, *77*, 3195–3213. [[CrossRef](#)] [[PubMed](#)]
55. Hoogerheide, D.P.; Gurnev, P.A.; Rostovtseva, T.K.; Bezrukov, S.M. Mechanism of α -synuclein translocation through a VDAC nanopore revealed by energy landscape modeling of escape time distributions. *Nanoscale* **2017**, *9*, 183–192. [[CrossRef](#)]
56. Devi, L.; Raghavendran, V.; Prabhu, B.M.; Avadhani, N.G.; Anandatheerthavarada, H.K. Mitochondrial import and accumulation of α -synuclein impair complex I in human dopaminergic neuronal cultures and Parkinson disease brain. *J. Biol. Chem.* **2008**, *283*, 9089–9100. [[CrossRef](#)]

57. Elkon, H.; Don, J.; Melamed, E.; Ziv, I.; Shirvan, A.; Offen, D. Mutant and wild-type α -synuclein interact with mitochondrial cytochrome C oxidase. *J. Mol. Neurosci.* **2002**, *18*, 229–238. [[CrossRef](#)]
58. Fritz, R.R.; Abell, C.W.; Patel, N.T.; Gessner, W.; Brossi, A. Metabolism of the neurotoxin in MPTP by human liver monoamine oxidase B. *FEBS Lett.* **1985**, *186*, 224–228. [[CrossRef](#)]
59. Jastroch, M.; Divakaruni, A.S.; Mookerjee, S.; Treberg, J.R.; Brand, M.D. Mitochondrial proton and electron leaks. *Essays Biochem.* **2010**, *47*, 53–67.
60. Ramonet, D.; Perier, C.; Recasens, A.; Dehay, B.; Bové, J.; Costa, V.; Scorrano, L.; Vila, M. Optic atrophy 1 mediates mitochondria remodeling and dopaminergic neurodegeneration linked to complex I deficiency. *Cell Death Differ.* **2013**, *20*, 77–85. [[CrossRef](#)]
61. Calabria, E.; Scambi, I.; Bonafede, R.; Schiaffino, L.; Peroni, D.; Potrich, V.; Capelli, C.; Schena, F.; Mariotti, R. Ascs-exosomes recover coupling efficiency and mitochondrial membrane potential in an in vitro model of ALS. *Front. Neurosci.* **2019**, *13*, 1070. [[CrossRef](#)]
62. Ricquier, D.; Bouillaud, F. The uncoupling protein homologues: UCP1, UCP2, UCP3, StUCP and AtUCP. *Biochem. J.* **2000**, *345*, 161–179. [[CrossRef](#)] [[PubMed](#)]
63. Porter, R.K. Mitochondrial proton leak: A role for uncoupling proteins 2 and 3? *Biochim. Biophys. Acta Bioenerg.* **2001**, *1504*, 120–127. [[CrossRef](#)]
64. Cannon, B.; Shabalina, I.G.; Kramarova, T.V.; Petrovic, N.; Nedergaard, J. Uncoupling proteins: A role in protection against reactive oxygen species-or not? *Biochim. Biophys. Acta Bioenerg.* **2006**, *1757*, 449–458. [[CrossRef](#)] [[PubMed](#)]
65. Ho, P.W.L.; Chan, D.Y.L.; Kwok, K.H.H.; Chu, A.C.Y.; Ho, J.W.M.; Kung, M.H.W.; Ramsden, D.B.; Ho, S.L. Methyl-4-phenylpyridinium ion modulates expression of mitochondrial uncoupling proteins 2, 4, and 5 in catecholaminergic (SK-N-SH) cells. *J. Neurosci. Res.* **2005**, *81*, 261–268. [[CrossRef](#)]
66. Chu, A.C.Y.; Ho, P.W.L.; Kwok, K.H.H.; Ho, J.W.M.; Chan, K.H.; Liu, H.F.; Kung, M.H.W.; Ramsden, D.B.; Ho, S.L. Mitochondrial UCP4 attenuates MPP⁺- and dopamine-induced oxidative stress, mitochondrial depolarization, and ATP deficiency in neurons and is interlinked with UCP2 expression. *Free Radic. Biol. Med.* **2009**, *46*, 810–820. [[CrossRef](#)] [[PubMed](#)]
67. Kwok, K.H.H.; Ho, P.W.L.; Chu, A.C.Y.; Ho, J.W.M.; Liu, H.F.; Yiu, D.C.W.; Chan, K.H.; Kung, M.H.W.; Ramsden, D.B.; Ho, S.L. Mitochondrial UCP5 is neuroprotective by preserving mitochondrial membrane potential, ATP levels, and reducing oxidative stress in MPP⁺ and dopamine toxicity. *Free Radic. Biol. Med.* **2010**, *49*, 1023–1035. [[CrossRef](#)] [[PubMed](#)]
68. Ho, P.W.L.; Ho, J.W.M.; Tse, H.M.; So, D.H.F.; Yiu, D.C.W.; Liu, H.F.; Chan, K.H.; Kung, M.H.W.; Ramsden, D.B.; Ho, S.L. Uncoupling protein-4 (UCP4) increases ATP supply by interacting with mitochondrial complex II in neuroblastoma cells. *PLoS ONE* **2012**, *7*, e32810. [[CrossRef](#)]
69. L'Episcopo, F.; Serapide, M.F.; Tirolo, C.; Testa, N.; Caniglia, S.; Morale, M.C.; Pluchino, S.; Marchetti, B. A Wnt1 regulated Frizzled-1/ β -catenin signaling pathway as a candidate regulatory circuit controlling mesencephalic dopaminergic neuron-astrocyte crosstalk: Therapeutic relevance for neuron survival and neuroprotection. *Mol. Neurodegener.* **2011**, *6*, 49. [[CrossRef](#)]
70. Shipley, M.M.; Mangold, C.A.; Szpara, M.L. Differentiation of the SH-SY5Y human neuroblastoma cell line. *J. Vis. Exp.* **2016**, *108*, 53193. [[CrossRef](#)]

Publisher's Note: MDPI stays neutral with regard to jurisdictional claims in published maps and institutional affiliations.



© 2020 by the authors. Licensee MDPI, Basel, Switzerland. This article is an open access article distributed under the terms and conditions of the Creative Commons Attribution (CC BY) license (<http://creativecommons.org/licenses/by/4.0/>).

Article 4.

Antioxidants

Post-translational modification analysis of VDAC1 in ALS-SOD1 model cells reveals specific asparagine and glutamine deamidation

Maria Gaetana Giovanna Pittalà¹, Simona Reina ^{1,4}, Salvatore Antonio Maria Cubisino¹, Annamaria Cucina², Beatrice Formicola³, Vincenzo Cunsolo², Salvatore Foti², Rosaria Saletti², Angela Messina^{1,4}

¹ Department of Biological, Geological and Environmental Sciences, Molecular Biology Laboratory, University of Catania, Via S.Sofia 64, 95123 Catania, Italy

² Department of Chemical Sciences, Organic Mass Spectrometry Laboratory, University of Catania, Via S.Sofia 64, 95123 Catania, Italy

³ School of Medicine & Surgery, Nanomedicine Center NANOMIB, University of Milano-Bicocca, Monza, 20900, Italy

⁴ we.MitoBiotech.srl, c.so Italia 172, 95129 Catania, Italy



Article

Post-Translational Modification Analysis of VDAC1 in ALS-SOD1 Model Cells Reveals Specific Asparagine and Glutamine Deamidation

Maria Gaetana Giovanna Pittalà ¹, Simona Reina ^{1,2}, Salvatore Antonio Maria Cubisino ¹, Annamaria Cucina ³ , Beatrice Formicola ⁴, Vincenzo Cunsolo ³ , Salvatore Foti ³ , Rosaria Saletti ^{3,*} and Angela Messina ^{1,2,*}

¹ Department of Biological, Geological and Environmental Sciences, Molecular Biology Laboratory, University of Catania, Via S. Sofia 64, 95123 Catania, Italy; marinella.pitt@virgilio.it (M.G.G.P.); simona.reina@unict.it (S.R.); salvatore.cubisino@phd.unict.it (S.A.M.C.)

² we.MitoBiotech.srl, c.so Italia 172, 95129 Catania, Italy

³ Department of Chemical Sciences, Organic Mass Spectrometry Laboratory, University of Catania, Via S. Sofia 64, 95123 Catania, Italy; annamaria.cucina@phd.unict.it (A.C.); vcunsolo@unict.it (V.C.); sfoti@unict.it (S.F.)

⁴ School of Medicine & Surgery, Nanomedicine Center NANOMIB, University of Milano-Bicocca, 20900 Monza, Italy; b.formicola@campus.unimib.it

* Correspondence: rsaletti@unict.it (R.S.); mess@unict.it (A.M.);
Tel.: +39-095-7385026 (R.S.); +39-095-7384231 (A.M.)

Received: 28 September 2020; Accepted: 28 November 2020; Published: 2 December 2020



Abstract: Mitochondria from affected tissues of amyotrophic lateral sclerosis (ALS) patients show morphological and biochemical abnormalities. Mitochondrial dysfunction causes oxidative damage and the accumulation of ROS, and represents one of the major triggers of selective death of motor neurons in ALS. We aimed to assess whether oxidative stress in ALS induces post-translational modifications (PTMs) in VDAC1, the main protein of the outer mitochondrial membrane and known to interact with SOD1 mutants related to ALS. In this work, specific PTMs of the VDAC1 protein purified by hydroxyapatite from mitochondria of a NSC34 cell line expressing human SOD1G93A, a suitable ALS motor neuron model, were analyzed by tryptic and chymotryptic proteolysis and UHPLC/High-Resolution ESI-MS/MS. We found selective deamidations of asparagine and glutamine of VDAC1 in ALS-related NSC34-SOD1G93A cells but not in NSC34-SOD1WT or NSC34 cells. In addition, we identified differences in the over-oxidation of methionine and cysteines between VDAC1 purified from ALS model or non-ALS NSC34 cells. The specific range of PTMs identified exclusively in VDAC1 from NSC34-SOD1G93A cells but not from NSC34 control lines, suggests the appearance of important changes to the structure of the VDAC1 channel and therefore to the bioenergetics metabolism of ALS motor neurons. Data are available via ProteomeXchange with identifier <PXD022598>.

Keywords: deamidation; amyotrophic lateral sclerosis; voltage dependent anion channel; post-translational modifications; mitochondria; ROS; mass spectrometry analysis; Orbitrap fusion tribrid; neurodegeneration; SOD1

1. Introduction

Amyotrophic lateral sclerosis (ALS) is a devastating neurodegenerative disease caused by progressive degeneration of the motor neurons in the brainstem and spinal cord that leads patients to death by respiratory paralysis within 2–5 years of onset [1]. While about 10% of ALS cases are

associated with genetic defects, 90% of ALS cases are sporadic. Several genetic risk factors are also implicated in sporadic ALS (sALS) [2].

Oxidative stress-induced damage is a major mechanism in the ALS pathophysiology and can result from an imbalance between free radical production and degradation. Free radicals, such as reactive oxygen species (ROS) and reactive nitrogen species (RNS), are generated from various cell sources. Mitochondria are the main source of ROS, while a smaller proportion of ROS and RNS is produced by non-mitochondrial oxidative enzymes [3]. Interestingly, non-mitochondrial ROS usually function as signaling molecules and are seldom involved in pathophysiological processes [4]. However, ROS produced through Nox enzymes have been implicated in ALS pathogenesis [5]. Free radicals cause oxidative damage to lipids, proteins, and nucleic acids contributing thus to trigger or amplify the pathological mechanisms related to ALS [6]. Therefore, mitochondrial dysfunction is both the main contributor to oxidative stress and its main consequence.

The Cu/Zn superoxide dismutase (SOD1) associates with about 20% of familial ALS (fALS) cases and over 180 mutant forms of enzymatically active or inactive SOD1 have been characterized in humans (<http://alsod.iop.kcl.ac.uk>) [7]. In affected tissues, toxic effects of SOD1 mutants are related to the formation of misfolded SOD1 aggregates upon the mitochondrial surface, leading to morphological degeneration and malfunctioning of the organelle [8,9].

In the spinal cord from ALS patients, voltage dependent anion selective channel isoform 1 (VDAC1) represents the docking site on the outer mitochondrial membrane for ALS-linked SOD1 mutants [10,11].

VDAC1 is the most abundant protein of the outer mitochondrial membrane and is evolutionary preserved from yeast to man [12–14]. As a voltage-dependent anionic channel, it carries ATP, ions, and other small metabolites. It is responsible for metabolic exchanges to and from the mitochondrion, thus controlling cell metabolism and mitochondrial function. VDAC1 also acts as a scaffold for important molecules, such as hexokinase and proteins from the Bcl2 family which regulate metabolism and apoptosis. Apoptotic stimuli also induce VDAC1 oligomerization that leads to mitochondrial permeability and apoptosis [15]. Therefore, due to its important role, dysfunction of the VDAC channel can lead to various diseases, such as cancer and neurodegenerative diseases like Parkinson's disease, Alzheimer's disease, and ALS [16,17].

In ALS, the VDAC1-SOD1 mutant interaction strongly affects the functional properties of VDAC1 channel suggesting a role in the impairment of the bioenergetics metabolism and oxidative stress of ALS motor neurons [10]. It is also known that low levels of hexokinase I (HK1) in the spinal cord make motor neurons more susceptible to ALS in comparison to other tissues. In particular, this reduction of HK1 levels increases the availability of VDAC1 to interact with mutant SOD1, thereby facilitating mitochondrial dysfunction and cell death [10].

Protein-protein interactions (PPI) at the surface of mitochondria are an emerging novelty nowadays, but still few information is available. The mitochondria-associated proteins interact with the organelle orchestrating its response in order to maintain proper cellular function. In fact, alterations in selective PPIs at the mitochondrial surface are the result of pathological associations that drive the progression of neurodegenerative disorders [18]. Protein PTMs guide the cellular response to specific insults, distinguishing toxic PTMs (e.g., oxidations) and protective PTMs (e.g., cysteinylolation); high levels of toxic changes or a varied set of PTMs are related to disease conditions.

Under physiological conditions, VDAC1 presents several post-translational changes (phosphorylation [19], acetylation [20], tyrosine nitration [21] and oxidation of cysteine and methionine) whose role in protein activity has only been partially clarified [22–24]. Moreover, VDAC1, like other mitochondrial proteins in the outer membrane, is a target for Parkin-mediated ubiquitination [25]. Ubiquitination, like phosphorylation and acetylation, is a reversible modification that allows the selection of dysfunctional mitochondria for clearance and regulates quality control pathways.

Recent advances in the study of molecular markers of ageing, hypoxia, and age-related neurodegenerative diseases have highlighted the important role of protein deamidation. As of today, no one studied possible deamidation of the VDAC channel.

The abnormal accumulation of misfolded proteins and dysfunctional mitochondria is a distinctive feature of ALS and many neurodegenerative diseases [26]. In addition, mitochondrial proteins undergo further PTMs in response to both physiological and pathological cell signals. It is known that PTMs influence the activity of the VDAC channel and thus the mitochondrial function and its fate [19,27]. For example, cysteines undergo reversible and irreversible redox reactions by ROS and are important for the stabilization of the VDAC structure [22,28].

In this work, by using a high-resolution mass spectrometry analysis we identified non-reversible post-translational changes in VDAC1 that may be involved in its specific interaction with ALS-related SOD1 mutants. Our findings allow us to hypothesize its further role in the disease and as a marker for irreparably damaged mitochondria.

2. Materials and Methods

2.1. Chemicals

All chemicals were of the highest purity commercially available and were used without further purification. Ammonium bicarbonate, calcium chloride, phosphate-buffered saline (PBS), Tris-HCl, Triton X-100, sucrose, mannitol, ethylene glycol tetraacetic acid (EGTA), ethylenediaminetetraacetic acid (EDTA), formic acid (FA), dithiothreitol (DTT) and iodoacetamide (IAA) were obtained from Sigma-Aldrich (Milan, Italy). High-glucose DMEM (Dulbecco's Modified Eagle Medium) and fetal bovine serum (FBS) were obtained from Gibco-Thermo Fisher Scientific (Milan, Italy). DMEM F12 and tetracycline-free FBS were obtained from Euro Clone. G418 and Doxycycline were obtained from Carlo Erba and Sigma-Aldrich (Milan, Italy), respectively. Trypsin/EDTA (for cell cultures) and penicillin-streptomycin (P/S) were purchased from Invitrogen. All the other stock solutions for cell culture were from Euroclone (Milan, Italy). Modified porcine trypsin and chymotrypsin were purchased from Promega (Milan, Italy). Water and acetonitrile (OPTIMA[®] LC/MS grade) for LC/MS analyses were provided from Fisher Scientific (Milan, Italy).

2.2. NSC34 Cell Lines

The mouse motor neuron-like NSC34 cell line were from CELLutions Biosystem Inc., Burlington, ON, Canada) and NSC34 cells stably transfected with pTet-ON plasmid (Clontech, Mountain View, CA, USA) harboring sequences encoding SOD1 wt (NSC34-SOD1WT) or G93A (NSC34-SOD1G93A) were used as non-ALS motor neuron line and ALS motor neuron line, respectively [9]. Cell maintenance, induction, and transfection condition were as in Magri et al., 2016 [10].

2.3. Extraction of Mitochondrial Proteins from NSC34 Cells under Reducing Condition

NSC34, NSC34-SOD1WT and NSC34-SOD1G93A cell lines were cultured in monolayer (75 cm² tissue culture flask) until 75% confluence. For mitochondria preparation about 80 million cells/culture were used; NSC34 cells were harvested by trypsin with 0.25% EDTA and washed with PBS three times before disruption. Every PBS wash was eliminated by centrifugation at 1500× g for 5 min at 4 °C. Purification of mitochondria from NSC34-SOD1WT and NSC34-SOD1G93A cell lines was carried out 48 h after doxycycline induction of human SOD1 protein expression.

The total cell pellet obtained was resuspended in 1 mL of hypotonic buffer (200 mM mannitol, 70 mM sucrose, 10 mM HEPES pH 7.5, 1 mM EGTA pH 8.0). The cells were incubated in ice for 10 min and then lysed. The lysate obtained was centrifuged (700× g for 25 min at 4 °C) to eliminate the non-lysed cells and the nuclei. To increase the yield, after recovering the supernatant, the pellet containing the mitochondria was suspended in hypotonic buffer. Again, the suspension was first lysed and then centrifuged (700× g for 25 min at 4 °C).

The resulting supernatants from the two centrifugations were combined and centrifuged at higher speed (7000× g for 15 min at 4 °C). The supernatant, containing the cytoplasmic fraction, was removed while the pellet was washed with hypotonic buffer.

The suspension was then centrifuged at high speed (7000× *g* for 15 min at 4 °C) and at the end, after removing the supernatant, the pellet containing the mitochondria, was resuspended in 500 µL of hypotonic buffer and stored at 4 °C.

The total yield (in 500 µL of hypotonic buffer) was determined by Bicinchoninic Acid Protein Assay (BCA method) resulting in 0.474 mg, 0.524 mg, 0.628 mg for NSC34, NSC34-SOD1WT, and NSC34-SOD1G93A, respectively. The hypotonic buffer was then removed by centrifugation (10,000× *g* for 20 min at 4 °C). Reduction/alkylation was carried on before VDACs purification to avoid any possible artifact due to air exposure. 0.237 mg, 0.262 mg and 0.314 mg of protein from intact mitochondria purified from NSC34, NSC34-SOD1WT and NSC34-SOD1G93A, respectively, were incubated for 3 h at 4 °C in 1 mL of Tris-HCl 10 mM (pH 8.3) containing 0.00474 mmol, 0.00524 mmol and 0.00628 mmol of DTT for each cell line: this corresponds to an excess of 50:1 (mol/mol) over the estimated protein thiol groups. The temperature was kept at 4 °C to avoid possible reduction of methionine sulfoxide to methionine by methionine sulfoxide reductase. The alkylation was performed by the addition of IAA at the 2:1 M ratio over DTT for 1 h in the dark at 25 °C. Mixture was centrifuged for 30 min at 10,000× *g* at 4 °C and the pellet was stored at −80 °C until further use.

Reduced and alkylated intact mitochondria were lysed in buffer A (10 mM TrisHCl, 1 mM EDTA, 3% Triton X-100, pH 7.0) in ratio 5:1 (mitochondria mg/buffer volume mL) [29] for 30 min on ice and centrifuged at 17,400× *g* for 30 min at 4 °C. The supernatant containing mitochondrial proteins was subsequently loaded onto a homemade glass column 5 × 80 mm, packed with 0.6 g of dry hydroxyapatite (Bio-Gel HTP, Biorad). The column was eluted with buffer A at 4 °C and fractions of 500 µL were collected and tested for protein content by a fluorometer assay (Invitrogen Qubit™ Protein Assay kit, ThermoFisher Scientific, Milan, Italy). Fractions containing proteins were pooled and dried under vacuum. The hydroxyapatite eluate was divided into two aliquots, which were reduced to less than 100 µL and purified from non-protein contaminating molecules with the PlusOne 2-D Clean-Up kit (GE Healthcare Life Sciences, Milan, Italy) according to the manufacturer's instructions. The desalted protein pellet was suspended in 100 µL of 50 mM ammonium bicarbonate (pH 8.3) and incubated at 4 °C for 15 min. Next, 100 µL of 0.2% RapiGest SF (Waters, Milan, Italy) in 50 mM ammonium bicarbonate were added and the samples were incubated at 4 °C for 30 min. Another aliquot of desalted protein pellet was suspended in 100 µL of 100 mM Tris-HCl, 10mM calcium chloride (pH 8.0) and incubated at 4 °C for 15 min. Next, 100 µL of 0.2% RapiGest SF in 100 mM Tris-HCl and 10 mM calcium chloride were added, and the samples were kept at 4 °C for 30 min. For each fraction, the recovered protein amount was determined in 100 µg by using a fluorometer assay. Reduced and alkylated proteins were then subjected separately to digestion using modified porcine trypsin and chymotrypsin, respectively. Tryptic digestion was carried out at an enzyme-substrate ratio of 1:50 at 37 °C for 4 h. Chymotryptic digestion was performed in Tris-HCl 100 mM, 10 mM calcium chloride (pH 8.0) at an enzyme-substrate ratio of 1:20, overnight at 25 °C.

2.4. Liquid Chromatography and Tandem Mass Spectrometry (LC-MS/MS) Analysis

Mass spectrometry data were acquired in triplicate for each sample assayed on an Orbitrap Fusion Tribrid (Q-OT-qIT) mass spectrometer (ThermoFisher Scientific, Bremen, Germany) equipped with a ThermoFisher Scientific Dionex UltiMate 3000 RSLCnano system (Sunnyvale, CA, USA), to assess the reproducibility of the available MS data. Samples obtained by in-solution tryptic and chymotryptic digestion were reconstituted in 30 µL of 5% FA aqueous solution and 1 µL was loaded onto an Acclaim® Nano Trap C18 column (100 µm i.d. × 2 cm, 5 µm particle size, 100 Å). After washing the trapping column with solvent A (H₂O + 0.1% FA) for 3 min at a flow rate of 7 µL/min, the peptides were eluted from the trapping column onto a PepMap® RSLC C18 EASY Spray, 75 µm × 50 cm, 2 µm, 100 Å column and were separated by elution at a flow rate of 0.250 µL/min, at 40 °C, with a linear gradient of solvent B (CH₃CN + 0.1% FA) in A from 5% to 20% in 32 min, followed by 20% to 40% in 30 min, and 40% to 60% in 20 min. Eluted peptides were ionized by a nanospray (Easy-spray ion source (ThermoFisher Scientific, Bremen, Germany), using a spray voltage of 1.7 kV and introduced

into the mass spectrometer through a heated ion transfer tube (275 °C). Survey scans of peptide precursors in the m/z range 400–1600 were performed at a resolution of 120,000 (@200 m/z) with an AGC target for the Orbitrap survey of 4.0×10^5 and a maximum injection time of 50 ms. Tandem MS was performed by isolation at 1.6 Th with the quadrupole, and high energy collisional dissociation (HCD) was performed in the Ion Routing Multipole (IRM), using a normalized collision energy of 35 and rapid scan MS analysis in the ion trap. Only those precursors with charge state 1–3 and intensity above the threshold of 5×10^3 were sampled for MS². The dynamic exclusion duration was set to 60 s with a 10-ppm tolerance around the selected precursor and its isotopes. Monoisotopic precursor selection was turned on. AGC target and maximum injection time for MS/MS spectra were 1.0×10^4 and 100 ms, respectively. The instrument was run in top speed mode with 3 s cycles, meaning the instrument would continuously perform MS² events until the list of non-excluded precursors diminishes to zero or 3 s, whichever is shorter. MS/MS spectral quality was enhanced enabling the parallelizable time option (i.e., by using all parallelizable time during full scan detection for MS/MS precursor injection and detection). Mass spectrometer calibration was performed using the Pierce[®] LTQ Velos ESI Positive Ion Calibration Solution (Thermo Fisher Scientific, Milan, Italy). MS data acquisition was performed using the Xcalibur v. 3.0.63 software (Thermo Fisher Scientific, Milan, Italy).

2.5. Database Search

LC–MS/MS data were processed by PEAKS de novo sequencing software (v. X, Bioinformatics Solutions Inc., Waterloo, ON, Canada). The data were searched against the 17,463 entries “Mus musculus” SwissProt database (release November 2019). The common Repository of Adventitious Proteins (c-RAP) contaminant database was included in the database search. Full tryptic or chymotrypsin peptides with a maximum of 3 missed cleavage sites were subjected to a bioinformatic search. Cysteine carboxyamidomethylation was set as the fixed modification, whereas oxidation of methionine, trioxidation and succination of cysteine, phosphorylation of serine, threonine and tyrosine, ubiquitin (m/z 114.0429) and ubiquitination (m/z 383.2281) of lysine, transformation of *N*-terminal glutamine and *N*-terminal glutamic acid residues in the form of pyroglutamic acid and *N*-terminal protein acetylation were included as variable modifications. The precursor mass tolerance threshold was 10 ppm, and the maximum fragment mass error was set to 0.6 Da. Peptide spectral matches (PSM) were validated using Target Decoy PSM Validator node based on *q*-values at a 0.1% False Discovery Rate (FDR). A protein was considered identified with a minimum of two peptides of which at least one had to be “unique”. Proteins containing the same peptides which could not be differentiated based on MS/MS analysis alone were grouped to satisfy the principles of parsimony. Finally, all the protein hits obtained were processed by using the InChorus function of PEAKS. This tool combines the database search results of PEAKS software with those obtained by the Mascot search engine with the aim not only to increase the coverage but also the confidence since the engines use independent algorithms and therefore the results confirm each other.

The raw data were also processed by MaxQuant 1.6.3.4 to further investigate deamidation. To this end, MaxQuant gives information about intensity of peptides in both unmodified and modified forms, allowing for an estimation of the deamidation ratio. The main parameters of the previous search were maintained: database, contaminant database, type of digestion, fixed and variable modifications. The principles of parsimony were still applied. Match type was “match from and to”. The decoy mode was “revert”. PSM, Protein and Site decoy fraction FDR were set at 0.01 as it was the threshold for peptide and protein identifications. All the other parameters were set as default.

2.5.1. Identification of Deamidation Sites on VDAC1

An estimation of the percentage of deamidation in VDAC1 for each cell line was calculated with the aid of a freely available command-line script for Python 2.x (<https://github.com/dblyon/deamidation>), which uses the MaxQuant “evidence.txt” file. It has to be considered that the method is intended for comparative purposes and not as an absolute measure of deamidation.

MaxQuant's "evidence.txt" file was used to calculate separate deamidation rates for Asparagine (N) and Glutamine (Q). The fraction of num_N (number of Asparagines) to num_N-2-D (number of deamidated Asparagines) and the fraction num_Q (number of Glutamines) to num_Q-2-E (number of deamidated Glutamines) were calculated for each peptide-to-spectrum match (PSM). The values obtained were termed respectively ratio_N-2-D and ratio_Q-2-E. The ratio_N-2-D or ratio_Q-2-E was multiplied for the "intensity" of the PTM, the values were summed, and the result divided by the total sum of all intensity values of the respective unmodified peptide sequence, obtaining a deamidation rate between 0 and 1 for each unique peptide sequence and charge state. For each peptide was calculated an average deamidation rate for Asparagine and Glutamine. The deamidation rates were averaged per sample. The latter set of values was sampled with replacement (bootstrapped) 1000 times. The mean, the standard deviation, and the 95% confidence intervals were calculated in order to achieve an estimate of the error of the calculation [30].

The program generates four delimited text files as output: (1) Deamidation.txt (Raw Files, deamidation for N and Q, as mean, standard deviation, 95% confidence lower and upper limit); (2) Number_of_Peptides_per_RawFile.txt; (3) Bootstrapped_values.txt (all the deamidation percentages calculated by e.g., 1000 bootstrap iterations, which are subsequently used to calculate the mean, std, and CI for shown in "Deamidation.txt"); (4) Protein_deamidation.txt (deamidation on the protein level).

2.5.2. Semi-Quantitative Analysis

A semi-quantitative analysis was performed by selecting the Fast LFQ (label-free quantification) option in MaxQuant 1.6.3.4. As recommended by Cox J. [31], "unique plus razor peptides" were included in the quantification. Razor-peptides are non-unique peptides assigned according to Occam's razor principle. Only unmodified peptides were used for quantification. "Advanced ratio estimation", "stabilize large LFQ ratios", "require MS/MS for comparisons" and "advanced site intensities" were selected. The runs were automatically aligned.

2.6. Modelling and Bioinformatics Analysis

Computational representation of the structures of VDAC1 N37D, N106D, N207D, N214D, N239D, 5Asn/Asp and 5Asn/Asp-2Gln/Glu were obtained by MODELLER v9.24 software (Webb & Sali, 2016) using the crystallographic structure of mouse VDAC1 WT (PDB: 3EMN) as template. Mutations were introduced by substitution of the selected amino acid residue(s) in the FASTA sequence. The same software was used for the evaluation of the energetic score associated with each structure. Graphical representation was obtained by using VMD—Visual Molecular Dynamic software (available at: <https://www.ks.uiuc.edu/Research/vmd/>). The root-means-square deviation (RMSD) analysis and the Ramachandran plots (RPs) were obtained by using specific tools in the VMD software. The number of α -helix, β -strand or unstructured domains was then analyzed and expressed as a percentage of the total.

3. Results

Our study was mainly focused on the identification of enzymatic and non-enzymatic PTMs in the VDAC1 protein from an established ALS mouse motor neuron-like cell line, especially considering the changes induced by oxidative stress typical of neurons affected by the disease.

Exactly, we searched, by mass spectrometry analysis, PTMs as oxidation and succination of cysteine residues, oxidation of methionine residue, phosphorylation of serine, tyrosine and threonine residues, ubiquitin and ubiquitination of lysine residues, and deamidation of asparagine and glutamine residues (Supplementary Figure S1).

To exclude the possibility that any unspecific and undesired oxidation could arise from the sample purification procedure, the reduction and alkylation of proteins were performed before VDACs purification. Hydroxyapatite (HTP) eluates of Triton X-100 extract were digested in-solution by trypsin and chymotrypsin and subsequently analysed in triplicate by liquid chromatography-mass

spectrometry. In this experiment, every protein in the HTP eluate was digested, thus a very complex peptide mixture was produced. Irrespective of the cell line from which the protein was isolated, nUHPLC/nESI-MS/MS analysis of the in-solution tryptic and chymotryptic digest of VDAC1 allowed to ascertain that the *N*-terminal methionine reported in the SwissProt database sequence (Acc. N. Q60932) was missing in the mature protein (Figure 1) analogously to the rat and human VDAC1 isoform [22,28]. Combining the results obtained in the complementary tryptic and chymotryptic digestions of the three cellular lines, a coverage of 96.8% of VDAC1 sequence was obtained (273 out of 282 amino acid residues; Figure 1). The regions not covered correspond to short traits or single amino acids (Thr¹⁹-Lys²⁰, Leu²⁹, Arg⁶³, Gly²²⁰-Lys²²⁴). MS analysis was also performed on VDAC1 samples purified from another series of NSC34, NSC34-SOD1WT, and NSC34-SOD1G93A cell cultures used in this work, in the same way as the first one. The data obtained were largely superimposable with the former (data not shown).

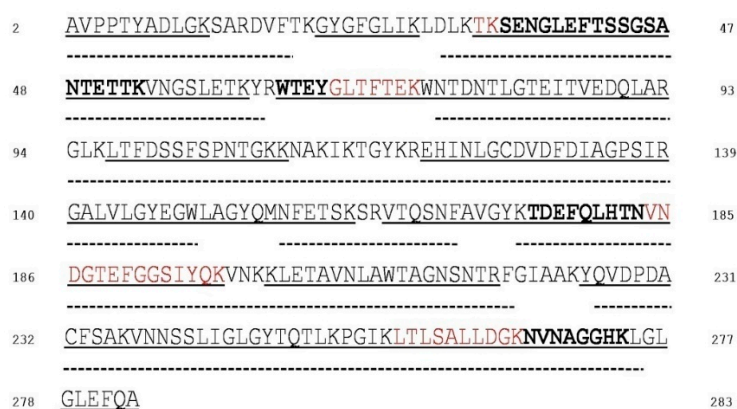


Figure 1. Sequence coverage map of VDAC1 from NSC34, NSC34-SOD1WT and NSC34-SOD1G93A cell lines obtained by tryptic and chymotryptic digestion. The solid line indicates sequence that was obtained from tryptic peptides; dotted lines: sequence obtained from chymotryptic peptides. Unique tryptic (indicated in bold) peptides originated by missed-cleavages were used to distinguish and cover sequences shared by isoforms. Sequences shared by more isoforms are reported in red. The numbering of the sequence considered the starting methionine residue, which is deleted during protein maturation.

The sequence of VDAC1 from *Mus musculus* contains one methionine in position 155, and two cysteines in position 127 and 232. It should be noted that the numeration adopted in the discussion starts from Met¹, which is absent in the mature protein.

3.1. Mass Spectrometry Analysis of VDAC1 from NSC34 Cell Line

The mass spectrometry analysis was first performed on material obtained from NSC34 wild-type cells, to establish a reference pattern and to compare the results with those reported for other cell lines.

Met¹⁵⁵ was identified in the normal form (Supplementary Table S1, fragment 10), but also as Met sulfoxide and Met sulfone (Supplementary Table S3, fragments 2 and 3). Supplementary Figure S2 shows the full scan and fragment ion mass spectrum of the molecular ion of the peptide G¹⁴⁰ALV**LG**YEGWLAGYQMN**FET**SK¹⁶¹ with Met¹⁵⁵ oxidized to methionine sulfoxide. The full scan mass spectrum of the molecular ion of the same peptide with Met¹⁵⁵ oxidized to methionine sulfone is reported in Figure S3. The MS/MS spectrum of Met sulfoxide presents the characteristic neutral loss of 64 Da corresponding to the ejection of methanesulfenic acid from the side chain of MetO [32].

Although from these data a precise determination of the amount of Met, Met sulfoxide, and Met sulfone cannot be obtained, a rough estimation of their relative abundance can be derived from the comparison of the absolute intensities of the multiply charged molecular ions of the respective peptides. From these calculations, a ratio of about 5:1 MetO/Met and 0.1:1 MetO₂/Met was found (Table S5).

Regarding the oxidation state of cysteines, mass spectral analysis indicated that Cys²³² was completely in the carboxyamidomethylated form (Supplementary Table S1, fragment 15), while Cys¹²⁷ was exclusively in the oxidized form of sulfonic acid (Supplementary Figure S4 and Supplementary Table S3, fragment 1), thus reproducing the same data obtained with the homologous human isoform [31]. Chymotryptic digestion was also performed and the data obtained confirmed the complete trioxidation of Cys¹²⁷ (Supplementary Table S4, fragment 1) and the total carboxyamidomethylation of Cys²³² (Supplementary Table S2, fragment 30).

3.2. Mass Spectrometry Analysis of VDAC1 from NSC34-SOD1WT Cell Line

In this section VDAC1 modifications found in NSC34 cells expressing a wt form of human SOD1 were analyzed. MS results indicate that the oxidation state of Met and Cys residues are very similar to the one reported for the same isoform from the NSC34 non transfected cells, discussed previously. In particular, in the tryptic digest Met¹⁵⁵ was detected both in the normal form (Supplementary Table S6, fragment 10) and oxidized to sulfoxide and sulfone, (Supplementary Figures S5 and S6 and Table S8, fragments 2 and 3) with a ratio of about 3:1 and 0.1:1 MetO/Met and MetO₂/Met, respectively (Supplementary Table S10). In addition, Cys¹²⁷ was detected only in the form of sulfonic acid (Supplementary Figure S7 and Table S8, fragment 1), whereas Cys²³² was fully carboxyamidomethylated (Supplementary Table S6, fragment 15).

These results were again confirmed by the complementary chymotryptic digestion (Supplementary Table S9, fragment 1, and Table S7, fragments 36 and 37).

3.3. Mass Spectrometry Analysis of VDAC1 from NSC34-SOD1G93A Cell Line

In this section VDAC modifications found in NSC34 cells expressing the G93A mutated sequence of the human SOD1 were analyzed. MS analysis of tryptic and chymotryptic digest of VDAC1 from NSC34-SOD1G93A cell revealed the presence of Cys²³² exclusively in the carboxyamidomethylated form (Supplementary Table S11, fragment 15; Table S12, fragment 25), and the partial oxidation of Met¹⁵⁵ to methionine sulfoxide and sulfone (Supplementary Figures S8 and S9 and Table S13, fragments 2 and 3, respectively). In contrast to the results found in other cells, a higher amount of methionine sulfoxide and sulfone was observed (Ox/Red ratio 61:1 and 4.7:1, respectively; Table 1). Furthermore, peptides containing Cys¹²⁷ residue in the carboxyamidomethylated form (Supplementary Table S11, fragment 9) and also oxidized to sulfonic acid were detected (Supplementary Figure S10 and Table S13, fragment 1) with a ratio of 24:1 (Table 1).

Table 1. Ratio of the absolute intensities of the molecular ions of the sulfur-containing tryptic peptides found in the analysis of VDAC1 from NSC34-SOD1G93A cells HTP-preparation reduced with DTT, carboxyamidomethylated and digested in-solution.

Technical Replicate	Peptide	Position in the Sequence	Measured Monoisotopic <i>m/z</i>	Absolute Intensity	Ratio Ox/Red
I	EHINLGCDVDFDIAGPSIR	121–139	1059.9921 (+2)	8.2 × 10 ⁵	29.3
I	EHINLGCDVDFDIAGPSIR		710.0155 (+3)	2.8 × 10 ⁴	
II	EHINLGCDVDFDIAGPSIR		1059.9915 (+2)	6.9 × 10 ⁵	19.2
II	EHINLGCDVDFDIAGPSIR		710.0140 (+3)	3.6 × 10 ⁴	
III	EHINLGCDVDFDIAGPSIR		1059.9928 (+2)	7.8 × 10 ⁵	23.6
III	EHINLGCDVDFDIAGPSIR		710.0140 (+3)	3.3 × 10 ⁴	
I	GALVLGYEGWLAGYQMNPFETSK	140–161	1225.5892 (+2)	4.5 × 10 ⁶	60.0
I	GALVLGYEGWLAGYQMNPFETSK		1217.5931 (+2)	7.5 × 10 ⁴	
II	GALVLGYEGWLAGYQMNPFETSK		1225.5897 (+2)	4.9 × 10 ⁶	71.0
II	GALVLGYEGWLAGYQMNPFETSK		1217.5913 (+2)	6.9 × 10 ⁴	
III	GALVLGYEGWLAGYQMNPFETSK		817.3946 (+3)	2.8 × 10 ⁶	51.9
III	GALVLGYEGWLAGYQMNPFETSK		812.0656 (+3)	5.4 × 10 ⁴	
I	GALVLGYEGWLAGYQMNPFETSK	140–161	822.7261 (+3)	2.2 × 10 ⁵	2.9
I	GALVLGYEGWLAGYQMNPFETSK		1217.5931 (+2)	7.5 × 10 ⁴	
II	GALVLGYEGWLAGYQMNPFETSK		822.7269 (+3)	4.5 × 10 ⁵	6.5
II	GALVLGYEGWLAGYQMNPFETSK		1217.5913 (+2)	6.9 × 10 ⁴	

Table 1. Cont.

Technical Replicate	Peptide	Position in the Sequence	Measured Monoisotopic m/z	Absolute Intensity	Ratio Ox/Red
III	GALVLYGEGWLAGYQMNFFETSK		822.7277 (+3)	2.6×10^5	4.8
III	GALVLYGEGWLAGYQMNFFETSK		812.0656 (+3)	5.4×10^4	

C: cysteine carboxyamidomethylated; C: cysteine oxidized to sulfonic acid; M: methionine sulfoxide; M: methionine sulfone.

3.4. Post-Translational Modifications Found in VDAC1 HTP-Prepared from Various NSC34 Cell Lines

3.4.1. Phosphorylation, Succination, Ubiquitin and Ubiquitination, and N-Terminal Acetylation

Mass spectral data were also analyzed to reveal the occurrence of serine, threonine, or tyrosine phosphorylation. In all the replicates of the three cellular lines, only Ser¹⁰⁴ was observed to be phosphorylated (Supplementary Tables S14–S16), even if always in a low amount (Supplementary Tables S17–S19), as indicated in the corresponding MS/MS spectra, which show typical losses of phosphoric acid (P) from fragment ions y , in accord with previous reports [33,34] (Supplementary Figures S11–S13).

The N-end Ala² is only present in acetylated form in all the replicates of the three cell lines (Supplementary Figure S14 and Table S1, fragment 1; Figure S15 and Table S6, fragment 1; Figure S16 and Table S11, fragment 1 respectively). These results were confirmed by the analysis of the chymotryptic digest (Supplementary Table S2, fragments 1 and 2; Table S7, fragments 1 and 2; Table S12, fragment 1). Moreover, succinated cysteines were not found in VDAC1 isoforms from any kind of studied NSC34 cell, as well as no evidence of ubiquitin and ubiquitination was detected.

3.4.2. Identification of VDAC1 Deamidation Sites from NSC34-SOD1G93A Cell Line

Deamidations of specific residues of asparagine and glutamine were detected only in VDAC1 purified from NSC34-SOD1G93A cells. This result was confirmed in each replicate analyzed (Table S15). Exactly, five asparagines (Asn³⁷, Asn¹⁰⁶, Asn²⁰⁷, Asn²¹⁴, and Asn²³⁹, Supplementary Table S20, fragments 1, 2, 3, 5, 6, and 8, and Figure 2 and Figure S17–S21) were transformed to aspartate and two glutamines (Gln¹⁶⁶ and Gln²²⁶, Table S20, fragments 4 and 7, and Supplementary Figures S22 and S23) to glutamate.

In particular, Table 2 suggests that an appreciable amount of Asn²⁰⁷ is deamidated (ratio deam/norm 0.6), whereas deamidated Gln¹⁶⁶ and Gln²²⁶ are visible in trace amounts (ratio deam/norm 0.002). Furthermore, for the other asparagines a ratio Asn-deamidated-to-Asp/Asn ranging from 0.01:1 to 0.04:1 was observed.

Table 2. Ratio of the absolute intensities of the molecular ions of tryptic peptides containing deamidated against not deamidated amino acids, found in the analysis of VDAC1 from NSC34-SOD1G93A cell HTP-preparation reduced with DTT, carboxyamidomethylated and digested in-solution.

Peptide	Position in the Sequence	Measured Monoisotopic m/z	Absolute Intensity	Ratio Deam/Norm
TKSENGLEFTSSGSANTETTK	33–53	730.6730 (+3)	6.3×10^6	0.02
TKSENGLEFTSSGSANTETTK		730.3450(+3)	3.3×10^8	
SENGLEFTSSGSANTETTK	35–53	654.2921 (+3)	6.3×10^5	0.01
SENGLEFTSSGSANTETTK		980.4425(+2)	1.4×10^8	
LTFDSSFSPNTGKK	97–110	510.5876 (+3)	1.3×10^6	0.01
LTFDSSFSPNTGKK		764.8857 (+2)	9.9×10^7	
VTQSNFAVGYK	164–174	607.8062 (+2)	1.4×10^6	0.002
VTQSNFAVGYK		607.3142 (+2)	6.2×10^8	

Table 2. Cont.

Peptide	Position in the Sequence	Measured Monoisotopic m/z	Absolute Intensity	Ratio Deam/Norm
KLETAVNLAWTAGNSNTR	201–218	649.6692 (+3)	9.6×10^6	0.6
KLETAVNLAWTAGNSNTR		649.3412 (+3)	1.6×10^7	
LETAVNLAWTAGNSNTR	202–218	909.9527(+2)	6.8×10^5	0.04
LETAVNLAWTAGNSNTR		909.4607 (+2)	1.9×10^7	
YQVDPDACFSAK	225–236	701.3032(+2)	1.6×10^6	0.002
YQVDPDACFSAK		700.8112(+2)	7.1×10^8	
VNNSSLIGLGYTQTLKPGIK	237–256	702.0598 (+3)	2.4×10^6	0.03
VNNSSLIGLGYTQTLKPGIK		701.7318 (+3)	7.4×10^7	

C: cysteine carboxyamidomethylated; N: asparagine deamidated; Q: glutamine deamidated.

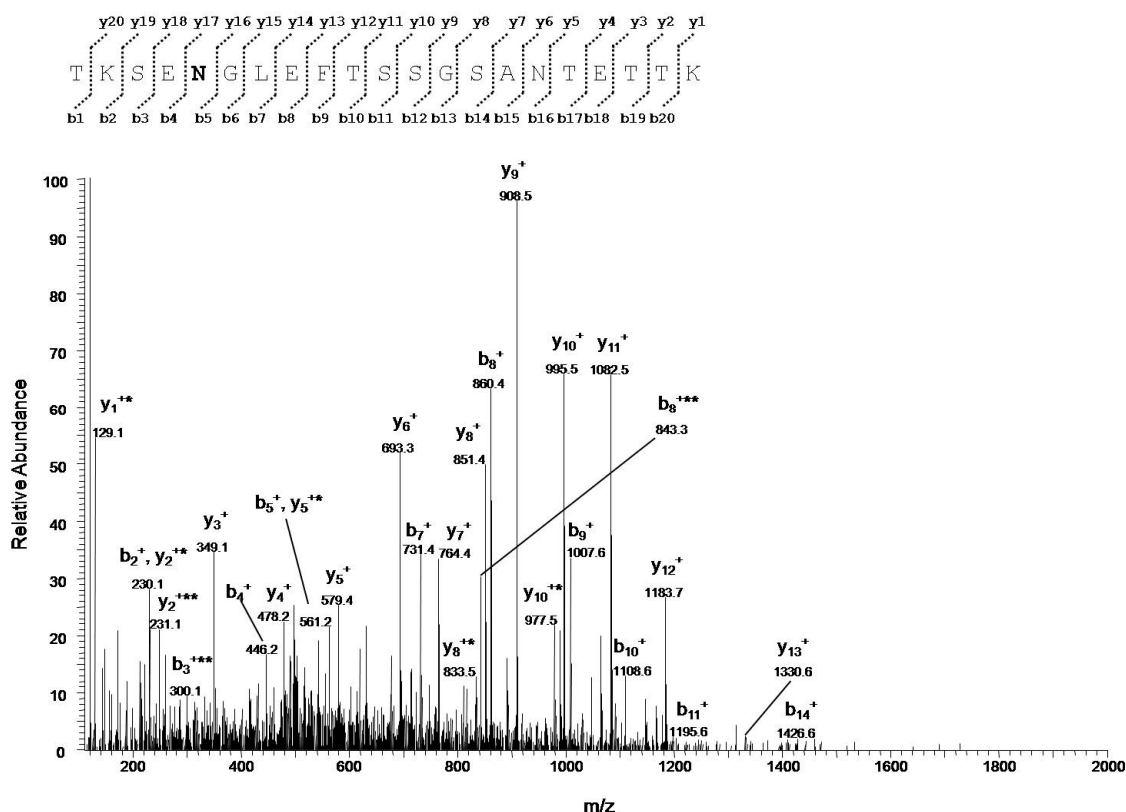


Figure 2. MS/MS spectrum of the triply charged molecular ion at m/z 730.6730 (calculated 730.6734) of the VDAC1 tryptic peptide from NSC34-SOD1G93A cell containing Asn residue 37 in the deamidated form. Fragment ions originated from the neutral loss of H_2O are indicated by an asterisk. Fragment ions originated from the neutral loss of NH_3 are indicated by two asterisk.

The occurrence of deamidation only in the NSC34-SOD1G93A cell line was also confirmed by the calculation of the percentage of deamidation in the VDAC1 for each cell line (Table 3). A remarkable difference in the deamidation between asparagine (mean 0.98) and glutamine residues (mean 0.02) was also found.

Table 3. Asparagine (N) and glutamine (Q) deamidation in the VDAC1 from NSC34 cells HTP-preparations. Mean, standard deviation, (95%) lower and upper confidence level and the number of scansions are reported.

Cell Lines	Residue	Mean	Std	CI_Low	CI_Up	N. of Scansions
NSC34	N	0	0	0	0	51
	Q	0	0	0	0	30
NSC34-SOD1WT	N	0	0	0	0	61
	Q	0	0	0	0	41
NSC34-SOD1G93A	N	0.98	0.81	0.04	2.76	87
	Q	0.02	0.02	0.00	0.06	47

(95%) lower and upper confidence level were obtained from 1000 bootstrap.

3.5. Semi-Quantitative Analysis of VDAC1 in NSC34 Cell Lines

The LFQ intensities obtained from MaxQuant search allowed for an estimation of the percentage of each VDAC in every cell line (Table 4). All three cell lines presented VDAC1 as the most abundant isoform (one order of magnitude higher than the other isoforms). However, NSC34 and NSC34-SOD1WT cell lines showed a similar profile for all the isoforms, whereas the NSC34-SOD1G93A cells had a difference in the abundance of VDAC2 and VDAC3. VDAC2 levels were higher in NSC34-SOD1G93A cells compared to NSC34 and NSC34-SOD1WT cell lines. In contrast, VDAC3 levels were lower in NSC34-SOD1G93A cells compared to NSC34 and NSC34-SOD1WT cell lines. The high complexity of the peptide mixtures could affect the reproducibility of the analysis, explaining the high standard deviation in NSC34-SOD1WT cells. Hence, caution about these results is required, although they may represent an interesting hint for further investigations.

Table 4. Relative percentage of each VDAC isoform in the three cell lines.

Protein	NSC34			NSC34-SOD1WT			NSC34-SOD1G93A		
	LFQ Intensity	SD%	%	LFQ Intensity	SD %	%	LFQ Intensity	SD %	%
VDAC1	1.10×10^9	1	66.71	1.19×10^9	27	65.67	1.10×10^9	7	64.08
VDAC2	2.40×10^8	4	14.55	2.46×10^8	20	13.59	3.51×10^8	11	20.43
VDAC3	3.09×10^8	15	18.74	3.75×10^8	16	20.74	2.66×10^8	13	15.50

f.e. $VDAC1(\%) = \frac{\text{mean}(\text{LFQ Intensity})_{VDAC1}}{[\text{mean}(\text{LFQ Intensity})_{VDAC1} + \text{mean}(\text{LFQ Intensity})_{VDAC2} + \text{mean}(\text{LFQ Intensity})_{VDAC3}]}$.

3.6. Bioinformatic Analysis Reveals an Increased Instability for Mutant Structures

To evaluate the stability of VDAC1 mutants, the mouse crystal structure from PDB [35] was modified with substitution of one or more asparagine or glutamine with aspartate or glutamate, as “virtual” deamidated amino acids. Root-mean-square deviation (RMSD) between the unmodified structure and those carrying such deamidations was analyzed. RMSD measures the distance between the atoms in the backbone and those of a reference structure in a protein structure alignment. All the generated mutant structures were superimposed to VDAC1 wt obtaining in all cases high RMSD values. In particular, for the single mutants, the average RMSD values were 5.16 Å for N37D, 5.28 Å for N106D, 5.17 Å for N214D, 4.79 Å for N239D and 5.20 Å for N207D. Similar values were obtained for multiple mutants (5.33 Å and 5.59 Å for 5 Asn/Asp and 5 Asn/Asp-2 Glu/Gln, respectively).

Overall, these results indicate that mutations produced a substantial modification in VDAC1 structure, likely affecting its molecule stability. Then, Ramachandran plots (RPs) were generated to determine ϕ and ψ angles for each amino acid residue (Table 5). This information, indeed, is very helpful for structure predictions since it describes the specific orientation of each residue in space. For example, RP for VDAC1 WT indicates that majority of amino acid residues are arranged in

a β -strand structure (about 78%) while the rest is distributed between α -helix (8.7%) and outlier conformations (12.3%).

As reported in Table 5, the presence of single mutations specifically affects the distribution of the secondary structures. However, most of the differences were observed for multiple mutants in which, in front of a slight decrease of β -strand structures, the percentage of α -helix increased proportionally to outlier reduction. Structural modifications produced by amino acid substitutions were confirmed by molecular modelling analysis (Figures 3–5). In Figures 3 and 4, structural reconstructions of the crystal and mutated sequences are shown. The models visually confirm the results obtained by RMSD calculations and outlined in the secondary structure content determined by the RPs.

Table 5. Distribution of secondary structures as predicted by Ramachandran Plot analysis. The table reports the percentage of allowed, favored and total secondary structure consisting of outliers, β -strand or α -helix, as obtained by RP analysis of VDAC1 WT and mutant structures.

	Outliers		β -Strand		α -Helix		
	Total	Allowed	Favored	Total	Allowed	Favored	Total
VDAC1 WT	12.4	11.3	67.6	78.9	6.3	2.4	8.7
VDAC1 N37D	10.6	13.5	63.2	76.7	7.8	4.9	12.7
VDAC1 N106D	8.8	12.8	65.4	78.2	7.0	6.0	13.0
VDAC1 N207D	9.1	13.6	64.6	78.2	7.4	5.3	12.7
VDAC1N214D	7.7	12.3	66.1	78.4	6.7	7.1	13.8
VDAC1N239D	8.1	12.3	66.4	78.7	7.1	6.1	13.2
VDAC1 5 Asn/Asp	7.3	16.6	60.7	77.3	8.4	7.0	15.4
VDAC1 5 Asn/Asp + 2 Gln/Glu	7.7	14.4	60.7	75.1	8.4	8.4	16.8

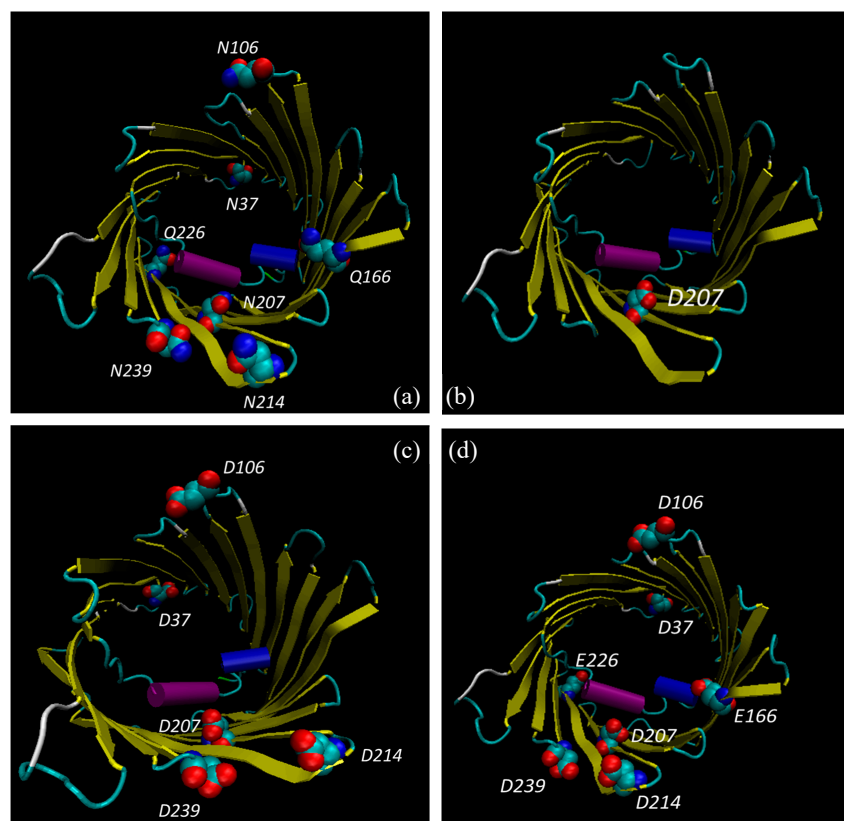


Figure 3. Top view of VDAC1 structures. Graphic representation of VDAC1 structures obtained by modelling WT (PDB: 3EMN) (a), mutant N207D (b), deamidated mutant 5 Asn/Asp (c) and deamidated mutant 5 Asn/Asp 2 Gln/Glu (d). N-terminal α -helix is shown in purple, β -strands in yellow, unstructured loops/regions in white and light blue. The amino acid residues Asn, Gln and Asp are evidenced. Dark blue was used for nitrogen, red for oxygen and light blue for carbon atoms.

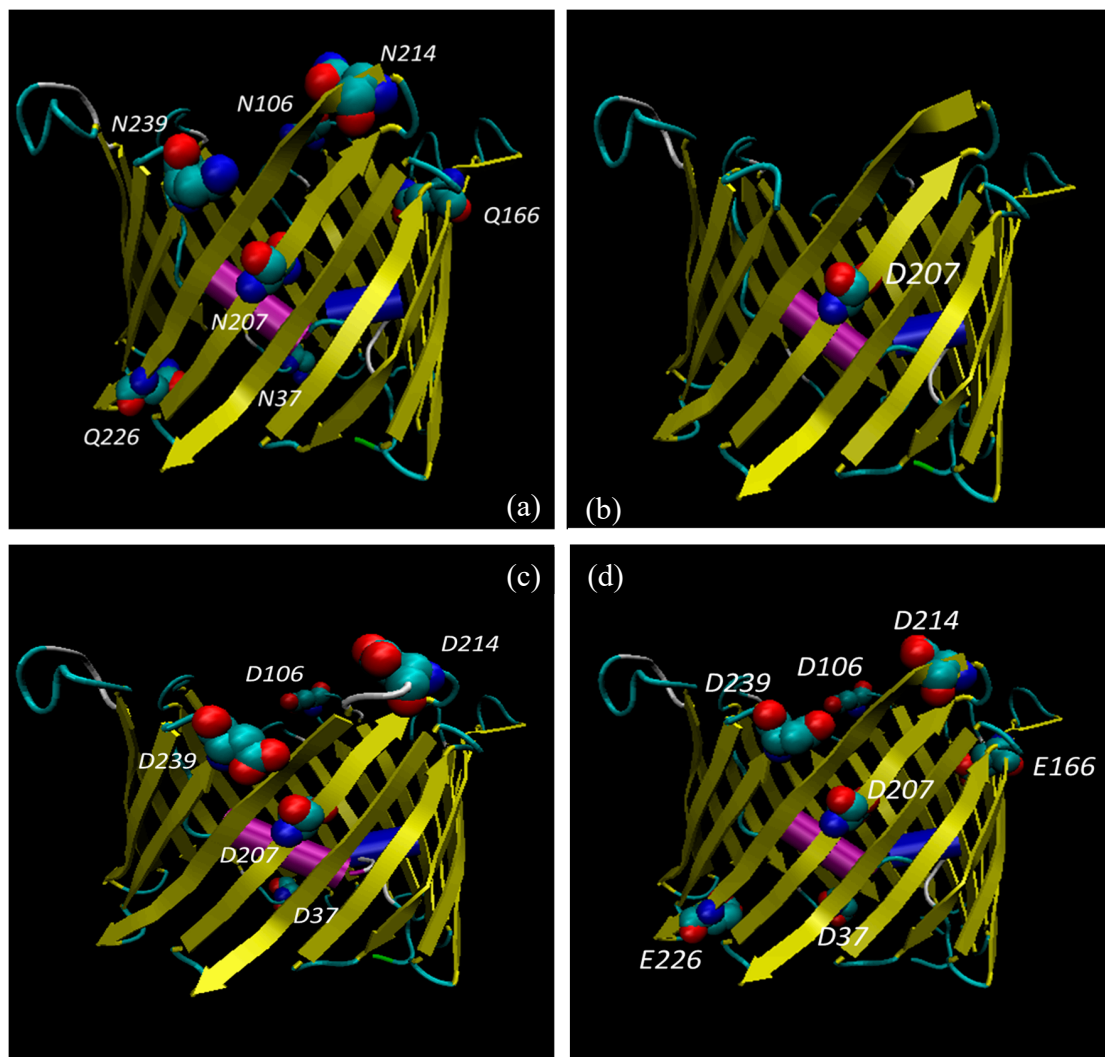


Figure 4. Lateral view of VDAC1 structures. Graphic representation of VDAC1 structures obtained by modelling of WT (PDB: 3EMN) (a), mutant N207D (b), deamidated mutant 5 Asn/Asp (c) and deamidated mutant 5 Asn/Asp 2 Gln/Glu (d). N-terminal α -helix is shown in purple, β -strands in yellow, unstructured loops/regions in white and light blue. The amino acid residues Asn, Gln and Asp were evidenced. Dark blue was used for nitrogen, red for oxygen and light blue for carbon atoms.

The deamidation of the selected asparagine and glutamine causes a crushing of the barrel (see Figure 4c, for example) and a shift of the global secondary structure composition from β -strand to α -helix. What is important is that even a single deamidation has a major structural effect (Figures 3 and 4).

It is interesting that the amino acids found deamidated in the cell expressing the mutated SOD1 are mostly located in loops or turns connecting the β -strands: they are, thus, in a water-exposed context where the effect of ROS can be faster. Only Asn³⁷ and Gln²²⁶ protrude in the intermembrane space, while Asn¹⁰⁶, Asn²¹⁴, Asn²³⁹ and Gln¹⁶⁶ protrude in the cytosol. The only exception is Asn²⁰⁷ which is located in the middle of a β -strand, even though it is exposed to the water interior of the pore, thus still accessible to ROS by diffusion. Interestingly, Asn²⁰⁷ is also the most frequently deamidated residue (see Table 6) and its modification results in a sensible change of the structure (Figures 3b and 4b), indicating a crucial function for this residue.

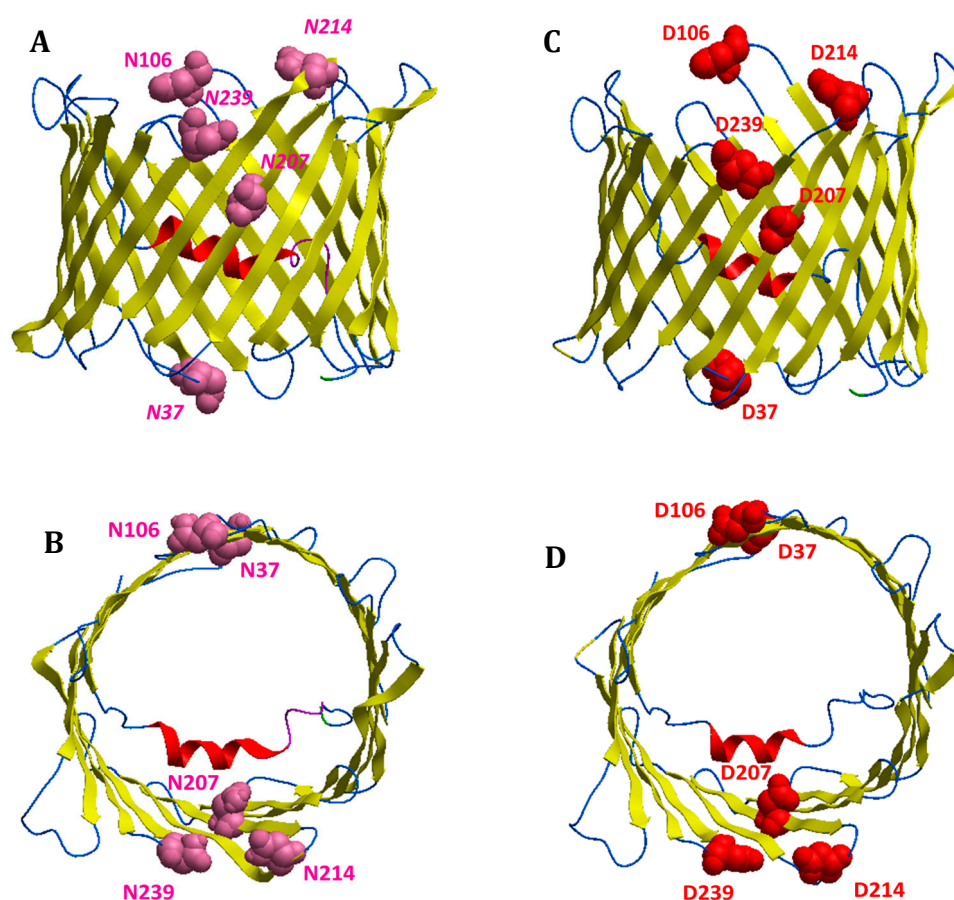


Figure 5. Polarity changes upon VDAC1 deamidation. Graphic representation of VDAC1 structures obtained by modelling in which polarity of specific amino acid residues has been highlighted. Lateral and top view of VDAC1 WT (A,C) and 5 Asn/Asp deamidated mutant (B,D). Pink color is used for amino acid residues having a neutral lateral chain, while red color is used for negatively charged residues.

Table 6. Modified residues found in VDAC1 from NSC34, NSC34-SOD1WT and NSC34-SOD1G93A cell lines. The ratio between modified and unmodified residues is shown in brackets; where the ratio is not indicated the residue is only present in a single form. The dashes indicate residues found exclusively in non-modified form. The asterisk indicates a fully carboxyamidomethylated form.

	Modified Residues in VDAC1		
	NSC34	NSC34-SOD1WT	NSC34-SOD1G93A
ALA ²	Acetylated	Acetylated	Acetylated
ASN ³⁷	-	-	Deamidated (0.01:1)
SER ¹⁰⁴	Phosphorylated (0.01:1)	Phosphorylated (0.01:1)	Phosphorylated (0.01:1)
ASN ¹⁰⁶	-	-	Deamidated (0.01:1)
CYS ¹²⁷	Sulfonic acid	Sulfonic acid	Sulfonic acid (24:1)
MET ¹⁵⁵	Met sulfoxide (5:1) Met sulfone (0.1:1)	Met sulfoxide (3:1) Met sulfone (0.1:1)	Met sulfoxide (61:1) Met sulfone (4.7:1)
GLN ¹⁶⁶	-	-	Deamidated (0.002:1)
ASN ²⁰⁷	-	-	Deamidated (0.6)
ASN ²¹⁴	-	-	Deamidated (0.04:1)
GLN ²²⁶	-	-	Deamidated (0.002:1)
CYS ²³²	*	*	*
ASN ²³⁹	-	-	Deamidated (0.03)

4. Discussion

The impairment of the bioenergetics metabolism strongly increases free radicals and oxidative stress, which, in turn, are involved in ALS onset and progression. Reactive species damage proteins by inducing various oxidative PTMs some of which are biological markers of misfolding disorders, including Parkinson's disease, Alzheimer's disease, and ALS [36–38]. In particular, carbonylation of spinal cord proteins has been proposed as a promoting factor of neuronal death in ALS [39,40]. Further reports showed the importance of other PTMs in ALS-related proteins. In particular, SOD1 mutants exhibit structural instability and propensity to exist in an unfolded state as well as presenting specific secondary post-translational changes [41]. Interestingly, by altering the normal set of PTMs [42,43] and/or inserting mutations which result in the same chemical structure as the PTM deamidation (N→D; Q→E), the wild type SOD1 becomes unstable and misfolds, acquiring properties similar to those of fALS-related SOD1 mutants [44]. Therefore, certain PTMs are responsible for important chemical and biophysical characteristics of mutant SOD1 and may be involved in sporadic ALS. Equally relevant to understanding the role of mitochondrial dysfunction in SOD1 linked-ALS are the non-inheritable PTMs of VDAC1, an outer mitochondrial membrane (OMM) scaffold protein able to interact with ALS-linked SOD1 mutants but not with SOD1 wt.

Evidence of oxidative damage to proteins, lipids and DNA has been found both in animal ALS models expressing mutated human SOD1 and in post-mortem tissues of patients with sporadic or familial ALS [7]. In particular, deamidation events were found in erythrocytes of sALS patients [45] and in other tissues from patients with ALS-SOD1G93A [44]. Specific PTM, including N-D e Q-E deamidation, were also found in TDP-43 aggregates from brains of ALS patients [46]. There is no report in the literature where deamidation PTMs were looked for in animals.

In this study, by high-resolution mass spectrometry analysis, possible signs of oxidative damage in VDAC1 from an ALS cell model were investigated. Using known techniques [22], difficulties associated with the analysis of membrane proteins were overcome and potential dangers of undesirable oxidation were avoided. We have achieved excellent VDAC1 sequence coverage from mitochondria isolated from NSC34 cell lines; 273 out of 282 amino acids in the VDAC1 sequence were identified (Figure 1). The non-covered regions corresponded to a few single amino acids and a short stretch (G220–A224) found in the β -strand 15. We accurately determined the oxidative states of the cysteine and methionine residues of NSC34 mouse VDAC1. VDAC1 contains a single inner methionine, Met¹⁵⁵, and only two cysteines, Cys¹²⁷ and Cys²³², located in β -strands 10, 8 and 16 respectively. According to VDAC1's three-dimensional structure [35,47,48], Met¹⁵⁵ and Cys¹²⁷ are embedded in the hydrophobic milieu of the OMM, whereas Cys²³² turns toward the water-filled pore. Mass spectrometry analysis revealed an evolutionarily conserved redox modification pattern of VDAC1 cysteine residues: both in human and rat, Cys¹²⁷ was exclusively found as trioxidized to sulfonic acid and Cys²³² was fully reduced and carboxyamidomethylated [22,28]. Still, a functional role for these residues has never been demonstrated. Data available so far report that cysteines in VDAC1 do not influence the channel activity [49] and are not involved in protein oligomerization [50].

In our study, only in NSC34-SOD1G93A cells, we found that Met¹⁵⁵ was oxidized to methionine sulfone and mostly over-oxidized to methionine sulfoxide also in much higher amounts than the one found for the same residue in the two non-ALS cell lines. Regarding the other residues, Cys²³² was confirmed as completely reduced or involved in forming disulfide bridges in ALS and non-ALS cell lines [28]. Conversely, Cys¹²⁷ from SOD1-ALS cells was over-oxidized to sulfonic acid, in a lower amount than in the two non-ALS cell lines.

Oxidative modifications in both Met¹⁵⁵ and Cys¹²⁷ could be explained by their localization in neighboring β -sheet where they face the lipid bilayer. Thus, we hypothesize that OMM lipids peroxidized by ALS pathogenesis [51] can modify susceptible residues oriented towards the membrane. A low amount of the Cys¹²⁷ was also in carboxyamidomethylated form, therefore in a reduced form or involved in an intermolecular disulfide bridge (due to cysteines position in VDAC1). The finding of a putatively reduced aliquot of Cys¹²⁷ could be a consequence of the destabilization of the VDAC1

structure following all the modifications we identified. Indeed, we have also revealed only in NSC34-SOD1G93A cells, the deamidation of specific asparagine and glutamine residues. This is the first time that these changes were reported in VDAC1. Deamidation is a non-inheritable PTM that introduces negative charges by removing amino groups from asparagine and, with a much lower frequency and rate, glutamine [52,53]. This modification is strongly associated with the regulation of protein folding and turnover. While *in vivo* enzymatic deamidation of Gln is known and is involved in several physiological and pathological processes, Asn deamidation is a non-enzymatic reaction and its process rate depends on several factors, including the protein sequence and structure, as well as temperature, ionic strength, and pH. In particular, the propensity to undergo deamidation is considerably increased if an Asn residue is in a protein sequence followed by small, flexible, or hydrophilic amino acids [54]. Several examples of human deamidated proteins are known, most of which are implicated in neurodegeneration [44,55–57].

As it causes critical alterations in peptide and protein structure, deamidation is suspected to contribute to the aging of proteins and protein folding disorders such as those observed in Alzheimer's disease [56–58]. It has also been demonstrated that specific deamidations of SOD1 wt determine aberrant conformations in the protein similar to those of the mutated forms associated with fALS [43,59].

In this work, we found the surprising result of identifying deamidation of five asparagine (Asn³⁷, Asn¹⁰⁶, Asn²⁰⁷, Asn²¹⁴, and Asn²³⁹) and two glutamine (Gln¹⁶⁶ and Gln²²⁶) residues, exclusively in VDAC1 purified from NSC34-SOD1G93A cell line (Figure 2, Tables 2, 5 and 6). In particular, we found that the deamidation level of the Asn²⁰⁷ residue was much higher than other asparagine residues converted to aspartate, and especially that the two glutamines were modified to glutamate in a very small quantity (Tables 2 and 6). This may depend on the particular position of Asn²⁰⁷ in the VDAC1 sequence. In fact, this residue is located in the centre of the β -strand 14 and is preceded and followed by non-bulky amino acid residues, such as the nearby residues in the flanking β -strands (Figures 3 and 4). As a result of this, the amido group of Asn²⁰⁷ can be particularly sensitive to ROS at the inner mitochondrial membrane (IMM) which are strongly increased in ALS, as well as being affected by the aggressive action of peroxidized lipids in the OMM. The lower level of deamidation of the Asn³⁷ residue could depend on its position in a loop, a domain that, although facing the oxidizing environment of the IMM, constitutes an unfolded region and therefore it is free to move and/or establish interactions with other molecules as well as to protect the Asn³⁷ from the action of ROS (Figures 3 and 4). The other three asparagine residues (Asn¹⁰⁶, Asn²¹⁴ and Asn²³⁹) are also found in the loops (Figures 3 and 4), but unlike Asn³⁷ these loops are exposed to the cytosol, a much less oxidizing environment than IMM.

We are sure that the different levels of oxidation and deamidation of VDAC1 identified in this study were not due to different protein expression in ALS motor neurons. In fact, an equal expression of VDAC1 was found in the three cell lines analysed, while VDAC2 levels were increased only in the ALS model NSC34 (Table 4). This result could be explained by considering the anti-apoptotic role of VDAC2 isoform, which could answer to degeneration signs characteristic of ALS. Deamidation introduces a negative charge in the protein sequence and, as a result, is often responsible for a serious change in its structure. RMSD analysis performed on the predicted structures for deamidated mouse VDAC1 showed that deamidation undoubtedly modifies the VDAC1 protein structure.

Structural predictions obtained by molecular modelling support data from RMSD analysis. Interestingly, conformational changes in deamidated VDAC mutants were found. In particular, it should be noted that the Asn²⁰⁷/Asp²⁰⁷ replacement alone causes structural modifications to the VDAC1 channel that becomes more and more marked as the number of deamidations increases (Figures 3 and 4). The distribution of the charges in the structures of the deamidated VDAC1 is also remarkably interesting: the replacement of the five asparagines and the two glutamines with the same number of aspartates and glutamates, respectively, increases the number of negative charges on the pore surfaces facing the cytosol and the intermembrane space (Figure 5). This different charge

distribution must have an impact on the physiological interactivity of VDAC1 and consequently on the functionality of the protein itself and of the whole mitochondrion.

Moreover, in the predicted structures we have also observed that Met¹⁵⁵ and Cys¹²⁷ in deamidated VDAC1 maintain their original arrangement, although the sulphur of Met¹⁵⁵ is further exposed to the lipid environment. In addition, we found that the atomic distance between Cys¹²⁷ and the nearby residues was for Leu¹²⁵ decreased from 10.2 Å in VDAC1 WT to 8.6 Å in deamidated VDAC1, shielding on one side the Cys¹²⁷ in the sulfonic acid form (data not showed). These data may explain the small amount of Cys¹²⁷ in reduced form found in ALS model cells.

RMSD data were confirmed by Ramachandran plot (RP) analysis for each single deamidated VDAC form identified in this study. Structural modifications were detected in the β -barrel regions of VDAC1 mutants together with an increased number of residues in the α -helix region, indicating a tendency for this domain to organise itself into a more stable structure. This effect, which causes destabilisation of the whole VDAC1 structure and pushes towards alpha helix formation, already occurred with the N207D mutant or any other evaluated single mutant. Interestingly, RPs show that this trend increases with the rise of deamidation sites. It is reasonable to believe that the different levels of deamidation of the residues identified in VDAC1 may depend on the degree of disease that NSC34-SOD1G93A cells reflect. It is conceivable that the level of deamidation of VDAC1 will gradually increase with the worsening of the disease (Figure 6). D'Angelo S. et al. [45] reported the abnormal deamidation of protein asparagine residues in erythrocytes from sALS patients. In this perspective, the search for deamidated VDAC in blood or cerebrospinal fluid could represent an innovative diagnostic and/or prognostic biomarker of amyotrophic lateral sclerosis.

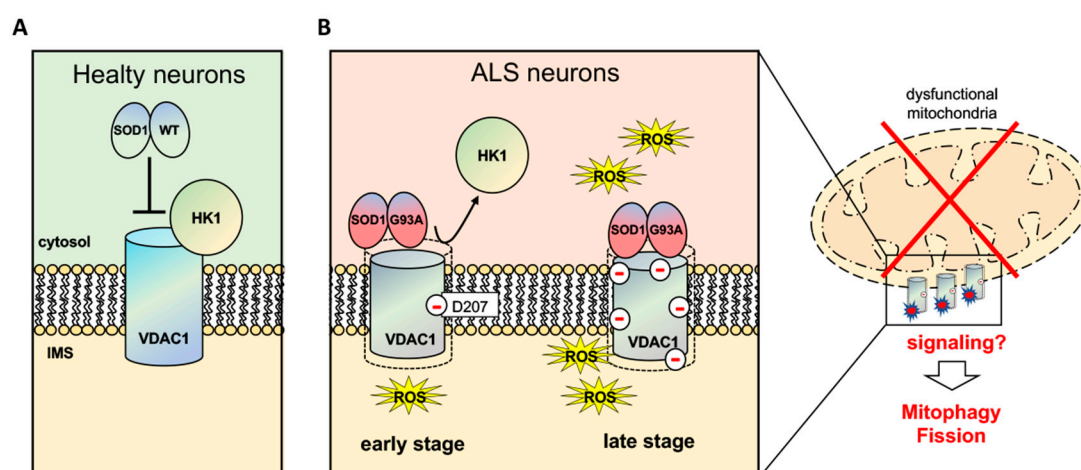


Figure 6. Deamidated VDAC1 in ALS motor neurons can promote mitochondrial dysfunction and ultimately lead to mitophagy. In physiological conditions (A), VDAC1 is the receptor of HK1 and of many other enzymes and metabolites (not shown), but not of SOD1WT. Conversely, in ALS (B), SOD1G93A is able to bind deamidated VDAC1 impairing thus the binding of HK1 and likely of others physiological interactors. We propose that deamidation of VDAC1 residues parallels oxidative stress levels, leading to the enhancement of SOD1 mutant binding to VDAC1. As a consequence, VDAC1 channel conductance and metabolic exchanges through VDAC1 are gradually affected, promoting a growing mitochondrial dysfunction. The oxidative damage that accumulates with disease progression produces therefore dysfunctional mitochondria tagged with deamidated VDAC1 that could be selected and forwarded to mitophagy or fission processes. In figure, red minus signs indicate deamidated VDAC1 amino acids.

5. Conclusions

In this work, we have established for the first time that in a motor neuron model of ALS, VDAC1 undergoes specific post-translational modifications, such as oxidations and deamidations. In addition, we have provided evidence of changes in the structure of deamidated VDAC1, a condition

sufficient to alter the physiological pool of interactors. These data are important to understand how the VDAC1 protein interacts uniquely with the mutant SOD1 mutant but also allows us to better understand ALS pathogenesis. Furthermore, a new role as a potential marker for degenerated and unrepairable mitochondria in ALS emerges for VDAC1.

Supplementary Materials: The following are available online at <http://www.mdpi.com/2076-3921/9/12/1218/s1>, Figure S1: Map of the modified residues found in VDAC1 from the analyzed NSC34 cell lines. Figure S2: MS/MS and full scan mass spectra of the triply charged molecular ion at m/z 817.3960 (calculated 817.3951) of the VDAC1 tryptic peptide from NSC34 cell line containing the methionine residue 155 in the oxidized form of methionine sulfoxide. Figure S3: Full scan mass spectrum of the doubly charged molecular ion at m/z 1233.5824 (calculated 1233.5862) of the VDAC1 tryptic peptide from NSC34 cell line containing the methionine residue 155 in the oxidized form of methionine sulfone. Figure S4: MS/MS and full scan mass spectra of the doubly charged molecular ion at m/z 1059.9929 (calculated 1059.9919) of the VDAC1 tryptic peptide from NSC34 cell line containing cysteine residue 127 in the form of sulfonic acid. Figure S5: MS/MS and full scan mass spectra of the triply charged molecular ion at m/z 817.3956 (calculated 817.3951) of the VDAC1 tryptic peptide from NSC34-SOD1WT cell line containing the methionine residue 155 in the oxidized form of methionine sulfoxide. Figure S6: Full scan mass spectrum of the doubly charged molecular ion at m/z 1233.5853 (calculated 1233.5862) of the VDAC1 tryptic peptide from NSC34-SOD1WT cell line containing the methionine residue 155 in the oxidized form of methionine sulfone. Figure S7: MS/MS and full scan mass spectra of the doubly charged molecular ion at m/z 1059.9924 (calculated 1059.9919) of the VDAC1 tryptic peptide from NSC34-SOD1WT cell line containing the cysteine residue 127 in the form of sulfonic acid. Figure S8: MS/MS and full scan mass spectra of the triply charged molecular ion at m/z 817.3946 (calculated 817.3951) of the VDAC1 tryptic peptide from NSC34-SOD1G93A cell line containing the methionine residue 155 in the oxidized form of methionine sulfoxide. Figure S9: Full scan mass spectrum of the triply charged molecular ion at m/z 822.7261 (calculated 822.7268) of the VDAC1 tryptic peptide from NSC34-SOD1G93A cell line containing the methionine residue 155 in the oxidized form of methionine sulfone. Figure S10: MS/MS and full scan mass spectra of the doubly charged molecular ion at m/z 1059.9921 (calculated 1059.9919) of the VDAC1 tryptic peptide from NSC34-SOD1G93A cell line containing the cysteine residue 127 in the form of sulfonic acid. Figure S11: MS/MS and full scan mass spectra of the doubly charged molecular ion at m/z 804.8689 (calculated 804.8692) of the VDAC1 tryptic peptide from NSC34 cell line containing the serine residue 104 in the phosphorylated form. Figure S12: MS/MS and full scan mass spectra of the doubly charged molecular ion at m/z 804.8690 (calculated 804.8692) of the VDAC1 tryptic peptide from NSC34-SOD1WT cell line containing the serine residue 104 in the phosphorylated form. Figure S13: MS/MS and full scan mass spectra of the triply charged molecular ion at m/z 536.9153 (calculated 536.9154) of the VDAC1 tryptic peptide from NSC34-SOD1G93A cell line containing the serine residue 104 in the phosphorylated form. Figure S14: MS/MS and full scan mass spectra of the doubly charged molecular ion at m/z 587.3116 (calculated 587.3111) of the N-terminal acetylated tryptic peptide of VDAC1 from NSC34 cell line. Figure S15: MS/MS and full scan mass spectra of the doubly charged molecular ion at m/z 587.3114 (calculated 587.3111) of the N-terminal acetylated tryptic peptide of VDAC1 from NSC34-SOD1WT cell line. Figure S16: MS/MS and full scan mass spectra of the doubly charged molecular ion at m/z 587.3113 (calculated 587.3111) of the N-terminal acetylated tryptic peptide of VDAC1 from NSC34-SOD1G93A cell line. Figure S17: MS/MS spectrum of the triply charged molecular ion at m/z 654.2921 (calculated 654.2925) of the VDAC1 tryptic peptide from NSC34-SOD1G93A cell line containing the asparagine residue 37 in the deamidated form. Figure S18: MS/MS spectrum of the triply charged molecular ion at m/z 510.5876 (calculated 510.5880) of the VDAC1 tryptic peptide from NSC34-SOD1G93A cell line containing the asparagine residue 106 in the deamidated form. Figure S19: MS/MS spectrum of the triply charged molecular ion at m/z 649.6692 (calculated 649.6696) of the VDAC1 tryptic peptide from NSC34-SOD1G93A cell line containing the asparagine residue 207 in the deamidated form. Figure S20: MS/MS spectrum of the doubly charged molecular ion at m/z 909.9527 (calculated 909.9530) of the VDAC1 tryptic peptide from NSC34-SOD1G93A cell line containing the asparagine residue 214 in the deamidated form. Figure S21: MS/MS spectrum of the triply charged molecular ion at m/z 702.0598 (calculated 702.0602) of the VDAC1 tryptic peptide from NSC34-SOD1G93A cell line containing the asparagine residue 239 in the deamidated form. Figure S22: MS/MS spectrum of the doubly charged molecular ion at m/z 607.8062 (calculated 607.8065) of the VDAC1 tryptic peptide from NSC34-SOD1G93A cell line containing the glutamine residue 166 in the deamidated form. Figure S23: MS/MS spectrum of the doubly charged molecular ion at m/z 701.3032 (calculated 701.3035) of the VDAC1 tryptic peptide from Mouse Motor Neuron-like NSC34-SOD1G93A cell line containing Cys²³² residue in the carboxyamidomethylated form and the glutamine residue 226 in the deamidated form. Table S1: Tryptic peptides found in the analysis of VDAC1 from NSC34 cell line after DTT reduction and carboxyamidomethylation. Table S2: Chymotryptic peptides found in the analysis of VDAC1 from NSC34 cell line after DTT reduction and carboxyamidomethylation. Table S3: Retention time, experimentally measured and calculated monoisotopic m/z of the molecular ions, position in the sequence and peptide sequence of sulfur containing tryptic fragments found in the analysis of VDAC1 from NSC34 cell line digest reduced with DTT, carboxyamidomethylated and digested in-solution. Table S4: Retention time, experimentally measured and calculated monoisotopic m/z of the molecular ion of the Chymotryptic peptide K¹¹⁹REHINLGCVDVF¹³¹ found in VDAC1 from NSC34 cell line digest reduced with DTT, carboxyamidomethylated and digested in-solution. Table S5: Ratio of the absolute intensities of the molecular ions of the sulfur and not sulfur containing tryptic peptide G¹⁴⁰ALVLGYEGWLAGYQMNFFETSK¹⁶¹ found in the analysis of VDAC1 from NSC34 cell line HTP-preparation reduced with DTT, carboxyamidomethylated and digested in-solution. Table S6: Tryptic peptides found in

the analysis of VDAC1 from NSC34-SOD1WT cell line after DTT reduction and carboxyamidomethylation. Table S7: Chymotryptic peptides found in the analysis of VDAC1 from NSC34-SOD1WT cell line after DTT reduction and carboxyamidomethylation. Table S8: Retention time, experimentally measured and calculated monoisotopic m/z of the molecular ions, position in the sequence and peptide sequence of sulfur containing tryptic fragments found in the analysis of VDAC1 from NSC34-SOD1WT cell line digest reduced with DTT, carboxyamidomethylated and digested in-solution. Table S9: Retention time, experimentally measured and calculated monoisotopic m/z of the molecular ion of the chymotryptic peptide K¹¹⁹REHINLGCDVDF¹³¹ found in the analysis of VDAC1 from NSC34-SOD1WT cell line digest reduced with DTT, carboxyamidomethylated and digested in-solution. Table S10: Ratio of the absolute intensities of the molecular ions of the sulfur and not sulfur containing tryptic peptide G¹⁴⁰ALVLGYEGWLAGYQMNFETSK¹⁶¹ found in the analysis of VDAC1 from NSC34-SOD1WT cell line digest reduced with DTT, carboxyamidomethylated and digested in-solution. Table S11: Tryptic peptides found in the analysis of VDAC1 from NSC34-SOD1G93A cell line after DTT reduction and carboxyamidomethylation. Table S12: Chymotryptic peptides found in the analysis of VDAC1 from NSC34-SOD1G93A cell line after DTT reduction and carboxyamidomethylation. Table S13: Retention time, experimentally measured and calculated monoisotopic m/z of the molecular ions, position in the sequence and peptide sequence of sulfur containing tryptic fragments found in VDAC1 from NSC34-SOD1G93A cell line digest reduced with DTT, carboxyamidomethylated and digested in-solution. Table S14: Retention time, experimentally measured and calculated monoisotopic m/z of the molecular ion of the phosphorylated tryptic peptide L⁹⁷TFDSSFSPNTGKK¹¹⁰ containing the Ser¹⁰⁴ phosphorylated found in VDAC1 from NSC34 cell line digest reduced with DTT, carboxyamidomethylated and digested in-solution. Table S15: Retention time, experimentally measured and calculated monoisotopic m/z of the molecular ion of the phosphorylated tryptic peptide L⁹⁷TFDSSFSPNTGKK¹¹⁰ containing the Ser¹⁰⁴ phosphorylated found in VDAC1 from NSC34-SOD1WT cell line digest reduced with DTT, carboxyamidomethylated and digested in-solution. Table S16: Retention time, experimentally measured and calculated monoisotopic m/z of the molecular ion of the phosphorylated tryptic peptide L⁹⁷TFDSSFSPNTGKK¹¹⁰ containing the Ser¹⁰⁴ phosphorylated found in VDAC1 from NSC34-SOD1G93A cell line digest reduced with DTT, carboxyamidomethylated and digested in-solution. Table S17: Ratio of the absolute intensities of the molecular ions of the phosphorylated and not phosphorylated tryptic peptide L⁹⁷TFDSSFSPNTGKK¹¹⁰ containing the Ser¹⁰⁴ phosphorylated found in the analysis of VDAC1 from NSC34 cell line digest reduced with DTT, carboxyamidomethylated and digested in-solution. Table S18: Ratio of the absolute intensities of the molecular ions of the phosphorylated and not phosphorylated tryptic peptide L⁹⁷TFDSSFSPNTGKK¹¹⁰ containing the Ser¹⁰⁴ phosphorylated found in the analysis of VDAC1 from NSC34-SOD1WT cell line digest reduced with DTT, carboxyamidomethylated and digested in-solution. Table S19: Ratio of the absolute intensities of the molecular ions of the phosphorylated and not phosphorylated tryptic peptide L⁹⁷TFDSSFSPNTGKK¹¹⁰ containing the Ser¹⁰⁴ phosphorylated found in the analysis of VDAC1 from NSC34-SOD1G93A cell line digest reduced with DTT, carboxyamidomethylated and digested in-solution. Table S20: Retention time, experimentally measured and calculated monoisotopic m/z of the molecular ions, position in the sequence and peptide sequence of tryptic fragments containing asparagine and glutamine residues in deamidated form found in VDAC1 from NSC34-SOD1G93A cell line digest reduced with DTT, carboxyamidomethylated and digested in-solution.

Author Contributions: Conceptualization, A.M.; methodology, M.G.G.P. and R.S.; software, S.A.M.C., V.C., M.G.G.P. and A.C.; validation, M.G.G.P., A.C. and S.R.; investigation, M.G.G.P., S.R. and B.F.; writing—original draft preparation, M.G.G.P., S.R., R.S. and A.M.; writing—review and editing, R.S. and A.M.; supervision, S.F., R.S. and A.M. All authors have read and agreed to the published version of the manuscript.

Funding: This research was funded by Italian Ministry of University and Research—Proof of Concept 2018, grant number PEPPLA POC 01_00054 to A.M. and Università di Catania—linea PIACERI, grant number ARVEST.

Acknowledgments: The authors are grateful to Francesca Re (University of Milano-Bicocca), Salvatore Oddo (University of Messina), Vito De Pinto (University of Catania) and Andrea Magri (University of Catania) for their valuable support, and to Maria Teresa Carri (Rome, University of Tor Vergata) for providing all NSC34 cells used in the work. Authors also acknowledge Fondi di Ateneo 2020–2022, Università di Catania, linea Open Access. The mass spectrometry proteomics data have been deposited to the ProteomeXchange Consortium (<http://proteomecentral.proteomexchange.org>) via the PRIDE [60] partner repository with the dataset identifier <PXD022598>.

Conflicts of Interest: The authors declare no conflict of interest.

References

1. Pasinelli, P.; Brown, R.H. Molecular biology of amyotrophic lateral sclerosis: Insights from genetics. *Nat. Rev. Neurosci.* **2006**, *7*, 710–723. [[CrossRef](#)] [[PubMed](#)]
2. Brown, R.H.; Al-Chalabi, A. Amyotrophic Lateral Sclerosis. *N. Engl. J. Med.* **2017**, *377*, 162–172. [[CrossRef](#)] [[PubMed](#)]
3. Barber, S.C.; Mead, R.J.; Shaw, P.L. Oxidative stress in ALS: A mechanism of neurodegeneration and a therapeutic target. *Biochim. Biophys. Acta* **2006**, *1762*, 1051–1067. [[CrossRef](#)] [[PubMed](#)]

4. Massaad, C.A.; Klann, E. Reactive Oxygen Species in the Regulation of Synaptic Plasticity and Memory. *Antioxid. Redox Signal.* **2011**, *14*, 2013–2054. [[CrossRef](#)]
5. Marden, J.J.; Harraz, M.M.; Williams, A.J.; Nelson, K.; Luo, M.; Paulson, H.; Engelhardt, J.F. Redox modifier genes in amyotrophic lateral sclerosis in mice. *J. Clin. Investig.* **2007**, *117*, 2913–2919. [[CrossRef](#)]
6. Zuo, L.; Zhou, T.; Pannel, B.K.; Ziegler, A.C.; Best, T.M. Biological and physiological role of reactive oxygen species—the good, the bad and the ugly. *Acta Physiol.* **2015**, *214*, 329–348. [[CrossRef](#)]
7. Kaur, S.J.; McKeown, S.R.; Rashid, S. Mutant Sod1 mediated pathogenesis of amyotrophic lateral sclerosis. *Gene* **2016**, *577*, 109–118. [[CrossRef](#)]
8. Vande Velde, C.; Miller, T.M.; Cashman, N.R.; Cleveland, D.W. Selective association of misfolded ALS-linked mutant SOD1 with the cytoplasmic face of mitochondria. *Proc. Natl. Acad. Sci. USA* **2008**, *105*, 4022–4027. [[CrossRef](#)]
9. Ferri, A.; Cozzolino, M.; Crosio, C.; Nencini, M.; Casciati, A.; Gralla, E.B.; Rotilio, G.; Valentine, J.S.; Carri, M.T. Familial ALS-superoxide dismutases associate with mitochondria and shift their redox potentials. *Proc. Natl. Acad. Sci. USA* **2006**, *103*, 13860–13865. [[CrossRef](#)] [[PubMed](#)]
10. Magri, A.; Belfiore, R.; Reina, S.; Tomasello, M.F.; Di Rosa, M.C.; Guarino, F.; Leggio, L.; De Pinto, V.; Messina, A. Hexokinase I N-terminal based peptide prevents the VDAC1-SOD1 G93A interaction and re-establishes ALS cell viability. *Sci. Rep.* **2016**, *6*, 34802. [[CrossRef](#)] [[PubMed](#)]
11. Israelson, A.; Arbel, N.; Da Cruz, S.; Ilieva, H.; Yamanaka, K.; Shoshan-Barmatz, V.; Cleveland, D.W. Misfolded Mutant SOD1 Directly Inhibits VDAC1 Conductance in a Mouse Model of Inherited ALS. *Neuron* **2010**, *67*, 575–587. [[CrossRef](#)]
12. Magri, A.; Di Rosa, M.C.; Orlandi, I.; Guarino, F.; Reina, S.; Guarnaccia, M.; Morello, G.; Spampinato, A.; Cavallaro, S.; Messina, A.; et al. Deletion of Voltage-Dependent Anion Channel 1 knocks mitochondria down triggering metabolic rewiring in yeast. *Cell. Mol. Life Sci.* **2020**, *77*, 3195–3213. [[CrossRef](#)]
13. Leggio, L.; Guarino, F.; Accardi-Gheit, R.; Reina, S.; Specchia, V.; Damiano, F.; Tomasello, M.F.; Tommasino, M.; Messina, A. Mechanism of translation control of the alternative *Drosophila melanogaster* Voltage Dependent Anion-selective Channel 1 mRNAs. *Sci. Rep.* **2018**, *8*, 5347. [[CrossRef](#)]
14. Guarino, F.; Zinghirino, F.; Mela, L.; Pappalardo, X.G.; Ichas, F.; De Pinto, V.; Messina, A. NRF-1 and HIF-1 α contribute to modulation of human VDAC1 gene promoter during starvation and hypoxia in HeLa cells. *Biochim. Biophys. Acta Bioenerg.* **2020**, *1861*, 148289. [[CrossRef](#)] [[PubMed](#)]
15. Keinan, N.; Tyomikin, D.; Shoshan-Barmatz, V. Oligomerization of the Mitochondrial Protein Voltage-Dependent Anion Channel Is Coupled to the Induction of Apoptosis. *Mol. Cell. Biol.* **2010**, *30*, 5698–5709. [[CrossRef](#)]
16. Reina, S.; De Pinto, V. Anti-cancer compounds targeted to VDAC: Potential and perspectives. *Curr. Med. Chem.* **2017**, *24*, 4447–4469. [[CrossRef](#)]
17. Magri, A.; Reina, S.; De Pinto, V. VDAC1 as pharmacological target in cancer and neurodegeneration: Focus on its role in apoptosis. *Front. Chem.* **2018**, *6*, 108. [[CrossRef](#)]
18. Zilocchi, M.; Moutaoufik, M.T.; Jessulat, M.; Phanse, S.; Aly, K.A.; Babu, M. Misconnecting the dots: Altered mitochondrial protein-protein interactions and their role in neurodegenerative disorders. *Expert Rev. Proteom.* **2020**, *17*, 119–136. [[CrossRef](#)]
19. Martel, C.; Wang, Z.; Brenner, C. VDAC phosphorylation, a lipid sensor influencing the cell fate. *Mitochondrion* **2014**, *19*, 69–77. [[CrossRef](#)]
20. Yu, H.; Diao, H.; Wang, C.; Lin, Y.; Yu, F.; Lu, H.; Xu, W.; Li, Z.; Shi, H.; Zhao, S.; et al. Acetylproteomic analysis reveals functional implications of lysine acetylation in human spermatozoa (sperm). *Mol. Cell. Proteom.* **2015**, *14*, 1009–1023. [[CrossRef](#)]
21. Yang, M.; Camara, A.K.; Wakim, B.T.; Zhou, Y.; Gadicherla, A.K.; Kwok, W.M.; Stowe, D.F. Tyrosine nitration of voltage-dependent anion channels in cardiac ischemia-reperfusion: Reduction by peroxynitrite scavenging. *Biochim. Biophys. Acta* **2012**, *1817*, 2049–2059. [[CrossRef](#)]
22. Saletti, R.; Reina, S.; Pittalà, M.G.G.; Magri, A.; Cunsolo, V.; Foti, S.; De Pinto, V. Post-translational modifications of VDAC1 and VDAC2 cysteines from rat liver mitochondria. *Biochim. Biophys. Acta Bioenerg.* **2018**, *1859*, 806–816. [[CrossRef](#)]
23. Reina, S.; Pittalà, M.G.G.; Guarino, F.; Messina, A.; De Pinto, V.; Foti, S.; Saletti, R. Cysteine Oxidations in Mitochondrial Membrane Proteins: The Case of VDAC Isoforms in Mammals. *Front. Cell. Dev. Biol.* **2020**, *8*, 397. [[CrossRef](#)]

24. Reina, S.; Checchetto, V.; Saletti, R.; Gupta, A.; Chaturvedi, D.; Guardiani, C.; Guarino, F.; Scorciapino, M.A.; Magri, A.; Foti, S.; et al. VDAC3 as a sensor of oxidative state of the intermembrane space of mitochondria: The putative role of cysteine residue modifications. *Oncotarget* **2016**, *7*, 2249–2268. [[CrossRef](#)]
25. Sarraf, S.A.; Raman, M.; Guarani-Pereira, V.; Sowa, M.E.; Huttlin, E.L.; Gygi, S.P.; Harper, J.W. Landscape of the PARKIN-dependent ubiquitylome in response to mitochondrial depolarization. *Nature* **2013**, *496*, 372–376. [[CrossRef](#)]
26. Herst, P.M.; Rowe, M.R.; Carson, G.M.; Berridge, M.V. Functional Mitochondria in Health and Disease. *Front. Endocrinol.* **2017**, *8*, 296.
27. Hoogerheide, D.P.; Gurnev, P.A.; Rostovtseva, T.K.; Bezrukov, S.M. Effect of a post-translational modification mimic on protein translocation through a nanopore. *Nanoscale* **2020**, *12*, 11070–11078. [[CrossRef](#)]
28. Pittalà, M.G.G.; Saletti, R.; Reina, S.; Cunsolo, V.; De Pinto, V.; Foti, S. A High Resolution Mass Spectrometry Study Reveals the Potential of Disulfide Formation in Human Mitochondrial Voltage-Dependent Anion Selective Channel Isoforms (hVDACs). *Int. J. Mol. Sci.* **2020**, *21*, 1468. [[CrossRef](#)]
29. De Pinto, V.; Benz, R.; Caggese, C.; Palmieri, F. Characterization of the mitochondrial porin from *Drosophila melanogaster*. *Biochim. Biophys. Acta* **1989**, *905*, 499–502. [[CrossRef](#)]
30. Mackie, M.; Rütther, P.; Samodova, D.; Di Gianvincenzo, F.; Granzotto, C.; Lyon, D.; Pegg, D.A.; Howard, H.; Harrison, L.; Jensen, L.J.; et al. Palaeoproteomic Profiling of Conservation Layers on a 14th Century Italian Wall Painting. *Angew. Chem. Int. Ed.* **2018**, *57*, 7369–7374. [[CrossRef](#)]
31. Cox, J.; Hein, M.Y.; Lubner, C.A.; Paron, I.; Nagaraj, N.; Mann, M. Accurate Proteome-wide Label-free Quantification by Delayed Normalization and Maximal Peptide Ratio Extraction, Termed MaxLFQ. *Mol. Cell. Proteom.* **2014**, *13*, 2513–2526. [[CrossRef](#)]
32. Guan, Z.Q.; Yates, N.A.; Bakhtiar, R. Detection and characterization of methionine oxidation in peptides by collision-induced dissociation and electron capture dissociation. *J. Am. Soc. Mass Spectrom.* **2003**, *14*, 605–613. [[CrossRef](#)]
33. Galliano, F.; Saletti, R.; Cunsolo, V.; Foti, S.; Marletta, D.; Bordonaro, S.; D'Urso, G. Identification and characterization of a new β -casein variant in goat milk by high-performance liquid chromatography with electrospray ionization mass spectrometry and matrix-assisted laser desorption/ionization mass spectrometry. *Rapid Commun. Mass Spectrom.* **2004**, *18*, 1972–1982. [[CrossRef](#)]
34. Cunsolo, V.; Muccilli, V.; Saletti, R.; Foti, S. Applications of mass spectrometry techniques in the investigation of milk proteome. *Eur. J. Mass Spectrom.* **2011**, *17*, 305–320. [[CrossRef](#)]
35. Ujwal, R.; Cascio, D.; Colletier, J.P.; Fahama, S.; Zhanga, J.; Torod, L.; Ping, P.; Abramson, J. The crystal structure of mouse VDAC1 at 2.3 Å resolution reveals mechanistic insights into metabolite gating. *Proc. Natl. Acad. Sci. USA* **2008**, *105*, 17742–17747. [[CrossRef](#)]
36. Didonna, A.; Benetti, F. Post-translational modifications in neurodegeneration. *AIMS Biophys.* **2016**, *3*, 27–49. [[CrossRef](#)]
37. Michalska, P.; When, R.L. It Comes to an End: Oxidative Stress Crosstalk with Protein Aggregation and Neuroinflammation Induce Neurodegeneration. *Antioxidants* **2020**, *9*, 740. [[CrossRef](#)]
38. Shadel, G.S.; Horvath, T.L. Mitochondrial ROS Signaling in Organismal Homeostasis. *Cell* **2015**, *163*, 560–569. [[CrossRef](#)]
39. Andrus, P.K.; Fleck, T.J.; Gurney, M.E.; Hall, E.D. Protein oxidative damage in a transgenic mouse model of familial amyotrophic lateral sclerosis. *J. Neurochem.* **1998**, *71*, 2041–2048. [[CrossRef](#)]
40. Niebroj-Dobosz, I.; Dziewulska, D.; Kwiecinski, H. Oxidative damage to proteins in the spinal cord in amyotrophic lateral sclerosis (ALS). *Folia Neuropathol.* **2004**, *42*, 151–156.
41. Wright, G.S.A.; Antonyuk, S.V.; Hasnain, S.S. The biophysics of superoxide dismutase-1 and amyotrophic lateral sclerosis. *Q. Rev. Biophys.* **2019**, *52*, e12. [[CrossRef](#)]
42. Martins, D.; English, A.M. SOD1 oxidation and formation of soluble aggregates in yeast: Relevance to sporadic ALS development. *Redox Biol.* **2014**, *26*, 632–639. [[CrossRef](#)]
43. Banks, C.J.; Andersen, J.L. Mechanisms of SOD1 regulation by post-translational modifications. *Redox Biol.* **2019**, *26*, 101270. [[CrossRef](#)]
44. Schmitt, N.D.; Agar, J.N. Parsing Disease-relevant Protein Modifications from Epiphenomena: Perspective on the Structural Basis of SOD1-Mediated ALS. *J. Mass Spectrom.* **2017**, *52*, 480–491. [[CrossRef](#)]

45. D'Angelo, S.; Trojsi, F.; Salvatore, A.; Daniele, L.; Raimo, M.; Galletti, P.; Monsurrò, M.R. Accumulation of altered aspartyl residues in erythrocyte membrane proteins from patients with sporadic amyotrophic lateral sclerosis. *Neurochem. Int.* **2013**, *63*, 626–634. [[CrossRef](#)]
46. Kametani, F.; Obi, T.; Shishido, T.; Akatsu, H.; Murayama, S.; Saito, Y.; Yoshida, M.; Hasegawa, M. Mass spectrometric analysis of accumulated TDP-43 in amyotrophic lateral sclerosis brains. *Sci Rep.* **2016**, *6*, 23281. [[CrossRef](#)]
47. Bayrhuber, M.; Meins, T.; Habeck, M.; Becker, S.; Giller, K.; Villinger, S.; Vonnrhein, C.; Griesinger, C.; Zweckstetter, M.; Zeth, K. Structure of the human voltage-dependent anion channel. *Proc. Natl. Acad. Sci. USA* **2008**, *105*, 15370–15375. [[CrossRef](#)]
48. Hiller, S.; Garces, R.G.; Malia, T.J.; Orekhov, V.Y.; Colombini, M.; Wagner, G. Solution structure of the integral human membrane protein VDAC-1 in detergent micelles. *Science* **2008**, *321*, 1206–1210. [[CrossRef](#)]
49. De Pinto, V.; Al Jamal, J.A.; Benz, R.; Genchi, G.; Palmieri, F. Characterization of SH groups in porin of bovine heart mitochondria. Porin cysteines are localized in the channel walls. *J. Biochem.* **1991**, *202*, 903–911. [[CrossRef](#)]
50. Aram, L.; Geula, S.; Arbel, N.; Shoshan-Barmatz, V. VDAC1 cysteine residues: Topology and function in channel activity and apoptosis. *Biochem. J.* **2010**, *427*, 445–454. [[CrossRef](#)]
51. Ravera, S.; Bonifacino, T.; Bartolucci, M.; Milanese, M.; Gallia, E.; Cortese, K.; Pandolfi, I.; Bonanno, G. Characterization of the Mitochondrial Aerobic Metabolism in the Pre- and Perisynaptic Districts of the SOD1G93A Mouse Model of Amyotrophic Lateral Sclerosis. *Mol. Neurobiol.* **2018**, *55*, 9220–9233. [[CrossRef](#)] [[PubMed](#)]
52. Wright, H.T. Nonenzymatic deamidation of asparaginyl and glutaminyl residues in proteins. *Crit. Rev. Biochem. Mol. Biol.* **1991**, *26*, 1–52. [[CrossRef](#)] [[PubMed](#)]
53. Robinson, N.E.; Robinson, Z.W.; Robinson, B.R.; Robinson, A.L.; Robinson, J.A.; Robinson, M.L.; Robinson, A.B. Structure-dependent nonenzymatic deamidation of glutaminyl and asparaginyl pentapeptides. *J. Pept. Res.* **2004**, *63*, 426–436. [[CrossRef](#)]
54. Mikkat, S.; Kischstein, T.; Kreutzer, M.; Glocker, M.O. Mass spectrometric peptide analysis of 2DE-separated mouse spinal cord and rat hippocampus proteins suggests an NGxG motif of importance for in vivo deamidation. *Electrophoresis* **2013**, *34*, 1610–1618. [[CrossRef](#)]
55. Robinson, N.E.; Robinson, M.L.; Schulze, E.S.; Lai, B.T.; Gray, H.B. Deamidation of alpha-synuclein. *Protein Sci.* **2009**, *18*, 1766–1773. [[CrossRef](#)]
56. Bastrup, J.; Kastaniegaard, K.; Asuni, A.A.; Volbracht, C.; Stensballe, A. Proteomic and Unbiased Post-Translational Modification Profiling of Amyloid Plaques and Surrounding Tissue in a Transgenic Mouse Model of Alzheimer's Disease. *J. Alzheimer's Dis.* **2020**, *73*, 393–411. [[CrossRef](#)]
57. Sadakane, Y.; Kawahara, M. Implications of Metal Binding and Asparagine Deamidation for Amyloid Formation. *Int. J. Mol. Sci.* **2018**, *19*, 2449. [[CrossRef](#)]
58. Shimizu, T.; Watanabe, A.; Ogawara, M.; Mori, H.; Shirasawa, T. Isoaspartate formation and neurodegeneration in Alzheimer's disease. *Arch. Biochem. Biophys.* **2000**, *381*, 225–234. [[CrossRef](#)]
59. Ayers, J.I.; Fromholt, S.E.; O'Neal, V.O.; Diamond, J.H.; Borchelt, D.R. Prion-like propagation of mutant SOD1 misfolding and motor neuron disease spread along neuroanatomical pathways. *Acta Neuropathol.* **2016**, *131*, 103–114. [[CrossRef](#)]
60. Perez-Riverol, Y.; Csordas, A.; Bai, J.; Bernal-Llinares, M.; Hewapathirana, S.; Kundu, D.J.; Inuganti, A.; Griss, J.; Mayer, G.; Eisenacher, M.; et al. The PRIDE database and related tools and resources in 2019: Improving support for quantification data. *Nucleic Acids Res.* **2019**, *47*, D442–D450. [[CrossRef](#)]

Publisher's Note: MDPI stays neutral with regard to jurisdictional claims in published maps and institutional affiliations.



© 2020 by the authors. Licensee MDPI, Basel, Switzerland. This article is an open access article distributed under the terms and conditions of the Creative Commons Attribution (CC BY) license (<http://creativecommons.org/licenses/by/4.0/>).

Article 5.

International Journal of Molecular Sciences

Specific Post-translational Modifications of VDAC3 in ALS-SOD1 Model Cells Identified by High-Resolution Mass Spectrometry

Maria Gaetana Giovanna Pittalà¹, Simona Reina², Stefano Conti Nibali², Annamaria Cucina¹, Salvatore Antonio Maria Cubisino², Vincenzo Cunsolo¹, Giuseppe Federico Amodeo³, Salvatore Foti¹, Vito De Pinto², Rosaria Saletti¹, Angela Messina⁴

¹ Organic Mass Spectrometry Laboratory, Department of Chemical Sciences, University of Catania, Via S.Sofia 64, 95123 Catania, Italy

² Department of Biomedical and Biotechnological Sciences, University of Catania, Via S.Sofia 64, 95123, Catania, Italy

³ Department of Neurology, Columbia University, New York, NY 10032, USA

⁴ Department of Biological, Geological and Environmental Sciences, University of Catania, Via S.Sofia 64, 95123 Catania, Italy



Article

Specific Post-Translational Modifications of VDAC3 in ALS-SOD1 Model Cells Identified by High-Resolution Mass Spectrometry

Maria Gaetana Giovanna Pittalà ¹, Simona Reina ², Stefano Conti Nibali ², Annamaria Cucina ¹ , Salvatore Antonio Maria Cubisino ², Vincenzo Cunsolo ¹ , Giuseppe Federico Amodeo ³ , Salvatore Foti ¹ , Vito De Pinto ² , Rosaria Saletti ^{1,*} and Angela Messina ⁴

¹ Organic Mass Spectrometry Laboratory, Department of Chemical Sciences, University of Catania, Via S. Sofia 64, 95123 Catania, Italy

² Department of Biomedical and Biotechnological Sciences, University of Catania, Via S. Sofia 64, 95123 Catania, Italy

³ Department of Neurology, Columbia University, New York, NY 10032, USA

⁴ Department of Biological, Geological and Environmental Sciences, University of Catania, Via S. Sofia 64, 95123 Catania, Italy

* Correspondence: rsaletti@unict.it; Tel.: +39-095-738-5026

Abstract: Damage induced by oxidative stress is a key driver of the selective motor neuron death in amyotrophic lateral sclerosis (ALS). Mitochondria are among the main producers of ROS, but they also suffer particularly from their harmful effects. Voltage-dependent anion-selective channels (VDACs) are the most represented proteins of the outer mitochondrial membrane where they form pores controlling the permeation of metabolites responsible for mitochondrial functions. For these reasons, VDACs contribute to mitochondrial quality control and the entire energy metabolism of the cell. In this work we assessed in an ALS cell model whether disease-related oxidative stress induces post-translational modifications (PTMs) in VDAC3, a member of the VDAC family of outer mitochondrial membrane channel proteins, known for its role in redox signaling. At this end, protein samples enriched in VDACs were prepared from mitochondria of an ALS model cell line, NSC34 expressing human SOD1G93A, and analyzed by nUHPLC/High-Resolution nESI-MS/MS. Specific over-oxidation, deamidation, succination events were found in VDAC3 from ALS-related NSC34-SOD1G93A but not in non-ALS cell lines. Additionally, we report evidence that some PTMs may affect VDAC3 functionality. In particular, deamidation of Asn215 alone alters single channel behavior in artificial membranes. Overall, our results suggest modifications of VDAC3 that can impact its protective role against ROS, which is particularly important in the ALS context. Data are available via ProteomeXchange with identifier PXD036728.

Keywords: voltage dependent anion channel; post-translational modifications; over-oxidation; deamidation; succination; amyotrophic lateral sclerosis; SOD1; mitochondria; neurodegeneration; high-resolution mass spectrometry



Citation: Pittalà, M.G.G.; Reina, S.; Nibali, S.C.; Cucina, A.; Cubisino, S.A.M.; Cunsolo, V.; Amodeo, G.F.; Foti, S.; De Pinto, V.; Saletti, R.; et al. Specific Post-Translational Modifications of VDAC3 in ALS-SOD1 Model Cells Identified by High-Resolution Mass Spectrometry. *Int. J. Mol. Sci.* **2022**, *23*, 15853. <https://doi.org/10.3390/ijms232415853>

Academic Editor: Takahiko Shimizu

Received: 11 October 2022

Accepted: 6 December 2022

Published: 13 December 2022

Publisher's Note: MDPI stays neutral with regard to jurisdictional claims in published maps and institutional affiliations.



Copyright: © 2022 by the authors. Licensee MDPI, Basel, Switzerland. This article is an open access article distributed under the terms and conditions of the Creative Commons Attribution (CC BY) license (<https://creativecommons.org/licenses/by/4.0/>).

1. Introduction

Amyotrophic lateral sclerosis (ALS) is an adult neurodegenerative disease characterized by the progressive loss of upper and lower motor neurons in the spinal cord and brainstem [1]. From its onset, the disease progresses rapidly, leading the patient to death [2]. To date, there are no effective treatments to counteract the outcome of the disease.

About 10% of ALS cases are associated with genetic defects (familial ALS, fALS), while the most common forms are sporadic (sALS, about 90–95% of cases). Although various environmental factors have been indicated as being responsible for sALS, the importance of the genetic component has also been demonstrated for these more common forms of the disease [3].

The Cu/Zn superoxide dismutase (SOD1) gene is responsible for about 20% of fALS cases [4] and SOD1 misfolded wild-type (SOD1WT) toxicity is involved in the pathogenesis of sALS where the toxic gain of function is due to redox disturbance that changes the biophysical properties of native SOD1 protein [5].

The exact mechanism of neurotoxicity associated with SOD1 mutants remains unknown, although several hypotheses have been proposed to elucidate the toxic effects dependent on mutated SOD1 and the subsequent neurodegeneration observed in ALS. These include mitochondrial dysfunction, oxidative stress, excitotoxicity caused by aberrant glutamate signaling, endoplasmic reticulum stress, and protein aggregation [6].

In particular, in NSC34 cells expressing the human SOD1 G93A ALS-associated mutant, oxidative stress was greater than in normal NSC34 cells or those transfected with wild-type human SOD1 [7,8]. In addition, the affected tissues of ALS patients are characterized by extensive mitochondrial dysfunction and oxidative damage to proteins, lipids, and nucleic acids as a result of an imbalance between free radical production and degradation [6,9]. It has been shown that, in the spinal cord of ALS patients, VDAC1, the most abundant of the mitochondrial porins called Voltage-Dependent Anion selective Channels (VDAC), is the docking site on the surface of mitochondria for SOD1-G93A mutants [10]. The interaction of VDAC1 with mutant SOD1 hinders the binding of cytosolic hexokinase I (HKI) and probably other physiological interactors, causing several dramatic consequences for mitochondrial function [11]. VDACs are relevant components of the outer mitochondrial membrane (OMM) whose main role is to form water-filled pores that allow the exchange of metabolites and molecules to and from the mitochondrion. In mammals, three genes encode three highly conserved isoforms named VDAC1, VDAC2 and VDAC3, agreeing to the order of their discovery. Under physiological conditions, VDACs play numerous roles in cellular metabolism and mitochondrial function [12] by interacting with important molecules involved in survival pathways. On the other hand, defective VDAC channels are associated with a myriad of cellular disease states such as cancer, diabetes, viral infections, and neurodegenerative diseases such as ALS but also Alzheimer's disease and Parkinson's disease [13,14].

In general, these diseases are not directly related to a single defective VDAC isoform, but mitochondria in the tissues of affected patients show morphological and biochemical abnormalities with alterations in protein-protein interactions [15].

Post-translational modifications (PTMs) are implicated in many cellular events as they modulate and alter the range of possible functions of proteins as well as make changes to their structure [16]. The PTMs of a protein can, thus, affect its localization, turnover, activity status, and interactions with other proteins [17].

The full set of PTMs that regulate the interactions of VDACs with other cytosolic and mitochondrial proteins is still an understudied field [18]. In recent years, the development of nano-reverse phase ultra-high performance liquid chromatography (nanoRP-UHPLC) and ultrasensitive high resolution mass spectrometry (HRMS) methods has expanded knowledge in this field [19]. However, there are still few studies on PTMs of VDAC proteins in pathological conditions such as neurodegeneration [19].

Recently, using mass spectrometry-based methods, we demonstrated for the first time that VDAC1 from a SOD1-ALS model cell line undergoes specific deamidation of asparagine and glutamine residues [20]. Bioinformatic analysis revealed increased channel instability in deamidated VDAC1, which is responsible for a broad conformational change that may alter the physiological pool of interactors and increase the binding of ALS-related mutant forms of SOD1 [20].

Although, the role of VDAC1 in neurodegeneration is well known [12,21,22], the involvement of the other two isoforms in these pathways remains poorly defined.

This is probably due to the greater relative abundance of VDAC1 compared with the other isoforms. In particular, although VDAC3 is the least abundant and least studied isoform, important functional roles, as an oxidative stress sensor or tumor suppressor, have been proposed for this isoform in cellular and animal models [16,23].

In this work, by combining HRMS analysis with “*in-solution*” digestion of an enriched fraction of VDACs, in VDAC3 purified from NSC34-SOD1G93A model ALS-SOD1 cells, we identified specific irreversible PTMs that can destabilize the channel by impacting its function.

2. Results

This work follows our previous study on NSC34 model SOD1-ALS cells. In that work, we had identified specific post-translational modifications in VDAC1 that can lead to important changes in the channel structure and, thus, in the bioenergetic metabolism of ALS motor neurons [20]. Considering that changes found are most likely consequential to the high levels of oxidative stress typical of motor neurons affected by ALS, in this work we wanted to extend our analysis also to the VDAC3 isoform purified from ALS-related NSC34-SOD1G93A cells and, as a control, from NSC34-SOD1WT or NSC34 cells. Recently, we established the important role played by VDAC3, but not VDAC1, in the cellular response to ROS-induced oxidative stress, showing in particular that VDAC3 cysteines are essential for the ability of the protein to control mitochondrial ROS homeostasis [24]. In particular, by using HRMS analysis we searched oxidized or succinate cysteines, oxidized or dioxidized methionines, ubiquitinated lysines, phosphorylated serines/threonines/tyrosines, citrullinated arginines, cysteinylated and deamidated asparagines and glutamines. Protein reduction and alkylation were performed before the purification of VDACs from mitochondria, to rule out the possibility of non-specific and/or unwanted oxidation occurring during the purification protocol. Hydroxyapatite (HTP) eluates were digested *in-solution* using trypsin and chymotrypsin, and then the highly complex enzyme peptide mixtures were analyzed in triplicate (technical replicates) by liquid chromatography–high resolution mass spectrometry.

The *Mus musculus* VDAC3 sequence (SwissProt Acc. N. Q60931) includes two methionines at positions 26 and 155, and six cysteines at positions 2, 8, 36, 65, 122, and 229. The numbering adopted here starts from Met¹, which is actually absent in the mature protein as confirmed by our MS data (Figure 1) and similar to rat and human VDAC3 isoforms [25,26].

2	CNTPTYCDLGKAAKDVFNKGYGFGMVKIDLK TKSCSGVEF STSGHAYTDTGKASGNLET	60
61	KYKVCNYGLTFTQK WNTDNTLGTEISWEN KLAEGLKLTLDTIFVPNTGKKSGKLGKASYRR	120
121	DCFSLGSNVDIDFSGPTIYGWAVLAFEGWLAGYQMSFDTAKSKLSQNNFALGYKAADFQL	180
181	HTHVNDGTEFGGSIYQKVNERIETSINLAWTAGSNTRFGIAAKY KLDCRTLSAKVNNA	240
241	SLIGLGYTQTLRPGVKLTLSALIDGKNFNAGGHKVG LGFELEA	283

Figure 1. Sequence coverage map of VDAC3 from NSC34, NSC34-SOD1WT and NSC34-SOD1G93A cell lines obtained by tryptic and chymotryptic digestion. The solid line indicates the sequence that was obtained from tryptic peptides; dotted lines: sequence obtained from chymotryptic peptides. Unique tryptic (indicated in bold and blue) and chymotryptic (indicated in bold and black) peptides originating from missed cleavages were used to distinguish and cover the sequences shared by isoforms. Sequences shared by multiple isoforms are shown in red. Sequence numbering considered the starting methionine residue, which is eliminated during protein maturation.

The results obtained from tryptic and chymotryptic fragments analyses yielded 98.9% protein coverage (279 of 282 amino acid residues) (Figure 1), with the exception of the dipeptide Arg119-Arg120 and Tyr225. Although some tryptic peptides are shared among the three VDAC isoforms, due to the identification of unique peptides originating from missed cleavages, the obtained sequence coverage unambiguously identifies the mouse VDAC3 protein (Figure 1). MS analysis performed on samples of VDAC3 prepared by the same procedure but purified from another set of cell cultures of NSC34, NSC34-SOD1WT, and NSC34-SOD1G93A (biological replicates) confirmed the results obtained and the reproducibility of the experimental data produced (data not shown).

2.1. Mass Spectrometry Analysis of VDAC3 from NSC34 Cell Line

In the nanoRP-UHPLC/High-Resolution ESI-MS/MS analysis of the enzyme digests, Met²⁶ and Met¹⁵⁵ were identified in the normal form (Table S1, fragment 2, and Table S2, fragments 4, 21), and also in the sulfoxide form (Table S3, fragments 1, 5, 6, and Table S4, fragments 1, 2). Figure S1A,B shows the full scan and fragment ion mass spectra of the doubly charged molecular ion of the peptide GYGFGMVK with Met²⁶ modified as methionine sulfoxide (Figure S1A), and the triply charged molecular ion of the peptide DCFSLGSNVDIDFSGPTIYGWAVLAFEGWLAGYQMSFD TAK with Met¹⁵⁵ as methionine sulfoxide (Figure S1B). This oxidation was confirmed by the presence in the MS/MS spectra of the characteristic neutral loss of 64 Da corresponding to the ejection of methanesulfenic acid from the side chain of MetO [27].

Although from these data it was not possible to obtain a precise determination of the relative amount of Met and Met sulfoxide, by comparing the absolute intensities of the multiply charged molecular ions of the respective peptides, a rough estimate of their relative abundance could be achieved. These calculations indicated a ratio of about 10:1 and 0.5:1 MetO/Met for Met²⁶ (Table 1, Table 2, Tables S5 and S6) and Met¹⁵⁵ (Table 2 and Table S6), respectively.

Table 1. Ox/Red ratio (average and standard deviation) of the absolute intensities of the molecular ions of sulfur containing tryptic peptides found in the analysis of VDAC3 from NSC34, NSC34-SOD1WT, NSC34-SOD1G93A cell lines reduced with DTT, carboxyamidomethylated and digested in-solution.

Peptide	Position in the Sequence	Calculated Monoisotopic <i>m/z</i>	Cell Lines	Ratio Ox/Red	
				Avg	Dev St
GYGFG <u>M</u> VK		437.7103 (2+)	NSC34	10.1	0.85
GYGFGMVK	21–28	429.7128 (2+)	NSC34-SOD1G93A	- Met ²⁶ totally oxidized	-
SCSGVEFSTSGHAYTDTGK		991.4079 (2+)	NSC34	0.08	0.01
SCSGVEFSTSGHAYTDTGK	35–53	995.9260 (2+)	NSC34-SOD1WT	0.05	0.01
SCSGVEFSTSGHAYTDTGK			NSC34-SOD1G93A	0.05	0.01
YKVC <u>N</u> YGLTFTQK		806.8877 (2+)	NSC34	0.87	0.06
YKVCNYGLTFTQK	62–74	811.4060 (2+)	NSC34-SOD1WT	0.6	0.10
YKVCNYGLTFTQK			NSC34-SOD1G93A	0.67	0.12
DCFSLGSNVDIDFSGPTIYGWAVLA-FEGWLAGYQ <u>M</u> SFD TAK		1518.0315 (3+)	NSC34-SOD1WT	6.63	1.33
DCFSLGSNVDIDFSGPTIYGWAVLA-FEGWLAGYQMSFD TAK	121–161	1512.6995 (3+)	NSC34-SOD1G93A	- Met ¹⁵⁵ totally oxidized	-

C: cysteine carboxyamidomethylated; C: cysteine oxidized to sulfonic acid; M: methionine sulfoxide.

Table 2. Ox/Red ratio (average and standard deviation) of the absolute intensities of the molecular ions of sulfur containing chymotryptic peptides found in the analysis of VDAC3 from NSC34, NSC34-SOD1WT, NSC34-SOD1G93A cell lines reduced with DTT, carboxyamidomethylated and digested in-solution.

Peptide	Position in the Sequence	Calculated Monoisotopic m/z	Cell Lines	Ratio Ox/Red	
				Avg	Dev St
GFG <u>M</u> VKIDL		498.2657 (2+)	NSC34	11.73	2.23
			NSC34-SOD1WT	12.07	1.27
GFGMVKIDL	23–31	490.2682 (2+)	NSC34-SOD1G93A	- Met ²⁶ totally oxidized	-
Q <u>M</u> SFDTAKSKL	154–164	636.3192 (2+)	NSC34	0.50	0.30
QMSFDTAKSKL		628.3217 (2+)			
KLD <u>C</u> RTSL	226–233	492.2455 (2+)	NSC34	0.10	0
			NSC34-SOD1WT	0.53	0.15
KLDCRTSL		496.7638 (2+)	NSC34-SOD1G93A	0.33	0.15

C: cysteine carboxyamidomethylated; C: cysteine oxidized to sulfonic acid; M: methionine sulfoxide.

Furthermore, partial oxidation of Cys³⁶, Cys⁶⁵, and Cys²²⁹ to sulfonic acid (Table S3, fragments 2–4, and Table S4, fragment 3) was revealed (Figure S2A–C). Again, from the absolute intensities of the multiply charged molecular ions of the tryptic peptides with Cys oxidized to sulfonic acid compared with the same fragments with Cys in carboxyamidomethylated form, an Ox/Red ratio of about 0.08, 0.9, and 0.1 was observed for Cys³⁶, Cys⁶⁵, and Cys²²⁹, respectively (Tables 1 and 2). As for the other cysteine residues, Cys 2, 8, and 122 were detected exclusively in the carboxyamidomethylated form (Table S1, fragment 1; Table S2, fragments 1–3; Table S3, fragment 5), with Cys² totally acetylated (Table S1, fragment 1, and Table S2, fragments 1, 2) (Figure S3).

2.2. Mass Spectrometry Analysis of VDAC3 from NSC34-SOD1WT Cell Line

The PTMs identified on purified VDAC3 from NSC34-SOD1WT control cells, which express the wt form of human SOD1, are similar to those of VDAC3 from parental NSC34 control cells and similar to what has been shown previously for the VDAC1 isoform [20]. Specifically, in addition to the peptides containing methionines 26 and 155 in normal form (Table S7, fragments 2, 11, and Table S8, fragments 6, 7), peptides with these residues oxidized to methionine sulfoxide (Table S9, fragment 5, and Table S10, fragments 1, 2, and Figure S4A,B) were also detected. The MetO/Met ratio was approximately 12:1 for Met²⁶ (Table 2 and Table S12) and 7:1 for Met¹⁵⁵ (Table 1 and Table S11), respectively.

In addition, the partial oxidation of Cys³⁶ (Table S9, fragment 2), Cys⁶⁵ (Table S9, fragments 3 and 4) and Cys²²⁹ (Table S10, fragment 3) to sulfonic acid was determined (Figure S5A–C). The Ox/Red ratios of cysteines 36, 65 and 229 were 0.05, 0.6 and 0.5, respectively (Table 1, Table 2, Tables S11 and S12). In contrast, cysteines 8 and 122 were exclusively in the carboxyamidomethylated form (Table S7, fragments 1, 11 and Table S8, fragments 1–4).

Furthermore, unlike in NSC34 cells, we identified Cys² in both reduced and acetylated form (Table S7, fragment 1, and Table S8, fragments 1–3) (Figure S6), and in both non-acetylated and oxidized to sulfonic acid (Table S9, fragment 1, and Figure 2).

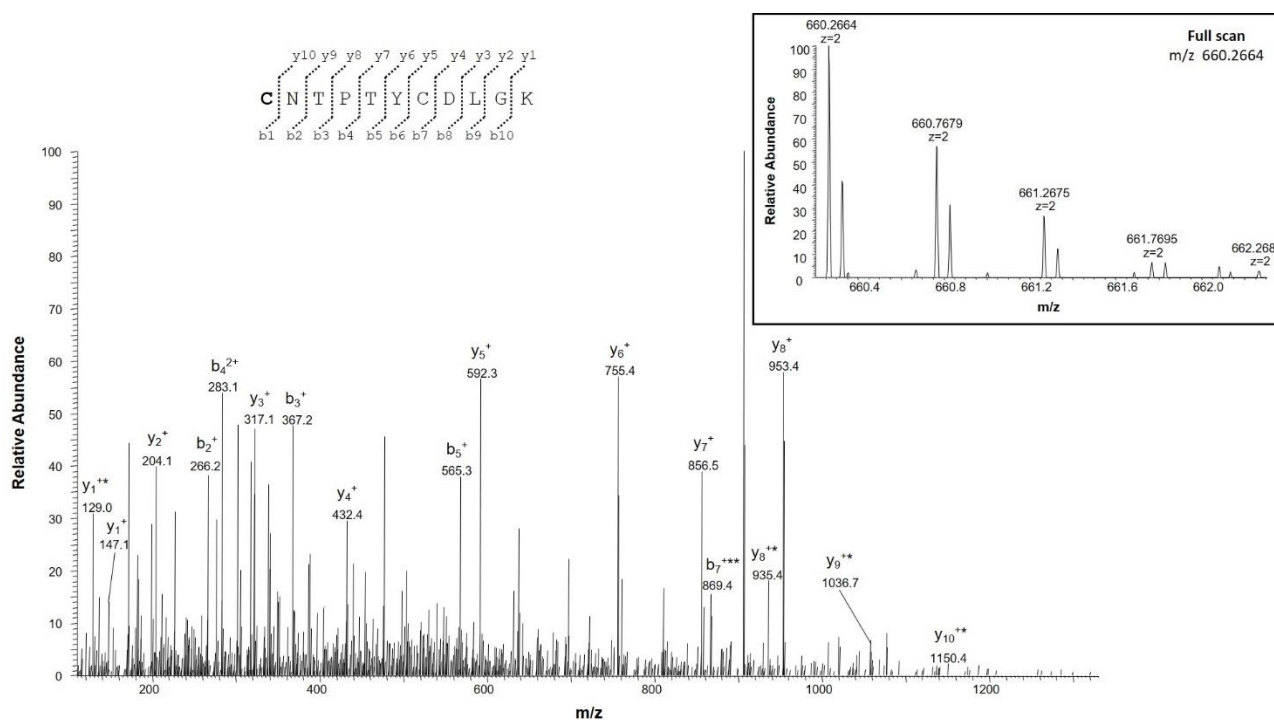


Figure 2. MS/MS spectrum of the doubly charged molecular ion at m/z 660.2664 (calculated 660.2663) of the N-terminal tryptic peptide of VDAC3 from NSC34-SOD1WT cell line with cysteine residue 2 in the form of sulfonic acid and cysteine residue 8 in the carboxyamidomethylated form. The inset shows the full scan mass spectrum of the molecular ion. Fragment ions originating from the neutral loss of H_2O are indicated by an asterisk. The fragment ion originating from the neutral loss of NH_3 is indicated by two asterisks.

2.3. Mass Spectrometry Analysis of VDAC3 from NSC34-SOD1G93A Cell Line

The same HRMS investigative approach was used to analyze PTMs of VDAC3 extracted from the ALS model NSC34-SOD1G93A cells, stably expressing the human SOD1G93A mutant. We identified Met²⁶ and Met¹⁵⁵ in the fully oxidized sulfoxide form (Tables 1 and 2, Table S13, fragments 2, 7, 8, Table S14, fragment 1) (Figure S7A,B). Moreover, cysteines 36, 65, and 229 were detected in both normal (Table S15, fragments 2–4, and Table S16, fragments 6, 37) and trioxidized form (Table S13, fragments 3–5, and Table S14, fragment 2) (Figure S8A–C), with an Ox/Red ratio of 0.06, 0.7, and 0.3, respectively (Table 1, Table 2, Tables S17 and S18).

In addition, complete carboxyamidomethylation of cysteines 8 and 122 was determined (Table S15, fragment 1; Table S16, fragments 1–4; Table S13, fragment 7). As in NSC34-SOD1WT cells, Cys² was identified in both reduced and acetylated form (Table S15, fragment 1; Table S16, fragments 1–3) (Figure S9), and both oxidized to sulfonic acid and were not acetylated (Table S13, fragment 1) (Figure S10).

2.4. Other Post-Translational Modifications of VDAC3

2.4.1. Succination, Ubiquitin and Ubiquitination, Phosphorylation, Citrullination, Cysteinylation, and Dioxidation

In addition to oxidations, other types of PTMs were sought in VDAC3 purified from all NSC34 cell lines analyzed. Specifically, we ascertained that in each of them, Cys⁶⁵ is succinated (Tables S19A–C and S20A–C) and in the NSC34-SOD1G93A ALS model cell line, this modification was interestingly present in greater amounts than in control cells (Table 3 and Figure S11A–C).

Table 3. Ox/Red ratio (average and standard deviation) of the absolute intensities of the molecular ions of tryptic peptides containing succinated and non-succinated cysteines found in the analysis of VDAC3 from NSC34, NSC34-SOD1WT, NSC34-SOD1G93A cell lines reduced with DTT, carboxyamidomethylated and digested in-solution.

Peptide	Position in the Sequence	Calculated Monoisotopic m/z	Cell Lines	Ratio Succinated/Red	
				Avg	Dev St
YKVCNYGLTFTQK	62–74	560.9367 (3+)	NSC34	0.3	0
YKVCNYGLTFTQK			NSC34-SOD1WT	0.40	0.10
YKVCNYGLTFTQK		811.4060 (2+)	NSC34-SOD1G93A	1.07	0.12

C: cysteine carboxyamidomethylated; C: cysteine succinated.

Furthermore, no ubiquitin and ubiquitination of lysine residues, phosphorylation of serine, threonine or tyrosine, citrullination of arginine, cysteinylolation, and dioxidation of methionines to sulfone were found.

2.4.2. Identification of Deamidation Sites

In this study, deamidation of asparagine and glutamines were identified exclusively in VDAC3 from the NSC34-SOD1G93A cell line, although deamidated glutamines were found in low amounts and the relative deamidate/normal ratio was, thus, not determined. Interestingly, we found that Asn²¹⁵ was converted to aspartate in significant amounts (deam/normal ratio 0.1) only in ALS cell model (Table 4 and Table S21, Table S22, fragments 4; Figure 3).

Table 4. Ox/Red ratio (average and standard deviation) of the absolute intensities of the molecular ions of tryptic peptides containing deamidated and non-deamidated asparagine found in the analysis of VDAC3 from NSC34-SOD1G93A cell line reduced with DTT, carboxyamidomethylated and digested in-solution.

Peptide	Position in the Sequence	Calculated Monoisotopic m/z	Ratio Deam/Norm	
			Avg	Dev St
WNTDNTLGTEISWENK	75–90	954.9344 (2+)	0.003	0
WNTDNTLGTEISWENK		954.4424 (2+)		
LTLDTIFVPNTGK	97–109	710.3904 (2+)	0.003	0
LTLDTIFVPNTGK		709.8984 (2+)		
LSQNNFALGYK	164–174	628.3197 (2+)	0.01	0
LSQNNFALGYK				
LSQNNFALGYK		627.8277 (2+)		
LSQNNFALGYK				
IETSINLAWTAGSNTR	202–218	924.9582 (2+)	0.1	0
IETSINLAWTAGSNTR		924.4662 (2+)		
VNNASLIGLGYTQTLRPGVK	237–256	701.3920 (3+)	0.01	0
VNNASLIGLGYTQTLRPGVK				
VNNASLIGLGYTQTLRPGVK		701.0640 (3+)		
VNNASLIGLGYTQTLRPGVK				

N: asparagine deamidated.

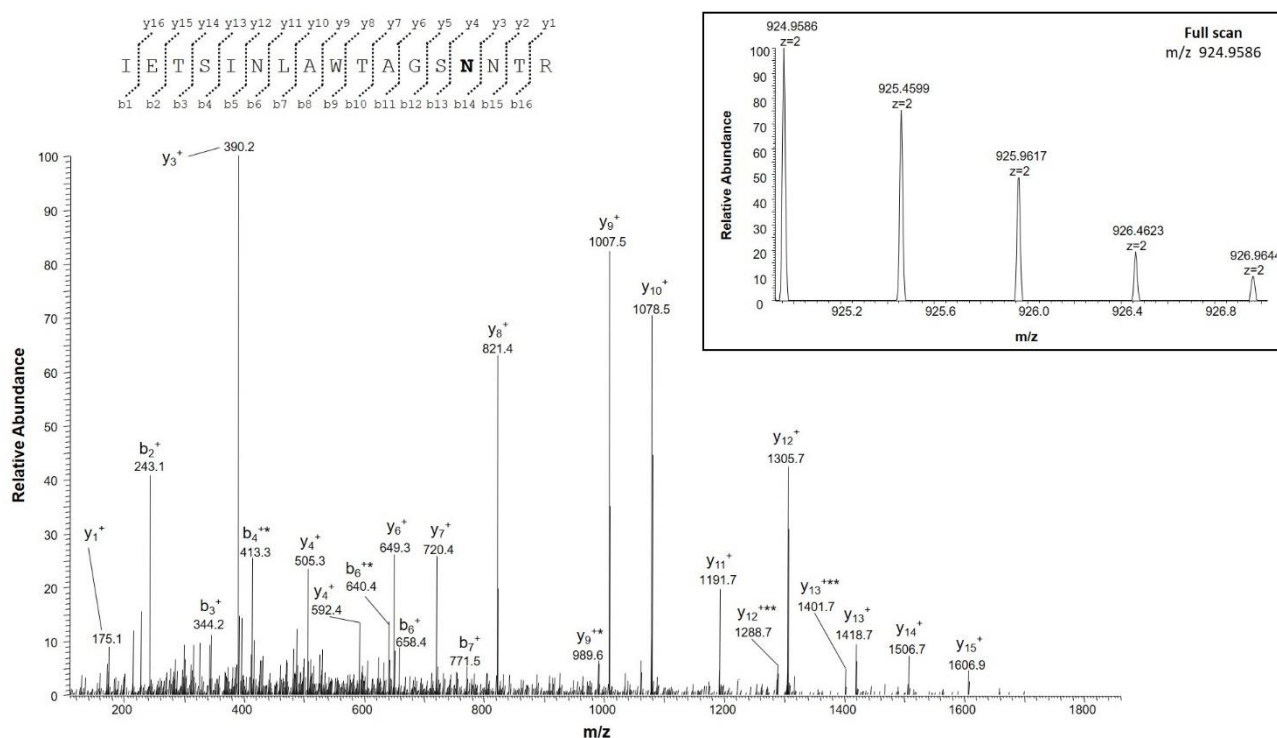


Figure 3. MS/MS spectrum of the doubly charged molecular ion at m/z 924.9586 (calculated 924.9582) of the VDAC3 tryptic peptide from NSC34-SOD1G93A cell line containing the asparagine residue 215 in the deamidated form. The inset shows the full scan mass spectrum of molecular ion. Fragment ions originated from the neutral loss of H_2O are indicated by an asterisk. Fragment ions originated from the neutral loss of NH_3 are indicated by two asterisks.

In contrast, asparagines 167, 238 and 239 were deamidated at minor level (deam/normal ratio 0.01) (Table 4 and Table S21, Table S22, fragments 3 and 5; Figure S12A–C), and asparagines 76, 106 and 168 were converted to aspartate only in trace amounts (deam/norm ratio 0.002–0.003) (Table 4 and Table S21, Table S22, fragments 1, 2, 3; Figure S12D–F).

In addition to Asn/Asp deamidation events, we analyzed VDAC3 for the presence of succinimide. Usually, succinimide intermediates are formed in the cell as a result of spontaneous deamidation of asparagine and dehydration of aspartic acid [28], and its accumulation represents a sign of aging or a response to cellular stress condition [29]. We identified succinimide at positions 167 and 168 of VDAC3 from all three cell lines studied (Tables S23–S25; Figure S13A–G), although with a different succ/norm ratio, and at position 238 only in the NSC34-SOD1WT cell line (Table S24, fragment 2; Figure S13H). It is worth noting that in the control NSC34 and NSC34-SOD1WT cell lines, asparagine-derived succinimide intermediates were visible in trace amounts (suc/norm ratio ranging from 0.002:1 to 0.004:1) (Table 5, Tables S26 and S27), whereas in the ALS model cell line NSC34-SOD1G93A they were observed in significantly larger amounts (Table 5 and Table S28).

Furthermore, the tryptic peptide Trp⁷⁵-Lys⁹⁰ containing Asp⁷⁶ as a succinimide intermediate and Asp⁷⁹ in the form of aspartate methyl ester, derived from the hydrolysis of succinimide to L-IsoAsp followed by enzymatic methylation [30], was detected only in the NSC34 and NSC34-SOD1WT cell lines (Table 6 and Figure S14A,B).

Table 5. Ox/Red ratio (average and standard deviation) of the absolute intensities of the molecular ions of tryptic peptides containing succinimide intermediate found in the analysis of VDAC3 from NSC34, NSC34-SOD1WT, NSC34-SOD1G93A cell lines reduced with DTT, carboxyamidomethylated and digested in-solution.

Peptide	Position in the Sequence	Calculated Monoisotopic m/z	Cell Lines	Ratio Succinimide/Norm	
				Avg	Dev St
<u>LSQNNFALGYK</u>	164–174	619.3144 (2+)	NSC34	0.002	0
LSQNNFALGYK			NSC34-SOD1WT	0.003	0
<u>LSQNNFALGYK</u>	237–256	627.8277 (2+)	NSC34-SOD1G93A	0.01	0
VNNASLIGLGYTQTLRPGVK			NSC34-SOD1WT	0.003	0
VNNASLIGLGYTQTLRPGVK		1051.0924 (2+)			

N: succinimide intermediate; NN: N167 or N168 residue in the succinimide intermediate form.

Table 6. Retention time, experimentally measured and calculated monoisotopic m/z of the molecular ions, position in the sequence, absolute intensities and peptide sequence of tryptic fragment containing asparagine residue 76 in succinimide intermediate form and asparagine residue 79 in isoaspartate methyl ester form found in the analysis of VDAC3 from NSC34 and NSC34-SOD1WT cell lines reduced with DTT, carboxyamidomethylated and digested in-solution.

Cell Lines	Peptide	Position in the Sequence	Rt (min)	Calculated Monoisotopic m/z	Absolute Intensity
NSC34	<u>WNTDNTLGTEISWENK</u>	75–90	52.07	953.4408 (2+)	$6.7 \cdot 10^3$
			51.55		$3.9 \cdot 10^3$
51.56			$1.1 \cdot 10^5$		
51.32			$1.3 \cdot 10^5$		
51.04			$6.1 \cdot 10^4$		
NSC34-SOD1WT					

N: succinimide intermediate; N: isoaspartate methyl ester.

2.5. Bioinformatic Prediction of VDAC3 N215D Mutant Structure

To evaluate the stability of VDAC3 N215D mutant, a computational structural prediction analysis was performed. The human VDAC3 (hVDAC3) structure was rebuilt by homology modelling starting from the VDAC1 PDB file (the crystallographic structure of VDAC3 has not yet been determined), while the VDAC3 N215D mutation was inserted using, as reference, the VDAC3 PDB file previous generated. Specifically, we used a simulation of the structure of human VDAC3 as the reference structure given the high percentage of identity (98.58%) and similarity (99%) with the mouse (Figure S15).

To assess the effect of the N215D mutation on channel conformation and stability, the tertiary structure model of human VDAC3 (hVDAC3) taken as a reference (Q9Y277.1) was modified by replacing Asn²¹⁵ with aspartate, thus mimicking deamidation at the same position (Figure 4A,B).

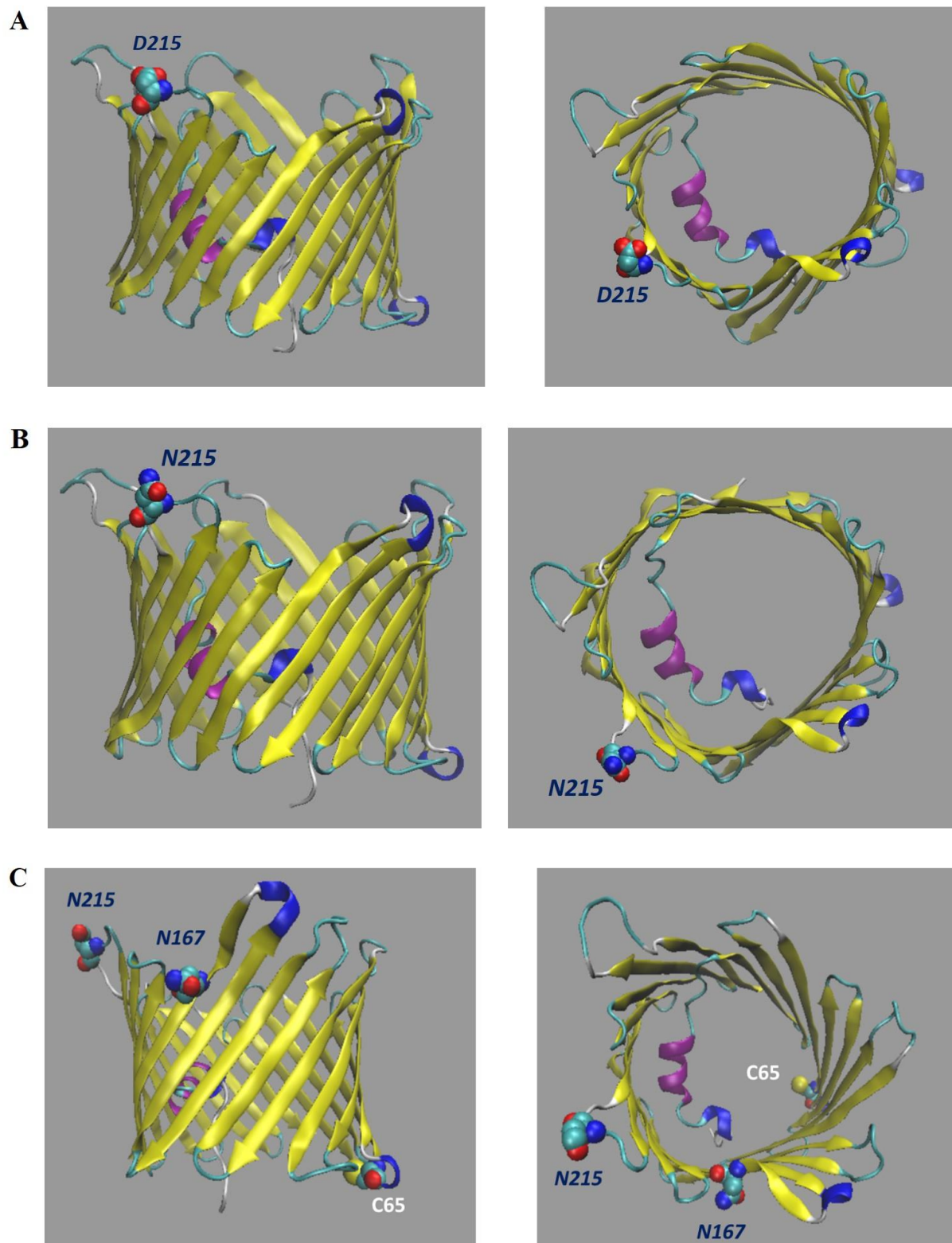


Figure 4. (A) Structural predictions of hVDAC3 N215D. Side view (on the left) and top view (on the right) were obtained by VMD software. In both figures, the top side represent the cytosolic environment. (B) Structural predictions of hVDAC3 wild type. Side view (on the left) and top view (on the right) were obtained by VMD software. In both figures, the top side represent the cytosolic environment. (C) Structural predictions of hVDAC3 N215D showing the localization of N167 and Cys65 residues. Side view (on the left) and top view (on the right) were obtained by VMD software. In both figures, the top side represent the cytosolic environment.

Ramachandran plots (RP) were also generated to evaluate the predicted conformation of the mutated VDAC3 channel by determining the orientation of each amino acid residue relative to the reference wild-type (wt) structure (Figure 4C).

The RP for VDAC3 wt indicates that almost all amino acid residues are distributed in favored regions (95.01%) (Table S29 and Figure S16). The remaining residues are either arranged in allowed regions (4.27%) but with a very high degree of stericality, or distributed in outlier (not allowed) conformations (0.72%).

The three amino acids located in regions are disallowed in the RP of VDAC3 N215D are Gly²³, Gly³⁸, Lys⁵³. These amino acids are found spread out in the channel and away from the Asn²¹⁵ residue (Figure S17). Therefore, it is unlikely that these residues can influence the structure of the channel or have an effect on Asn²¹⁵, also because two of the three residues are glycine.

No major differences were observed in amino acid arrangement by comparing the RP of VDAC3 wt with that of VDAC3 N215D (Figure 4C). The percentages of each individual region of both RP are shown in Table S29.

Overall, the single deamidation event on Asn²¹⁵ does not seem to affect the channel stability or produce a substantial modification in the VDAC3 channel structure. This result is not surprising, considering that the mutated residue resides not in the pore wall or in the alpha-helical stretch but in a loop.

2.6. Electrophysiological Properties of VDAC3 N215D Mutant

Considering the specific PTMs found in VDAC3 from the NSC34 SOD1-G93A cell line, we wanted to investigate their possible impact on channel functionality. Since it is impossible to produce recombinant proteins with specific oxidated or succinated residues, we focused on evaluating the effects of the most significant deamidation event found in VDAC3, namely the Asn/Asp substitution at the residue 215 residue. For this purpose, we first expressed, purified and refolded the mVDAC3 N215D mutant. Then, using a Planar Lipid Bilayer (PLB) instrument, the electrophysiological properties of the VDAC3 mutant were thoroughly investigated after reconstitution in a lipid bilayer. Measurements of single channel conductance, registered in 1 M KCl upon non-reducing conditions, revealed a slight increase in the pore diameter of VDAC3 mutant (approx. 600 pS) compared to the wild-type protein, mVDAC3 wt (approx. 450 pS). Histograms of the amplitude values as a function of the number of events indicate that N215D mutation also affects electrophysiological stability of the channel (Figure 5). As shown in Figure 5B,D, the presence of Asp²¹⁵ residue caused a different distribution of low- and high-conducting states of VDAC3. Under applied voltage (+10 mV), the mutant protein widened the distribution of the amplitude values corresponding to low-conducting state/s (L), concurrently doubling the conductance in the low-conductance state to approx. 3 pA and abolishing the main peak of VDAC3 wild type (VDAC3 wt) high conducting state (H). These results suggest that VDAC3 N215D undergoes more rapid fluctuations between the high and the low conducting state/s than the wild-type protein. The effect of asparagine deamination on the voltage dependence of VDAC3 was monitored by triangular voltage ramps in the presence or absence of DTT.

As already reported elsewhere [31,32], in non-reducing conditions, the VDAC3 was found to be insensitive to the applied voltage as the channel current steadily increased and decreased in the range of ± 50 mV (Figure 6A) without any variation in the slope of the current vs. voltage (I–V) plot (Figure 6B).

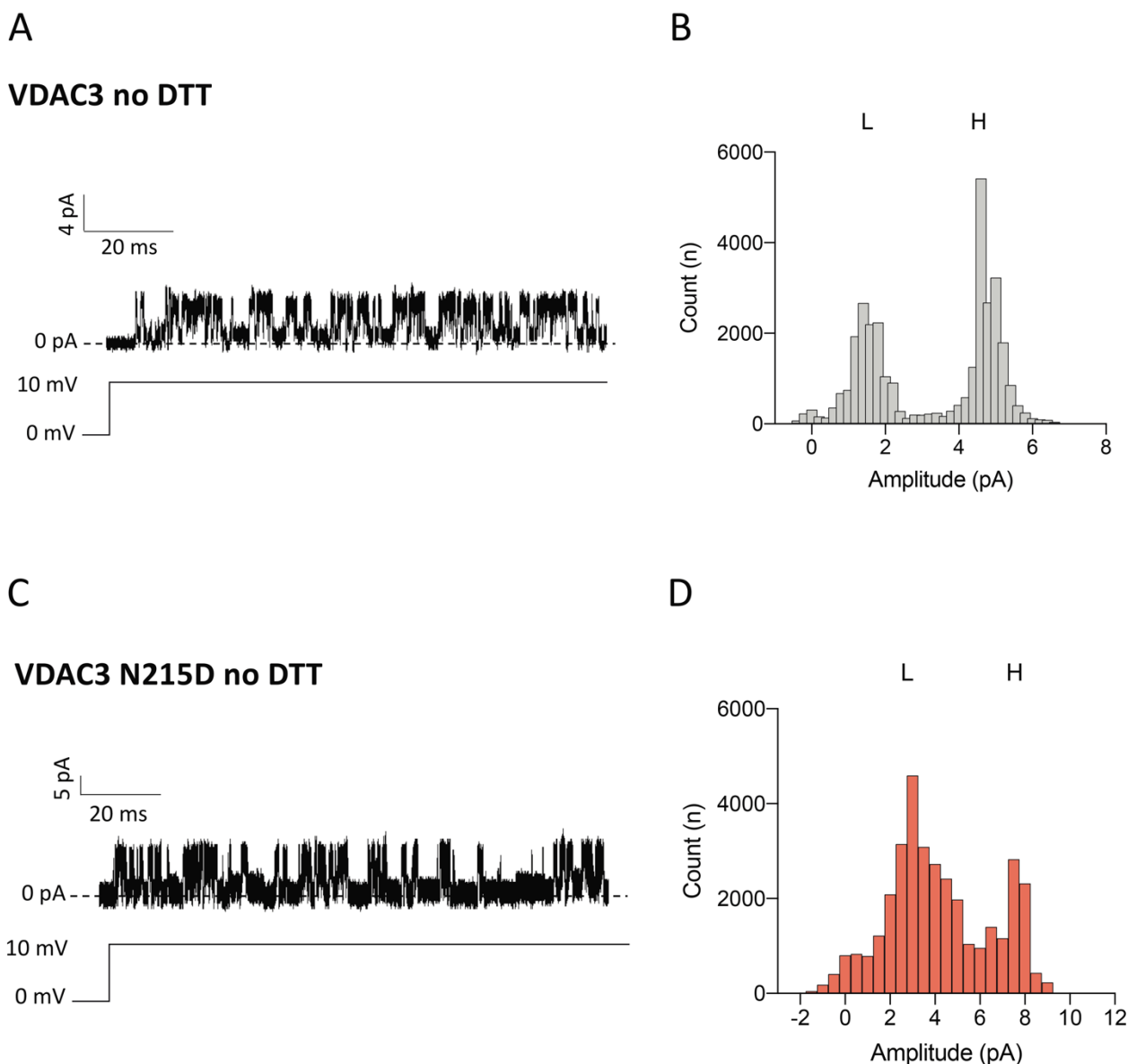


Figure 5. Amplitude distribution of VDAC3 wt and N215D channels in non-reducing conditions. (A) Representative current trace of VDAC3 wt in 1 M KCl at +10 mV applied. (B) Amplitude histograms of single channel recording data of VDAC3 wt. (C) Representative current trace of VDAC3 N215D in 1 M KCl at +10 mV applied. (D) Amplitude histograms of single channel recording data of VDAC3 N215D.

Consistent with the previous findings, VDAC3 N215D demonstrated a dramatic fluctuation in pore conductance upon raising the transmembrane voltage: continuous and very fast switching from open to closed states was observed mostly at positive potential (Figure 6C). The I–V plot shown in Figure 6D further emphasizes the current transitions corresponding to substantial changes in the slope of the curve. The graph of the normalized average conductance G/G_0 plotted as a function of membrane voltage (V_m) (Figure 6E) depicts an almost flat line for wild-type VDAC3.

Vice versa, the G/G_0 ratio of VDAC3 N215D does not remain constant and looks more like the characteristic bell-shaped curve of VDAC channels, with lower conductance values at higher membrane potentials.

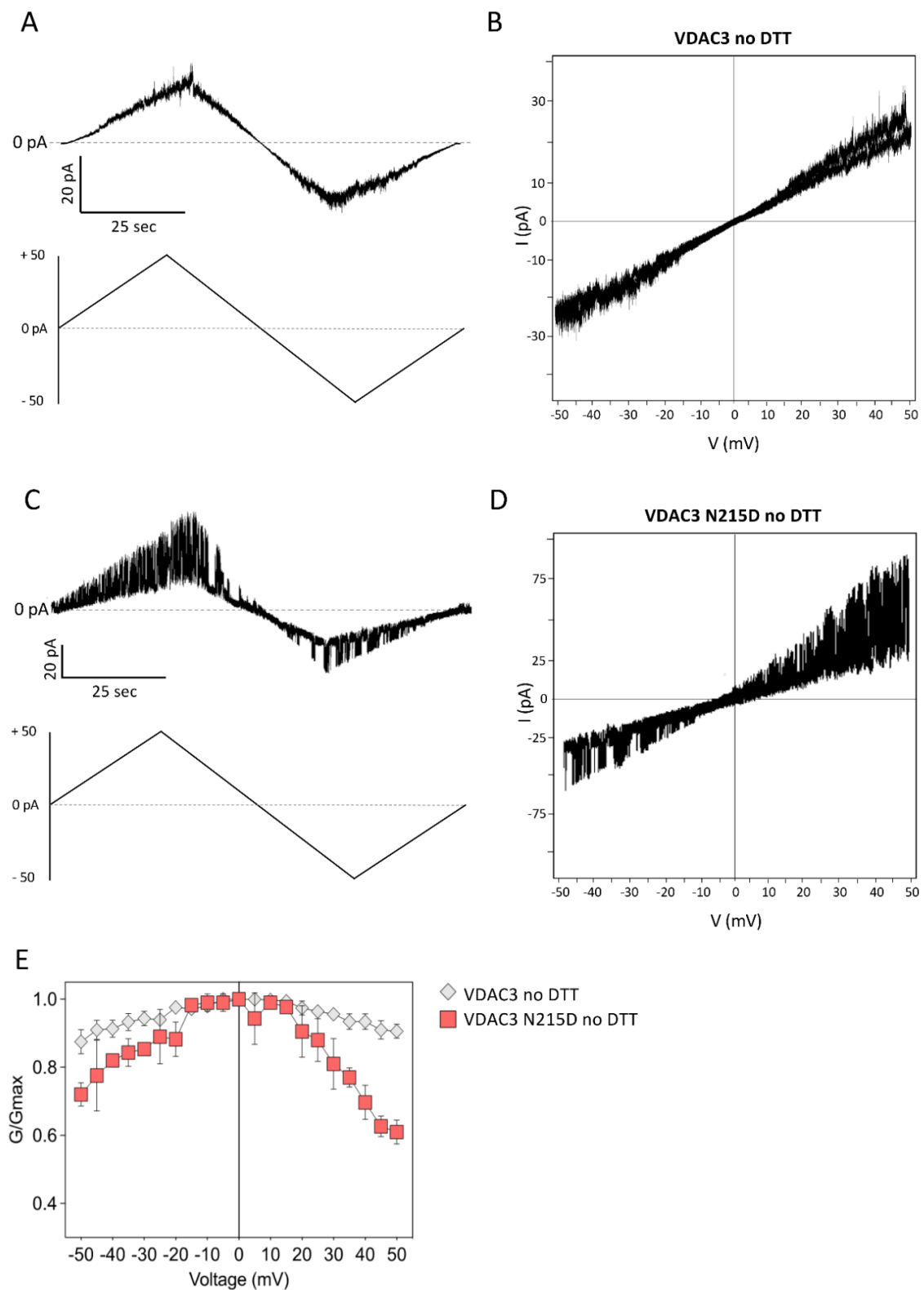


Figure 6. Voltage dependence analysis of VDAC3 wt and N215D in non-reducing conditions. (A) Voltage ramp from 0 to ± 50 mVA of VDAC3 wt. (B) Current vs. voltage (I–V) plot of VDAC3 wt. (C) Voltage ramp from 0 to ± 50 mVA of N215D VDAC3. (D) Current vs. voltage (I–V) plot of N215D VDAC3. (E) Voltage dependence graph of wt and mutated VDAC3. The normalized average conductance G/G_0 was plotted as a function of applied voltage (V_m).

Voltage dependence analysis was also performed after pre-incubating VDAC3 wt and N215D with 5 mM DTT. As shown in Figure 7A,B, treatment of the protein with a reductant completely changes the current profile of VDAC3 in response to a voltage ramp from 0 to ± 50 mV: channel closure is readily observed at both positive and negative potentials. Under these experimental conditions, however, there are no appreciable differences in the voltage response of VDAC3 N215D (Figure 7C,D) compared with the wild-type protein, as demonstrated by the current vs. voltage (I–V) plot of the mutant that almost completely overlaps those of VDAC3 wt (Figure 7E). The only remark is that negative voltages starting from -40 mV close the VDAC3 N215D channel more steadily than the wild-type one (Figure 7B,D).

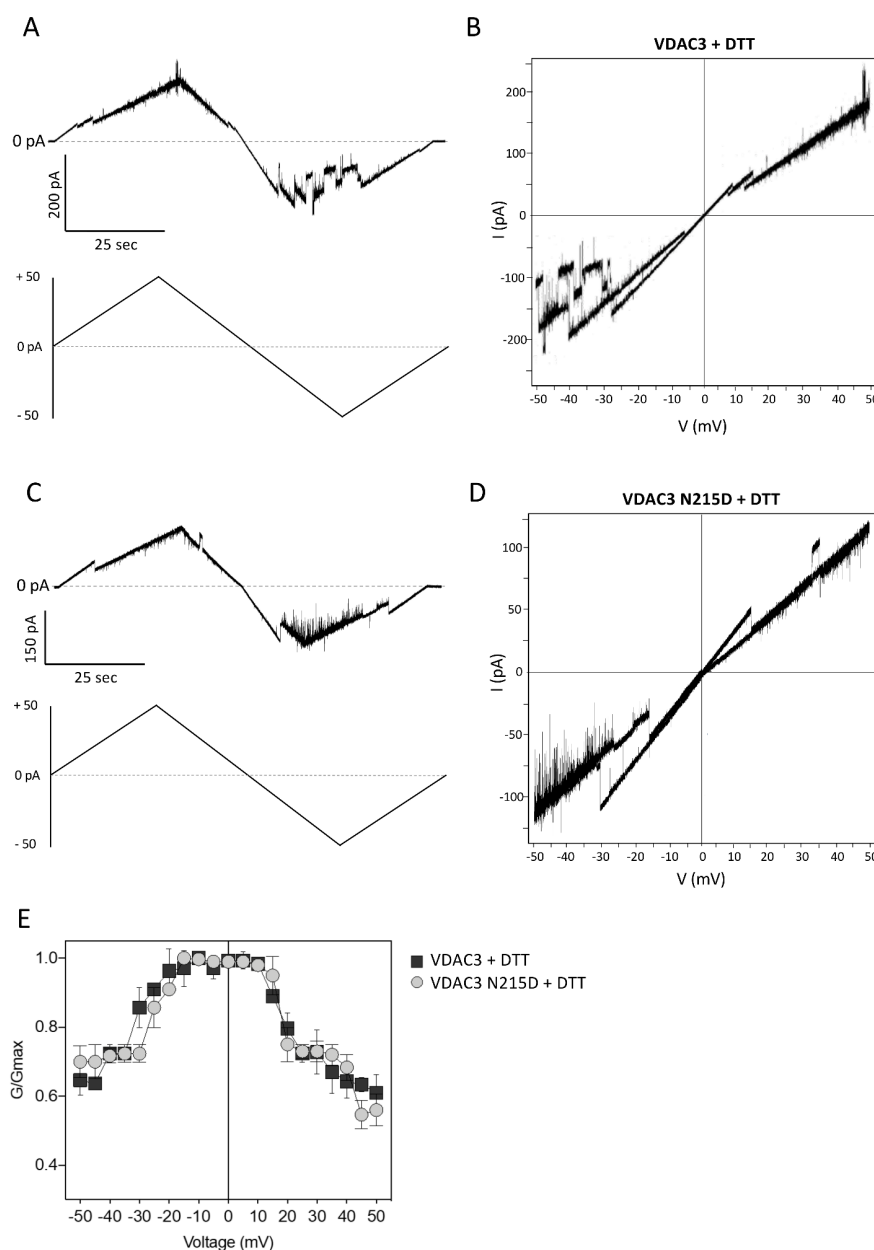


Figure 7. Voltage dependence analysis of VDAC3 wt and N215D preincubated with 5 mM DTT. (A) Voltage ramp from 0 to ± 50 mV of VDAC3 wt. (B) Current vs. voltage (I–V) plot of VDAC3 wt. (C) Voltage ramp from 0 to ± 50 mV of N215D VDAC3. (D) Current vs. voltage (I–V) plot of N215D VDAC3. (E) Voltage dependence graph of wt and mutated VDAC3. The normalized average conductance G/G_0 was plotted as a function of applied voltage (V_m).

3. Discussion

Multiple dysregulated mechanisms have been implicated in the pathogenesis of ALS, as of several neurodegenerative diseases. In particular, a mechanistic interplay between protein misfolding, oxidative stress and mitochondrial dysfunction in ALS has been highlighted. VDAC channel, the main protein at the outer mitochondrial membrane, is known to interact with SOD1 mutants linked to ALS. Recently, a specific range of non-enzymatic PTMs were identified in VDAC1 from NSC34-SOD1G93A cells, suggesting the appearance of important structural changes in the channel well correlated with defective mitochondrial metabolism in ALS motor neurons.

Unlike enzymatic PTMs, non-enzymatic PTMs mostly include irreversible chemical modifications on proteins, mediated by reactive compounds as ROS [33,34]. Despite these PTMs represent signs of aging or endogenous cell chemical damage, their role in neurodegenerative contexts has not yet been properly investigated.

Considering all of the above, in this work we investigated PTMs of the VDAC3 isoform from the NSC34 SOD1-G93A ALS cell model. Although the high sequence similarity between VDAC1 and VDAC3 is indicative of a similar pore-forming structure, a physiological unique role of redox sensor has been suggested for the VDAC3 isoform [23,35].

A function also supported by previous interactomics data shows the involvement of VDAC3 in important cellular signaling pathways [36].

Additionally, of interest are scientific validations of interactions between the SOD1 enzyme (whose mutants cause ALS1) and various VDAC3 interactors (PRDX5, TBP1, 37LRP, EF1D) reported at <https://www.uniprot.org>, accessed on 1 December 2021. Taken together, this information, combined with the already known presence of specific PTMs in VDAC1 from NSC34 SOD1G93A, suggests a role of the VDAC3 isoform in the pathogenesis of ALS.

In this work, to identify PTMs in VDAC3, we used high-resolution mass spectrometry [19,20,25,26], an extremely refined tool that provides particularly useful information for the interpretation of the biological functions of the proteins studied. Moreover, thanks to an “*in-solution*” digestion of the HTP eluate, we overcame the problems associated with the purification of membrane proteins, such as their very high hydrophobicity and low solubility. In addition, the difficulty in isolating individual VDAC isoforms resulted in the need to analyze them as components of a complex mixture, with HRMS investigation of the VDAC3 protein being particularly difficult because this isoform is generally the least expressed among VDACS. More importantly, these refined technical procedures avoided the dangers of unwanted oxidation due the sample preparation step as in [20].

In this study we obtained an excellent sequence coverage (about 99%), with the only uncovered moieties corresponding to Arg¹¹⁹-Arg¹²⁰ and Tyr²²⁵. Furthermore, the oxidation state of methionine and cysteine residues was precisely determined. Interestingly, we found in the VDAC3 sequence both Met²⁶ and Met¹⁵⁵ fully oxidized to methionine sulfoxide exclusively in NSC34-SOD1G93A cells, while in non-ALS control cell lines they were found to be partially oxidized. Met²⁶ localizes in the cytosolic rim of VDAC3, at the beginning of the first beta strand and facing partly inward in the pore. A position that could expose this residue to the effect of excess of ROS accumulated in the compartments as a result of pathology. As VDAC1 from the same ALS cell model [20], oxidative modifications of Met¹⁵⁵ could be indeed explained by its localization in β -sheet 10, facing the lipid bilayer. Thus, it is possible that OMM lipids peroxidized by ALS pathogenesis [37] can modify susceptible residues oriented towards the membrane.

We found no relevant differences in the over-oxidation of cysteines between VDAC3 purified from ALS model or non-ALS NSC34 cells. Indeed, Cys³⁶, Cys⁶⁵ and Cys²²⁹, all of which faced the IMM, were detected either in tri-oxidized and reduced (carboxyamidomethylated) forms in both ALS and control cells, with a similar Ox/Red ratio for homologous cysteines. This most likely means that the level of cysteine oxidation has already reached the maximum stage compatible with the functionality of the protein.

Furthermore, Cys⁸ and Cys¹²², respectively located in the N-terminal alpha helix and within an IMM-facing loop, are always in the carboxyamidomethylated form, thus suggesting their potential availability to form disulfide bridges.

In addition, Cys² was found to be both reduced and acetylated (the “normal” situation) and, unexpectedly, oxidized to sulfonic acid and was not acetylated, neither in cells expressing human SOD1 wt nor the mutated form. The presence of a cysteine at the N-terminus is a unique feature of the VDAC3 isoform. Evidently, just the peculiar positioning of this cysteine at the beginning of the N-terminal alpha helix could already promote its over-oxidation in cells that over-express SOD1wt. Indeed, high levels of native SOD1 are known to result in misfolding and aggregation of SOD1 itself, correlating with forms of sALS [5].

The oxidative stress condition, typical of all forms of ALS, as well as the results obtained in the previous work on VDAC1 [20], prompted us to search the sequence of VDAC3 for asparagine and glutamine deamidation events in addition to oxidations. Asparagine and glutamine deamidation are spontaneous, non-enzymatic and post-biosynthetic modifications affecting structure, stability, folding, and aggregation of proteins [38–41]. Besides playing a role in cataract formation, its importance has also been established in Alzheimer’s, Parkinson’s, and ALS as other degenerative diseases [20,42–44]. Moreover, being a modification that proteins accumulate with cellular aging and following pathological conditions, it could be useful as a biomarker of disease [45,46]. The deamidation mechanism involves the formation of an unstable cyclic succinimidyl intermediate, which is hydrolyzed to yield Asp or isoAsp, with an approximate ratio of 3:1 [47,48]. Isoaspartic acid is an isomer of aspartic acid with the C_β incorporated into the backbone. These isopeptide bonds are known to impair protein structure/function or enhance the aggregation process, contributing to protein aging and folding disorders typical of neurodegenerative diseases. In this regard, it has been reported that in erythrocytes of ALS patients there is an accumulation of L-isoaspartyl residues [30]. Consistent with the known data, our analysis showed a higher amount of succinimidyl intermediate in the VDAC3 of the NSC34-SOD1G93A cell line than in the other two NSC34 non-SLA cell lines. Additionally, we detected the presence of asparagine 79 as aspartate methyl ester in the NSC34 cells and in those expressing the SOD1 wt, but not in the cell line expressing the mutated SOD1 G93A. This can be explained considering that the free α-carbonyl group of the dangerous L-isoAsp is methylated by the enzyme L-isoaspartyl/(D-asp) methyltransferase (PIMT) and S-adenosylmethionine (AdoMet) as a methyl donor. Subsequently, hydrolysis of the methyl ester leads to the reformation of the intermediate L-succinimide which is then partly hydrolyzed to L-Asp, thus completing the physiological repair reaction that counteracts the accumulation of dysfunctional proteins [49–51].

In addition, only in NSC34-SOD1G93A cells did we detect very high levels (10% of molecules) of deamidated Asn²¹⁵ (Table 4 and Figure 4C). Considering the potential impact of this modification on protein structure/function, we assessed the stability of the VDAC3 N215D mutant by performing a molecular modeling analysis. For this purpose, we replaced Asn²¹⁵ with an aspartate in the structure model of human VDAC3. The results show no significant changes in the pore structure of the VDAC3 N215D mutant. In both Ramachandran plots of VDAC3 wt and N215D there is a predominance of residues located in the β region, suggesting for both structures the typical β-barrel motif that characterizes all isoforms of VDAC (Figure S15). Notably, the Asn/Asp substitution would not seem to result in any change in structure, and this could be due to the position that residue 215 has within the structure. Indeed, this asparagine is located in the center of a loop connecting two β-strands (Figure 4C), with the side chain protruding toward the cytosol, with no apparent involvement in the formation of the pore wall. In addition, results on mVDAC3 N215D were produced using the model of human VDAC3, reconstructed by homology to the crystallographic structure of human VDAC1, as the reference structure. This model, although predictively very similar, may, in reality, have some differences.

Then, considering the little information provided by homology analysis, we wanted to further investigate whether deamidation of Asn215 was capable of producing effects on protein function. Therefore, we produced, purified and folded the mVDAC3 N215D mutant protein and analyzed its electrophysiological characteristics at PLB. Through this analysis, we ascertained that the N215D mutation results in a significant increase in the fluctuation of pore conductance under non-reducing conditions. In contrast, the voltage dependence analysis performed under reducing conditions indicates that the VDAC3 mutant has a behavior mostly overlapping with the wt protein. Furthermore, VDAC3 N215D shows voltage dependence already in non-reducing conditions, at a variance of the wt VDAC3, indicating that the residue may be involved in the voltage-sensor structure. On the other hand, in reducing conditions, no special difference between the wt and pathological forms are strikingly apparent.

As previously pointed out, Asn²¹⁵ localizes in a loop formed by six amino acids (212–217) and is exposed toward the cytosolic environment, i.e., in a water-exposed context where ROS can make their effect felt faster. Although the other asparagines of VDAC3 would also appear to be mostly exposed toward the cytosolic environment, they exhibit lower levels of deamidation than Asn²¹⁵. This difference might depend on the nearby amino acids as well as on the specific interactors with which each residue is physiologically engaged [35]. Specifically, Asn²¹⁵ might be in a suitable position to establish interactions with cytosolic molecules important for VDAC3 function and whole organelle homeostasis.

It is noteworthy that the higher level of succinimide intermediate was detected for Asn¹⁶⁷ (much less for Asn¹⁶⁸) of VDAC3 from ALS model cells compared with the protein purified from control lines (Table 5). This finding could depend on the fact that the aspartyl and iso-aspartyl residues produced by deamidation of Asn¹⁶⁷ dehydrate faster (or hydrate more slowly) in the reaction that still reforms the intermediate succinimide. The reduced levels of Asp produced by deamidation from Asn¹⁶⁷ could be explained as follows, as the positioning in the pore of this residue could also favor the formation of the intermediate. Indeed, Asn¹⁶⁷ localizes in the central portion of the 11th beta strand, protruding toward the membrane lipid environment, preceded by two polar amino acids (serine and glutamine) (Figure 4C). The latter condition is favorable for the deamidation reaction. Furthermore, the exposure of Asn¹⁶⁷ toward the lipid bilayer allows us to hypothesize that OMM lipids peroxidized by ALS pathogenesis [36] may modify sensitive membrane-oriented residues, as previously reported for VDAC1 from the same cell type [20].

Another interesting result, only discovered in the VDAC3 from NSC34-SOD1G93A cells, concerns the much higher levels of Cys⁶⁵ succination compared with the control NSC34 cell lines. Succination, or the formation of S-(2-succino) cysteine (2SC), is a non-enzymatic and irreversible modification that physiologically occurs by fumarate adduction to the sulfhydryl group of Cys only, through a Michael-type reaction [52]. Succination preferentially targets cysteine residues with low pKa values (up to 3–4), such as those located in protein active sites or placed in a suitable biological context [53]. For this reason, 2SC is a recognized biomarker of metabolic stress and, more specifically, mitochondrial stress. In addition, this PTM increases with aging, when there is an excess of nutrients, a high ATP/ADP and/or NADH/NAD⁺ ratio, or, more generally, when there is an abnormal increase in Krebs cycle intermediates. It is, therefore, associated with mitochondrial dysfunction and increased ROS, resulting in neuronal damage [54].

It is, thus, not surprising that we found high levels of succination in VDAC3 of the ALS model cell line. Specifically, succinated Cys⁶⁵ found in VDAC3 is located on the edge of the pore looking toward the IMM, usually in itself a highly oxidizing environment, but even more exacerbated in the ALS pathological context due to the impairment of antioxidant defenses. It is noteworthy that several proteins known to interact with VDAC3 have been found succinated in other cell types [35,55]. Interestingly, among the interactors of VDAC3, succination of Protein Disulfide Isomerase was reported, thus providing a link between mitochondrial stress and endoplasmic reticulum stress [56]. Succination of α - and β -tubulins is also known [57] as a mechanism that can inhibit their polymerization and,

thus, alter mitochondrial dynamics. The latter aspect has an important consequence for ALS, and neurodegeneration in general, as neurons are cells incredibly dependent on their cytoskeletal transport mechanism. Indeed, in the cell body and axons of mature neurons, the cytoskeleton enables fundamental processes, such as movement of every component, delivery of new proteins and organelles to distal sites, as well as removals of aged ones [58].

4. Materials and Methods

4.1. Chemicals

All chemicals were of the highest purity commercially available and were used without further purification. Ammonium bicarbonate, calcium chloride, phosphate-buffered saline (PBS), Tris-HCl, Triton X-100, sucrose, mannitol, ethylene glycol tetraacetic acid (EGTA), ethylenediaminetetraacetic acid (EDTA), formic acid (FA), dithiothreitol (DTT) and iodoacetamide (IAA) were obtained from Sigma-Aldrich (Milan, Italy). High-glucose DMEM (Dulbecco's Modified Eagle Medium) and fetal bovine serum (FBS) were obtained from Gibco-Thermo Fisher Scientific (Milan, Italy). DMEM F12 and tetracycline-free FBS were obtained from Euro Clone. G418 and Doxycycline were obtained from Carlo Erba and Sigma-Aldrich, respectively. Trypsin/EDTA (for cell cultures) and penicillin-streptomycin (P/S) were purchased from Invitrogen. All other stock solutions for cell cultures were from Euroclone (Milan, Italy). Modified porcine trypsin and chymotrypsin were purchased from Promega (Milan, Italy). Water and acetonitrile (OPTIMA[®] LC/MS grade) for LC/MS analyses were provided from Fisher Scientific (Milan, Italy).

4.2. NSC34 Cell Lines

NSC34 cell lines (mouse motor neuron-like) obtained from CELLutions Biosystem Inc. were stably transfected with pTet-ON plasmid (Clontech, Mountain View, CA, USA) harboring sequences encoding human SOD1 wt (NSC34-SOD1WT) or G93A (NSC34-SOD1G93A) and used as non-ALS motor neuron line and ALS motor neuron line, respectively [59]. The cell lines were maintained as in Magrì et al. [60].

4.3. Extraction of Mitochondrial Proteins from NSC34 Cells under Reducing Conditions

Extraction of mitochondrial proteins from NSC34 cells under reducing conditions was performed as described in [20].

4.4. Liquid Chromatography and Tandem Mass Spectrometry (LC-MS/MS) Analysis and Database Search

Mass spectrometry data were acquired and processed as described in [20].

Identification of Deamidation Sites on VDAC3

A freely available command-line script for Python 2.x (<https://github.com/dblyon/deamidation>), accessed on 1 December 2021 which uses the MaxQuant "evidence.txt" file, was used to estimate the percentage of deamidation in VDAC 3 for each cell line, as in [20].

4.5. Expression, Purification and Refolding of Recombinant VDAC3 Proteins

The sequence encoding mouse VDAC3 (mVDAC3) was cloned in pET21a vector (Novagen) as reported in [23]. Mutagenesis of mVDAC3 was achieved using a specific couple of primers designed to replace Asn²¹⁵ residue with Asp according to the protocol already described in [61]. The single mutation was confirmed by DNA sequencing.

Vectors containing native or mutagenized mVDAC3 (i.e., VDAC3 wt and VDAC3 N215D, respectively) coding sequence were used to transform Escherichia coli BL21(DE3) cells. Recombinant VDAC3 proteins expression, purification and refolding were carried out as in [11].

4.6. Lipid Bilayer Experiments

Planar lipid bilayer experiments were performed as described previously [62,63]. Artificial membranes made of 1% (*w/v*) diphytanoyl phosphatidylcholine (DiphPC) (Avanti Polar Lipids, Alabaster, AL, USA) in *n*-decane were painted on a 200 μm hole in a Derlin cuvette (Warner Instruments, Hamden, CT, USA). All the experiments were carried out at RT. Membrane capacitances of 100–150 pF were established for appropriate lipid bilayers. Mutant or native mVDAC3 were added from the protein stock solution of 1 mg/mL to the cis side of the cuvette filled with symmetrical 1 M KCl/10 mM HEPES pH 7.0. The single channel conductance of the pores was measured upon application of a fixed membrane potential (+10 mV) [58]. The voltage dependence was calculated by applying a triangular voltage ramp from 0 to ± 50 mV of 100 ms duration, with a frequency of 10 mHz. At least three independent experiments were performed for each protein. A Bilayer Clamp amplifier (Warner Instruments) at 100 ms/point and filtered at 300 Hz was used for data acquisition. Analyses were performed with the pClamp software (Ver-10; Molecular Devices, San Jose, CA, USA).

4.7. Modelling and Bioinformatics Analysis

The structures of VDAC3 N215D shown in this work were obtained computationally with MODELLER software v9.24 [64] using the structure of human VDAC1 WT as a template. N215D mutations were introduced by substitution of the selected amino acid residue in the FASTA sequence. The same software was used for evaluation of the energetic score associated with each structure. Graphical representation was obtained by using VMD—Visual Molecular Dynamic software (available at: <https://www.ks.uiuc.edu/Research/vmd/>), accessed on 1 January 2022. The root means square deviation (RMSD) analysis and the Ramachandran plots (RPs) were obtained both through the free online software at <https://zlab.umassmed.edu/bu/rama/>, accessed on 1 January 2022 and by using specific tools in the VMD software.

5. Conclusions

In this work, combining HRMS analysis with “*in-solution*” digestion of an enriched VDACS fraction, we found specific and irreversible PTMs in VDAC3 purified from the ALS model cell line. In particular, in VDAC3 we identified channel oxidation, deamidation and succination events and provided experimental evidence of functional changes of deamidated VDAC3. The impact of the most abundant deamidation event was verified by reconstituting its activity in a functional assay.

Overall, our data complete the picture we have drawn with previous results about VDAC1 from the same cell type. Specifically, the post-translational modifications identified and discussed here may represent sufficient conditions to alter the physiological pool of interactors of VDAC3 and modify its specific ability to buffer ROS, possibly impacting IMM redox signaling in ALS.

Supplementary Materials: The following supporting information can be downloaded at: <https://www.mdpi.com/article/10.3390/ijms232415853/s1>.

Author Contributions: Conceptualization and experimental design, A.M.; MS analysis, R.S.; methodology, M.G.G.P., S.R., S.C.N., V.C. and R.S.; databases and software, M.G.G.P., A.C., S.A.M.C. and G.F.A.; validation, M.G.G.P., A.C. and S.R.; investigation, M.G.G.P., S.R. and A.C.; writing—original draft preparation, M.G.G.P., S.R., S.F., R.S. and A.M.; writing—review and editing, R.S. and A.M.; supervision, S.F., V.D.P., R.S. and A.M. All authors have read and agreed to the published version of the manuscript.

Funding: This research was supported by University of Catania “Piano della Ricerca di Ateneo PI-ACERI 2020” grants “ARVEST” and “VDAC” for A.M. and V.D.P., respectively, and by the MIUR PNR “Proof of Concept 2018” grant (codex: PEPSLA POC 01_00054) for A.M.

Institutional Review Board Statement: Not applicable.

Informed Consent Statement: Not applicable.

Data Availability Statement: Data are available via ProteomeXchange with identifier PXD036728.

Acknowledgments: The authors gratefully acknowledge the Bio-Nanotech Research and Innovation Tower of the University of Catania (BRIT; PON project financed by the Italian Ministry for Education, University and Research MIUR).

Conflicts of Interest: The authors declare no conflict of interest.

References

1. Rowland, L.P.; Shneider, N.A. Amyotrophic Lateral Sclerosis. *N. Engl. J. Med.* **2001**, *344*, 1688–1700. [[CrossRef](#)]
2. Pasinelli, P.; Brown, R.H. Molecular biology of amyotrophic lateral sclerosis: Insights from genetics. *Nat. Rev. Neurosci.* **2006**, *7*, 710–723. [[CrossRef](#)] [[PubMed](#)]
3. Brown, R.H.; Al-Chalabi, A. Amyotrophic Lateral Sclerosis. *N. Engl. J. Med.* **2017**, *377*, 162–172. [[CrossRef](#)] [[PubMed](#)]
4. Kaur, S.J.; McKeown, S.R.; Rashid, S. Mutant SOD1 mediated pathogenesis of Amyotrophic Lateral Sclerosis. *Gene* **2016**, *577*, 109–118. [[CrossRef](#)]
5. Sanghai, N.; Tranmer, G.K. Hydrogen Peroxide and Amyotrophic Lateral Sclerosis: From Biochemistry to Pathophysiology. *Antioxidants* **2021**, *11*, 52. [[CrossRef](#)]
6. Prudencio, M.; Borchelt, D.R. Superoxide dismutase 1 encoding mutations linked to ALS adopts a spectrum of misfolded states. *Mol. Neurodegener.* **2011**, *6*, 77. [[CrossRef](#)] [[PubMed](#)]
7. Mondola, P.; Damiano, S.; Sassa, A.; Santillo, M. The Cu, Zn Superoxide Dismutase: Not Only a Dismutase Enzyme. *Front. Physiol.* **2016**, *7*, 594. [[CrossRef](#)]
8. Wang, F.; Lu, Y.; Qi, F.; Su, Q.; Wang, L.; You, C.; Che, F.; Yu, J. Effect of the human SOD1-G93A gene on the nrf2/ARE signaling pathway in NSC-34 cells. *Mol. Med. Rep.* **2014**, *9*, 2453–2458. [[CrossRef](#)]
9. Marden, J.J.; Harraz, M.M.; Williams, A.J.; Nelson, K.; Luo, M.; Paulson, H.; Engelhardt, J.F. Redox modifier genes in amyotrophic lateral sclerosis in mice. *J. Clin. Investig.* **2007**, *117*, 2913–2919. [[CrossRef](#)]
10. Israelson, A.; Arbel, N.; Da Cruz, S.; Ilieva, H.; Yamanaka, K.; Shoshan-Barmatz, V.; Cleveland, D.W. Misfolded Mutant SOD1 Directly Inhibits VDAC1 Conductance in a Mouse Model of Inherited ALS. *Neuron* **2010**, *67*, 575–587. [[CrossRef](#)]
11. Shteinfein-Kuzmine, A.; Argueti, S.; Gupta, R.; Shvil, N.; Abu-Hamad, S.; Gropper, Y.; Hoeber, J.; Magri, A.; Messina, A.; Kozlova, E.N.; et al. A VDAC1-Derived N-Terminal Peptide Inhibits Mutant SOD1-VDAC1 Interactions and Toxicity in the SOD1 Model of ALS. *Front. Cell. Neurosci.* **2019**, *13*, 346. [[CrossRef](#)] [[PubMed](#)]
12. Shoshan-Barmatz, V.; De Pinto, V.; Zweckstetter, M.; Raviv, Z.; Keinan, N.; Arbel, N. VDAC, a multi-functional mitochondrial protein regulating cell life and death. *Mol. Asp. Med.* **2010**, *31*, 227–285. [[CrossRef](#)] [[PubMed](#)]
13. Magri, A.; Messina, A. Interactions of VDAC with Proteins Involved in Neurodegenerative Aggregation: An Opportunity for Advancement on Therapeutic Molecules. *Curr. Med. Chem.* **2017**, *24*, 4470–4487. [[CrossRef](#)] [[PubMed](#)]
14. Shoshan-Barmatz, V.; Ben-Hail, D. VDAC, a multi-functional mitochondrial protein as a pharmacological target. *Mitochondrion* **2012**, *12*, 24–34. [[CrossRef](#)] [[PubMed](#)]
15. Reina, S.; Guarino, F.; Magri, A.; De Pinto, V. VDAC3 As a Potential Marker of Mitochondrial Status Is Involved in Cancer and Pathology. *Front. Oncol.* **2016**, *6*, 264. [[CrossRef](#)]
16. Wang, Y.-C.; Peterson, S.E.; Loring, J.F. Protein post-translational modifications and regulation of pluripotency in human stem cells. *Cell Res.* **2013**, *24*, 143–160. [[CrossRef](#)]
17. Duan, G.; Walther, D. The Roles of Post-translational Modifications in the Context of Protein Interaction Networks. *PLoS Comput. Biol.* **2015**, *11*, e1004049. [[CrossRef](#)]
18. Reina, S.; Pittalà, M.G.G.; Guarino, F.; Messina, A.; De Pinto, V.; Foti, S.; Saletti, R. Cysteine Oxidations in Mitochondrial Membrane Proteins: The Case of VDAC Isoforms in Mammals. *Front. Cell Dev. Biol.* **2020**, *8*, 397. [[CrossRef](#)]
19. Pittalà, M.G.G.; Nibali, S.C.; Reina, S.; Cunsolo, V.; Di Francesco, A.; De Pinto, V.; Messina, A.; Foti, S.; Saletti, R. VDACs Post-Translational Modifications Discovery by Mass Spectrometry: Impact on Their Hub Function. *Int. J. Mol. Sci.* **2021**, *22*, 12833. [[CrossRef](#)]
20. Pittalà, M.G.G.; Reina, S.; Cubisino, S.A.M.; Cucina, A.; Formicola, B.; Cunsolo, V.; Foti, S.; Saletti, R.; Messina, A. Post-Translational Modification Analysis of VDAC1 in ALS-SOD1 Model Cells Reveals Specific Asparagine and Glutamine Deamidation. *Antioxidants* **2020**, *9*, 1218. [[CrossRef](#)]
21. Magri, A.; Reina, S.; De Pinto, V. VDAC1 as Pharmacological Target in Cancer and Neurodegeneration: Focus on Its Role in Apoptosis. *Front. Chem.* **2018**, *6*, 108. [[CrossRef](#)] [[PubMed](#)]
22. Smilansky, S.; Dangoor, L.; Nakdimon, I.; Ben-Hail, D.; Mizrachi, D.; Shoshan-Barmatz, V. The Voltage-Dependent Anion Channel 1 mediates amyloid beta toxicity and represents a potential target for Alzheimer's disease therapy. *JBC* **2015**, *290*, 30670–30683. [[CrossRef](#)] [[PubMed](#)]
23. Reina, S.; Checchetto, V.; Saletti, R.; Gupta, A.; Chaturvedi, D.; Guardiani, C.; Guarino, F.; Scorciapino, M.A.; Magri, A.; Foti, S.; et al. VDAC3 as a sensor of oxidative state of the intermembrane space of mitochondria: The putative role of cysteine residue modifications. *Oncotarget* **2016**, *7*, 2249–2268. [[CrossRef](#)] [[PubMed](#)]

24. Reina, S.; Nibali, S.C.; Tomasello, M.F.; Magri, A.; Messina, A.; De Pinto, V. Voltage Dependent Anion Channel 3 (VDAC3) protects mitochondria from oxidative stress. *Redox Biol.* **2022**, *51*, 102264. [[CrossRef](#)] [[PubMed](#)]
25. Saletti, R.; Reina, S.; Pittalà, M.G.; Belfiore, R.; Cunsolo, V.; Messina, A.; De Pinto, V.; Foti, S. High resolution mass spectrometry characterization of the oxidation pattern of methionine and cysteine residues in rat liver mitochondria voltage-dependent anion selective channel 3 (VDAC3). *Biochim. Biophys. Acta (BBA) Biomembr.* **2017**, *1859*, 301–311. [[CrossRef](#)]
26. Pittalà, M.G.G.; Saletti, R.; Reina, S.; Cunsolo, V.; De Pinto, V.; Foti, S. A High Resolution Mass Spectrometry Study Reveals the Potential of Disulfide Formation in Human Mitochondrial Voltage-Dependent Anion Selective Channel Isoforms (hVDACs). *Int. J. Mol. Sci.* **2020**, *21*, 1468. [[CrossRef](#)]
27. Guan, Z.; Yates, N.A.; Bakhtiar, R. Detection and characterization of methionine oxidation in peptides by collision-induced dissociation and electron capture dissociation. *J. Am. Soc. Mass Spectrom.* **2003**, *14*, 605–613. [[CrossRef](#)]
28. Cournoyer, J.J.; Pittman, J.L.; Ivleva, V.B.; Fallows, E.; Waskell, L.; Costello, C.E.; O'Connor, P.B. Deamidation: Differentiation of aspartyl from isoaspartyl products in peptides by electron capture dissociation. *Protein Sci.* **2005**, *14*, 452–463. [[CrossRef](#)]
29. Jové, M.; Pradas, I.; Mota-Martorell, N.; Cabré, R.; Ayala, V.; Ferrer, I.; Pamplona, R. Succination of Protein Thiols in Human Brain Aging. *Front. Aging Neurosci.* **2020**, *12*, 52. [[CrossRef](#)]
30. D'Angelo, S.; Trojsi, F.; Salvatore, A.; Daniele, L.; Raimo, M.; Galletti, P.; Monsurrò, M.R. Accumulation of altered aspartyl residues in erythrocyte membrane proteins from patients with sporadic amyotrophic lateral sclerosis. *Neurochem. Int.* **2013**, *63*, 626–634. [[CrossRef](#)]
31. Checchetto, V.; Reina, S.; Magri, A.; Szabo, I.; De Pinto, V. Recombinant Human Voltage Dependent Anion Selective Channel Isoform 3 (hVDAC3) Forms Pores with a Very Small Conductance. *Cell Physiol. Biochem.* **2014**, *34*, 842–853. [[CrossRef](#)] [[PubMed](#)]
32. Nibali, S.C.; Di Rosa, M.C.; Rauh, O.; Thiel, G.; Reina, S.; De Pinto, V. Cell-free electrophysiology of human VDACs incorporated into nanodiscs: An improved method. *Biophys. Rep.* **2021**, *1*, 100002.
33. Liddy, K.A.; White, M.Y.; Cordwell, S.J. Functional decorations: Post-translational modifications and heart disease delineated by targeted proteomics. *Genome Med.* **2013**, *5*, 20. [[CrossRef](#)] [[PubMed](#)]
34. Tomin, T.; Schittmayer, M.; Honeder, S.; Heining, C.; Birner-Gruenberger, R. Irreversible oxidative post-translational modifications in heart disease. *Expert Rev. Proteom.* **2019**, *16*, 681–693. [[CrossRef](#)] [[PubMed](#)]
35. Okazaki, M.; Kurabayashi, K.; Asanuma, M.; Saito, Y.; Dodo, K.; Sodeoka, M. VDAC3 gating is activated by suppression of disulfide-bond formation between the N-terminal region and the bottom of the pore. *Biochim. Biophys. Acta* **2015**, *1848*, 3188–3196. [[CrossRef](#)] [[PubMed](#)]
36. Messina, A.; Reina, S.; Guarino, F.; Magri, A.; Tomasello, F.; Clark, R.E.; Ramsay, R.R.; De Pinto, V. Live cell interactome of the human voltage dependent anion channel 3 (VDAC3) revealed in HeLa cells by affinity purification tag technique. *Mol. BioSyst.* **2014**, *10*, 2134–2145. [[CrossRef](#)] [[PubMed](#)]
37. Ravera, S.; Bonifacino, T.; Bartolucci, M.; Milanese, M.; Gallia, E.; Provenzano, F.; Cortese, K.; Panfoli, I.; Bonanno, G. Characterization of the Mitochondrial Aerobic Metabolism in the Pre- and Perisynaptic Districts of the SOD1G93A Mouse Model of Amyotrophic Lateral Sclerosis. *Mol. Neurobiol.* **2018**, *55*, 9220–9233. [[CrossRef](#)]
38. Hains, P.G.; Truscott, R.J.W. Age-Dependent Deamidation of Life long Proteins in the Human Lens. *Investig. Ophthalmol. Vis. Sci.* **2010**, *51*, 3107–3114. [[CrossRef](#)]
39. Hooi, M.Y.S.; Raftery, M.J.; Truscott, R.J.W. Racemization of Two Proteins over Our Lifespan: Deamidation of Asparagine 76 in γ S Crystallin Is Greater in Cataract than in Normal Lenses across the Age Range. *Investig. Ophthalmol. Vis. Sci.* **2012**, *53*, 3554–3561. [[CrossRef](#)]
40. Truscott, R.J.W. Are Ancient Proteins Responsible for the Age-Related Decline in Health and Fitness? *Rejuvenation Res.* **2010**, *13*, 83–89. [[CrossRef](#)]
41. Lindner, H.; Helliger, W. Age-dependent deamidation of asparagine residues in proteins. *Exp. Gerontol.* **2001**, *36*, 1551–1563. [[CrossRef](#)] [[PubMed](#)]
42. Robinson, N.E.; Robinson, M.L.; Schulze, S.E.S.; Lai, B.T.; Gray, H.B. Deamidation of α -synuclein. *Protein Sci.* **2009**, *18*, 1766–1773. [[CrossRef](#)] [[PubMed](#)]
43. Shimizu, T.; Watanabe, A.; Ogawara, M.; Mori, H.; Shirasawa, T. Isoaspartate Formation and Neurodegeneration in Alzheimer's Disease. *Arch. Biochem. Biophys.* **2000**, *381*, 225–234. [[CrossRef](#)] [[PubMed](#)]
44. Vigneswara, V.; Cass, S.; Wayne, D.; Bolt, E.L.; Ray, D.E.; Carter, W.G. Molecular Ageing of Alpha- and Beta-Synucleins: Protein Damage and Repair Mechanisms. *PLoS ONE* **2013**, *8*, e61442. [[CrossRef](#)]
45. Bastrup, J.; Kastaniegaard, K.; Asuni, A.A.; Volbracht, C.; Stensballe, A. Proteomic and Unbiased Post-Translational Modification Profiling of Amyloid Plaques and Surrounding Tissue in a Transgenic Mouse Model of Alzheimer's Disease. *J. Alzheimer's Dis.* **2020**, *73*, 393–411. [[CrossRef](#)]
46. Wilmarth, P.A.; Tanner, S.; Dasari, S.; Nagalla, S.R.; Riviere, M.A.; Bafna, V.; Pevzner, P.A.; David, L.L. Age-related changes in human crystallins determined from comparative analysis of post-translational modifications in young and aged lens: Does deamidation contribute to crystallin insolubility? *J. Proteome Res.* **2006**, *5*, 2554–2566. [[CrossRef](#)]
47. Catak, S.; Monard, G.; Aviyente, V.; Ruiz-Lo'pez, M.F. Deamidation of Asparagine Residues: Direct Hydrolysis versus Succinimide-Mediated Deamidation Mechanisms. *J. Phys. Chem.* **2009**, *113*, 1111–1120. [[CrossRef](#)]
48. Geiger, T.; Clarke, S. Deamidation, isomerization, and racemization at asparaginyl and aspartyl residues in peptides. Succinimide-linked reactions that contribute to protein degradation. *J. Biol. Chem.* **1987**, *262*, 785–794. [[CrossRef](#)]

49. Reissner, K.J.; Aswad, D.W. Deamidation and isoaspartate formation in proteins: Unwanted alterations or surreptitious signals? *Cell Mol. Life Sci.* **2003**, *60*, 1281–1295. [[CrossRef](#)]
50. Shimizu, T.; Matsuoka, Y.; Shirasawa, T. Biological Significance of Isoaspartate and Its Repair System. *Biol. Pharm. Bull.* **2005**, *28*, 1590–1596. [[CrossRef](#)]
51. Galletti, P.; De Bonis, M.L.; Sorrentino, A.; Raimo, M.; D'Angelo, S.; Scala, I.; Andria, G.; D'Aniello, A.; Ingrosso, D.; Zappia, V. Accumulation of altered aspartyl residues in erythrocyte proteins from patients with Down's syndrome. *FEBS J.* **2007**, *27*, 5263–5277. [[CrossRef](#)] [[PubMed](#)]
52. Alderson, N.L.; Wang, Y.; Blatnik, M.; Frizzell, N.; Walla, M.D.; Lyons, T.J.; Alt, N.; Carson, J.A.; Nagai, R.; Thorpe, S.R.; et al. S-(2-Succinyl)cysteine: A novel chemical modification of tissue proteins by a Krebs cycle intermediate. *Arch. Biochem. Biophys.* **2006**, *450*, 1–8. [[CrossRef](#)] [[PubMed](#)]
53. Saletti, R.; Reina, S.; Pittalà, M.G.; Magrì, A.; Cunsolo, V.; Foti, S.; De Pinto, V. Post-translational modifications of VDAC1 and VDAC2 cysteines from rat liver mitochondria. *Biochim. Biophys. Acta Bioenerg.* **2018**, *1859*, 806–816. [[CrossRef](#)] [[PubMed](#)]
54. Guan, R.; Wang, J.; Cai, Z.; Li, Z.; Wang, L.; Li, Y.; Xu, J.; Li, D.; Yao, H.; Liu, W.; et al. Hydrogen sulfide attenuates cigarette smoke-induced airway remodeling by upregulating SIRT1 signaling pathway. *Redox Biol.* **2020**, *28*, 101356. [[CrossRef](#)]
55. Merkley, E.D.; Metz, T.O.; Smith, R.D.; Baynes, J.W.; Frizzell, N. The succinated proteome. *Mass Spectrom. Rev.* **2014**, *32*, 98–109. [[CrossRef](#)]
56. Manuel, A.M.; Walla, M.D.; Faccenda, A.; Martin, S.L.; Tanis, R.M.; Piroli, G.G.; Adam, J.; Kantor, B.; Mutus, B.; Townsend, D.M.; et al. Succination of Protein Disulfide Isomerase Links Mitochondrial Stress and Endoplasmic Reticulum Stress in the Adipocyte During Diabetes. *Antioxid. Redox Signal* **2017**, *27*, 1281–1296. [[CrossRef](#)]
57. Piroli, G.G.; Manuel, A.M.; Walla, M.D.; Jepson, M.J.; Brock, J.W.C.; Rajesh, M.P.; Tanis, R.M.; Cotham, W.E.; Frizzell, N. Identification of protein succination as a novel modification of tubulin. *Biochem. J.* **2014**, *462*, 231–245. [[CrossRef](#)]
58. Twelvetrees, A.E. The lifecycle of the neuronal microtubule transport machinery. *Semin. Cell Dev. Biol.* **2020**, *107*, 74–81. [[CrossRef](#)]
59. Ferri, A.; Cozzolino, M.; Crosio, C.; Nencini, M.; Casciati, A.; Gralla, E.D.; Rotilio, G.; Valentine, J.S.; Carrì, M.T. Familial ALS-superoxide dismutases associate with mitochondria and shift their redox potentials. *Proc. Natl. Acad. Sci. USA* **2006**, *103*, 13860–13865. [[CrossRef](#)]
60. Magrì, A.; Belfiore, R.; Reina, S.; Tomasello, M.F.; Di Rosa, M.C.; Guarino, F.; Leggio, L.; De Pinto, V.; Messina, A. Hexokinase I N-terminal based peptide prevents the VDAC1-SOD1 G93A interaction and re-establishes ALS cell viability. *Sci. Rep.* **2016**, *6*, 34802. [[CrossRef](#)]
61. Aiello, R.; Messina, A.; Schiffler, B.; Benz, R.; Tasco, G.; Casadio, R.; De Pinto, V. Functional characterization of a second porin isoform in *Drosophila melanogaster*—DmPorin2 forms voltage-independent cation-selective pores. *J. Biol. Chem.* **2004**, *279*, 25364–25373. [[CrossRef](#)] [[PubMed](#)]
62. Reina, S.; Magrì, A.; Lolicato, M.; Guarino, F.; Impellizzeri, A.; Maier, E.; Benz, R.; Ceccarelli, M.; De Pinto, V.; Messina, A. Deletion of β -strands 9 and 10 converts VDAC1 voltage-dependence in an asymmetrical process. *Biochim. Biophys. Acta Bioenerg.* **2013**, *1827*, 793–805. [[CrossRef](#)] [[PubMed](#)]
63. Guardiani, C.; Magrì, A.; Karachitos, A.; Di Rosa, M.C.; Reina, S.; Bodrenko, I.; Messina, A.; Kmita, H.; Ceccarelli, M.; De Pinto, V. γ VDAC2, the second mitochondrial porin isoform of *Saccharomyces cerevisiae*. *Biochim. Biophys. Acta Bioenerg.* **2018**, *1859*, 270–279. [[CrossRef](#)] [[PubMed](#)]
64. Webb, B.; Sali, A. Comparative Protein Structure Modeling Using MODELLER. *Curr. Protoc.* **2016**, *54*, 5–6.